Millimeter Wave Hybrid Beamforming Systems

Author:
Manish Nair

Supervisors:
Dr. Huiling Zhu
Professor Nathan J. Gomes
Professor Jiangzhou Wang

A thesis submitted in fulfillment of the requirements
for the degree of Doctor of Philosophy

Electronics Engineering

Communications Research Group
School of Engineering & Digital Arts

October 21, 2019

Abstract

The motivation for this thesis is the design of millimetre wave (mmWave) hybrid beamforming systems for supporting high user density. mmWave systems with hybrid digital-to-analogue beamforming (D-A BF) have the potential to fulfil 5G traffic demands. However, the capacity of mmWave systems is severely limited as each radio frequency (RF) transceiver chain in current sub-array mmWave base station (BS) architectures support only a particular user. Therefore, two new algorithms have been proposed for broadband mmWave systems. The algorithms operate on the principles of selection combining (SC) and principal component (PC). SC is a spatio-temporal hybrid D-A BF which has been designed to exploit multipath diversity, which is a characteristic feature of broadband propagation at mmWave. A novel low-complexity variant of SC, called low-complexity selection combining (LC-SC) has also been proposed for supporting high user density for such sub-array mm-Wave BS.

mmWave lens-antenna systems are an emergent beamforming technology. They are novel because they eliminate the requirement of traditional analog beamformers. In this context, a low-complexity beam allocation (LBA) algorithm, proposed in an earlier research, has been applied to solve the challenging problem of maximizing sum data-rates in switched-beam mmWave systems. However, there are practical limitations, such as restrictions in the number of available RF chains at the BS, sensitivity to sidelobe interference and the beam generation techniques. Using generalized beam-patterns, the maximum sum data-rates achievable in switched-beam mmWave systems is compared to fixed-beam systems by applying LBA. Then, the impact on maximum sum data-rates of actual beam-patterns, obtained from a practical mmWave lens-antenna, which have higher and non-uniform sidelobes compared to the theoretical beams, is assessed.

Non-orthogonal multiple access (NOMA) relay with hybrid digital-to-analog precoding (D-A P) as a promising solution for supporting high user densities in overloaded millimeter wave (mmWave) systems is investigated. To support high user densities in current mmWave hybrid D-A P systems, an idea based on exploiting the concept of NOMA relay to support $2K$ users per RF chain is proposed, where $2K \geq M$. To design the hybrid D-A P systems, the SC and PC algorithms are combined with NOMA relay to support significantly higher user densities.

In future research, performance impairments in beamforming assisted mmWave NOMA systems due to far-user's angle-of-departure (AoD) divergence with respect to the near-user is being investigated. This investigation is novel since most literature in NOMA considers both the near-user and far-user pairs static with respect to one another.

Acknowledgments

First of all, I bow with utmost humility and gratitude to my principal supervisors Dr. Huiling Zhu, Prof. Nathan J. Gomes and Prof. Jiangzhou Wang for their invaluable support and guidance throughout my Ph.D. Their constant encouragement and mentoring helped me to raise the potential and impact of my research. I am indeed deeply grateful to Dr. Junuyan Wang for her help and directions throughout. I am also very grateful to Dr. Qasim Z. Ahmed for his insightful discussions and advice.

During this period, I had the honour of being a member of the EU-Japan collaborative project "RAPID-5G", which funded my Ph.D. studies. I wish to thank all the members for the joint effort and technical discussions we had during the project. Especially Yigal Leiba of SIKLU Communication Ltd. for providing the measurement data of their prototype millimeter-wave 60GHz beamsteering lens-antenna system.

My gratitude goes to all staff in the School of Engineering and Digital Arts and in particular to the staff of IT technical support department for their help. Also, to my colleagues in the laboratory, Dr. M. Usman Habib, Dr. Osama Alluhaibi and Estela Carmona Cejudo for their collaboration and support.

Finally, I am indebted to my parents for their perpetual prayers and steadfast support throughout my life.

List of Publications

1. **M. Nair**, Y. Pan, J. Wang, H. Zhu, N. J. Gomes and J. Wang, "Performance Impairments in Beamforming Assisted Millimeter-Wave Non-Orthogonal Multiple Access Systems due to Far-User Angle-of-Arrival (AoA) Divergence", *to be submitted for IEEE Transactions in Wireless Communications*, 2019.

2. **M. Nair**, J. Wang, Y. Leiba, H. Zhu, N. J. Gomes and J. Wang, "Exploiting Low Complexity Beam Allocation in Multi-User Switched Beam Millimeter Wave Systems," *IEEE Access*, December 2018, pp. 1-11.

3. O. Alluhaibi, **M. Nair**, A. Hazzaa, A. Mihbarey and J. Wang, "3D Beamforming for 5G Millimeter Wave Systems Using Singular Value Decomposition and Particle Swarm Optimization Approaches," *2018 International Conference on Information and Communication Technology Convergence (ICTC)*, Jeju, 2018, pp. 15-19.

4. **M. Nair**, Q. Z. Ahmed, J. Wang and H. Zhu, "Low-Complexity Hybrid Digital-to-Analog Beamforming for Millimeter-Wave Systems with High User Density," *2017 IEEE 85th Vehicular Technology Conference (VTC Spring)*, Sydney, NSW, 2017, pp. 1-5.

5. U. Habib, A. E. Aighobahi, **M. Nair**, H. Zhu, T. Quinlan, S. D. Walker and N. J. Gomes, "Performance Improvement for OFDM-RoF Transported 60 GHz System Using Spatial Diversity and Multiplexing," *2017 IEEE International Conference on Communications Workshops (ICC Workshops)*, Paris, 2017, pp. 211-216.

6. **M. Nair**, Q. Z. Ahmed and H. Zhu, "Hybrid Digital-to-Analog Beamforming for Millimeter-Wave Systems with High User Density," *2016 IEEE Global Communications Conference (GLOBECOM)*, Washington DC, 2016, pp. 1-6.

Contents

List of Figures

List of Tables

List of Abbreviations

5G	Fifth Generation
A-BF	Analogue Beamforming
AoA	Angle-of-Arrival
AoD	Angle-of-Departure
AF	Amplify and Forward
AP	Analogue Precoding
AWGN	Additive White Gaussian Noise
BS	Base Station
CAP	Continuous Aperture Phase
CIR	Channel Impulse Response
CSI	Channel State Information
CP	Cyclic Prefix
D-BF	Digital Beamforming
D-A BF	Digital-to-Analogue Beamforming
D-A P	Digital-to-Analogue Precoding
DLA	Discrete Lens Array
D-P	Digital Precoding
KB	Kaiser-Bessel
PC	Principal Component
PSO	Particle Swarm Optimization
LC-PC	Low Complexity Principal Component
LC-SC	Low-Complexity Selection Combining
MIMO	Multiple Input Multiple Output
MMSE	Minimum Mean Squared Error
MRC	Maximum Ratio Combining
mmWave	Millimetre Wave
MUI	Multi-User Interference
MVD	Minimum Variance Distortion
NOMA	Non-Orthogonal Multiple Access
OFDM	Orthogonal Frequency Division Multiple Access
RF	Radio Frequency
RoF	Radio-Over-Fiber
RRH	Remote Radio Head
SC	Selection Combining
SE	Spectral Efficiency
SIC	Successive Interference Cancellation
SINR	Signal-to-Interference and Noise Ratio
SISO	Single Input Single Output
SNR	Signal-to-Noise Ratio

STBC	Space-Time Block Code
SV	Saleh-Valenzuela
SVD	Singular Value Decomposition
SWIPT	Simultaneous Wireless Information and Power Transfer
TDD	Time Division Duplexing
UE	User Equipment
UWB	Ultra-Wide-Band
ZF	Zero Forcing

Chapter 1

Introduction

1.1 Motivation

Multiple-input multiple-output (MIMO) technology, that is, the use of multiple antennas at transmitter (Tx) and receiver (Rx), has been recognized since the seminal works of Winters, Foschini and Gans, and Telatar, as an essential approach to high spectral efficiency (SE) and capacity. In its form of multi-user MIMO (MU-MIMO), it improves SE and capacity in two forms:

- A base station (BS) can communicate simultaneously with multiple user equipments (UEs) on the same time-frequency resources.
- Multiple data streams can be sent between the BS and each UE.

The total number of data streams (summed over all UEs in a cell) is upper bounded by the smaller of the number of BS antenna elements, and the sum of the number of all UE antenna elements. While MU-MIMO has been studied for more than a decade, the seminal work of Marzetta introduced the exciting new concept of "massive MIMO," where the number of antenna elements at the BS reaches dozens or hundreds. Not only does this allow increasing the number of data-streams in the cell to very large values, it also simplifies signal processing, creates "channel hardening" such that small-scale fading is essentially eliminated, and reduces the required transmission energy due to the large beamforming gain [105]. Massive MIMO is essential in the millimeter-wave (mmWave) bands, since the high free-space path-loss at those frequencies necessitates large array gains to obtain sufficient signal-to-noise ratio (SNR), even at moderate distances of about 100m. However, the large number of antenna elements in massive MIMO also poses major challenges:

- A large number of radio frequency (RF) chains (one for each antenna element) increases cost and energy consumption.
- Determining the channel state information (CSI) between each transmit and receive antenna uses a considerable amount of spectral resources.

A promising solution to these problems lies in the concept of hybrid digital-toanalog (D-A BF) transceivers, which use a combination of analog beamformers (A-BF) in the RF domain, together with digital beamforming (D-BF) in the baseband, connected to the RF with a smaller number of up/downconversion chains. Hybrid beamforming was first introduced and analyzed in the mid-2000s by one of the authors

and collaborators in [199],[160]. It is motivated by the fact that the number of up-downconversion chains is only lower-bounded by the number of data streams that are to be transmitted, while the beamforming gain and diversity order is given by the number of antenna elements if suitable RF beamforming is done. While formulated originally for MIMO with arbitrary number of antenna elements (i.e., covering both massive MIMO and small arrays), the approach is of interest in particular to massive MIMO. Interest in hybrid D-A BF transceivers has therefore been revived, especially following the papers of Heath, Chi-Lin I, Aryanfar et. al.[16, 77, 144], where various structures have been proposed in different papers.

The key idea of hybrid D-A BF is thus to partition the signal processing intoanalog and digital domains, which are realized by analog phase shifters and baseband digital signal processing with limited number of RF chains, respectively. By adjusting the number of available RF chains, hybrid processing offers an effective technique to balance between performance and RF chain cost. However, this approach may suffer from inefficiency of power amplifier (PA) at high carrier frequency, non-linearity of PA, and heat dissipation and imbalances/nonideality of the phase shifter responses. Besides, compared to fully digital processing, the precoding/combiner design and channel estimation for hybrid D-A BF processing become much more challenging, especially for wideband mmWave systems. A potential technique to mitigate the above issues is to realize the hybrid D-A BF architecture by employing switched-beam mmWave systems together with lensantenna arrays [195, 194, 148, 33, 69, 190].

A particular limitation in switched-beam systems, however, is the frequent hand-offs when the user moves from the sector of one beam to another, as the flexibility of continuous steering is not provided [192]. Although codebook based beamforming systems [82, 36, 141] have addressed the hand-off issue by beam-training and beam-alignment, however, they cannot be directly adopted into switchedbeam systems. Moreover, inmmWave systems, the beams have narrow beamwidths, and together with a large number of predefined beams, codebooks cause very high frequency hand-off having a huge signaling overhead. Nevertheless, despite these disadvantages, switched-beam approach is economically expedient, easy to deploy and maintain as compared to completely adaptive systems in [130],[83], and, in conjunction with lens-antennas, simplifies mmWave practical hardware design.

While each RF chain in hybrid D-A BF BS can accommodate a large number of antennas, scaling up the number of users in practice, however, and tracking them by solely using the angle of azimuth becomes impractical in 5G. Therefore, angles of elevation and azimuth will be utilized to track and separate them from one another. Therefore, the three dimensional (3D) beamforming systems have received great interest recently because of the spatial diversity advantage and capability for full-dimensional beamforming, making them promising candidates for practical realization of mmWave systems [203],[176].

The 60GHz band has attracted substantial interest in recent research due to its unlicensed 7GHz frequency band [93]. When adopting 60GHz in indoor environments, the integration of mmWave front end wireless links with Radio-over-Fiber (RoF)

transmission is an attractive approach [205]. Properties of optical fiber communication such as ultra-high capacity and low loss propagation make it easy to realize a robust architecture for data transport between the Central Unit (CU) and the remote antenna unit (RAU). The RoF part serves as a backbone for the whole network and provides centralized control [39].

RAU communication with the mobile user (MU) at 60GHz can then be achieved using compact integrated transmitter and receiver units. Since 60GHz wireless links rely on line-of-sight (LoS) conditions with narrow-beam antennas to compensate for the high path-loss [73], the coverage for multiple MU locations is still a challenge for 60GHz communication systems that needs to be addressed, and has been highlighted in recent research [113]. Theoretical analysis has been presented for the indoor coverage of 60GHz systems [110] and the use of repeaters has been proposed to address the coverage issue [153]. However experimental implementations for 60GHz transmission which show coverage improvement are lacking. Furthermore, such experimental implementations, in order to assess their performance and feasibility at longer transmission distances, require the careful modeling of the 3D mmWave channel environment.

Non-orthogonal multiple access (NOMA) has been proposed as one of the future wireless multiple access techniques for fifth generation (5G) cellular networks, where all the users are served at the same time, frequency and code in the works of Zhu and Wang et. al. in [75]. Furthermore, MIMO offers excess degrees of freedom to further improve the system throughput of NOMA [54]. In scenarios with single-antenna nodes, channels are scalar and it is straightforward to order the users based their channel conditions. However, in MIMO, channels are in form of matrices or vectors, which makes the ordering of users complex. Therefore, the key challenge in MIMO-NOMA is the design of optimal precoding and detection strategies [54]. In [80], different beams were assigned to different users, and the quality-of-service (QoS) was satisfied by forcing the beams to follow a predefined order. In [54], MIMO-NOMA was reduced to separated single-inputsingle-output (SISO)-NOMA system by designing a detector which satisfied a predefined energy constraint. Signal alignment was applied in [56] to decompose MIMO-NOMA into SISO-NOMA channels, where a ZF precoding scheme was designed to force signal alignment between two users from the same pair. Nevertheless, supporting a high user density in mmWave systems and understanding hitherto unexplored, to the best of the author's knowledge, performance impairments in multi-user mmWave NOMA systems is a key future research focus for us. In the following section, building upon these motivations, the objectives the research have been addressed in further detail.

1.2 Objectives of the Research

Hybrid D-A BF proposed in [77],[144], where the D-BF is equivalent to an identity matrix and the A-BF is equivalent to the hermitian of the channel. It is also shown that the overall capacity of the hybrid D-A BF system is limited as compared to the complete D-BF system because of the number of RF chains [77]. The major drawback in this type of hybrid D-A BF structure is that each RF chain can only support a

particular user [77]. Therefore, the maximum number of users that can be supported by the BS cannot exceed the number of RF chains [77]. This will severely limit mobile capacity in future mm-Wave networks especially in high density user environments like train stations, stadiums or shopping malls. Therefore, new hybrid D-A BF schemes are required, which can support multiple users by employing a BS RF chain to achieve similar capacity gains as promised by the D-BF systems. Superposition coding can be applied to the Tx symbols on a single stream to support multiple users through a RF chain. However, it cannot serve multiple users simultaneously as only a single 3 dimensional (3D) beam is formed [57].

Hence, firstly, new hybrid D-A BF algorithms for supporting multiple users per RF chain at mmWave have been proposed in this thesis. With these employed techniques, each user will have its own separate 3D beam assisting in supporting multiple users simultaneously. These algorithms are implemented with the help of selection combining (SC) and principal component (PC). Our proposed hybrid D-A BF algorithms also accounts for the 3D mm-Wave channel for a multiuser system which is generated when planar antenna arrays are deployed [15],[187].

Secondly, a low complexity-selection combining (LC-SC) hybrid D-A BF has been proposed, which is a space-time A-BF technique, that has a lower computational complexity as compared to the previously proposed SC.

In multi-usermmWave systems, adaptive-beam and switched-beam based beamforming have been investigated [130],[83]. In adaptive beamforming, codebookbased signal processing algorithms are utilized for generating beamforming weights at the BS, which are continuously adjusted to simultaneously generate and steer several directional beams towards the respective mobile users [65],[138]. However, such a strategy requires obtaining and continual updating of the direction-ofarrival (DoA) of signals from all mobile users, along with full CSI. Furthermore, the generation and update of the beamforming codebook involves computationally intensive matrix operations such as a pseudo-inverse [82]. [36] proposes a codebook of beamforming vectors over an initial beam alignment phase, followed by a learning phase where each mobile user estimates the "top-P" beams, and reports the beam indices as well as the received signal-to-interference plus noise ratios (SINR) to the BS.

However, such an approach can incur considerable feedback overhead between the mobile users and the BS. In [141], a combination of generalized eigenvector codebook and SINR based codeword selection metric with limited feedback is shown to lead to improved ergodic sum data-rates. However, this cannot be adopted into switched beam based beamforming systems. This is because, by contrast, switched-beam based beamforming systems have to choose from one of several predefined directional spatial beams within a cell in order to enhance the received SINR at the mobile user [136]. The BS determines the beam that is best aligned to the user signal's DoA, and switches to that beam to communicate with the user. The cell is sectorized by many narrow beams with each beam serving an individual user or a group of users. The spatially separated directional beams lead not just to an increase in the possible reuse of frequency channels by reducing potential inter-beam-interference, but also to an increase in transmission range [85],[107].

In switched-beam systems where the number of possible beams N is much larger than the number of users K, the low complexity beam allocation (LBA) algorithm, proposed in [175], offers a low computational complexity beam-user search approach to what could be a significant algorithmic problem of maximizing sum data-rates [45, 43, 183, 172]. For example, the simplest greedy algorithm in [172] has a complexity of $\mathcal{O}(KN^2)$, which is too high when the number of beams is large. By contrast, LBA algorithm attains nearly the same sum-data rate as compared to an optimal brute-force search based beam allocation, albeit with a much lower complexity of $\mathcal{O}(K \log N)$. In LBA, only those beams with the highest user directivity, known as active beams, are selected for data transmission, and then, to maximize sum data rate, only those users which have the highest receive SINR are selected. The remaining users are discarded and the unselected beams are turned off, focusing transmit power only onto the selected beams/users, and reducing inter-beam interference through having fewer beams. However, in [175], practical limitations, including the number of available RF chains and higher and non-uniform sidelobe levels, were not considered.

Hence, thirdly, using generalized beam-patterns, the maximum sum data-rates achievable in switched-beam mmWave systems compared to fixed-beam systems by applying LBA is presented. Then, the impact on maximum sum data rates of actual beam-patterns, obtained from a practical mmWave lens antenna, which have higher and non-uniform sidelobes compared to the theoretical beams, is assessed.

Fourthly, as a guide for practical wireless system design, benchmarks are established for relative sidelobe levels that provide acceptable sum data-rate performance when considering generalized beam patterns.

Beamforming for planar arrays has been implemented earlier in [86, 147, 101]. In [86], the 3D beamforming is investigated from the array factor point of view. However, the beamforming weight vector was designed based on elevation angle vector only without exploiting the both angles. To address this issue, researchers in [86, 147, 72] designed 3D beamforming weight vectors based on minimum variance distortion (MVD). The MVD approach finds the weight vector in $x-$axes and the weight vector in $y-$axes. Nevertheless, 3D mmWave channel measurements in [61] showed that kronecker product for x and $y-$axes is required which means a joint xy-axes 3D beamforming weight vectors are demanded. In this case, MVD cannot achieve the optimal solution unless the beamformer weights are independent, which is not this case here because of the kronecker product.

Hence, fifthly, two new beamforming algorithms with aim of designing joint $xy-$axes weights vectors is proposed. These algorithms utilize both angles of azimuth and elevation to maximize the SNR of the system, unlike other algorithms which maximize the SNR of the system in one dimension[86, 147, 72]. *The proposed algorithms work on principle of singular value decomposition (SVD)*[46],[135] *and particle swarm optimization (PSO).*

In the SVD approach, the channel matrix is factorized into singular values which are then used to design the weights of the beamformer. To reduce the complexity of SVD, a second approach based on PSO is proposed. PSO is a stochastic iterative

optimization technique which neither requires any matrix inversion nor any matrix factorization to find the weights of the beamformer.

60GHz system architectures with Radio over Fiber (RoF) transport and integrated transmitters/receivers provide a comprehensive solution for future mobile systems. Since 60GHz communication relies on line-of-sight (LoS) conditions and narrow-beam antennas to compensate the high path-loss, it has limitations in terms of coverage for multiple user locations. A proof of concept to improve the performance of 60GHz transmission to multiple user locations in indoor environments by using spatial diversity and spatial multiplexing has been demonstrated by extending a previous research by N.J. Gomes et. al. [74]. The experimental setup consists of OFDM-RoF transport and upconversion to 60GHz using an integrated transmitter unit. Wireless transmission through 0.5m, 1m and 1.5m channels and performance analysis has been conducted at different user locations. Nonetheless, in order to extend the results to longer distances, simulations by modelling the experimental clustered multipath mmWave environment are necessary.

To perform theoretical analysis for mmWave transmission systems, channel modeling at 60GHz has always been a challenge due to high path-loss and broadband, and conventional channel models cannot be applied since they are based on assumptions of narrowband.

Hence, sixth-ly, in this thesis, the propagation model which applies a modified Saleh Valenzuela (SV) [64] *channel model which accurately models a broadband mmWave channel is used to analyze the system performance at extended indoor distances. Furthermore, in order to experimentally analyze the performance of Alamouti STBC and ZF algorithms, the channel estimation at various transmitter and receiver locations have been performed.*

In heterogeneous networks, there is redundant information inherited by users in NOMA systems, i.e., users with better channel conditions can decode the information sent to the other users [56]. This makes the application of NOMA relays appealing in heterogeneous systems [56] and [55]. In NOMA relays, the term relay-user denotes the near-user, and the term destination-user is used to denote the far-user. A relay assisted NOMA system has been introduced in [115], SWIPT has been applied to achieve data transmission at the destination-user by simultaneous symbol transmission over two orthogonal time-slots. Here, in the direct transmission phase, the BS transmits a superposed NOMA signal to both the relay and destination users. The relay-user applies SIC and decoding, i.e. it first decodes the destination-user's signal, subtracts it from the received signal, and decodes its own signal next. The destination-user decodes its own signal directly. Then in the relay phase, the relay-user forwards the destination-user's message, and the destination-user combines this with the message received from the BS earlier, using maximum ratio combining (MRC).

However, these proposed systems have not explicitly considered high user density that will be prevalent in mm-Wave environments. Therefore, it is essential to design new schemes in NOMA based cooperative relay systems which can support high

density of users by employing a single RF chain while maintaining the user data-rate than in the current hybrid D-A BF techniques [77] and [144] or commonly used NOMA systems in [100] and [42].

Motivated by this issue, seventh-ly, the two hybrid D-A BF algorithms, SC and PC, proposed in this thesis have been extended to operate a relay NOMA based SWPIT system employing amplify-and-forward (AF).

Lastly, certain hitherto unexplored issues in beamforming assisted mmWave NOMA systems due to the AoA divergence between near-user and its corresponding far-user pair are being explored. This forms the framework and scope of the author's future research objectives.

Having elaborated in detail on the objectives of the research, the contributions of the thesis are concisely summarized as follows.

1.3 Contributions of the Thesis

The unique contributions of this thesis include

- Two new hybrid D-A BF algorithms for supporting multiple users at mmWave is proposed. With these employed techniques, each user will have its own separate 3D beam assisting in supporting multiple users simultaneously. These algorithms are implemented with the help of selection combining (SC) and principal component (PC). multi-user interference (MUI) from the beamformed signals. Therefore, a low complexity MUI cancelling technique is proposed at the receiver (Rx).
- A low-complexity adpatation of SC, known as low-complexity selection combining (LC-SC), has been proposed. LC-SC is a space-time A-BF technique which attains lower computational complexity as compared to the SC, yet the reduction in capacity gains are fairly marginal.
- Two 3D beamforming algorithms with aim of tracking users in both the azimuth and elevation planes have been proposed. Our proposed beamforming algorithms operates based on the principles of singular value decomposition (SVD) and particle swarm optimization (PSO). Furthermore, these beamforming algorithms are designed to have limited or negligible side lobes, which cause less interference to the other users operating in the same cell. been chosen over other channel models, such as Rayleigh or Rician channel which are valid only for narrowband propagation environments [64],[7]. Furthermore, other channel models such as WINNER 2, which have been previously used at mmWave, are also narrowband and hence cannot be applied to the 305MHz bandwidth system.
- A low complexity beam allocation (LBA) algorithm has been applied to a switched-beam mmWave system with a limited number of RF chains. Generalized, theoretical beam patterns based on element fed arrays, having an idealized main lobe with fixed beam gain and angular resolution, along with

exponentially decaying sidelobes, have been developed. Using these theoretical beam patterns, the performance benefit of switched-beam systems, using the LBA, over comparable fixed-beammmWave systems, which are practically simple but constantly generate fixed numbers of beams, are shown.

- A relay NOMA based mmWave system is proposed to support high user density in mmWave systems having M antennas per RF chain, firstly. The two methods of designing hybrid D-A BF based on selection combining (SC) and principal component (PC) have been incorporated in this NOMA system, which can support up to K user pairs per RF chain in the mmWave relay NOMA system.

1.4 Thesis Outline

The thesis is based on eight chapters, including this one which presents the objectives, contributions and an outline of the other chapters. The detailed contents for rest of the chapters is as follows:

Chapter 2 presents a detailed study of beamforming system architectures and approaches. A review of smart antenna systems, array radiation patterns, array factor, various beamforming techniques in literature, including lens-antenna assisted beamforming has been presented. It also presents a background on mmWave beamforming, and describes mmWave propagation characteristics, ultra wideband (UWB) communication and indoor mmWave beamforming.

In chapter 3 two types of 3D beamforming algorithms are proposed for mmWave system. SVD, obtained by the factorizing the 3D channel into its unitary matrices and singular values, and PSO, which an iterative algorithm that uses swarm optimization technique to obtain the global best solution, are analyzed.

Chapter 4 introduces hybrid D-A BF by exploiting clustered multipath diversity for high user density millimeter wave systems. After describing the 3D mmWave clustered multipath channel model, hybrid D-A BF with SC and a lower complexity PC are presented and computational complexity analysis is carried out.

Chapter 5 presents the low-complexity selection combining (LC-SC) proposed for supporting high user density for mm-Wave BS. which is an low computational complexity adaptation of SC. After describing the space-time LC-SC A-BF, beamformer computational complexity analysis is shown. Simulation results discuss the trade off in spectral efficiency (SE) as a function of SINR and the number of massive MIMO antennas, when compared to the previously proposed SC.

Chapter 6 describes the modeling of mmWave beamforming for an indoor experimental RoF set up. The experiential set up and results are first presented. Then, the experimental results are extended by applying the 3D mmWave modified SV channel model simulations.

Chapter 7 presents the exploitation of low complexity beam allocation (LBA) in multi-user switched beam mmWave systems. After describing an application scenario for switched-beam mmWave systems, LBA is introduced to serve multiple users with limited RF chains in a switched-beam mmWave system with idealized beams. Maximum sum data-rates expression is derived. User scheduling, SINR constraints and user fairness are discussed. Fixed-beam benchmarkes are introduced, and the coverage of fixed and switched-beam systems are analyzed. Sum data-rate of switched-beam systems with idealized beams are obtained. Then, mmWave beam generation with lens-antenna is discussed, and, the sum data-rates of the lens-antenna beams and idealized beams are compared. Lastly, the impact of sidelobe interference on sum data-rates is presented.

In Chapter 8, the two hybrid D-A BF algorithms, SC and PC, proposed in Chapter 4 have been extended to operate a relay NOMA based SWPIT system employing amplify-and-forward (AF) for effectively doubling number of users supported, and by extension, the capacity.

Chapter 9 concludes the work presented in this thesis. It also highlights the future work in this field that is being currently investigated.

Chapter 2

Background Study and Literature Review: Beamforming for Millimeter Wave Communications

2.1 A Brief History of Millimeter Wave Cellular Communications

Data traffic in the manifold wireless communications application categories is projected to increase significantly in the foreseeable future [48]. In order to meet this challenging demand, the issue of capacity enhancement of wireless links needs to be addressed. In this backdrop, mmWave technology for indoor and outdoor wireless communication has emerged as a new frontier to deploy high speed data links. The feasibility of indoor implementation of mmWave links has been successfully demonstrated by stakeholders [179],[81]. This is evident from the emergence of standards which include the IEEE 802.15.3c [1] wireless personal area network (WPAN), wireless high definition (WiHD) [180], European computer manufacturers association (ECMA) [63], and IEEE 802.11ad wireless local area network (WLAN) [2]. mmWave technology is also being envisaged as a promising alternative for 5G cellular networks [143], [30].

mmWave communications span a wide frequency range from 30GHz to 300 GHz offering exciting new opportunities to utilize the spectrum for broadband applications. A maximum data rate of 6.756Gbps is achievable using suitable modulation and coding schemes under the ambit of the IEEE 802.11ad standard developed for 60GHz indoor communications [2]. This has spurred further interest to explore other frequencies in the millimeter wave spectrum such as the frequency bands in the 28˜38GHz and 70˜90GHz range, particularly for outdoor applications in 5G cellular mobile systems, local multipoint distribution services (LMDS), cellular backhaul and intra-cell communication systems.

Moreover, the Federal Communications Commission (FCC) in the United States recently increased the maximum outdoor emission power limits for operation in the unlicensed millimeter wave band from 57 GHz to 64 GHz [66]. This development is expected to provide the impetus for further research to harness the 60 GHz band for new applications with improved system link margin.

The gain realized through antenna beamforming can compensate for the excessive path and penetration losses at millimeter wave frequencies. The mmWave channel characteristics, to a large extent, dictate the choice of physical (PHY) layer and medium access control (MAC) layer schemes as well as the hardware implementation [191],[53]. From this perspective, multiple antenna technology is a key enabler to efficiently utilize the mmWave band as it can increase the link capacity by employing directional communication. The small wavelengths in the mmWave regime has facilitated array architectures embedded into portable devices with a compact form factor, making beamforming an attractive proposition [164].

Multiple antennas can be used at the transmitter and/or receiver to achieve multiplexing gain (simultaneous transmission of parallel data streams over multiple antennas to improve bit error rate), diversity gain (redundant data streams using space-time coding to reduce bit error rates), or antenna gain (beamforming to improve the signal-to-noise ratio (SNR) at the receiver and to suppress co-channel interference in a multiuser scenario) [126]. The impact of directional multi-antenna beamformers with suitable antenna configurations is also shown to improve SNR, enhance the Ricean factor gain, and reduce the root-mean-squared (RMS) delay spread due to multipath dispersion at the receiver [189].

Signal processing for fixed weight and adaptive beamforming in traditional microwave systems with limited number of antenna elements can be conveniently performed in digital baseband. However, for large scale antenna mmWave systems, digital baseband beamforming is prohibitively complex and costly due to the requirement of a dedicated radio frequency (RF) chain for each antenna element and higher dynamic range for analog front end RF circuitry. Also, sophisticated adaptive beamforming methods have not been extensively used thus far in millimeter wave communications due to increased signal processing overheads and latency. Thus, low complexity analog beamforming methods have been largely adopted for short range (4˜10m) indoor mmWave communications in the 60GHz band [192],[88]. Based on considerations of high propagation and penetration losses, the focus for outdoor mmWave communications has been on frequency bands centered at 28GHz, 38GHz, 73GHz, and in the 81˜86GHz range[164]. Due to hardware cost constraints, and the need for multi-stream/multi-user support, a promising method known as hybrid beamforming has emerged as a leading contender for outdoor mmWave communications.

2.2 Classical Beamforming System Architectures and Approaches

Classically, beamforming is essentially a spatial filtering operation typically using an array of radiators to capture or radiate energy in a specific direction over its aperture. The improvement achieved over omnidirectional transmission/reception is the transmit/receive gain.

Modern communication systems deploy smart antenna systems, which can combine array gain with diversity gain along with interference mitigation to further increase

the capacity of the communication link. This is achieved by electronic beam steering using a phased array, which is a multi-element radiation device with a specific geometric configuration.

The output spatial power distribution, termed as the array radiation pattern, is determined by the vector sum of the fields radiated by individual elements. It can be expressed in terms of the individual element radiation pattern and the array factor, which is a function of the array geometry and amplitude/phase shifts applied to individual elements[29]. Fig. 1 depicts the typical system configurations for antenna beamforming using phased arrays[137].

2.2.1 Fixed Weight Beamforming

In fixed weight beamforming, constant antenna weights (amplitude and/or phase) are applied in the analog or digital domain to the array elements to steer the main beam[170, 167, 103, 22].

2.2.2 Adaptive Beamforming

As compared to fixed weight beamforming, a more powerful technique is adaptive beamforming since it has the ability to adapt (in real time) the RF radiation pattern. Adaptive beamforming is particularly useful in mobile communications where a recursive update of the weight vector is required due to the time varying direction-of-arrival (DoA). Adaptive arrays utilize efficient signal-processing algorithms [72] to continuously resolve the desired, multipath, and interfering signals. As depicted in Fig. 2, the antenna weight vectors are continuously updated to steer the main beam dynamically in the desired direction. The optimal weight vectors are determined based on a specified error minimization criteria. Training based algorithms require only one reference signal whereas blind methods require DoA estimate, and the rest of the information is obtained from the received signal.

2.2.3 Analog Baseband and Analog RF Beamforming

In the temporal domain, antenna weights can either be applied using time delay elements or equivalently phase shifting the signal before radio frequency upconversion (analog baseband beamforming) or after the upconversion stage (analog RF beamforming) [114],[94].

2.2.4 Digital Beamforming

In digital beamforming, the control signals originate at the digital baseband, and processing for beamforming is done using a digital signal processor, which provides greater flexibility with more degrees of freedom to implement efficient beamforming algorithms. As shown in Fig. 2.1, the method requires a dedicated RF chain

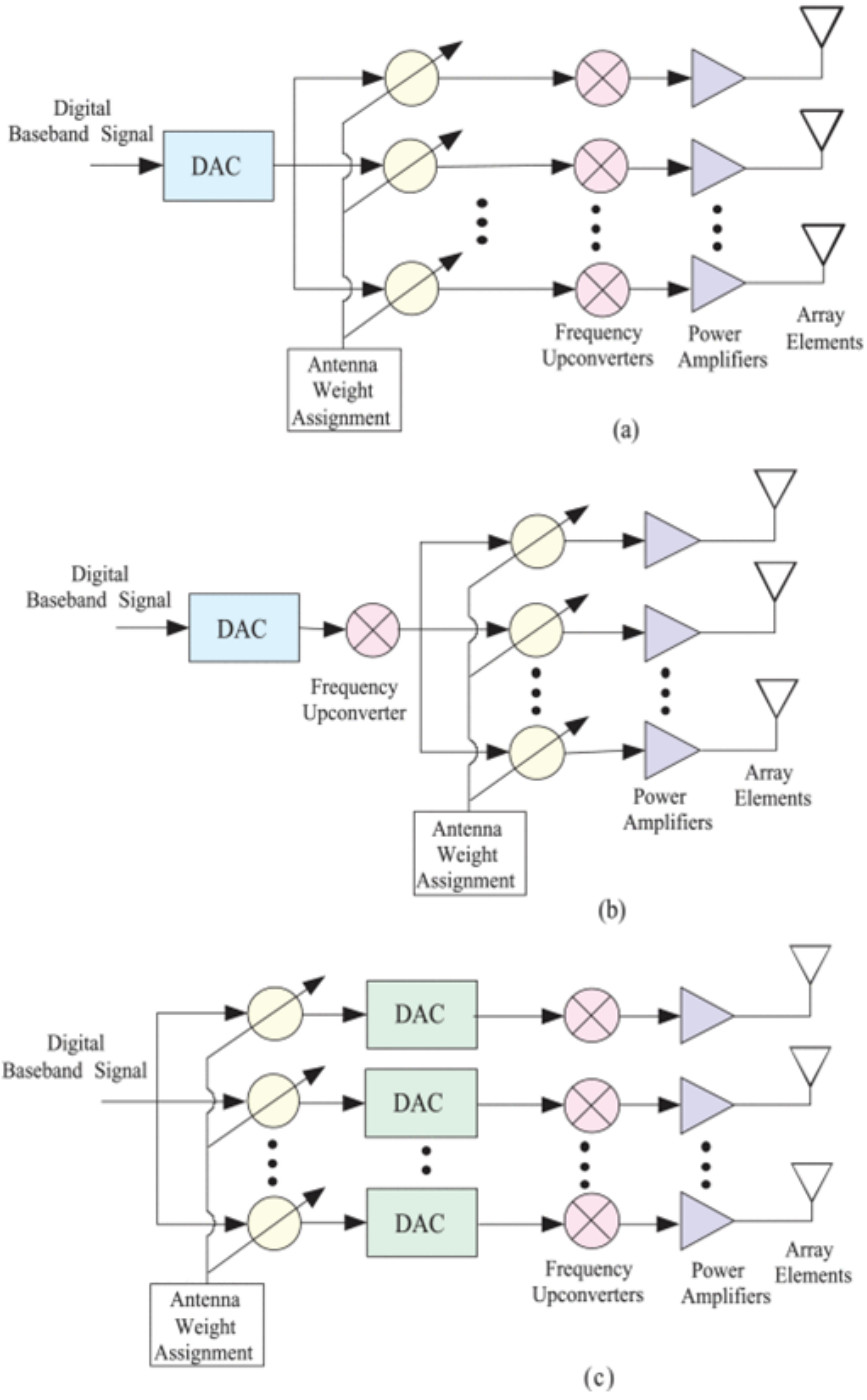

FIGURE 2.1: Fixed weight transmit beamforming architectures: (a) Analog baseband, (b) Analog RF, and, (c) Digital baseband [22].

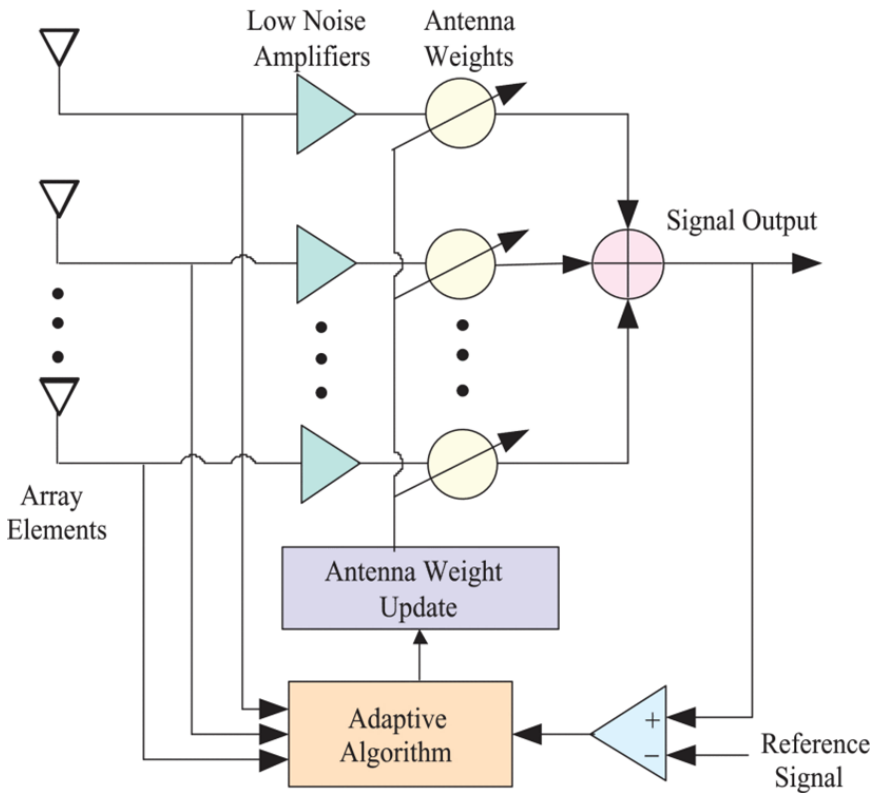

FIGURE 2.2: A general adaptive (receive) beamforming architecture [72].

for each antenna element, which results in high power consumption and a complex architecture.

2.2.5 Frequency Domain Beamforming

In frequency domain beamforming, the signal is processed entirely in the frequency domain using transform domain tools followed by inverse transforming the result[94].

The beamforming procedure adopted for a given application largely depends upon the capabilities of the transmitter and the receiver, the radio channel characteristics, and the bandwidth of the transmitted signal. At the transmitter, beamformers can be employed between the signal source and the radiating elements to direct the resulting radiated electromagnetic field in three dimensional space based on receiver localization, a process termed as transmit beamforming.

In receivers, beamforming can be realized between the antenna arrays and receiver modules to control the relative spatial sensitivity of the antenna to signals in its capture range, a technique referred to as receive beamforming, which generally requires DoA estimation. Classical DoA estimation methods [35, 104, 158, 159] first determine the spatial spectrum, and then estimate DoA by identifying the local maxima of the spectrum. However, the classical methods are characterized by high computational complexity. Sub-space based methods [150],[145] aim to separate the observation space in a signal subspace, containing only useful information, and its

orthogonal complement, called noise subspace. This decomposition results in robust spectral analysis, and improves the spectral resolution significantly, thus delivering high angular resolution of the arriving signal direction.

2.2.6 Implicit and Explicit Beamforming

In a multipath environment, implicit and explicit beamforming [49],[116] can be employed to calculate antenna steering vectors. In implicit (open loop) beamforming, the transmitter performs a channel sounding procedure based on the channel reciprocity assumption. It sends training sequences to calibrate the phase-shift differences due to multipath in order to calculate the elements of the steering matrix. The advantage of this method is in terms of its reduced overhead, and works well in a scenario where the transmitter may have better array processing capabilities than the receiver.

The problem in explicit beamforming, however, is to accurately perform channel calibration, due to the underlying reciprocity assumption. In explicit (closed loop) beamforming the receiver estimates the channel, and the information is fed back to the transmitter. There are three commonly used modes of explicit beamforming;

- The uncompressed mode where the feedback comprises of the steering matrix as calculated by the receiver,
- The compressed mode, in which the receiver sends a compressed steering matrix to the transmitter, and,
- The channel state information (CSI) feedback mode, where the receiver simply sends back the raw channel estimates to the transmitter for calculation of the steering matrix. Generally, explicit transmit beamforming outperforms the implicit method, albeit with an increase in computational complexity and overhead.

2.2.7 Opportunistic Beamforming and OSDMA

One approach to reduce feedback requirements is to employ the opportunism inherent in multiuser communication systems [173],[152]. Probably the best known approach is opportunistic beamforming (OBF) [173, 152, 47]. With OBF, the base station randomly selects a beam for transmission and uses it to send a training sequence. The users send back their SNR corresponding to this beam and the base station schedules the user with the highest SNR (or uses another scheduling rule) for transmission. The OBF approaches the performance of the optimal beamforming strategy for a large number of users [173].

In opportunistic space division multiple access (OSDMA) the BS sends orthogonal beams [151]. In this case each user reports the best beam and their SINR to the BS. The BS then schedules transmissions to multiple users based on the received SINR. As with OBF, this approach requires a large number of users to approach full-CSI capacity gains.

TABLE 2.1: A classification of beamforming approaches.

Based On	Beamforming Approach
Weight Vector Application	1. Fixed Weight Beamforming 2. Adaptive Beamforming a. Training Based b. Blind
Signal Domain	1. Frequency/Transform Domain Beamforming 2. Space-Time Beamforming a. Analog Beamforming · Baseband · RF b. Digital Beamforming
Location	Tramsmit Beamforming Receive Beamforming
Channel Estimation	1. Implicit Beamforming 2. Explicit Beamforming
Signal Bandwidth	1. Narrowband Beamforming 2. Wideband Beamforming
Received Data	1. Data Independent Beamfroming 2. Statistically Optimum Beamforming

2.2.8 Statistically Optimum Beamformers

Unlike data independent beamformers, the statistics of array data are used by statistically optimum beamformers to determine optimum antenna weights for a specified response in signal/interference scenarios [120]. Table 1 classifies these discussed beamforming approaches for reference.

2.3 Millimetre Wave Beamforming for Massive MIMO

Due to the high propagation loss at mmWave, transmit and receive antenna gains are crucial in the design of a feasible and sustainable mmWave communication link. To realize efficient system level optimization for practical mmWave beamforming, various aspects including signal processing complexity, power efficiency, and hardware cost need to be addressed.

Path Loss: Due to smaller wavelengths at mmWave frequencies, the free space propagation loss, which according to the Friis law is inversely proportional to the wavelength, is several dB more as compared to the legacy sub−6GHz [67] bands. However, for the same antenna aperture size, the gain of a directional antenna is considerably more as compared to an omnidirectional or sectored pattern antenna used in sub−6GHz systems. Thus, the excess free space propagation loss in mmWave can be compensated using directional antennas with beamforming. Albeit,

- mmWave signal penetration losses [53], particularly through concrete wall, are substantially high.
- Attenuation due to rainfall has an adverse impact on mmWave signal propagation depending on the rainfall rate [164],[200].
- Absorption due to atmospheric gases (ITU-R P.676 − 10) at certain frequencies including 60GHz can lead to considerable attenuation if transmission distances exceed an order of few tens of metres.

Therefore, the 60GHz band is only suited for indoor short range millimeter wave communication for a maximum Tx-Rx separation distance of about 10m, whereas the 28GHz, 38GHz and 73GHz bands are being investigated for their potential to support outdoor mmWave communication for medium range links of over 200m.

Clustered Multipath Structure: Since millimeter wavelengths are small compared to the size of the objects encountered during propagation, diffraction is poor leading to pronounced shadowing [164, 192, 88]. Also, though scattering occurs due to irregularities and roughness of surfaces, the scattered multipath components at the receiver are few in number due to the high path loss. Consequently, mmWave channels exhibit clustered multipath structure with a limited number of clusters arriving from discrete directions the receiver. A cluster is a group of multipath components with similar angular properties.

Dominant LoS Component: The LoS component accounts for a sizable percentage of received power, and is crucial to the operation of a relaible mmWave link. mmWave propagation is susceptible to shadowing [143], and LoS obstruction by objects such as buildings could lead to signal outage.

Wideband Communication: mmWave channels are expected to support wideband signal propagation [124]. In certain cases the bandwidth being of the order of a few GHz. This leads to SNR degradation due to wideband noise. Low SNR prior to establishment of a beamformed link is a particularly concerning problem since array gains are limited during the training phase due to the use of broader beam width for user localization and association. Also, despite large channel coherence bandwidth, mmWave communication systems will require sophisticated equalization schemes due to very short symbol periods of the order of a few ns [164].

3**D spatio-temporal modeling:** In order to overcome excessive path loss, mmWave communications are essentially directional in nature. Therefore, the spatial propagation characteristics, primarily the azimuth and elevation transmit angle-of-departure (AoD) and angle-of-arrival (AoA) statistics, can be leveraged to ensure reliable communication. Holistic 3D MIMO directional channel models [165] with joint spatial and temporal statistics will aid the design of efficient beamforming for mmWave communication systems.

Performance of indoor millimeter wave in the presence of multipath is significantly improved using directional antennas. Simulation using the ray tracing approach and backed with propagation measurements [122] result in a RMS delay spread of less than 5ns which could be realized over a wide area using directional antennas with a 3dB narrow beamwidth of 10 degrees using a standard horn antenna. In [123] it is shown that the combined use of directional antennas and circular polarization results in further reduction of the multipath spread by a factor of half.

For indoor WPAN [121] the introduction of spatial reuse mode through beamforming using steerable antenna with 8 parallel communication links increases the overall millimeter wave WPAN system throughput by $3-5$ times in comparison with the conventional time division mode.

Measures adopted to counter LoS blockage include beam steering towards NLoS links and use of reflectors [21], and relay-based schemes [188]. A multiple access point (AP) diversity scheme has been explored in [198] to improve throughput in the event of LoS blockage. Authors in [155] have proposed a multi-hop MAC architecture to recover from link blockages.

The study of intrinsic capacity improvement analysis [79] for orthogonal frequency division multiplexing (OFDM) reveals that a hybrid approach by combining spatial multiplexing and beamforming is a promising alternative to achieve optimum performance in low as well as high SINR regimes. The PHY and MAC layer aspects of beamforming are specified in the IEEE802.11ad standard, which intended for indoor WLAN operation in the 60GHz band.

Emerging applications for outdoor mmWave communications range from dense cellular networks with limited coverage (upto 200m) to wireless backhaul [143]. Frequency bands centered around the 28GHz and 38GHz are under active consideration for mmWave cellular and backhaul system deployment. To support multi-user/multistream transmission, base stations are expected to utilize large antenna arrays, with limited MIMO support at mobile stations.

Although analog beamforming has been the mainstay for indoor mmWave systems, the need for additional signal processing to facilitate multi-stream transmission, and interference management in a multi-user environment mandates the requirement of digital baseband precoding and combining. Low power MIMO architectures with analog beamforming and baseband processing have been proposed in literature [171]. Besides, MIMO based RF-baseband antenna selection schemes have been well explored in literature [199],[160]. However, the suitability and performance of these schemes for wideband mmWave outdoor channels remains to be seen. On the other hand, an exclusive digital beamforming architecture (widely used for MIMO precoding in traditional microwave communications) is infeasible due to increased hardware complexity and power consumption owing to the large number of RF chains which scales with the number of antenna elements.

In essence, unlike indoor mmWave systems, it is expected that beamforming architectures for outdoor millimeter wave communications will leverage the benefits of analog as well as digital beamforming. In this context, a hybrid beamforming architecture [96] with analog phase shifters has emerged as an attractive proposition

for next generation millimeter wave massive broadband (MMB) systems, and heterogeneous networks (HetNets) [125]. The hybrid beamforming scheme assumes particular importance in the context of large scale antenna systems (LSAS) in view of its reduced hardware cost [77],[144].

The principle of hybrid beamforming is to divide signal processing into digital and analog domains in order to support multi-stream (and possibly multi-user) communication with an objective to maximize the sum rate with minimum interference. The hybrid beamforming architecture consists of a limited number of RF chains which facilitate multi-stream digital baseband processing followed by analog (baseband or RF) processing to realize antenna beamforming gain.

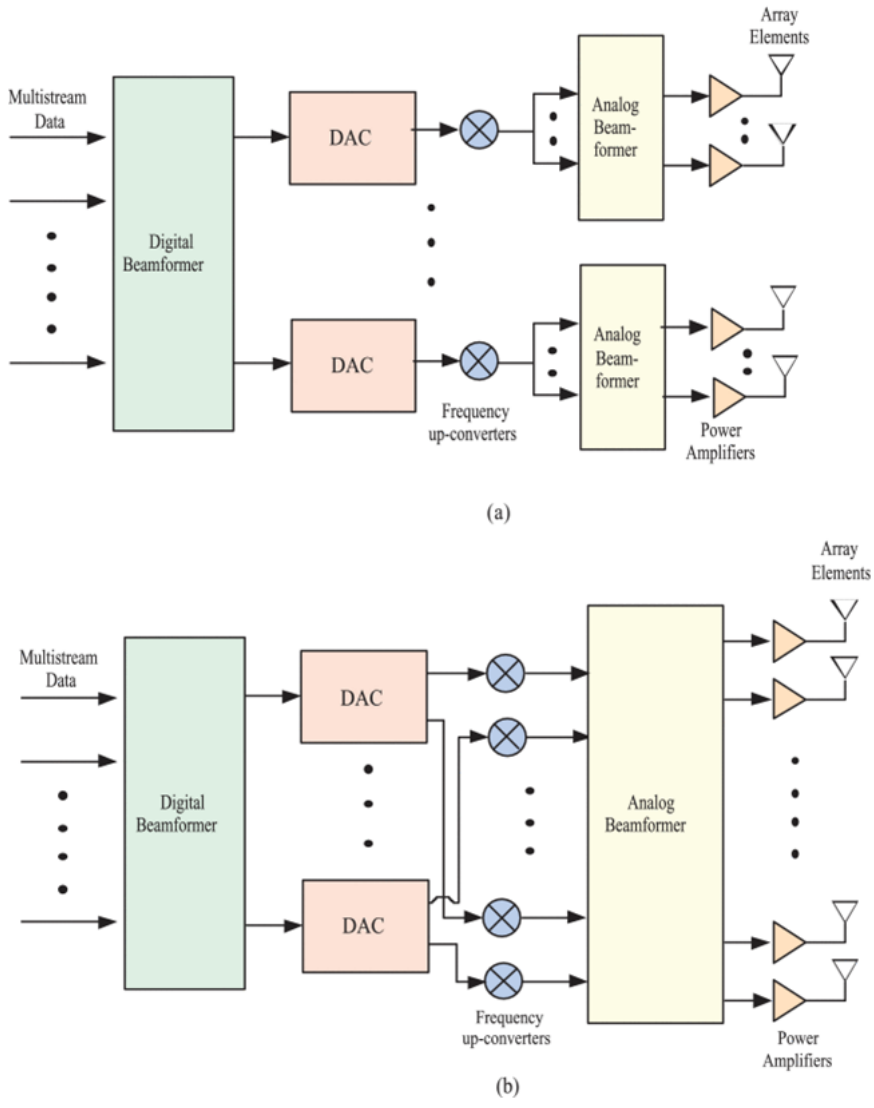

FIGURE 2.3: Typical hybrid beamforming system architectures. (a) Subarray, and, (b) Full-array [26].

Fig. 2.3 depicts typical hybrid beamforming architectures. The architecture depicted in Fig. 3(a) is based on a sub-array configuration [26] where each user's multi-stream data is first digitally precoded, and fed to the analog beamforming block via a dedicated RF chain. The signal is then transmitted using a set of antenna elements

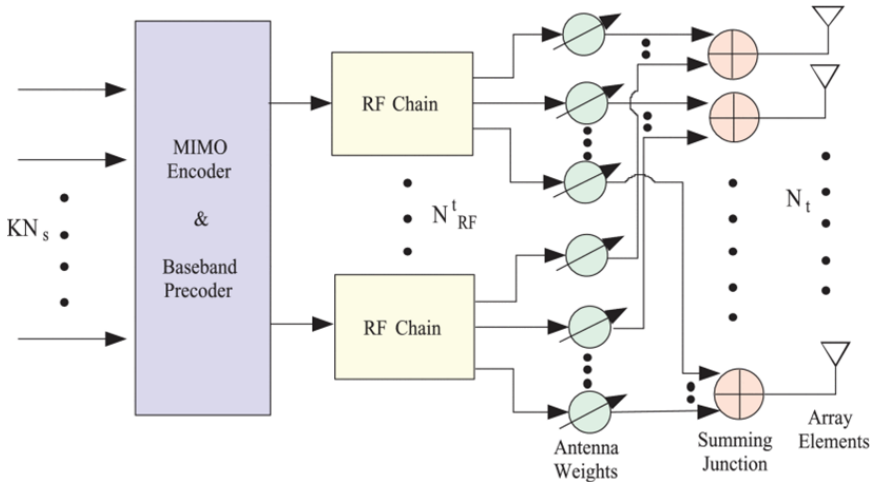

FIGURE 2.4: A hybrid (transmit) beamforming architecture for large scale millimeter wave spatial processing [97].

constituting a sub-array. Alternatively, the analog beamforming block can also be implemented prior to frequency upconversion (analog baseband) [89]. The user signal in the full-array based architecture as shown in Fig. 3(b) [97] is first digitally precoded, then processed by every RF chain, and transmitted using all antenna elements in the array through a common analog beamforming unit. There exists a complexity-gain tradeoff between the two architectures. For N_{RF} number of RF chains and N number of antenna elements, the number of signal processing paths for the sub-array based structure is $N_{RF} \times N$, whereas for the full-array architecture it is $N_{RF}^2 \times N$. However, the beamforming gain realized in sub-array architecture is lesser compared to the full-array architecture by a factor of $\frac{1}{N_{RF}}$.

A hybrid beamforming architecture proposed for MMB systems [97] based on the full-array architecture is illustrated in Fig. 4. The architecture for hybrid large scale spatial processing at the transmitter consists of N^t antennas, N_{RF}^t RF chains, transmitting N_s independent data streams to K users with $N_s < N_{RF}^t < N_t$ with a similar arrangement at the receiving end. The signal is first digitally precoded by a baseband precoder, followed by a analog phase-only RF precoder.

The multiplexing gain of the hybrid beamforming architecture is limited by $N_s \leq \min(N_{RF}^t, N_{RF}^r)$, where N_{RF}^r denotes the number of RF chains at the receiver.

From an outdoor mmWave communications perspective, hybrid beamforming precoder/combiner solutions [17] are based on certain key design challenges listed as follows:

Architecture configuration: Determining the optimal number of RF chains, analog phase shifters under considerations of number of multiplexed streams and antenna elements constitutes an interesting problem. The overall objective is to approach the optimal capacity as achieved in digital beamforming under the cost constraints associated with hardware complexity and power consumption.

Precoder/combiner design: Joint design of baseband and RF precoders is generally based on sum-rate maximization subject to the practical constraints of constant amplitude and quantized phases of the analog phase shifter. From an implementation perspective, algorithms that enable parallel hardware architecture for efficient signal processing and very large scale integration (VLSI) implementation are desirable. Associated algorithm design to mitigate in-cell and out-of-cell interference in a multi-user cellular framework, and optimal joint design of Tx-Rx precoder and combiner is a formidable challenge.

Channel estimation: Optimal precoding/combining gains can only be realized with full channel knowledge. However, the limited number of RF chains as compared to the number of antenna elements presents a bottleneck for direct channel estimation. Thus, the channel estimation in hybrid beamforming is an optimization problem where optimal analog RF transmit-receive beams pairs are determined to maximize mutual information. mmWave channel sparsity in the angular domain can be exploited to apply compressed sensing techniques to reduce the number of estimated channel parameters. This leads to a significant reduction in channel matrix dimensions resulting in efficient signal processing and simplicity of precoder/combiner design.

Beam training and feedback: Design of reference signal sequences for joint baseband and RF beamforming in order to reduce training and feedback overhead can yield low complexity power efficient schemes. Considerations include adapting to dynamic channel conditions, user localization and tracking, and low SNR prior to beamforming.

RF hardware limitations: Precoder/combiner design is more constrained for hybrid beamforming as compared to digital beamforming due to the use of constant gain analog phase shifters and low-resolution quantized phase control, motivating the need for novel beamforming algorithm and codebook design.

For outdoor mmWave communications, the seminal work by Ayach et al. shows that precoder/combiner for capacity-achieving rate-maximizing optimal solutions correspond to traditional beam steering solutions in single-user multi-stream transmission in the large array regime [25]. It has been shown through simulations that for the sum-rate performance achieved by hybrid analog-digital schemes in geometric channels is similar to that achieved by multi-user massive MIMO digital beamforming schemes, and can be reduced by decreasing the number of multiplexed symbols for a fixed number of RF chains [32]. Further, for a fixed number of multiplexed streams, the achievable sum rate increases with the number of RF chains. Thus, there exists a trade-off between hardware complexity and achievable spectral efficiency.

Developing low complexity joint baseband-RF precoding/ combining solutions with the practical requirements due to the uniform antenna elemental power constraints [201] for large array configurations is a non-trivial problem. An algorithmic solution

in [64] harnesses the inherent sparsity of outdoor millimeter wave channels, and employs a variant of orthogonal matching pursuit (OMP) [168] to realize theoretically achievable spectral efficiency. The work is applicable for limited feedback reciprocal channels, and assumes perfect channel knowledge at the receiver.

Since a direct solution to the constrained joint optimization of baseband-RF precoder/combiner is an intractable problem, the method involves a two-stage procedure. In the first stage the baseband signal is transformed under unconstrained conditions yielding the optimal baseband precoder/combiner matrices, followed by the sub-optimal design accounting for the subsequent RF signal processing constraints. The finite resolution RF beamsteering codebook with vectors defining quantized phase shifts is adopted due to its small size. The concept in [24] has been further extended to develop an iterative training algorithm for precoder design based on partial channel knowledge at the transmitter and receiver [15] along with a study on the adverse impact on quantized phase resolution.

An open loop channel estimator for mmWave hybrid MIMO system [106] uses a dense grid in the neighborhood of AoD/AoA only to further reduce the computational complexity of the OMP algorithm. A compressed sensing based adaptive algorithm in [14] is shown to achieve spectral efficiency and precoding gains similar to that attained by exhaustive search, yielding optimal coverage in interference-limited multi-user cellular environments.

The fast iterative training mechanism is shown to accurately estimate multipath channel parameters, and accounts for the limitation of quantized beam directions, thereby considering the practical limitations. Moreover, the work in [14] also proposes a hierarchical multi-resolution codebook capable of generating variable beam width radiation patterns, which facilitates the usage of robust adaptive multipath channel estimation algorithms.

The work in [12] explores the hybrid beamforming in limited feedback channels [117]. The system model in [12] assumes a hybrid beamforming precoding/combining architecture at the base station with analog-only combining at the mobile station. The work provides insights on the impact of RF beam angle quantization due to finite resolution codebooks. It is shown that the digital precoding layer at the base station must have enough quantization levels with a sufficiently large gain over analog precoding gain so as to minimize the sensitivity of hybrid precoding gain to RF beam quantization which has the potential to increase the average rate loss.

A novel multi-layer precoding scheme considering 3D channel covariance matrices to manage in-cell and out-of-cell interference in a multi-user cellular environment is proposed in [13]. The three layers are designed to meet specific objectives which include inter-cell interference management, desired signal beamforming based on large channel statistics, and multi-user interference. The scheme is shown to deliver improved performance in terms of achievable sum-rate, and cell coverage probability over conventional MIMO beamforming due to its superior interference management ability. In pursuance to the compressed sensing based sparse precoding concept in [15, 106, 14, 12, 117, 13], a low complexity [146] mmWave MIMO scheme exploits the array geometry to reduce the search space in the array manifold.

2.3.1 Rotman Lens Antenna Arrays

Fundamentally, RF lenses are phase shifting devices, which convert a divergent wavefront from a point source into a plane wave. A common topology reported in the literature is known as a Rotman lens array, which uses a uniform linear array (ULA) of antennas for signal transmission and/or reception [70]. Fig. 5 shows a schematic representation of a general Rotman lens with N_{bp} beam ports and N_{ap} antenna ports. Without loss of generality, it can be assumed that $N_{bp} = N_{ap} = N_p$. Generally

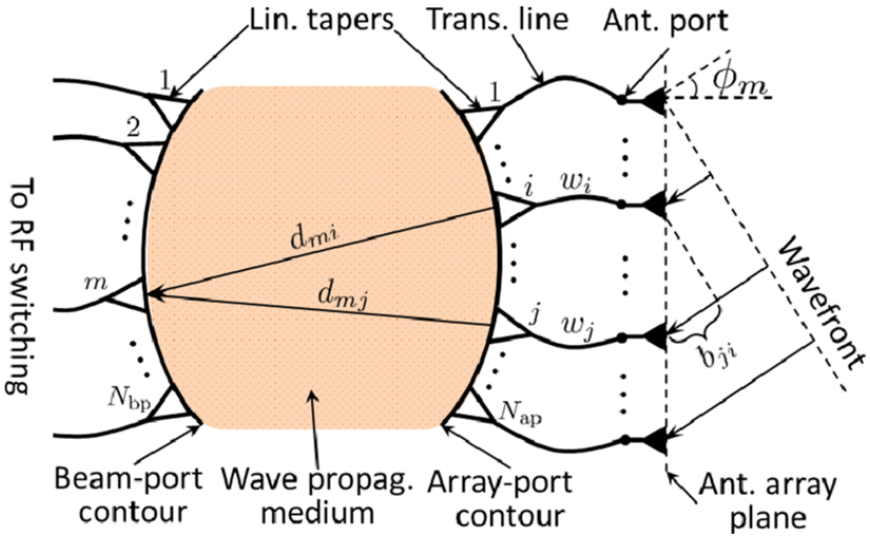

FIGURE 2.5: Schematic representation of Rotman lens with antenna elements and incident wave (top view) [70].

speaking, the $N_p \times N_p$ Rotman lens collects the incident RF signals from Np antennas to form Np beams corresponding to N_p AoAs. The transmit case is similar to the receive case, where the RF signals from the $m-$th beam port will be transmitted along the direction ϕ_m. Fig. 6 illustrates an uplink hybrid uplink MU–MIMO system with a Rotman lens embedded receive antenna array.

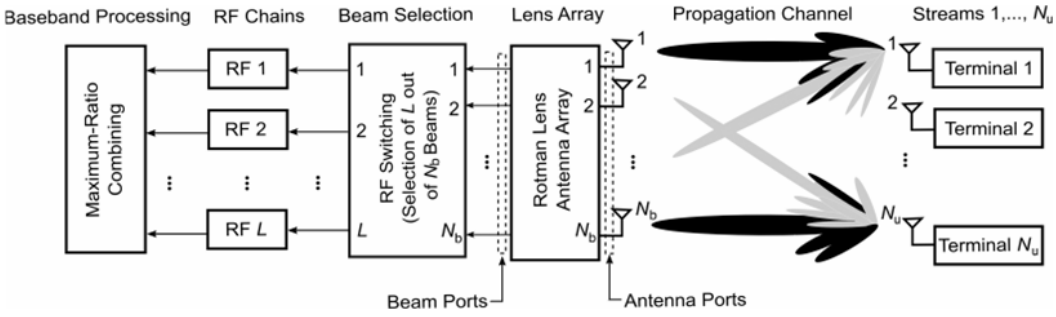

FIGURE 2.6: Hybrid (RF-baseband) uplink MU–MIMO system model with a Rotman lens embedded receive antenna array [70].

In the context of the Rotman Lens, discrete lens arrays (DLAs) were considered for point-to-point MIMO systems in [33],[148]. The DLA concept was based on

beamspace MIMO, where uplink/downlink signals sampled on the ULA are equivalently represented in the beamspace domain via a discrete Fourier transformation (DFT) [149]. As shown in [33],[148], for LoS mmWave channels, the equivalent beamspace representation leverages the sparse nature of the propagation channel, and devises a capacity achieving technique called continuous aperture phased MIMO (CAP-MIMO). CAP-MIMO was extended to multiuser mmWave systems in [34].

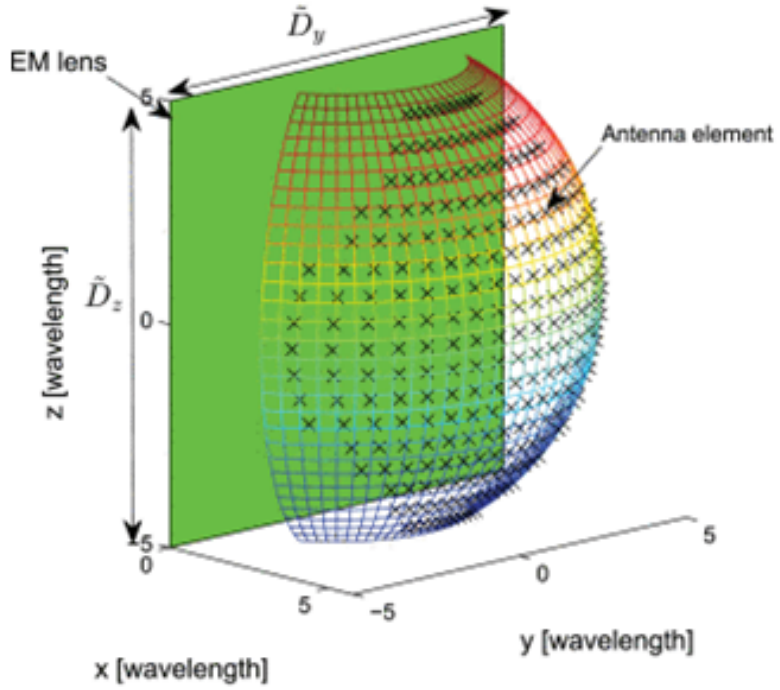

FIGURE 2.7: Illustration of the FD lens antenna array. The lens is placed in the $y-z$ plane [34].

In addition to the above research, literature also reports a parallel direction of work employing flat RF lenses, where unlike the Rotman structure, the array elements are non-uniformly located on the focal arc of the lens [194],[193]. The equivalent capacity achieving technique for flat lens arrays is known as path-division multiplexing for both point-to-point and MU-MIMO systems, as demonstrated in [194],[193]. Fig. 7 provides a schematic illustration of a lens antenna array in 3D coordinate system, which consists of a planar EM lens with negligible thickness in the $y-z$ plane centered at the origin, together with the antenna elements located in the focal surface of the EM lens.

2.4 Contemporary Research in Millimeter Wave Beamforming

In the previous sections, the evolution of beamforming techniques for indoor and outdoor mmWave communication has been presented, highlighting the strengths and

drawbacks of various schemes. Now, research areas which have received considerable attention in recent years and are expected to be the subject of future investigations are discussed.

2.4.1 Millimeter Wave MIMO Beamforming

SVD Based: The one dimensional transmit receive mmWave beamforming is found to be spectrally inefficient due to the use of a single data stream. This has motivated the study of the general singular value decomposition (SVD) based transmit precoding and receive combining methods to provide multi-stream support [184]. Under LoS conditions, it is found [182] that narrow and wideband direction based beamformers approach the upper bound on SNR improvement set by the SVD beamformer.

MIMO Beamforming: MIMO beamforming is expected to be a key technology in the evolution of the next generation of 60GHz standards delivering data rates of the order of tens of Gbps. For outdoor cellular communications, the concept of massive MIMO which employs a multitude of antennas at each base station has recently emerged as a promising alternative to achieve huge gains [163]. The energy and spectral efficiency of very large multi-user MIMO systems is the subject of investigations [129].

Spatial Multiplexing: The feasibility and performance of spatial multiplexing at mmWave carrier frequencies can be assessed by determining the fundamental limits in LoS environments, and further in the presence of multipath. Based on the properties of prolate spheroidal wave functions, a linear sparse array producing a spatially uncorrelated channel matrix effectively provides the maximum number of spatial degrees of freedom in a LoS environment [166]. A denser array could be used to provide additional beamforming gain. A mmWave MIMO architecture with a system of sub-arrays provides directivity as well as spatial multiplexing gain.

DFT Codebook: For indoor mmWave systems, an efficient Discrete Fourier Transform (DFT) codebook based MIMO beamforming training scheme for estimating the antenna weight vectors employs an iterative training algorithm that uses only one weight vector feedback to obtain the best transmit and receive weight vector pair [202]. The beam pattern search for refinement is limited only to the region corresponding to the initial selection and their angular rotated adjacent beams. The proposed method outperforms the IEEE 802.11ad beam training and reduces beamforming training time significantly.

2.4.2 Multi User Concurrent Beamforming

Existing indoor mmWave communication standards [1],[2] schedule a single transmission per time slot. The high propagation loss in millimeter wave links can be exploited to establish multiple communication links with directional antennas which can operate simultaneously to improve the network capacity. However, the problem of mutual interference generated due to the concurrent links in short coverage area, which can greatly affect the concurrent throughput, needs to be addressed. The solution lies in the design of efficient MAC/cross-layer protocols and transmission scheduling for spatially multiplexed concurrent links [157].

Concurrent beamforming for multiple simultaneous links must take into account the mutual interference to identify the best transmission/reception beam for each link. The selection of beams for such concurrent links is based on optimizing the sum rates and not individual rate. Iterative search algorithms can find the sub-optimal solution by maximizing the received SINR for two or more simultaneous links [139].

A recent work based on the hybrid beamforming spatial multiplexing, the multiple paths multi-hop (MPMH) scheduling scheme is shown to improve spatial reuse in millimeter wave WPAN through optimum path selection, traffic distribution, and transmission scheduling [131]. The joint consideration of beam selection and transmission scheduling is addressed in [154], based on which the authors have provided useful insights in terms of optimal choice of beam width and number of concurrent scheduled links.

The multi-user concurrent beamforming concept can be extended to evaluate its performance for 5G outdoor millimeter wave systems and cellular backhaul links. This will provide vital inputs for the design and deployment of dense HetNets in the future.

2.4.3 Joint Transmit-Receive Beamforming

Setting optimum antenna weight vectors at the transmit and receive ends to maximize revived SNR/SINR prior to signal transmission can yield a high array gain. If CSI is available at both ends, the optimum weight vectors can be directly found by maximizing an appropriate performance criteria such as the receiver SNR.

The design of joint transmitter-receiver analog beamforming algorithms is challenging for frequency selective channels with a large number of multipath due to the constraint of a constant scalar weight per antenna. Iterative joint algorithms takes this constraint into account and computes the transmit and receive weights to maximize SNR, where the energy in the delayed paths is treated as additional noise input to the equalizer. However, this sub-optimal method requires complete knowledge of the channel impulse response (CIR) pairs of the MIMO channel at both transmit and receive sides, which introduces huge overheads and is not desirable for high data rate systems.

[133] exploits the energy in the delayed paths to increase the average symbol energy at the input of the equalizer. Consequently, the required CSI for joint optimization is

only the inner products between all transmit-receive CIR pairs. Thus, the amount of CSI to be estimated in real-time depends only on the number of transmit and receive antennas and not on the time dispersion due to the channel.

The need to obtain CSI can be avoided using codebook based switched beamforming technique. Another alternative is to apply adaptive beamforming, which is more robust. However, this necessitates the development of novel joint beamforming methods which do not require a priori CSI [185].

2.4.4 Hybrid Beamforming

In the recent past, there has been considerable research focus on hybrid beamforming, which has emerged as a low complexity and cost effective solution for mmWave communications employing large scale antenna systems.

Optimal Precoding Solutions: Optimal precoding solutions for hybrid beamforming explored in have been discussed in a preceding section.

Joint Optimal Transmit Precoding and Receive Combining: Joint optimal transmitter precoding and receiver combining remains a formidable challenge. A joint transmit-receive mixed analog/digital beamforming algorithm in [132] for 60GHz frequency selective MIMO channels is shown to outperform classical digital beamforming based antenna selection schemes in terms of achievable average SNR gain.

Time Domain Hybrid Beamforming: A cost effective time-domain hybrid beamforming method [181] exploits the directionality provided by phased antenna arrays in RF beam patterns and the spatial diversity offered by multiple baseband processing modules. To maintain the signal quality under unpredictable multiple access and inter-symbol interference scenarios in wireless multimedia streaming, a robust beamformer is designed to maintain the SINR for each user with minimum total transmit power. However, the extent to which the target SINR can be achieved is sensitive to uncertainties in the phase shifters. The proposed scheme jointly mitigates the interference and phase uncertainties.

Multi Beam Transmit Diversity Scheme: A multi-beam transmit diversity scheme for single user MIMO (SU-MIMO) with single stream transmission based on a hybrid beamforming architecture [99] combines analog beamforming with array antennas and digital precoding with multiple RF chains. The method employs quantized limited feedback to obtain information about the preferred analog beams and the digital precoder. Baseband processing is performed at receiver for practical CSI measurement.

Minimizing Hardware Cost: A hybrid beamforming architecture for mmWave downlink multi-user MIMO channels based on a dual polarized planar antenna array introduced in [40] minimizes hardware cost.

Joint Baseband RF Precoder Design: The authors in [99] propose an iterative algorithm for the joint design of baseband and RF precoder, as well as baseband equalizer, and determine the power allocation in the frequency domain to maximize the minimum SINR of multi-stream data.

2.4.5 Beamforming for Green Communications

While the research next generation on 5G communications is focussed on coping up with the projected huge traffic demand in order to provide seamless ubiquitous connectivity, it is also imperative to pay due attention to the design of energy-efficient systems with minimal footprint [77],[91]. Energy efficiency assumes particular importance for LSAS based massive MIMO technology [119]. In this context, among several issues, the energy efficiency-spectral efficiency (EE-SE) co-design aspect attracts attention in particular [109].

To further leverage the power savings offered by the hybrid beamforming architecture, there has been an effort to determine the optimal operating point, also known as the green point, on the EE-SE curve, under considerations of a variable number of RF chains and number of antenna elements [77]. The basic idea is to optimize system parameters to maximize EE for a specified SE. The EE-SE relationship at the green point is analyzed in [76], with a corresponding derivation for the optimal number of RF chains to achieve optimal EE-SE performance.

2.4.6 Beamforming for Secure Communications

Antenna Subset Modulation: Antenna Subset Modulation [169] is novel method in which the antenna radiation pattern is modulated at the symbol rate driven by a subset of antennas in the array. This results in a directional radiation pattern that projects a sharply defined constellation in the desired direction and randomized constellation in other directions. The method exploits the large antenna array deployment feature of mmWave systems to realize a low complexity directional modulation system with a robust inherent security mechanism in the presence of eavesdroppers.

Coding: Coding with analog beamforming in MMB systems can be used to achieve secure downlink communication in cellular networks [177]. Using delay-tolerant and delay-limited base station transmission modes, it is shown that the secrecy throughput is significantly higher than conventional cellular systems. Also, the upper bound for secrecy throughput in the delay-limited mode is achieved in the delay-tolerant mode when large antenna arrays are employed. For large mmWave bandwidths the secrecy throughput achieved is very high.

2.4.7 Compressed Sensing for Beamforming

Compressed channel sensing offers a promising method to estimate the sparse multipath channels, and has been used extensively to reduce the signal processing complexity in hybrid beamforming systems [28].

Least Squares Estimator: The conventional least squares estimator requires a pilot sequence length of K which is of the order of N_t , where N_t is the number of transmit antenna elements, as compared to that using compressed sensing method which requires a significantly lower value of K of the $\mathcal{O}(\log N_t)$ [62]. This considerably reduces the number of preamble overheads. The compressed sensing approach is also used for channel acquisition and tracking [142].

Adaptive Compressed Sensing: Adaptive compressed estimation technique for multipath mmWave channels does not require channel feedback information and uses multi-level beamforming codebooks to adaptively refine the estimates for angles of arrival and departure of every sparse channel multipath. Simulation results demonstrate that the precoding gains achieved by the proposed algorithms are similar to that obtained with systems incorporating feedback channels [18].

SVD Based Compressed Sensing for Large mmWave MIMO: A two-step procedure comprising of coarse and fine channel estimation uses compressive sensing for large mmWave MIMO systems [23]. The implementation involves SVD based beamforming methods. Under low SNR conditions the method yielded reasonably good performance upto a distance of 10 meters.

Compressed Sensing based Beam Selection Recently, a promising compressed sensing based approach has been adopted for beam selection in mmWave uplink multi-user channel, without the need for explicit channel estimation [41].

2.5 Summary

Beamforming for mmWave communication is a crucial aspect in link budget analysis for feasible system design. The publication of IEEE 802.15.3c and IEEE 802.11ad standards paved the way for deployment of indoor mmWave WPAN and WLAN systems, respectively, which use the beam switching technique during the beam search phase to reduce overheads. To this end, there have been notable contributions in further decreasing the number of search steps and computational complexity in order to reduce the delay in setting up the beamformed link.

Hybrid beamforming, comprising of baseband precoding with limited number of RF chains and constant amplitude analog phase shifters, are shown to be effective in terms of achieving the desired performance for mmWave MIMO systems. To reduce

the hardware cost, the precoding circuit can be jointly designed in both analog and digital domains to reduce the required number of RF chains. Beam search procedures for large scale mmWave arrays using hybrid beamforming pose a unique set of challenges including antenna selection strategies and design of low complexity beam search algorithms. Capacity maximizing iterative RF beam search algorithms with varying complexities need to be further explored.

Beamforming is also expected to be the key enabler for mmWave indoor and outdoor backhaul networks. The major challenge in this application is to address link maintenance issues through accurate pointing and tracking under varying environmental conditions.

Contemporary trends in mmWave beamforming research include solving complex issues related to hybrid beamforming, polarization diversity, optimization of beam search process, concurrent beamforming protocols, robust adaptive beamforming, exploiting channel sparsity and 3D beamforming. These solutions must meet the objectives of reducing the computation cost, delay and power consumption during the beamforming process while maintaining an acceptable quality of service at multi-Gbps data rates.

Chapter 3

3D Beamforming for 5G Millimeter Wave Systems Using Singular Value Decomposition and Particle Swarm Optimization Approaches

3.1 Introduction

Mobile networks have been growing exponentially and have led to scarcity of bandwidth since current mobile communication systems (2G-4G) operate below the 5GHz band[118, 59, 203, 17, 178, 186]. 90% of the spectrum falls in the millimeter wave (mmWave) band i.e. $>$ 6GHz, qualifying it as one of the viable solutions for future mobile networks [162]. Deployment of mmWave remains a largely unexplored frontier in mobile communication, and many issues are required to be addressed [90]. One of the key issues when designing beamforming algorithms for mmWave is that it experiences strong path loss due to higher frequencies. On the other hand, these higher frequencies allow us to pack a large number of antennas, resulting in strong diversity gains which can overcome the high path loss [176]. Due to this reason, mmWave base stations (BS)s can have massive number of antennas [52]. Scaling up the number of users in practice, however, tracking them by solely using the angle of azimuth becomes impractical in 5G. Therefore, angles of elevation and azimuth will be utilized to track and separate them from one another. Therefore, the three dimensional (3D) beamforming systems have received great interest recently because of the spatial diversity advantage and capability for full-dimensional beamforming, making them promising candidates for practical realization of mmWave systems [203],[176].

Beamforming for planar arrays has been implemented earlier in [86, 147, 102]. In [86], the 3D beamforming is investigated from the array factor point of view. However, the beamforming weight vector was designed based on elevation angle vector only without exploiting the both angles. To address this issue, researchers in [147, 102, 72] are designed 3D beamforming weight vectors based on minimum variance distortion (MVD). The MVD approach finds the weight vector in $x-$axes and the weight vector in $y-$axes. Nevertheless, 3D mmWave channel measurements in [61] showed that kronecker product for x and y-axes is required which means a joint xy-axes 3D beamforming weight vectors are demanded. In this case, MVD cannot

achieve the optimal solution unless the beamformer weights are independent, which is not this case here because of the kronecker product. In this chapter, two new beamforming algorithms with aim of designing joint xy-axes weights vectors is proposed. These algorithms utilize both angles of azimuth and elevation to maximize the SNR of the system, unlike other algorithms which maximize the SNR of the system in one dimension [147, 102, 72]. The propose algorithms work on principle of singular value decomposition (SVD) [46],[135] and particle swarm optimization (PSO). In the first approach, the channel matrix is factorized into singular values which are then used to design the weights of the beamformer. In SVD approach the matrix inversion increases the computational complexity of the system especially when massive number of antennas are allocated in the BS. To reduce the complexity of SVD, a second approach based on PSO is proposed. PSO is a stochastic iterative optimization technique which neither requires any matrix inversion nor any matrix factorization to find the weights of the beamformer.

Moreover, 3D mmWave channel measurements in [61] showed that the effect of side lobs on the beampattern is high which has not been considered in [86, 147, 102]. In this chapter, Kaiser Bessel (KB) filters are designed for the 3D beamforming. The KB filters can reduce the side lobes and make the beam more directional causing less interference to users operating in the same area. The key contributions of the chapter are as follows

- Two beamforming algorithms for mmWave system which operate on the principles of SVD and PSO are constructed.
- Applying KB filtering for reducing the side lobes and improving the directivity of the beampattern.

Based on this analysis, some valuable insights are obtained. The proposed algorithms are shown to perform well in achieving considerable capacity and lower side lobes.

Notation: Bold upper case letters, $\boldsymbol{X}$, and lower case letters, $\boldsymbol{x}$, denote matrices and vectors, respectively. Transposition and conjugate transposition of a matrix are respectively denoted by $(\cdot)^T$ and $(\cdot)^T$. Determinant of the matrix $\boldsymbol{X}$ is given as $|det(\boldsymbol{X})|$. While, the (m,n)th element of a matrix $\boldsymbol{X}$ is denoted by x_{mn} and mth column vector of a matrix $\boldsymbol{X}$ is denoted by x_m. The element wise multiplication is denoted by $\odot$ and the kronecker product is denoted by $\otimes$, respectively.

3.2 Downlink Communication Channel

Consider a system with $N_t = N \times N$ transmitted antennas as shown in Fig. 3.1. From the figure, it can be observed that a beamformed signal is transmitted by a mmWave BS to a mobile station (MS). Unlike, the two dimension (2D) transmit beamformer, this beamformer will account for both the elevation and azimuth angles. The received signal at the MS in the time domain is given by

$$\boldsymbol{y} = \boldsymbol{HWs} + \boldsymbol{u}, \tag{5.1}$$

where $\boldsymbol{s}$ is the transmitted data stream drawn from the uniform distribution of equally likely BPSK symbols, having symbol energy E_s at every time slot. $\boldsymbol{H}$ consists of 3D channel, $\boldsymbol{W}$ is the designed beamformer, and $\boldsymbol{u}$ is the complex Gaussian noise vector. Each element of $\boldsymbol{n}$ is modeled as independent and identical distributed (iid) complex Gaussian random variable with zero mean and σ^2 variance of the noise. SNR represents the average SNR per receive antenna, which in this case is expressed as

$$\text{SNR} = \frac{\left| det[\boldsymbol{H}^H \boldsymbol{W}^H \boldsymbol{W} \boldsymbol{H}] \right|}{\sigma^2}. \tag{5.2}$$

As the capacity of the system increase logarithmically with SNR, maximizing SNR will improve the capacity of the system. From (5.2), it can be observed the SNR is a function of beamformer weights $\boldsymbol{W}$. Our approach is to design a beamformer weight matrix which is of dimension $N \times N$ such that it maximizes the SNR as mentioned in (5.2). Designing beamforming weights will be covered in detail in upcoming Section III.

3.2.1 3D Channel

Winner II which is a stochastic based geometry model has been considered in this chapter [95],[128]. The channel response is given by

$$\boldsymbol{H} = \sqrt{10^{\frac{-PL+\sigma_{SF}}{10}}} \left(\sqrt{\frac{1}{K+1}} \begin{bmatrix} \boldsymbol{a}_x(\phi,\theta) \\ \boldsymbol{a}_y(\phi,\theta) \end{bmatrix} + \sqrt{\frac{K}{K+1}} \begin{bmatrix} \boldsymbol{a}_x(\phi,\theta) \\ \boldsymbol{a}_y(\phi,\theta) \end{bmatrix} \right) e^{(j\boldsymbol{\gamma}\cdot\boldsymbol{r})}, \tag{5.3}$$

where PL is the path loss, σ_{SF} is the log normal fading coefficients, and, K represents the Rician factor. $\boldsymbol{a}_x$ and $\boldsymbol{a}_y$ are the beamforming steering vector in x and y axes, respectively. ϕ represents the angle of azimuth while θ represents the elevation angle. In (5.3), r denotes the radial position of the MS and γ will be the angle of departure

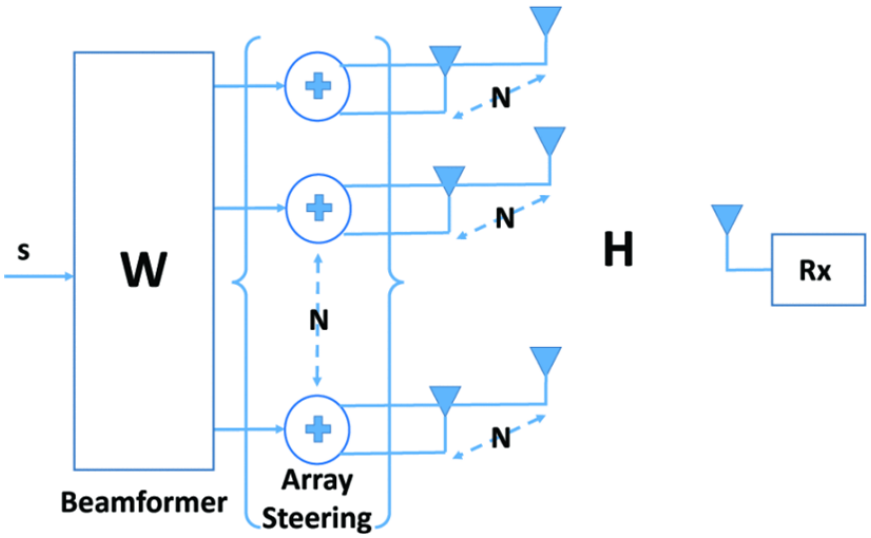

FIGURE 3.1: Block diagram of mmWave system

(AoD) for the BS and is given by

$$\boldsymbol{\gamma} = [\cos\phi\sin\theta, \sin\phi\sin\theta, \sin\phi]^T. \tag{5.4}$$

In case of a uniform planar array (UPA) with $N_t = N \times N$ elements, the response vector in x and y axes are given as [64]

$$\boldsymbol{a}_x(\phi,\theta) = \frac{1}{\sqrt{N}}[1, e^{j\beta_x}, \cdots, e^{j(N-1)\beta_x}]^T, \tag{5.5}$$

$$\boldsymbol{a}_y(\phi,\theta) = \frac{1}{\sqrt{N}}[1, e^{j\beta_x}, \cdots, e^{j(N-1)\beta_y}]^T, \tag{5.6}$$

where $0 \leq n < N, \beta_x$ and β_y are the path differences along x and y axes, respectively. It can be observed that each of the above vectors consists of N entries, with each entry corresponding to an antenna element, given by

$$\beta_x = -2\pi\lambda^{-1}d_x\cos\phi\sin\theta, \tag{5.7}$$

$$\beta_y = -2\pi\lambda^{-1}d_y\sin\phi\sin\theta, \tag{5.8}$$

where dx and dy is the inter element spacing in x and y axes respectively. In this work, dx and dy are fixed at $\lambda/2$, where λ is the wavelength of the mmWave signal. For mmWave systems, higher frequencies will lead to smaller wavelengths and therefore more antennas elements can be packed for a given size. The array steering matrix is given by [78]

$$\boldsymbol{A} = \boldsymbol{a}_x(\phi,\theta) \otimes \boldsymbol{a}_y(\phi,\theta)^T. \tag{5.9}$$

If the 3D beampattern is generated using (5) and (6), unwanted side lobes will also be generated, radiating energy in unwanted directions. This will cause interference to users operating in the same area. KB filters have the capability of attenuating side lobes, and thus making the beampattern more directional. By introducing KB filters in the synthesis of the beampattern, side lobes can be decreased and directivity of the antenna can be improved. The KB filter is defined as [72]

$$\boldsymbol{z}_n = \begin{bmatrix} \dfrac{I_0\left(\mu\sqrt{\left(1-\left(\frac{2n}{N}-1\right)\right)}\right)}{I_0(\mu)}, & \text{if } 0 \leq n \leq N-1 \\ 0, & \text{Otherwise} \end{bmatrix}. \tag{5.10}$$

In (5.10), $\boldsymbol{I}_0$ is the zeroth order modified Bessel function of the first kind and μ is the design parameter that is used to calculate the side lobe attenuation level. The array steering as defined in (5.5) and (5.6) are now combined with KB filters in (5.10), yielding

$$\boldsymbol{a}_x(\phi,\theta) = \frac{1}{\sqrt{N}}[z_1, z_2 e^{j\beta_x}, \cdots, z_{N-1}e^{j(N-1)\beta_x}]^T, \tag{5.11}$$

$$\boldsymbol{a}_y(\phi,\theta) = \frac{1}{\sqrt{N}}[z_1, z_2 e^{j\beta_y}, \cdots, z_{N-1}e^{j(N-1)\beta_y}]^T, \tag{5.12}$$

where $z_1, z_2, \cdots, z_n$ are the weights of the KB filter defined in (5.10).

3.3 Beamformer Design

In this section, two types of beamformers are considered for mmWave system. Initially, SVD approach is adopted to design the weights of the beamformer. Finally, the PSO algorithm is proposed. Further, to compare these algorithms, the antennas transmit power is kept the same by placing a constraint on beamforming matrix such that $|det(\boldsymbol{WHW})| = 1$. Moreover, if all the antenna elements are required to transmit at the same maximum power level, all diagonal elements of the matrix $\boldsymbol{WW}^H$ must be identical. Therefore, the beamforming matrix $\boldsymbol{W}$ cannot be chosen freely and has to satisfy the following two constraints:

1. $|det(\boldsymbol{WHW})| = 1$, i.e. (all) the algorithms have same transmitted power.
2. $w_{mm} = \boldsymbol{WW}^H(m,m) = \frac{1}{N}, m = 1,2,\cdots,N$, forcing the norm of each column of $\boldsymbol{W}$ to be equal to unity.

While the first constraint is specific to implementation of each algorithm, the general proof of the second constraint has been presented below.

$$\boldsymbol{W} = \left[\frac{\boldsymbol{w}_{1n}}{N\sqrt{\sum_{n=1}^{N} w_{1n}^2}}, \frac{\boldsymbol{w}_{2n}}{N\sqrt{\sum_{n=1}^{N} w_{2n}^2}}, \cdots, \frac{\boldsymbol{w}_{N,n}}{N\sqrt{\sum_{n=1}^{N} w_{N,n}^2}}\right]^T, \tag{5.13}$$

where $\boldsymbol{w}_{1,n}, \boldsymbol{w}_{2n}, \cdots, \boldsymbol{w}_{Nn}$ are the column vectors of $\boldsymbol{W}$. Therefore, the diagonal elements of the matrix $\boldsymbol{WW}^H$ can be given by

$$\begin{aligned} diag\left[\boldsymbol{WW}^H\right] = \Bigg[&\frac{w_{11}w_{11}^* + w_{12}w_{12}^* + \cdots + w_{1N}w_{1N}^*}{w_{11}w_{11}^* + w_{12}w_{12}^* + \cdots + w_{1N}w_{1N}^*}, \\ &\frac{w_{21}w_{21}^* + w_{22}w_{22}^* + \cdots + w_{2N}w_{2N}^*}{w_{21}w_{21}^* + w_{22}w_{22}^* + \cdots + w_{2N}w_{2N}^*} \\ &\cdots, \\ &\frac{w_{N1}w_{N1}^* + w_{N2}w_{N2}^* + \cdots + w_{NN}w_{NN}^*}{w_{N1}w_{N1}^* + w_{N2}w_{N2}^* + \cdots + w_{NN}w_{NN}^*}\Bigg] \end{aligned} \tag{5.14}$$

or $diag[\boldsymbol{WW}^H]$=[1,1,$\cdots$,1]. Each algorithm is now discussed in details.

3.4 Proposed Architectures

3.4.1 Singular Value Decomposition

In SVD beamforming, the channel matrix is factorized into singular values and unitary matrices. The SVD of the $N \times N$ matrix $\boldsymbol{H}$ is given by $\boldsymbol{H} = \boldsymbol{UH\Sigma V}^H$ where $\boldsymbol{U}$ and $\boldsymbol{V}$ (also having dimensions of $N \times N$) are special matrices: a) They are unitary and hence $\boldsymbol{U}^H\boldsymbol{U} = \boldsymbol{V}^H\boldsymbol{V} = \boldsymbol{I}$; b) The columns of $\boldsymbol{U}$ and $\boldsymbol{V}$ are the eigen vectors of $\boldsymbol{HH}^H$ and $\boldsymbol{H}^H\boldsymbol{H}$ respectively; c) The columns of $\boldsymbol{U}$ and $\boldsymbol{V}$ are also the orthonormal basis vectors of $\boldsymbol{HH}^H$ and $\boldsymbol{H}^H\boldsymbol{H}$ respectively, and; d) $\boldsymbol{U}$ and $\boldsymbol{V}$ are orthogonal to

each other as well. Lastly, $\Sigma = diag[\sigma_1, \sigma_2, \cdots, \sigma_N]$ is an $N \times N$ diagonal matrix comprising of the N singular values of $\boldsymbol{H}$. These N singular values are the square root of the N eigen values of both $\boldsymbol{H}\boldsymbol{H}^H$ and $\boldsymbol{H}^H\boldsymbol{H}$. The weights of the SVD beamformer which maximizes the received SNR are formulated as

$$\boldsymbol{W} = \boldsymbol{V}\Sigma^{-1}\boldsymbol{U} \tag{5.15}$$

This beamformer satisfies the constraint 1 as follows:

$$\begin{aligned} \left|det(\boldsymbol{W}^H\boldsymbol{W})\right| &= \left|det((\boldsymbol{V}\Sigma^{-1}\boldsymbol{U})^H\right| \\ \stackrel{\boldsymbol{a}}{=} \left|det(\boldsymbol{U}^H\Sigma^{-1}\underbrace{\boldsymbol{V}^H\boldsymbol{V}}_{\boldsymbol{I}:identity})\Sigma^{-1}\boldsymbol{U}\right|, &\stackrel{\boldsymbol{b}}{=} \left|det(\boldsymbol{U}^H\underbrace{\Sigma^{-1}\Sigma^{-1}}_{\Sigma^{-2}}\boldsymbol{U})\right| \\ \stackrel{\boldsymbol{c}}{=} \left|det(\boldsymbol{U}^H\Sigma^{-2}\boldsymbol{U})\right|, &\stackrel{\boldsymbol{d}}{=} |det(\boldsymbol{Z})| = 1 \end{aligned} \tag{5.16}$$

a: $(\boldsymbol{V}\boldsymbol{\Sigma}^{-1}\boldsymbol{U})^H = \boldsymbol{U}^H\Sigma^{-1}\boldsymbol{V}^H$ and $(\boldsymbol{\Sigma}^{-1})^H = \boldsymbol{\Sigma}^{-1}$ because $\boldsymbol{\Sigma}^{-1}$ is an $N \times N$ diagonal matrix.

b: $\boldsymbol{V}^H\boldsymbol{V} = \boldsymbol{I}$, where $\boldsymbol{I}$ is the $N \times N$ identity matrix.

c: $\boldsymbol{\Sigma}^{-1}\boldsymbol{\Sigma}^{-1} = \boldsymbol{\Sigma}^{-2}$ because $\boldsymbol{\Sigma}^{-1}$ is an $N \times N$ diagonal matrix.

d: where $\boldsymbol{Z}$ is $N \times N$ an unitary matrix and unitary matrices have a determinant of unity. The SNR achieved by the SVD beamformer weights formulated by (5.2) is given by

$$\begin{aligned} \text{SNR} &= \frac{\left|det[\boldsymbol{H}^H\boldsymbol{W}^H\boldsymbol{W}\boldsymbol{H}]\right|}{\sigma^2} \\ \stackrel{\boldsymbol{a}}{=} \frac{\left|\det\left[\boldsymbol{V}\Sigma\overbrace{\boldsymbol{U}\boldsymbol{U}^H}^{\boldsymbol{I}}\Sigma^{-2}\overbrace{\boldsymbol{U}\boldsymbol{U}^H}^{\boldsymbol{I}}\Sigma\boldsymbol{V}^H\right]\right|}{\sigma^2}, &\stackrel{\boldsymbol{b}}{=} \frac{\left|\det\left[\boldsymbol{V}\overbrace{\Sigma\Sigma^{-2}\Sigma}^{E_S}\boldsymbol{v}^H\right]\right|}{\sigma^2} \\ \stackrel{\boldsymbol{c}}{=} \frac{E_s\left|\det\left[\overbrace{\boldsymbol{V}\boldsymbol{V}^H}^{\boldsymbol{I}}\right]\right|}{\sigma^2}, &\quad \stackrel{\boldsymbol{d}}{=} \frac{E_s}{\sigma^2} \end{aligned} \tag{5.17}$$

a: $\boldsymbol{H}^H = (\boldsymbol{U}^H\boldsymbol{\Sigma}\boldsymbol{V}^H)^H = \boldsymbol{V}\boldsymbol{\Sigma}\boldsymbol{U}, \boldsymbol{W}^H\boldsymbol{W} = \boldsymbol{U}^H\boldsymbol{\Sigma}^{-2}\boldsymbol{U}$

b: $\boldsymbol{U}\boldsymbol{U}^H = \boldsymbol{I}$ because $\boldsymbol{U}$ is a unitary matrix.

c: $\boldsymbol{\Sigma}\boldsymbol{\Sigma}^- - 2\boldsymbol{\Sigma} = E_s$ where E_s was defined as the symbol power per time slot.

d: $det(\boldsymbol{V}\boldsymbol{V}^H) = 1$ because $\boldsymbol{V}$ is a unitary matrix, $\boldsymbol{V}\boldsymbol{V}^H = \boldsymbol{I}$ and $det(\boldsymbol{I} = 1)$.

It can be observed that the SVD algorithm requires the factorization of the 3D channel matrix. In this case, SVD algorithm still have similar computation complexity as that of finding the inverse of the received correlation matrix.

3.4.2 Particle Swarm Optimization

This algorithm does not require any matrix inversion as in MVD or any matrix factorization as proposed in SVD. It assumes random weights and adaptively optimizes the weights that maximizes the SNR as shown in (5.2). The iterative steps in PSO algorithm are as follows:

Step 1. Initialize, P weights $\boldsymbol{W}_1(0), \boldsymbol{W}_2(0), \cdots, \boldsymbol{W}_p(0)$ with Gaussian random numbers. All weights will be of dimension $N \times N$. To force the constraint on the diagonal element $w_{mm} = \boldsymbol{W}\boldsymbol{W}^H(m,m) = 1$, every row of $\boldsymbol{W}_i(0)$ is divided by $\sqrt{\frac{1}{N}\Sigma_{n=1}^{N} w_{m,n}^2}$ where $1 \leq m \leq N$ is the mth row of $\boldsymbol{W}_i(0)$, and $1 \leq n \leq N$ is the nth column of $\boldsymbol{W}_i(0)$.

Step 2. Initialize the velocity of the i-th weight, $\boldsymbol{V}_i$, with a uniform random variable. The velocity will also be an $N \times N$ dimensional matrix.

Step 3. For each weight's position the value of the signal power is evaluated. The weight which gives the best signal power is found. This weight is denoted by $\boldsymbol{G}_{best} = \boldsymbol{W}_{best}$, and is the global best weight. Because the constraints 1 and 2 are enforced in **Step 1**, $|det(\boldsymbol{W}_{best}^H \boldsymbol{W}_{best})| = 1$ and $\boldsymbol{W}_{best}\boldsymbol{W}_{best}^H(m,m) = 1$.

Step 4. The velocity $\boldsymbol{V}_i$ and weights $\boldsymbol{W}_i$ of i-th weight are updated as

$$\begin{aligned}\boldsymbol{V}_i(\text{iter}+1) &= \boldsymbol{V}_i(\text{iter}) \\ &+ c_1 \text{rand}(L) \odot (\boldsymbol{W}^i_{\text{best}}(\text{iter}) - \boldsymbol{W}^i_{\text{current}}(\text{iter})) \\ &+ c_2 \text{rand}(L) \odot (\boldsymbol{G}_{\text{best}} - \boldsymbol{W}^i_{\text{current}}(\text{iter})),\end{aligned} \tag{5.19}$$

and the beamforming weight is given as

$$\boldsymbol{W}_i(\text{iter}+1) = \boldsymbol{W}_i(\text{iter}) + \boldsymbol{V}_i(\text{iter}+1). \tag{5.17}$$

In (5.18), $\boldsymbol{W}^i_{best}$ is the best and $\boldsymbol{W}^i_{current}$ is the current weight after the i-th iteration. The c_1 and c_2 are constants and their values are kept close to 2. In the first iteration, $\boldsymbol{W}_{best}$ is considered equal to the $\boldsymbol{W}^i_{current}(0)$ for $i = 1, 2, 3, \cdots, P$. This step is repeated for each weight.

Step 5. Once the value of the i-th weight is updated its fitness is evaluated. If the updated fitness of the weight is less then the previous best-fitness of the weight then $\boldsymbol{W}^i_{best}(iter) = \boldsymbol{W}^i_{current}(iter)$.

Step 6. The best-weight, $\boldsymbol{W}_{best}$, whose fitness is the best fit signal power is found.

The SNR attained by the PSO algorithm can be obtained by substituting the global best weight $\boldsymbol{W}_{best}$ in (5.2).

3.5 Simulation Results

In this section, the simulation results are presented to validate the performance of the proposed algorithms when combined with KB filters. Initially, the beam pattern of this system synthesized with and without KB filters is plotted. After that the capacity of the system per time slot versus the SNR per antenna element is measured when using PSO, SVD and MVD beamformers.

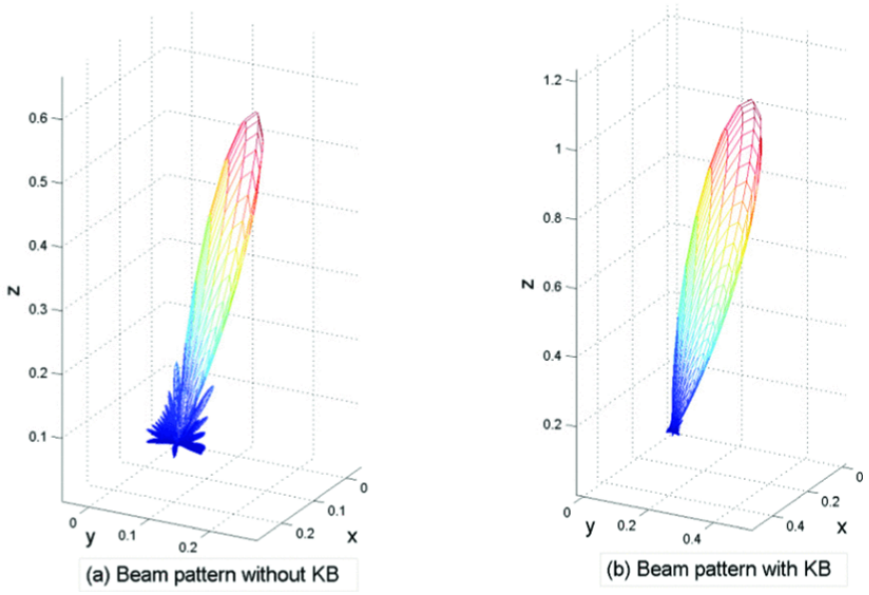

FIGURE 3.2: Comparison of beam pattern for $N_t = 16 \times 16$ antennas.

Fig. 3.2 plots the beam pattern of the system when synthesized with and without KB filter for $N_t = 16 \times 16$ antennas. The angle of azimuth ϕ is fixed to 45-degrees, while the elevation angle θ is 30-degrees. From the figure, it can be observed that when KB filters are not applied, there are strong side lobes. These side lobes will affect the received SNR of the system as a significant loss is observed in the gain of the synthesized beam pattern when comparing it with the system that adopts KB filters.

Fig. 3.3 compares the gain of the beam pattern in dB with and without KB filters. It can be clearly observed that while the system with KB filter not only achieves a higher gain in the main beam and hence higher beam directionality, the side lobes are also suppressed by at least an order of magnitude. This implies that the KB filter attenuates the side lobes by steering the energy from the side lobes into the main beam. These lower side lobes will help cause less interference.

Fig. 3.4 shows the capacity versus SNR of the mmWave system for all the algorithms with and without KB filters for $N_t = 16 \times 16$ antennas. It can be observed that with the application of KB filters, the capacity of the system improves. All these algorithms use the KB filters. It can be observed that the PSO and SVD beamformers attain higher capacity than MVD. This verifies the suboptimal nature of the MVD

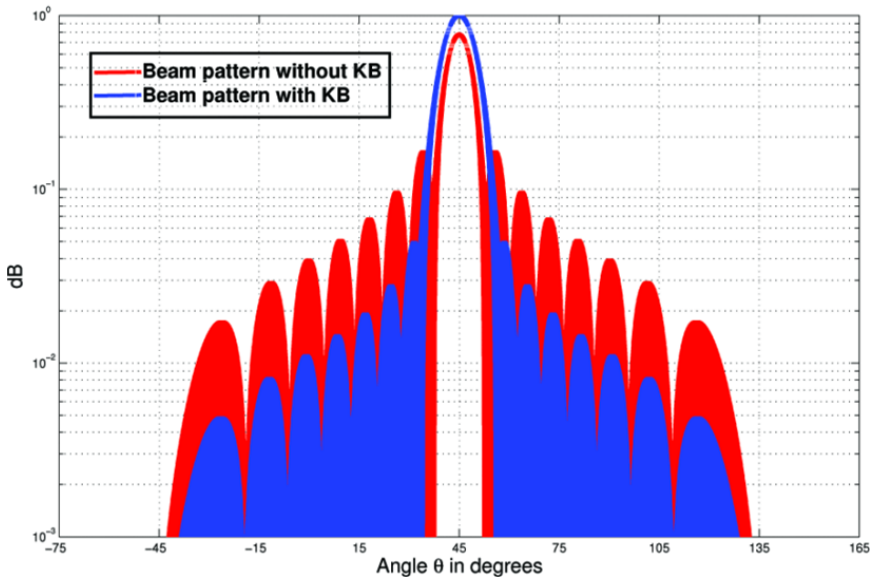

FIGURE 3.3: Beam pattern gain in dB with and without KB filter.

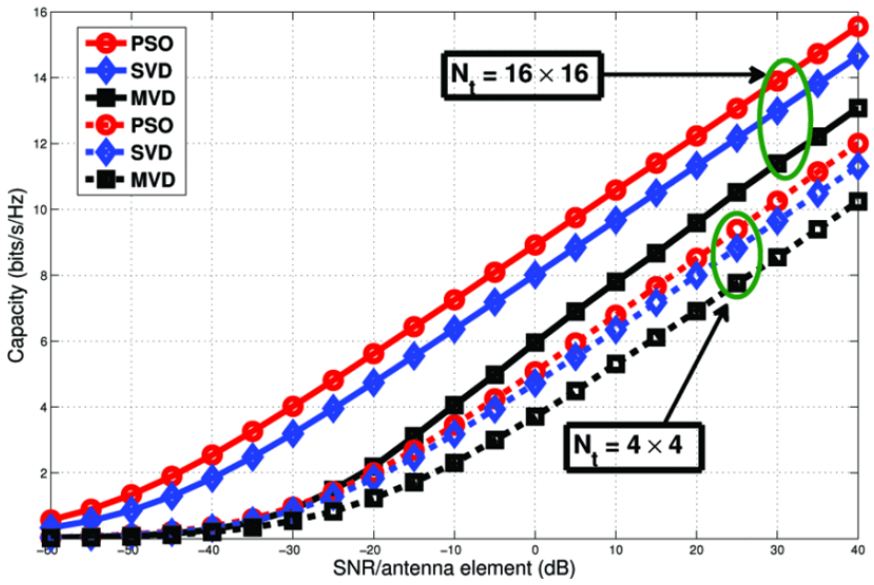

FIGURE 3.4: Capacity of the mmWave system with KB filter.

beamformer in the joint xy plane. Furthermore, PSO offering better performance of all.

3.6 Summary

In this chapter, two types of 3D beamforming algorithms were proposed for mmWave system. SVD was obtained by the factorizing the 3D channel into its unitary matrices and singular values, and PSO was an iterative algorithm that uses swarm optimization technique to obtain the global best solution. These beamformers can improve the

capacity performance of a mmWave system when communicating over Rician fading channels. Due to the large number of antennas in the system, SVD approach has a high computational complexity. To reduce the computational complexity of SVD, another approach were proposed in this chapter based on PSO. Furthermore KB filters are proposed for attaining high directionality and side lobe attenuation. From the simulations, it was observed that the PSO beamformer outperforms the SVD and MVD beamformers in terms of capacity. With the application of KB filters, a highly directional beam is attained and side lobes are also attenuated significantly.

Chapter 4

Hybrid Digital-to-Analog Beamforming for Millimeter-Wave Systems with High User Density

4.1 Introduction

Millimeter-wave (mm-Wave) frequencies have the potential of addressing spectrum scarcity and capacity demands in current cellular bands[162]. Full scale implementation of digital system by deploying a radio frequency (RF) transceiver chain per antenna element is impossible due to the constraints of cost, power consumption and signal processing complexity imposed by the RF front end and mixed signal components[17]. A practical solution will be to deploy a much smaller number of RF chains where each RF chain can support a large number of transmit (Tx) antenna elements, resulting in a hybrid digital-to analog (D-A BF) system. Therefore, hybrid D-A BF is one of the techniques of reducing the number of RF chains[52] - [32].

Hybrid D-A BF have been proposed in [77] - [144], where the digital beamformer is equivalent to an identity matrix and the analog beamformer is equivalent to the hermitian of the channel. It is also shown that the overall capacity of the hybrid D-A BF system is limited as compared to the complete digital beamforming (D-BF) system because of the number of RF chains[77]. The major drawback in this type of hybrid D-A BF structure is that each RF chain can only support a particular user[77]. Therefore, the maximum number of users that can be supported by the BS cannot exceed the number of RF chains[77]. This will severely limit mobile capacity in future mm-Wave networks especially in high density user environments like train stations, stadiums or shopping malls. Therefore, new hybrid D-A BF schemes are required, which can support multiple users by employing a BS RF chain to achieve similar capacity gains as promised by the D-BF systems.

Superposition coding can be applied to the Tx symbols on a single stream to support multiple users through a RF chain. However, it cannot serve multiple users simultaneously as only a single 3 dimensional (3D) beam is formed[57]. In this chapter, two new hybrid D-A BF algorithms for supporting multiple users is proposed. With these employed techniques, each user will have its own separate 3D beam assisting

in supporting multiple users simultaneously. These algorithms are implemented with the help of selection combining (SC) and principal component (PC).

- The SC algorithm is an analog beamforming (A-BF) technique which modifies the A-BF matrix by designating each and every antenna element to the selected users. The users and antennas are selected depending upon their instantaneous channel state information (CSI). However, the users experience multi-user interference (MUI) from the beamformed signals. Therefore, a low complexity MUI cancelling technique is proposed at the receiver (Rx).
- In the PC algorithm, the joint design of the hybrid D-A BF matrices is carried out by implementing the eigenvalue decomposition (EVD) of the normalized instantaneous channel realization matrix. The dominant eigenvalues are assigned to the D-BF matrix, and the corresponding eigenvectors are assigned to the A-BF matrix.

From the simulations, it can be observed that the proposed hybrid D-A BFs using SC and PC algorithms achieve superior capacity gains to other hybrid D-A algorithms as proposed in [77] - [144]. Furthermore, the complexity of the SC and the PC algorithms in terms of the number of matrix computations per symbol vectors is analyzed, and has been compared with the existing hybrid D-A BF in [77] - [144]. Our proposed hybrid D-A BF algorithms also accounts for the 3D mm-Wave channel for a multi-user system which is generated when planar antenna arrays are deployed [15] - [187].

The reminder of this chapter is organized as follows. In Section II, the system model is described. In Section III, the hybrid D-A BF SC and PC based algorithms are proposed. In Section IV, the complexity analysis of the SC and PC hybrid D-A BF algorithms are compared to the current known hybrid D-A BFs as proposed in [77] - [144]. In Section V, the simulation results for the mentioned BF techniques are discussed. Finally, the chapter is concluded in Section VI. Upper case and lower case boldfaces are used for matrices and vectors, respectively. Given a matrix $\boldsymbol{X}$, $\boldsymbol{X}^T$, $\boldsymbol{X}^H$, $\mathrm{Tr}(\boldsymbol{X})$ and $\mathrm{diag}(\boldsymbol{X})$ denote its transpose, hermitian, trace and diagonal respectively.

4.2 Description of the Hybrid D-A BF System

The block diagram of the hybrid D-A BF system is shown in Fig. 4.1. This structure is preferred as it is common to the current cellular BS systems[77]. Each of the N RF chains is connected to a large-scale array of M identical antennas. The analysis is carried out considering a downlink scenario for the i-th RF chain supporting the k-th user. For the i-th RF chain the A-BF is performed over only M antennas by the analog beamformer $\boldsymbol{A}_i$. As the channel experiences L resolvable multipath, the digital beamformer for the i-th chain is represented as $\boldsymbol{D}_i$ having dimensions $ML \times ML$. The complete digital beamformer $\boldsymbol{D}$ is given as:

$$\boldsymbol{D} = \mathrm{diag}[\boldsymbol{D}_1, \boldsymbol{D}_2, \cdots, \boldsymbol{D}_N], \tag{4.1}$$

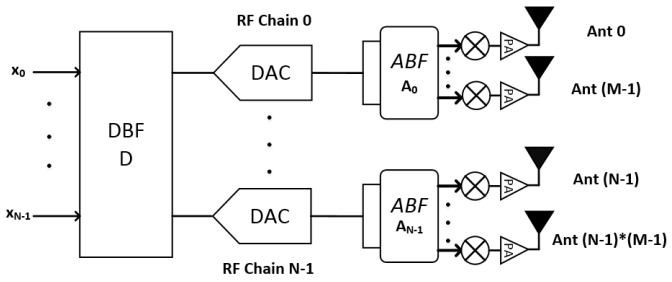

FIGURE 4.1: Hybrid BF Structure

where $\boldsymbol{D}$ accounts for N-RF chains in the BS and is $NML \times NML$ dimensional.

4.2.1 3D mm-Wave Channel Model

The 3D mm-Wave modified Saleh-Valenzuela (SV) channel impulse response (CIR) for the i-th RF chain and the m-th Tx antenna is given by [64]-[5]:

$$\begin{aligned} h^k_{i,m}(t) &= \sum_{v=0}^{V-1}\sum_{u=0}^{U-1} \alpha^k_{i,m,uv} h^k_{i,m,uv} \delta(t-\tau_v-\tau_{uv}) \\ &= \sum_{l=0}^{L-1} \alpha^k_{i,m,l} h^k_{i,m,l} \delta(t-l\tau), \end{aligned} \tag{4.2}$$

where $h^k_{i,m,l}$ is the k-th user CIR of l-th resolvable multi-path for the m-th Tx antenna of the i-th RF chain. V denotes the number of clusters, U the number of of resolvable multi-paths in one cluster, and $L = UV$ is the total number of resolvable multi-paths at the receiver. l is related to u and v by $l = vU + u$. In (2) $h^k_{i,m,uv} = |h^k_{i,m,uv}|e^{j\theta_{uv}}$ represents the fading gain of the u-th resolvable multi-path in the v-th cluster connecting the m-th antenna in the i-th RF chain to the k-th user. τ_v is the time-of-arrival (ToA) of the v-th cluster and $\tau_{uv} = u\tau$ denotes the ToA of the u-th resolvable multi-path in the v-th cluster. In the proposed mm-Wave channel, it is assumed that the average power of a multi-path at a given delay is related to the power of the first resolvable multi-path of the first cluster through the following relationship[5]:

$$P^k_{uv} = P^k_{00}\exp\Big(-\frac{\tau_v}{\Psi}\Big)\exp\Big(-\frac{\tau_{uv}}{\psi}\Big), \tag{4.3}$$

where $P^k_{uv} = P^k_l = |h^k_{i,m,uv}|^2$ represents the expected power of the u-th resolvable multi-path in the v-th cluster connecting the k-th user to the m-th antenna in the i-th RF BS chain. Ψ and ψ are the corresponding power delay constants of the cluster and the resolvable multi-path respectively. For the channel model to be generic, it is assumed that the delay spread, which is $(L-1)\tau$ of the mm-Wave channel spans $g \geq 1$ data bits, satisfying $(g-1)N_\tau \leq (L-1) \leq gN_\tau$, where N_τ is the number of time slots per symbol. Secondly, it is assumed that the L number of resolvable multipath components are randomly distributed, but they are the same over each symbol. Due to the wider bandwidth at mm-Wave, all the L multi-path components

can be resolved at the Rx side[11] - [146], and multi-path diversity will be exploited in the analog beamformer to significantly improve capacity in the proposed system.

The CIR experienced by the i-th RF chain and the k-th user is given as:

$$\boldsymbol{H}_i^k(t) = diag\left[\boldsymbol{H}_{i,0}^k(t),\ \ \boldsymbol{H}_{i,1}^k(t),\ \ \cdots\ \ ,\boldsymbol{H}_{i,M-1}^k(t)\right], \tag{4.4}$$

where $\boldsymbol{H}_{i,m}^k(t)$ is the $L \times (2L-1)$ dimensional Block-Toeplitz temporal CIR convolution matrix associated with the i-th RF chain, m-th Tx antenna and the k-th user, given by (3.5) at the bottom of the page. Finally, $\boldsymbol{H}_i^k(t)$ will also be a temporal matrix be of dimension $ML \times M(2L-1)$.

The k-th user 3D BF gain $\alpha_{i,m,uv}^k = \alpha_{i,m,l}^k$ for every Tx antenna element of the i-th RF chain is given in (3.6). $F_{Rx,V}$ and $F_{Rx,H}$ are the Rx beam pattern for the vertical (V) and horizontal (H) polarizations, respectively. $F_{Tx,i,V}$ and $F_{Tx,i,H}$ are the Tx beam pattern for the i-th RF chain. $\phi_l^{VV}, \phi_l^{VH}, \phi_l^{HV}, \phi_l^{HH}$ are the initial random phases for vertical (VV), cross (VH, HV), and horizontal polarizations (HH) for the l resolvable multi-path. κ_m is the intra-cluster Rician K-factor associated with the m-th Tx antenna cluster[187]. ϑ_l and φ_l are the elevation and azimuth angle-of-arrival (AoA), respectively. Finally, $\theta_{l,m}$ and $\phi_{l,m}$ are the elevation and azimuth angle-of-departure (AoD) of the l-th resolvable multi-path and m-th Tx antenna in the i-th RF chain.

4.2.2 Received Symbols of Hybrid D-A BF

The L samples of received signal at the k-th user from the i-th RF chain is expressed as:

$$\boldsymbol{y}_i^k(t) = \boldsymbol{H}_i^k(t)\boldsymbol{A}_i(t)\boldsymbol{D}_i\boldsymbol{x}_i^k(t) + \boldsymbol{n}_i^k(t), \tag{4.7}$$

where

$$\boldsymbol{x}_i^k(t) = \left[\boldsymbol{x}_{i,0}^k(t), \boldsymbol{x}_{i,1}^k(t), \cdots, \boldsymbol{x}_{i,M-1}^k(t)\right]^T \tag{4.8}$$

are the $ML \times 1$ dimensional transmitted uncorrelated data symbols to the k-th user from the i-th RF chain. $\boldsymbol{x}_{i,m}^k(t) = [x_{i,m}^k(t), x_{i,m}^k(t-1), \cdots, x_{i,m}^k(t-L+1)]$ are the L symbol samples for all the l resolvable multi-paths, corresponding to the m-th Tx antenna in the i-th chain. BF design will be discussed in detail in the following section. $\boldsymbol{n}_i^k(t)$ is modelled as independent and identical distributed (iid) complex Gaussian random noise with zero mean and a variance of σ_i^2 for the k-th user. The

$$\boldsymbol{H}_{i,m}^k(t) = \begin{bmatrix} h_{i,m,0}^k(t) & h_{i,m,1}^k(t) & \cdots & h_{i,m,L-1}^k(t) & 0 & \cdots & 0 \\ 0 & h_{i,m,0}^k(t-1) & h_{i,m,1}^k(t-1) & \cdots & h_{i,m,L-1}^k(t-1) & \cdots & 0 \\ \vdots & \ddots & \ddots & \ddots & \ddots & \vdots & \vdots \\ 0 & \cdots & 0 & h_{i,m,0}^k(t-L+1) & h_{i,m,1}^k(t-L+1) & \cdots & h_{i,m,L-1}^k(t-L+1) \end{bmatrix} \tag{4.5}$$

$$\alpha_{i,m,l}^k = \sum_{l=1}^{L} \sqrt{P_l^k} \begin{bmatrix} F_{Rx,V}(\varphi_l, \vartheta_l) \\ F_{Rx,H}(\varphi_l, \vartheta_l) \end{bmatrix}^T \begin{bmatrix} e^{j\phi_l^{VV}} & \sqrt{\kappa_m^{-1}} e^{j\phi_l^{VH}} \\ \sqrt{\kappa_m^{-1}} e^{j\phi_l^{HV}} & e^{j\phi_l^{HH}} \end{bmatrix} \begin{bmatrix} F_{Tx,i,V}(\phi_{l,m}, \theta_{l,m}) \\ F_{Tx,i,H}(\phi_{l,m}, \theta_{l,m}) \end{bmatrix} \tag{4.6}$$

signal to noise ratio (SNR) of the i-th RF chain is denoted by γ_i and is given as:

$$\gamma_i(\boldsymbol{D}_i, \boldsymbol{A}_i(t), \boldsymbol{H}_i^k(t)) = \gamma_0 \frac{|\boldsymbol{H}_i^k(t)\boldsymbol{A}_i(t)\boldsymbol{D}_i\boldsymbol{x}_i^k(t)|^2}{\sigma_i^2}, \tag{4.9}$$

where γ_0 is the average input SNR. Maximizing this SNR will lead to improved system capacity (in bit per second per Hz) for the k-th user associated with the i-th RF chain, and calculated as:

$$C_i^k = \log_2[1 + \gamma_i(\boldsymbol{D}_i, \boldsymbol{A}_i(t), \boldsymbol{H}_i^k(t))]. \tag{4.10}$$

Let us now proceed towards designing the BF matrices which maximize the SNR of the i-th RF chain.

4.3 Beamformer Design for Hybrid D-A BF

In this section, two types of hybrid D-A BF are considered for supporting a high density of users in mm-Wave systems. In the separate design of hybrid D-A BF as proposed in [77] - [144], the analog beamformer $\boldsymbol{A}_i = \boldsymbol{H}_i^H / ||\boldsymbol{H}_i||_F$ is equal to the normalized hermitian of the channel. $||\boldsymbol{H}_i||_F$ is the Frobenius norm of the channel. The digital beamformer, $\boldsymbol{D}_i = \boldsymbol{I}$ is an identity matrix of size L. The BF matrix in this case is simply a matched filter (MF) as $\boldsymbol{A}_i\boldsymbol{D}_i = \boldsymbol{H}_i^H / ||\boldsymbol{H}_i||_F$. However, high user density environment cannot be supported by this method. Therefore, the SC and PC algorithms are proposed. SC is an A-BF technique while PC designs the hybrid D-A jointly.

4.3.1 Hybrid D-A BF with Selection Combining (SC)

In SC algorithm, M antenna elements in the i-th RF chain have to be allocated to K users. K represents the total number of users in a high user density environment, that have to be supported by the i-th RF chain such that $K \leq M$. The allocation of antenna elements is based on the calculation of expected power of the 3D mm-Wave modified SV channel of every user. For the m-th antenna element in the i-th RF chain, the channel power associated with the k-th user is calculated as follows:

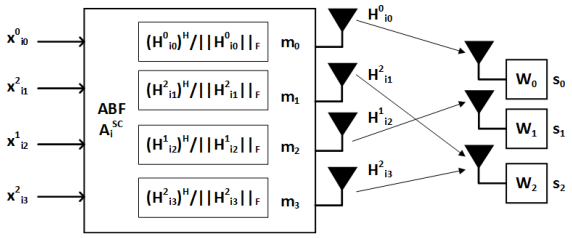

FIGURE 4.2: SC Antenna Allocation for the i-th RF chain

$$p_{i,m}^{k} = \sum_{l=1}^{L} |h_{i,m,l}^{k}|^2 \tag{4.11}$$

This process is repeated for all the K users for the m-th antenna element. The m-th antenna is then assigned to that user which has the maximum power:

$$k_m = \underset{k \in K}{\text{argmax}} \left\{ p_{i,m}^{1}, p_{i,m}^{2}, \cdots, p_{i,m}^{K} \right\}, \tag{4.12}$$

where argmax calculates the maximum value. This process is repeated M times until all the M antennas are allocated to the S users where $S \leq K$. The remaining $(K - S)$ users are not supported. It is clear that SC algorithm allocates non-contiguous antenna elements to the respective users. Therefore, the users will experience MUI from the beamformed signals generated from antenna elements that are allocated to other users. Interference from the undesired beamformed signals can be eliminated at every user by a set of receive BF weights. It is assumed that the SC antenna allocation information is available at the receiver. For example, consider a scenario in which the number of antenna elements in the i-th RF chain is $M = 4$, the total number of single antenna users to be supported by this i-th RF chain is $S = 3$, and where the SC antenna allocation for the i-th RF chain that follows the pattern as shown in Fig. 2. In this scenario, antenna m_0 is allocated to user s_0; m_1 and m_3 to s_2; and m_2 to s_1. As shown in the figure, A-BF $\boldsymbol{A}_i^{SC}(t)$ is performed over each of the M antennas, where as MUI suppression is implemented by the weights $\boldsymbol{w}_s$ at the s-th user. The A-BF matrix $\boldsymbol{A}_i^{SC}(t)$, as depicted in Fig. 4.2 is given by:

$$\boldsymbol{A}_i^{SC}(t) = diag \begin{bmatrix} \boldsymbol{H}_{i,0}^{0\ H}(t)/||\boldsymbol{H}_{i,0}^{0}||_F \\ \boldsymbol{H}_{i,1}^{2\ H}(t)/||\boldsymbol{H}_{i,1}^{2}||_F \\ \boldsymbol{H}_{i,2}^{1\ H}(t)/||\boldsymbol{H}_{i,2}^{1}||_F \\ \boldsymbol{H}_{i,3}^{2\ H}(t)/||\boldsymbol{H}_{i,3}^{2}||_F \end{bmatrix}, \tag{4.13}$$

where $\boldsymbol{H}_{i,m}^{s}(t)$ represents the CIR from the m-th Tx antenna to the s-th user as was defined in (3.5). Now let us examine the case of user s_2. The received signal at s_2 can be represented as:

$$\begin{aligned} \boldsymbol{y}_i^{s_2}(t) &= \boldsymbol{w}_2 \boldsymbol{H}_{i,1}^{2}(t) \boldsymbol{A}_i^{SC}(t) \boldsymbol{x}_i(t) + \boldsymbol{w}_2 \boldsymbol{H}_{i,3}^{2}(t) \boldsymbol{A}_i^{SC}(t) \boldsymbol{x}_i(t) \\ &+ \underbrace{\boldsymbol{w}_2 \boldsymbol{H}_{i,0}^{2}(t) \boldsymbol{A}_i^{SC}(t) \boldsymbol{x}_i(t)}_{\text{Interference from user } s_0} + \underbrace{\boldsymbol{w}_2 \boldsymbol{H}_{i,2}^{2}(t) \boldsymbol{A}_i^{SC}(t) \boldsymbol{x}_i(t)}_{\text{Interference from user } s_1} \\ &+ \boldsymbol{w}_2 \boldsymbol{n}_{i,2}(t) \end{aligned} \tag{4.14}$$

In (3.14), $\boldsymbol{x}_i(t) = [\boldsymbol{x}_{i,0}^{0}(t), \boldsymbol{x}_{i,1}^{2}(t), \boldsymbol{x}_{i,2}^{1}(t), \boldsymbol{x}_{i,3}^{2}(t)]^T$ is the $ML \times 1$ symbol vector for the i-th chain, where $\boldsymbol{x}_{i,m}^{s}(t) = [x_{i,m}^{s}(t), x_{i,m}^{s}(t-1), \cdots, x_{i,m}^{s}(t-L+1)]$ is the $L \times 1$ symbol vector assigned to the m-th antenna that is allocated to the s-th user by the SC algorithm. $\boldsymbol{n}_{i,2}(t)$ is the iid complex Gaussian random noise for the user s_2 with a variance of $\sigma_{i,2}^2$. $\{\boldsymbol{H}_{i,m}^{2}(t) \boldsymbol{A}_i^{SC}(t)\}$ is the $ML \times ML$ signal received at s_2 after analog preprocessing at the Tx and channel conditioning given by (3.15) at the bottom of the page. In (3.15) $h_{i,m,l}^{2}(t)$ is the l-th resolvable multi-path at time instant t

$$\boldsymbol{H}^2_{i,m}(t)\boldsymbol{A}^{SC}_i(t) \quad = diag\begin{bmatrix}\boldsymbol{H}^2_{i,0}(t)\boldsymbol{H}^0_{i,0}(t)^H/||\boldsymbol{H}^0_{i,0}||_F\\ \boldsymbol{H}^2_{i,1}(t)\boldsymbol{H}^2_{i,1}(t)^H/||\boldsymbol{H}^2_{i,1}||_F\\ \boldsymbol{H}^2_{i,2}(t)\boldsymbol{H}^1_{i,2}(t)^H/||\boldsymbol{H}^1_{i,2}||_F\\ \boldsymbol{H}^2_{i,3}(t)\boldsymbol{H}^2_{i,3}(t)^H/||\boldsymbol{H}^2_{i,3}||_F\end{bmatrix} = \quad diag\begin{bmatrix}\sum_{l=0}^{L-1}|h^2_{i,0,l}(t)h^0_{i,0,l}(t)|/||\boldsymbol{H}^0_{i,0}||_F\\ \sum_{l=0}^{L-1}|h^2_{i,0,l}(t-1)h^0_{i,0,l}(t-1)|/||\boldsymbol{H}^0_{i,0}||_F\\ \vdots\\ \sum_{l=0}^{L-1}|h^2_{i,0,l}(t-L+1)h^0_{i,0,l}(t-L+1)|/||\boldsymbol{H}^0_{i,0}||_F\\ \sum_{l=0}^{L-1}|h^2_{i,1,l}(t)|^2/||\boldsymbol{H}^2_{i,1}||_F\\ \sum_{l=0}^{L-1}|h^2_{i,1,l}(t-1)|^2/||\boldsymbol{H}^2_{i,1}||_F\\ \vdots\\ \sum_{l=0}^{L-1}|h^2_{i,1,l}(t-L+1)|^2/||\boldsymbol{H}^2_{i,1}||_F\\ \sum_{l=0}^{L-1}|h^2_{i,2,l}(t)h^1_{i,2,l}(t)|/||\boldsymbol{H}^1_{i,2}||_F\\ \sum_{l=0}^{L-1}|h^2_{i,2,l}(t-1)h^1_{i,2,l}(t-1)|/||\boldsymbol{H}^1_{i,2}||_F\\ \vdots\\ \sum_{l=0}^{L-1}|h^2_{i,2,l}(t-L+1)h^1_{i,2,l}(t-L+1)|/||\boldsymbol{H}^1_{i,2}||_F\\ \sum_{l=0}^{L-1}|h^2_{i,3,l}(t)|^2/||\boldsymbol{H}^2_{i,3}||_F\\ \sum_{l=0}^{L-1}|h^2_{i,3,l}(t-1)|^2/||\boldsymbol{H}^2_{i,3}||_F\\ \vdots\\ \sum_{l=0}^{L-1}|h^2_{i,3,l}(t-L+1)|^2/||\boldsymbol{H}^2_{i,3}||_F\end{bmatrix} \tag{3.15}$$

as defined previously. The $1 \times ML$ Rx-BF selection weights $\boldsymbol{w}_2 = [\mathbf{0},\mathbf{1},\mathbf{0},\mathbf{1}]$, where the $\mathbf{0}$'s and $\mathbf{1}$'s are L dimensional, operating on $\{\boldsymbol{H}^2_{i,m}(t)\boldsymbol{A}^{SC}_i(t)\}$, will cancel the MUI from the unwanted beamformed signals that are generated by antenna elements allocated to the other users by the SC algorithm. It can be observed that the pattern of zeros follow the MUI's from the respective antenna elements which need to be eliminated. $\boldsymbol{D}_i$ is identity similar to [77] - [144]. The weights for the other users for mitigating MUI can be similarly derived as $\boldsymbol{w}_0 = [\mathbf{1},\mathbf{0},\mathbf{0},\mathbf{0}]$ and $\boldsymbol{w}_1 = [\mathbf{0},\mathbf{0},\mathbf{1},\mathbf{0}]$ respectively, and can be extended for any SC antenna allocation. In this way, the receiver complexity can be reduced significantly because processing is moved to the Tx side. To satisfy the total power constraint the signal power of the i-th RF chain is:

$$\frac{1}{M}\sum_{m=1}^{M}\sum_{k=1}^{S} p^k_{i,m} \leq \sigma_i^2\gamma_i \tag{4.16}$$

Finally, the SNR for the i-th RF chain and the s-th user for the SC algorithm is calculated as follows [71]:

$$\begin{aligned}\gamma_i(\boldsymbol{w}_s,\boldsymbol{D}_i,\boldsymbol{A}^{SC}_i(t),\boldsymbol{H}^s_i(t)) = \frac{M_s\gamma_0}{M}|&(\sigma^2_{i,s}\boldsymbol{w}_s^H)^{-1}\boldsymbol{w}_s^H\boldsymbol{H}^s_i(t)\\ &\times \boldsymbol{A}^{SC}_i(t)\boldsymbol{D}_i\boldsymbol{D}_i^H\boldsymbol{A}^{SC^H}_i(t)\\ &\times \boldsymbol{H}^{s^H}_i(t)\boldsymbol{w}_s|,\end{aligned} \tag{17}$$

where M_s is the number of antennas allocated to the s-th user and $\sigma^2_{i,s}$ is the corresponding iid noise variance.

4.3.2 Hybrid D-A BF using Principal Component (PC)

In the SC algorithm, $(K-S)$ users had to be discarded because of the power constraint at the i-th RF chain. Furthermore, the D-BF matrix was unchanged as it remained identity. To support maximum number of users, the PC algorithm was proposed. First, the CIR matrix for the K users is obtained, and is given by:

$$\boldsymbol{H}_i^{PC}(t) = diag\left[\boldsymbol{H}_i^1(t),\ \boldsymbol{H}_i^2(t),\ \cdots\ ,\boldsymbol{H}_i^K(t)\right], \tag{4.18}$$

where $\boldsymbol{H}_i^k$ is the 3D mm-Wave modified SV CIR experienced by the k-th user at the i-th RF chain as explained in (5). Then, the normalized instantaneous channel realization matrix $\boldsymbol{R}_i^{PC}$ is calculated as:

$$\boldsymbol{R}_i^{PC}(t) = \frac{\left(\boldsymbol{H}_i^{PC}(t)\right)^H \boldsymbol{H}_i^{PC}(t)}{||\left(\boldsymbol{H}_i^{PC}(t)\right)^H \boldsymbol{H}_i^{PC}(t)||_F} \tag{4.19}$$

The EVD of $\boldsymbol{R}_i^{PC}(t)$ is then performed to obtain the eigenvalues and the eigenvectors. Then, for the k-th user, the dominant eigenvalues $\boldsymbol{\lambda}_{k,i}^{PC}$, and its corresponding eigenvectors $\boldsymbol{\Phi}_{k,i}^{PC}$, are selected to compute the joint hybrid D-A BF beamfromer $\boldsymbol{G}_i^{PC}$ for the i-th RF chain, given in (3.20) at the top of the next page. In order to allocate the M Tx antennas among all the K users, it is ensured that $\sum_{k=1}^{K} m_k = ML$. Therefore, the k-th user is allocated m_k antenna elements from the i-th RF chain. To satisfy the total power constraint the signal power of the ith RF chain should satisfy:

$$\begin{aligned} ||\boldsymbol{G}_i^{PC}||^2 &= ||\boldsymbol{D}_i^{PC}\boldsymbol{A}_i^{PC}||^2 \\ &= \mathrm{Tr}(\boldsymbol{D}_i^{PC}\boldsymbol{A}_i^{PC}\left(\boldsymbol{A}_i^{PC}\right)^H\left(\boldsymbol{D}_i^{PC}\right)^H) \\ &\leq \sigma_i^2\gamma_i \end{aligned} \tag{4.21}$$

$$\boldsymbol{G}_i^{PC} = \underbrace{\begin{bmatrix} \underbrace{\begin{pmatrix} \lambda_{1,i}^1 & \cdots & 0 \\ \vdots & \ddots & \vdots \\ 0 & \cdots & \lambda_{m_1,i}^1 \end{pmatrix}}_{\boldsymbol{\lambda}_{1,i}^{PC}} & \begin{matrix} 0 & \cdots & 0 \\ \vdots & \ddots & \vdots \\ 0 & \cdots & 0 \end{matrix} & \cdots & \begin{matrix} 0 & \cdots & 0 \\ \vdots & \ddots & \vdots \\ 0 & \cdots & 0 \end{matrix} \\ \begin{matrix} 0 & \cdots & 0 \\ \vdots & \ddots & \vdots \\ 0 & \cdots & 0 \end{matrix} & \underbrace{\begin{pmatrix} \lambda_{1,i}^2 & \cdots & 0 \\ \vdots & \ddots & \vdots \\ 0 & \cdots & \lambda_{m_2,i}^2 \end{pmatrix}}_{\boldsymbol{\lambda}_{2,i}^{PC}} & \cdots & \begin{matrix} 0 & \cdots & 0 \\ \vdots & \ddots & \vdots \\ 0 & \cdots & 0 \end{matrix} \\ \vdots & \vdots & \ddots & \vdots \\ \begin{matrix} 0 & \cdots & 0 \\ \vdots & \ddots & \vdots \\ 0 & \cdots & 0 \end{matrix} & \begin{matrix} 0 & \cdots & 0 \\ \vdots & \ddots & \vdots \\ 0 & \cdots & 0 \end{matrix} & \cdots & \underbrace{\begin{pmatrix} \lambda_{1,i}^K & \cdots & 0 \\ \vdots & \ddots & \vdots \\ 0 & \cdots & \lambda_{m_K,i}^K \end{pmatrix}}_{\boldsymbol{\lambda}_{K,i}^{PC}} \end{bmatrix}}_{\boldsymbol{D}_i^{PC}} \underbrace{\begin{bmatrix} \underbrace{\begin{pmatrix} \boldsymbol{\Phi}_{1,i}^1 \\ \vdots \\ \boldsymbol{\Phi}_{m_1,i}^1 \end{pmatrix}}_{\boldsymbol{\Phi}_{1,i}^{PC}} \\ \underbrace{\begin{pmatrix} \boldsymbol{\Phi}_{1,i}^2 \\ \vdots \\ \boldsymbol{\Phi}_{m_2,i}^2 \end{pmatrix}}_{\boldsymbol{\Phi}_{2,i}^{PC}} \\ \vdots \\ \underbrace{\begin{pmatrix} \boldsymbol{\Phi}_{1,i}^K \\ \vdots \\ \boldsymbol{\Phi}_{m_K,i}^K \end{pmatrix}}_{\boldsymbol{\Phi}_{K,i}^{PC}} \end{bmatrix}^T}_{\boldsymbol{A}_i^{PC}} \tag{4.20}$$

Finally, the SNR for the i-th RF chain with U users for the PC algorithm is derived as:

$$\gamma_i^{PC}(\boldsymbol{D}_i^{PC}, \boldsymbol{A}_i^{PC}, \boldsymbol{H}_i^{PC}(t)) = \gamma_0 \frac{|\boldsymbol{H}_i^{PC}(t)\boldsymbol{A}_i^{PC}\boldsymbol{D}_i^{PC}\boldsymbol{x}_i|^2}{\sigma_i^2} \tag{4.22}$$

4.4 Complexity Analysis

Now, the computational complexity of the SC and PC hybrid D-A BF algorithms as compared the current known hybrid D-A BF which has been proposed in [77], [144] will be analyzed. For the hybrid D-A BF preprocessing of ML symbols of the Tx signal $\boldsymbol{H}_i^k(t)\boldsymbol{A}_i(t)\boldsymbol{D}_i\boldsymbol{x}_i^k(t)$ as given by (3.6) for the k-th user, $M^3L^2(2L-1)(ML+1)$ scalar multiplications and $(M(2L-1)-1)(ML-1)$ scalar additions need to be performed[50]. In the SC algorithm, the number of scalar multiplications and additions are $\sum_{s=0}^{S-1} M_s^3L^2(2L-1)(M_sL+1)$ and $(\sum_{s=0}^{S-1} M_s(2L-1)-1)(\sum_{s=0}^{S-1} M_sL-1)$ receptively, where M_s is the number of antenna elements allocated to the s-th user as discussed previously. In the context of PC algorithm, it takes about $N_\tau + L - 1$ multiplications to calculate the eigenvalue from the normalized instantaneous channel realization matrix $\boldsymbol{R}_i^{PC}$ given by (19), where N_τ is the number of time slots per symbol as discussed in Section II [51]. When the eigenvectors are calculated, it takes $(N_\tau + L - 1)^3$ number of additions and $(N_\tau + L - 1)^3$ number of multiplications to determine the required eigenvectors [51]. Furthermore, the number of multiplications and additions that are performed for ML symbols will be $M^2L^2(M(2L-1)+1)$ and M^2L^2-1 respectively. Table 3.1 summarizes the number of computations required.

TABLE 4.1: Computational complexity.

Algorithm	Number of operations per ML symbols	
	Additions	Multiplications
Separate Hybrid D-A BF	$(M(2L-1)-1)(ML-1)$	$M^3L^2(2L-1)(ML+1)$
SC Algorithm	$(\sum_{s=0}^{S-1} M_s(2L-1)-1)(\sum_{s=0}^{S-1} M_sL-1)$	$\sum_{s=0}^{S-1} M_s^3L^2(2L-1)(M_sL+1)$
PC Algorithm	$(N_\tau+L-1)^3 + M^2L^2 - 1$	$(N_\tau+L-1)^3 + M^2L^2(M(2L-1)+1)$

4.5 Simulation Results

TABLE 4.2: 3D mm-Wave Modified SV Channel Parameters

Description	Unit	Value
Inter-cluster inter-arrival rate	1/ns	0.21
Intra-cluster inter-arrival rate	1/ns	0.77
Inter-cluster decay factor	ns	4.19
Intra-cluster decay factor	ns	1.07
Small-scale fading RMS	dB	1.26
Inter-cluster Rician K-factor	dB	-10
Intra-cluster Rician K-factor	dB	-10

Fig. 4.6 plots the beam patterns generated by the $M = 16 \times 16$ planar BS antenna array in the i-th RF chain. Fig. 4.6a shows the pattern for a single user, with separate hybrid D-A BF design as in [77] - [144]. Fig. 4.6b shows the pattern generated for a second and a third user in addition to the first user for the same RF chain using the SC algorithm. It can be observed from Fig. 4.6b that while SC achieves user separation, the directivity of the beams are reduced. This is because the number of antenna elements allocated per user is reduced, and at the same time, selection combining does not design the D-BF matrix, keeping it as identity as in the case of separate hybrid D-A BF design. Fig. 4.6c shows the pattern generated for the users using the PC algorithm that jointly designs the hybrid D-A BF matrices. It should be noted that despite the available number of antenna array elements remaining the same, the directivity of the beams are enhanced in PC as compared to SC. In these simulations, the number of BS antenna array elements is chosen considering the processing and bandwidth limitations of the massive multiple-input multiple-output (MIMO) architectures.

Therefore, it has been proven that the proposed hybrid D-A BF techniques based on the SC and PC algorithm provide an alternative for supporting more than a particular

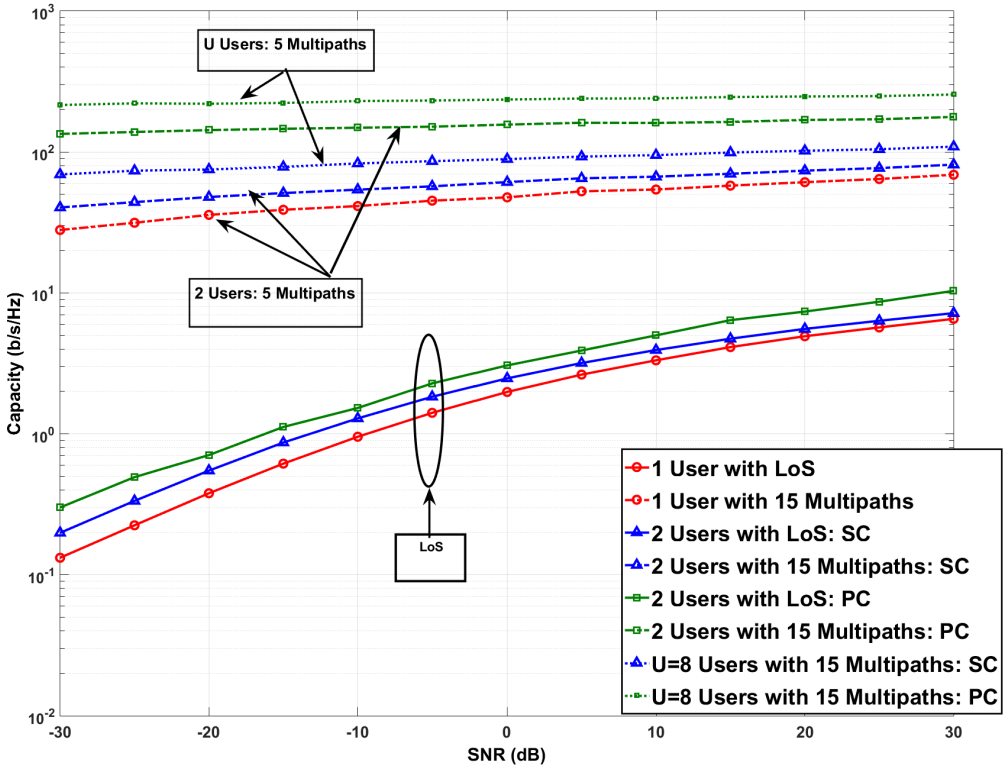

FIGURE 4.3: Capacity of the proposed hybrid D-A BF systems as a function of SNR. Results are reported for a downlink mmWave system with $M = 16 \times 16$ BS antennas from SNR of -30dB to 30dB. The simulated environment includes both a single LoS channel and $L = 15$ multi-path.

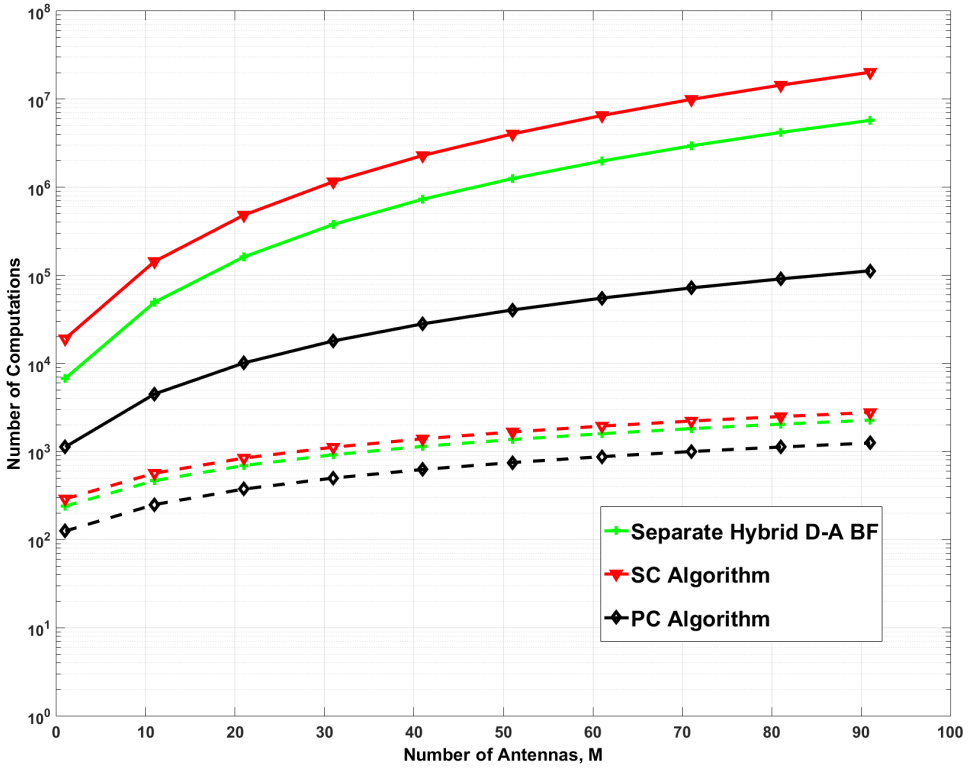

FIGURE 4.4: Number of matrix computations of the proposed hybrid D-A BF systems as a function of the number of antennas. Results are reported for $L = 15$ multi-path per cluster for up-to $M = 10 \times 10$ antenna array.

user per RF chain[134].

In this section, beam pattern, capacity performance and the complexity analysis of three different kinds of hybrid D-A BF algorithms are investigated. SC and PC based hybrid D-A BF are compared with one another. The parameters for generating the 3D mm-Wave modified SV channel model are mentioned in Table 3.2[187]. Perfect channel knowledge is assumed between the Tx antennas and Rx antenna. Two different environments are considered in the simulations. In the first environment perfect line-of-sight (LoS) is available. While, in the second environment, multipath are present, and the number of resolvable multipath is assumed to be 15. A uniform planar array of $M = 16 \times 16$ antennas is considered.

Fig. 4.3 shows the capacity of this hybrid D-A BF system when using i-th RF chain. In this figure, it can be observed that the PC based algorithm achieves the upper bound of capacity for all the simulated environments. This is because the PC algorithm accomplishes the joint design of the A-BF and D-BF matrices, and assigns diagonal weights to the D-BF matrix, as compared to identity weights in SC or separate hybrid D-A BFs as proposed in [77] - [144]. Furthermore, Fig. 8.3 also indicates that by using the SC and PC algorithms to design the hybrid D-A BF system, the capacity increases when the number of users per RF chain increases. This is because

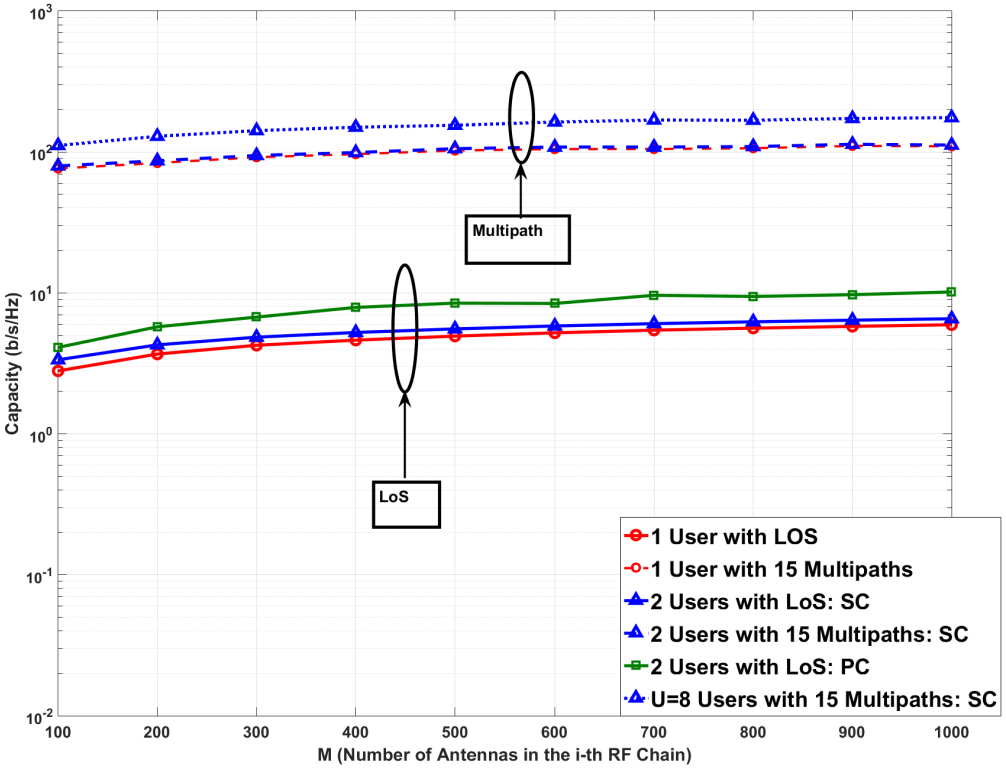

FIGURE 4.5: Capacity of the proposed hybrid D-A BF systems as a function of number of antenna elements. Results are reported for a downlink mm-Wave system with $M = 10 \times 10$ BS antennas for an SNR of -30dB. The simulated environment includes both a single LoS channel and $L = 15$ multi-path.

with a larger number of users, the number of resolvable multi-path in the mm-Wave channel increases which are combined using A-BF to improve the SNR at the respective users. In this way, multi-path diversity has been exploited in the proposed mm-Wave system. This is observed in the curves with $K = 8$ users and $L = 15$ resolvable multipath per Tx antenna cluster attaining the upper bound as compared to the single user case with $L = 15$ resolvable multipath. $K = 8$ users per RF chain in a BS is chosen to represent a high user density scenario in mm-Wave systems. However, capacity gains from multi-path diversity will be offset by the power constraint in the i-th RF chain, and it will tend to saturate. From this figure, it can also be observed that PC and SC algorithms outperform the separate hybrid D-A BF design. Substantial gains in terms of performance are achieved by using these algorithms.

Fig. 4.4 shows the capacity of this hybrid D-A BF system when using i-th RF chain versus the number of antenna elements for an SNR of -10dB. It can be observed that the capacity of the hybrid D-ABF system saturates. This is because of the power constraint imposed on the i-th RF chain, adding antenna elements and thus increasing the number of multi-path clusters does not improve the diversity order at the user.

Now, the plots for complexity analysis of the proposed hybrid D-A BF systems based

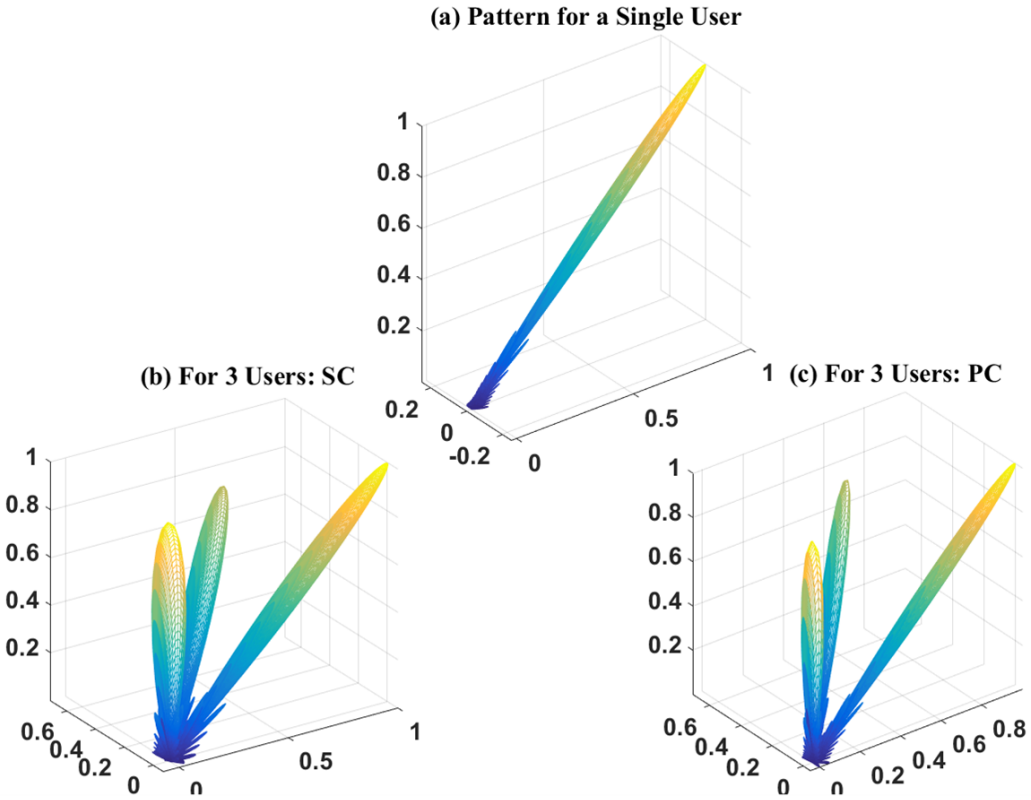

FIGURE 4.6: Normalized beam pattern for $M = 16 \times 16$ planar array using separate hybrid D-A BF design, SC and PC. (a) Beam pattern of the original user in Separate Hybrid D-A BF Design. The angular location of the user is at $\theta = 0^\circ$ from the y-z plane $\phi = 30^\circ$ from the x-z plane, (b) Hybrid D-A BF design using SC. The combined beam patterns for the 3 users. The angular location of the 1-st user is unchanged, where as that of the 2-nd user is $\theta = 45^\circ$ from the y-z plane $\phi = 45^\circ$ from the x-z plane, and that of the 3-rd user is $\theta = 0^\circ$ from the y-z plane $\phi = 90^\circ$ from the x-z plane, and (c) Hybrid D-A BF design using PC. Combined beam patterns for the 1-st, 2-nd and 3-rd user using PC. The beam directivity is enhanced using PC.

on the analysis in Section IV will be discussed. Fig. 4.5 plots number of matrix multiplications and matrix additions for the separate hybrid D-A BF design, SC and PC algorithms as a function of the number of antennas. As predicted in Section IV, the computational complexity of the PC technique in the case of multiplications is lower than the separate design and the SC technique by at least an order of 2 and 4 respectively. No special algorithms for improving the speed of matrix computations is assumed in these results.

4.6 Summary

In this chapter, two new algorithms which operate on the principles of SC and PC have been proposed for hybrid D-A BF based mm-Wave system. From the proposed algorithms, it was possible to support more than a single user per RF chain. These algorithms have a significant impact when higher density of users were present and the particular RF chain had to support multiple users. From the simulations, it was observed that the proposed hybrid D-A BF using SC and PC achieves higher capacity as compared to the known hybrid D-A BF and supports higher density of users per RF chain. Lastly, it has been also proved that the PC algorithm which jointly designed the hybrid D-A BF matrix attained lower computational complexity.

Chapter 5

Low-Complexity Hybrid Digital-to-Analog Beamforming for Millimeter-Wave Systems with High User Density

In the previous chapter, the novel SC and LC-PC algorithms had been proposed for supporting high user density in hybird D-A BF systems. In this chapter, low complexity variants of SC and PC, the LC-SC and LC-PC have been proposed, with every user will have its own separate 3D beam. These algorithms are implemented with the help of low-complexity selection combining (LC-SC) and low complexity principal component (LC-PC).

- The LC-SC algorithm is a space-time analog beamforming (A-BF) technique which modifies the A-BF matrix by designating each and every antenna element to the selected users. The users and antennas are selected depending upon their instantaneous channel state information (CSI). Multi-user interference (MUI) from the beamformed signals at the users is also accounted for. However, this technique will increase the complexity of the analog beamformer.
- In the LC-PC algorithm, the joint design of the hybrid D-A BF matrices is carried out by implementing the eigenvalue decomposition (EVD) of the normalized instantaneous channel realization matrix. The dominant eigenvalues are assigned to the D-BF matrix, and the corresponding eigenvectors are assigned to the A-BF matrix.

From the simulations, it can be observed that the proposed hybrid D-A BFs using LC-SC and LC-PC algorithms achieve superior SE as compared to other hybrid D-A BF algorithms as proposed in [77],[144]. Furthermore, the complexity of the LC-SC and the LC-PC algorithms in terms of the number of matrix computations per symbol vectors is analyzed, and is compared with the existing hybrid D-A BF in [77],[144]. Our proposed hybrid D-A BF algorithms also accounts for the 3D mm-Wave channel for a high user density mm-Wave system which is generated when planar antenna arrays are employed[187].

The reminder of this chapter is organized as follows. In Section II, the system model is described. In Section III, the hybrid D-A BF LC-SC and LC-PC algorithms are

proposed. In Section IV, the beamformer complexity analysis of the LC-SC and LC-PC hybrid D-A BF algorithms are compared to the current known hybrid D-A BFs as proposed in [77],[144]. In Section V, the simulation results are discussed. The chapter is concluded in Section VI. Upper case and lower case boldfaces are used for matrices and vectors, respectively. $\boldsymbol{X}$, $\boldsymbol{X}^T$, $\boldsymbol{X}^H$, $\mathrm{Tr}(\boldsymbol{X})$ denote a matrix transpose, hermitian, and trace respectively.

5.1 Description of the Hybrid D-A BF System

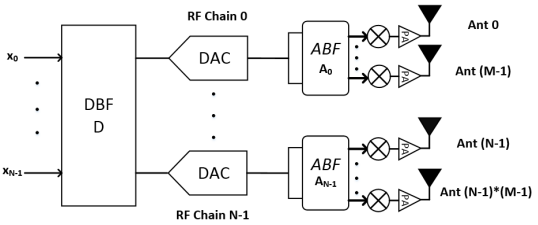

FIGURE 5.1: Hybrid BF Structure

The block diagram of the current hybrid D-A BF BS system is shown in Fig. 5.1 [77],[144]. Each of the N RF chains is connected to a large-scale array of M identical antennas. In this chapter, The analysis is initially carried out considering a downlink scenario for an i-th RF chain supporting only a particular k-th user, where $0 < i \leq N-1$ and $0 < k \leq K-1$. Subsequently, two hybrid D-A BF algorithms, LC-SC and LC-PC, are considered for scaling-up the number of users supported by the i-th RF chain by upto K, where $K \leq M$. Furthermore, for the i-th RF chain, the A-BF is performed over M antennas and L time-slots by the space-time analog beamformer $\boldsymbol{a}_i(t)$. The complete digital beamformer $\boldsymbol{D} = \mathrm{diag}[d_1, d_2, \cdots, d_N]$ is an $N \times N$ matrix accounting for all N RF chains of the BS.

5.1.1 3D mm-Wave Modified SV Channel Model

The 3D mm-wave modified Saleh-Valenzuela (SV) channel modeled by L multi-path coefficients[64, 6, 5] is given by:

$$\begin{aligned} h_{i,m,k}(t) &= \sum_{v=0}^{V-1} \sum_{u=0}^{U-1} \beta_{i,m,uv,k} h_{i,m,uv,k}(t - \tau_v - \tau_{uv}) \\ &= \sum_{l=0}^{L-1} \beta_{i,m,l,k} h_{i,m,l,k}(t - l\tau) \end{aligned} \tag{5.1}$$

In (4.1), $h_{i,m,l,k}$ is the k-th user convolutional impulse response (CIR) of l-th resolvable multi-path for the m-th Tx antenna in the i-th RF chain. V denotes the number of clusters, U the number of of resolvable multi-path in one cluster, and $L = UV$ is the total number of resolvable multi-paths at the receiver. l is related to u and v by $l = vU + u$. $h_{i,m,uv,k} = |h_{i,m,uv,k}| e^{j\theta_{uv}}$ represents the fading gain of the u-th resolvable multi-path in the v-th cluster connecting the m-th antenna in the i-th RF chain to

$$\beta_{i,m,l,k} = \sqrt{P_{l,k}} \begin{bmatrix} F_{Rx,V}(\varphi_l, \vartheta_l) \\ F_{Rx,H}(\varphi_l, \vartheta_l) \end{bmatrix}^T \begin{bmatrix} e^{j\phi_l^{VV}} & \sqrt{\kappa_m^{-1}} e^{j\phi_l^{VH}} \\ \sqrt{\kappa_m^{-1}} e^{j\phi_l^{HV}} & e^{j\phi_l^{HH}} \end{bmatrix} \begin{bmatrix} F_{Tx,i,V}(\phi_{l,m}, \theta_{l,m}) \\ F_{Tx,i,H}(\phi_{l,m}, \theta_{l,m}) \end{bmatrix} \quad (5.3)$$

the k-th user. τ_v is the time-of-arrival (ToA) of the v-th cluster and $\tau_{uv} = u\tau$ denotes the ToA of the u-th resolvable multi-path in the v-th cluster. In the mm-Wave channel, it is assumed that the average power of a multi-path at a given delay is related to the power of the first resolvable multi-path of the first cluster through the following relationship[6],[5]:

$$P_{uv}^k = P_{00}^k \exp\Big(-\frac{\tau_v}{\Psi}\Big) \exp\Big(-\frac{\tau_{uv}}{\psi}\Big), \quad (5.2)$$

where $P_{uv}^k = P_l^k = |h_{i,m,uv}^k|^2$ represents the expected power of the u-th resolvable multi-path in the v-th cluster connecting the k-th user to the m-th antenna in the i-th RF BS chain. Ψ and ψ are the corresponding power delay constants of the cluster and the resolvable multi-path respectively. For the channel model to be generic, it is assumed that the delay spread, which is $(L-1)\tau$ for the mm-Wave channel, spans $g \geq 1$ data bits, satisfying $(g-1)N_\tau \leq (L-1)\tau \leq gN_\tau$, where N_τ is the number of time slots per symbol[6],[5]. Secondly, it is assumed that the L number of resolvable multi-path components are randomly distributed, but they are the same over each symbol. Due to the wider bandwidth at mm-Wave, all the L multi-path components can be potentially resolved at the receiver (Rx) side[11]. Lastly, the k-th user 3D BF gain $\beta_{i,m,uv,k} = \beta_{i,m,l,k}$ for every Tx antenna element of the i-th RF chain is given in (3) shown at the bottom of this page. In (4.3), $F_{Rx,V}$ and $F_{Rx,H}$ are the Rx antenna element radiation patterns for the vertical (V) and horizontal (H) polarizations, respectively. $F_{Tx,i,V}$ and $F_{Tx,i,H}$ are the corresponding i-th RF chain Tx antenna element radiation patterns vertical (V) and horizontal (H) polarizations. $\phi_l^{VV}, \phi_l^{VH}, \phi_l^{HV}, \phi_l^{HH}$ are the initial random phases for vertical (VV), cross (VH, HV), and horizontal polarizations (HH) for the l resolvable multi-path. κ_m is the intra-cluster Rician K-factor associated with the m-th Tx antenna cluster. ϑ_l and φ_l are the elevation and azimuth angle-of-arrival (AoA), respectively at the k-th user. Finally, $\theta_{l,m}$ and $\phi_{l,m}$ are the elevation and azimuth angle-of-departure (AoD) of the l-th resolvable multi-path at m-th Tx antenna in the i-th RF chain.

5.1.2 Received Symbols of the Hybrid D-A BF System

The k-th user $L \times 1$ received symbol vector is given by:

$$\boldsymbol{y}_{i,k}(t) = \boldsymbol{H}_{i,k}(t)\boldsymbol{z}_i(t) + \boldsymbol{n}_{i,k}(t), \quad (5.4)$$

where $\boldsymbol{H}_{i,k}(t)$ is the $L \times M(2L-1)$ space-time channel matrix associating the i-th RF chain having M Tx antennas with k-th user, and is given by (4.6) in the following page. In (4.6), $\boldsymbol{H}_{i,m,k}(t)$ is the $L \times (2L-1)$ Block-Toeplitz space-time CIR matrix associating the m-th Tx antenna of the i-th RF chain with the k-th user, and is given by (7). In (4) $\boldsymbol{z}_i(t) = [z_0(t), z_1(t-1), \cdots, z_{t-L+1}(t-L+1)]^T$ is the $ML(2L-$

$$\boldsymbol{H}_{i,k}(t) = \underbrace{[\boldsymbol{H}_{i,0,k}(t), \boldsymbol{H}_{i,1,k}(t), \cdots, \boldsymbol{H}_{i,M-1,k}(t)]}_{L\times M(2L-1)} \tag{5.6}$$

$$\boldsymbol{H}_{i,m,k}(t) = \underbrace{\begin{bmatrix} h_{i,m,0,k}(t) & h_{i,m,1,k}(t) & \cdots & h_{i,m,L-1,k}(t) & 0 & \cdots & 0 \\ 0 & h_{i,m,0,k}(t-1) & h_{i,m,1,k}(t-1) & \cdots & h_{i,m,L-1,k}(t-1) & \cdots & 0 \\ \vdots & \ddots & \ddots & \ddots & \ddots & \ddots & \vdots \\ 0 & \cdots & 0 & h_{i,m,0,k}(t-L+1) & h_{i,m,1,k}(t-L+1) & \cdots & h_{i,m,L-1,k}(t-L+1) \end{bmatrix}}_{L\times(2L-1)} \tag{5.7}$$

$$\boldsymbol{a}_i(t) = \underbrace{[\boldsymbol{a}_{i,0}^T(t), \boldsymbol{a}_{i,1}^T(t), \cdots, \boldsymbol{a}_{i,M-1}^T(t)]^T}_{M(2L-1)\times 1}$$

$$\text{where } \boldsymbol{a}_{i,m}(t) = \underbrace{\left[\frac{\underbrace{h_{i,m,0,k}^*(t)}_{t\text{-th time slot}}, \underbrace{h_{i,m,1,k}^*(t-1)}_{t-1\text{-th time slot}}, \cdots, \underbrace{h_{i,m,L-1,k}^*(t-L+1)}_{t-L+1\text{-th time slot}}, \underbrace{0, \cdots, 0}_{L-1 \text{ time slots}}}{\sqrt{h_{i,0,0,k}^2(t)+h_{i,0,1,k}^2(t-1)+\cdots+h_{i,0,L-1,k}^2(t-L+1)}}\right]^T}_{(2L-1)\times 1} \text{ where } m = 0, 1, \cdots, M-1 \tag{5.8}$$

$$\boldsymbol{H}_{i,k}(t)\boldsymbol{a}_i(t) = \sum_{m=0}^{M-1} \boldsymbol{H}_{i,m,k}(t)\boldsymbol{a}_{i,m}(t) \tag{5.9a}$$

$$= \underbrace{\begin{bmatrix} \frac{|h_{i,0,0,k}|^2+\cdots+|h_{i,0,L-1,k}|^2+|h_{i,1,0,k}|^2+\cdots+|h_{i,1,L-1,k}|^2+\cdots+|h_{i,M-1,0,k}|^2+\cdots+|h_{i,M-1,L-1,k}|^2}{\sqrt{h_{i,0,0,k}^2(t)+h_{i,0,1,k}^2(t-1)+\cdots+h_{i,0,L-1,k}^2(t-L+1)}} \\ \frac{h_{i,0,0,k}(t)h_{i,0,1,k}^*(t-1)+\cdots+h_{i,0,L-2,k}(t)h_{i,0,L-1,k}(t-1)+\cdots+h_{i,M-1,L-2,k}(t)h_{i,M-1,L-1,k}^*(t-1)}{\sqrt{h_{i,1,0,k}^2(t)+h_{i,1,1,k}^2(t-1)+\cdots+h_{i,1,L-1,k}^2(t-L+1)}} \\ \vdots \\ \frac{h_{i,0,0,k}(t)h_{i,0,L-1,k}^*(t-1)+h_{i,1,0,k}(t)h_{i,1,L-1,k}^*(t-1)+\cdots+h_{i,M-1,0,k}(t)h_{i,M-1,L-1,k}^*(t-1)}{\sqrt{h_{i,1,M-1,k}^2(t)+h_{i,1,M-1,k}^2(t-1)+\cdots+h_{i,M-1,L-1,k}^2(t-L+1)}} \end{bmatrix}^T}_{L\times 1} \tag{5.9b}$$

$1) \times 1$ beamformed data symbol vector associated with the i-th RF chain. $\boldsymbol{n}_{i,k}(t)$ is modelled as the $L \times 1$ complex Gaussian channel vector with a co-variance of $2\sigma_i^2\boldsymbol{I}$ for the k-th user, where $\boldsymbol{I}$ is the $L \times L$ identity matrix.

5.1.3 Space-Time Analog Beamformer for the mm-Wave Hybrid D-A BF System

The beamformed data vector $\boldsymbol{z}_i(t)$ in (4) is generated by the $M(2L-1) \times 1$ space-time analog beamformer $\boldsymbol{a}_i(t)$ operating over the the space-time channel matrix $L \times M(2L-1)$ $\boldsymbol{H}_{i,k}(t)$ as well as the information bearing symbol $x_{i,k}(t)$, and it can be represented as:

$$\boldsymbol{z}_i(t) = \boldsymbol{a}_i(t)d_i x_{i,k}(t), \tag{5.5}$$

where d_i is the i-th element of the D-BF matrix in Fig. 1 which corresponds to the i-th RF chain of the BS. The D-BF matrix is initially taken as identity[77],[144]. Therefore in (4.5), $d_i = 1$. $\boldsymbol{a}_i(t)$ is the $M(2L-1) \times 1$ proposed novel space-time analog beamformer given by (8), where the m-th element of $\boldsymbol{a}_i(t)$, denoted by $\boldsymbol{a}_{i,m}(t)$, is a normalized $(2L-1) \times 1$ vector. The $L \times 1$ k-th user Rx signal from the i-th RF

chain, after A-BF pre-processing and channel conditioning, is denoted by the vector $\boldsymbol{H}_{i,k}(t)\boldsymbol{a}_i(t)$ in (4.9). Lastly, the dimensions of $(4.6)-(4.9)$ have been indicated by their respective under-braces.

5.1.4 Cost Benefit Analysis of the Proposed Space-Time A-BF Scheme

Upon inspection, it can be observed that the $L \times 1$ elements in vector (4.9b) are the channel gains. On the other hand, since it has been stated previously that all the multi-path components can be potentially resolved at the Rx side[11]. Furthermore, the analog beamformer sounding $L-1$ zeroes to the channel from $t = L$-th to $t = 2L-1$-th time instant ($L-1$ time slots in total) as represented in (4.10) will impact the spectral efficiency (SE) Techniques for improving SE have been extensively investigated in literature[98],[196]. Lastly, as compared to the separate hybrid D-A BF design in [77],[144]; or the SC based design in having higher complexity since the analog beamformer is the normalized hermitian of the channel, the novel LC analog beamformer $\boldsymbol{a}_i(t)$ in this chapter samples only M symbols at any time instant. This reduces the computational complexity of the hybrid D-A BF system. Beamformer design and computational complexity will be discussed in detail in the subsequent sections.

5.1.5 Receive SNR and Spectral Efficiency for the Hybrid D-A BF System

The signal to noise ratio (SNR) of the i-th RF chain is denoted by γ_i and is given as[71]:

$$\gamma_i\big(d_i, \boldsymbol{a}_i(t), \boldsymbol{H}_{i,k}(t)\big) = \frac{\gamma_0}{\sigma_i^2} \sum_{l=0}^{L-1} \big|\big|\boldsymbol{H}_{i,k}(t)\boldsymbol{a}_i(t)d_i\big|\big|^2, \tag{5.10}$$

where γ_0 is the average input SNR and $\sum_{l=0}^{L-1} \big|\big| \cdot \big|\big|$ represents the norm operation. Maximizing this SNR will lead to improved system SE (bp/s/Hz) for the k-th user associated with the i-th RF chain, and calculated as in[71]:

$$\eta_{i,k} = \log_2\big[1 + \gamma_i\big(d_i, \boldsymbol{a}_i(t), \boldsymbol{H}_{i,k}(t)\big)\big] \tag{5.11}$$

5.2 Beamformer Design for Hybrid D-A BF

In this section, two types of hybrid D-A BF systems are considered for supporting a high density of users in mm-Wave systems. In the separate design of hybrid D-A BF as proposed in [77],[144], the analog beamformer is the normalized hermitian of the CIR, where as the digital beamformer, $\boldsymbol{D} = \boldsymbol{I}$ is an identity matrix of size N. Therefore, the BF matrix is simply a matched filter (MF)[77],[144]. However, high

user density environment cannot be supported by this method because the i-th RF chain can support only a particular user. Therefore, the LC-SC and LC-PC algorithms are proposed. LC-SC is a space-time A-BF technique whereas LC-PC designs the hybrid D-A BF jointly.

5.2.1 Low Complexity Selection Combining (LC-SC) with Space Time Hybrid D-A Beamformer

Let there be K users to be supported by the i-th RF chain (which previously only supported a particular k-th user) having M antenna elements, where $K \leq M$. The allocation of antenna elements is based on the calculation of instantaneous power of the 3D mm-Wave modified SV channel for every user. For the m-th antenna element in the i-th RF chain, the channel power associated with the k-th user is calculated as:

$$p_{i,m,k} = \sum_{l=0}^{L-1} |h_{i,m,l,k}|^2, \tag{5.12}$$

where $1 < k \leq K$. This process is repeated for all the K users for the m-th antenna element. The m-th antenna is then assigned to that user which has the maximum power:

$$k_m = \underset{k \in K}{\operatorname{argmax}} \left\{ p_{i,m,0}, p_{i,m,1}, \cdots, p_{i,m,K-1} \right\}, \tag{5.18}$$

where argmax calculates the maximum value. This process is repeated M times until all the M antennas are allocated to the S users where $S \leq K$. The remaining $(K-S)$ users are not supported. Since S users are selected for the i-th RF chain, S continuous symbols from the i-th symbol stream have to be multiplexed. This chapter proposes using S orthogonal time slots from the i-th symbol stream, to create S continuous symbol-streams for each of the s-th user, where $1 < s \leq S$. The resulting trade-offs in complexity and performance will be discussed in further detail in Section IV and Section V respectively.

As the LC-SC algorithm allocates non-contiguous antenna elements to the s-th user, it will experience MUI from the beamformed signals generated from antenna elements that are allocated to other users. MUI can be eliminated at every s-th user by the combination of analog pre-processing, mm-Wave SV channel effects and a set of simple Rx BF weights at every s-th user. It is assumed that the LC-SC antenna allocation information is available at each user. For example, consider a scenario depicted in Fig. 4.2 in which:

- The number of antenna elements in the i-th RF chain is $M = 4$.
- The total number of single antenna users to be supported by this i-th RF chain is $S = 3$.
- The SC antenna allocation for the i-th RF chain that follows the pattern as shown in Fig. 2. In this scenario, antenna $m = 0$ is allocated to user $s = 0$; $m = 1$ and $m = 3$ to $s = 2$; and $m = 2$ to $s = 1$.

$$\boldsymbol{a}_{i,SC}(t) = \Big[\overbrace{\boldsymbol{a}_{i,0,0}^T(t)}^{\text{A-BF for 0-th ANT } m_0} \;,\; \overbrace{\boldsymbol{a}_{i,1,2}^T(t)}^{\text{A-BF for 1-st ANT } m_1} \;,\; \overbrace{\boldsymbol{a}_{i,2,1}^T(t)}^{\text{A-BF for 2-nd ANT } m_2} \;,\; \overbrace{\boldsymbol{a}_{i,3,2}^T(t)}^{\text{A-BF for 3-rd ANT } m_3}\Big]^T$$

$$\text{where } \boldsymbol{a}_{i,m,s} = \underbrace{\left[\frac{\underbrace{h_{i,m,0,s}^*(t)}_{t\text{-th time slot}}, \underbrace{h_{i,m,1,s}^*(t-1)}_{t-1\text{-th time slot}}, \cdots, \underbrace{h_{i,m,L-1,s}^*(t-L+1)}_{t-L+1\text{-th time slot}}, \underbrace{0,\cdots,0}_{t-L\text{-th time slot to } t-2L+2\text{-th time slot}}}{\sqrt{h_{i,m,0,s}^2(t)+h_{i,m,1,s}^2(t-1)+\cdots+h_{i,m,L-1,s}^2(t-L+1)}}\right]^T}_{(2L-1)\times 1 = 4(2L-1)\times 1} \tag{5.13}$$

$$\boldsymbol{H}_{i,2}(t) = \underbrace{\big[\boldsymbol{H}_{i,0,2}(t), \boldsymbol{H}_{i,1,2}(t), \boldsymbol{H}_{i,2,2}(t), \boldsymbol{H}_{i,3,2}(t)\big]}_{L\times M(2L-1)=L\times 4(2L-1)} \tag{5.14}$$

$$y_{i,2}(t) = \underbrace{\boldsymbol{w}\boldsymbol{H}_{i,0,2}(t)\boldsymbol{a}_{i,SC}(t)x_{i,0}(t)}_{\text{MUI at user } s=2 \text{ from user } s=0} + \boldsymbol{w}\boldsymbol{H}_{i,1,2}(t)\boldsymbol{a}_{i,SC}(t)x_{i,2}(t) + \underbrace{\boldsymbol{w}\boldsymbol{H}_{i,2,2}(t)\boldsymbol{a}_{i,SC}(t)x_{i,1}(t)}_{\text{MUI at user } s=2 \text{ from user } s=1} + \boldsymbol{w}\boldsymbol{H}_{i,3,2}(t)\boldsymbol{a}_{i,SC}(t)x_{i,2}(t) + \boldsymbol{w}\boldsymbol{n}_{i,2}(t) \tag{5.15}$$

$$\boldsymbol{H}_{i,2}(t)\boldsymbol{a}_{i,SC}(t) = \sum_{m=0}^{M=3} \boldsymbol{H}_{i,m,2}(t)\boldsymbol{a}_{i,m,SC}(t)$$

$$= \left[\underbrace{\frac{\begin{array}{c}\underbrace{h_{i,0,0,2}(t)h_{i,0,0,0}^*(t)+\cdots+h_{i,0,L-1,2}(t)h_{i,0,L-1,0}^*(t)}_{L\text{multi-path terms}} + \underbrace{|h_{i,1,0,2}(t)|^2+|h_{i,1,0,2}(t)|^2+\cdots+|h_{i,1,L-1,2}(t)|^2}_{L\text{signal terms}} \\ + \underbrace{h_{i,2,0,2}(t)h_{i,2,0,1}^*(t)+\cdots+h_{i,2,L-1,2}(t)h_{i,2,L-1,1}^*(t)}_{L\text{multi-path terms}} + \underbrace{|h_{i,3,0,2}(t)|^2+\cdots+|h_{i,3,L-1,2}(t)|^2}_{L\text{signal terms}}\end{array}}{\sqrt{h_{i,0,0,0}^2(t)+h_{i,0,1,0}^2(t-1)+\cdots+h_{i,0,L-1,0}^2(t-L+1)}}}_{\text{Signal term of interest at user } s_2 \text{ at } t\text{-th time slot}}\right.$$

$$\left.\underbrace{\frac{\begin{array}{c}\underbrace{h_{i,0,0,2}(t-1)h_{i,0,1,0}^*(t)+\cdots}_{L-1\text{MUI terms}} + \underbrace{h_{i,0,L-2,2}(t-1)h_{i,1,L-1,0}^*(t)}_{L-1\text{MUI terms}} \\ + \underbrace{h_{i,1,0,2}(t-1)h_{i,1,1,2}^*(t)+\cdots}_{L-1\text{MUI terms}} + \underbrace{h_{i,1,L-2,2}(t-1)h_{i,1,L-1,2}^*(t)}_{L-1\text{MUI terms}} \\ + \underbrace{h_{i,2,0,2}(t-1)h_{i,2,0,1}^*(t)+\cdots}_{L-1\text{MUI terms}} + \underbrace{h_{i,2,L-2,2}(t-1)h_{i,2,L-1,0}^*(t)}_{L-1\text{MUI terms}} \\ + \underbrace{h_{i,3,0,2}(t-1)h_{i,3,1,2}^*(t)+\cdots}_{L-1\text{MUI terms}} + \underbrace{h_{i,3,L-2,2}(t-1)h_{i,3,L-1,2}^*(t)}_{L-1\text{MUI terms}}\end{array}}{\sqrt{h_{i,2,0,1}^2(t)+h_{i,2,1,1}^2(t-1)+\cdots+h_{i,2,L-1,1}^2(t-L+1)}}}_{\text{MUI from } s_0,s_1 \text{ at } s_2 \text{ at } t-1\text{-th time slot}}\right.$$

$$\left.\begin{array}{c}\vdots \\ \Big\} L-3 \text{ MUI terms}\end{array}\right.$$

$$\left.\underbrace{\frac{\underbrace{h_{0,0,2}(t-L+1)h_{0,1,0}^*(t)}_{1\text{-st MUI term}} + \underbrace{h_{1,0,2}(t-L+1)h_{1,1,2}^*(t)}_{2\text{-nd MUI term}} + \underbrace{h_{2,0,2}(t-L+1)h_{2,0,1}^*(t)}_{3\text{-rd MUI term}} + \underbrace{h_{3,0,2}(t-L+1)h_{3,1,2}^*(t)}_{4\text{-th MUI term}}}{\sqrt{h_{i,3,0,2}^2(t)+h_{i,3,1,2}^2(t-1)+\cdots+h_{i,3,L-1,2}^2(t-L+1)}}}_{\text{MUI from } s_0,s_1 \text{ at } s_2 \text{ at } t-L+1\text{-th time slot}}\right] \tag{5.16}$$

$$\boldsymbol{w}\boldsymbol{H}_{i,2}(t)\boldsymbol{a}_{i,SC}(t) = \underbrace{\left[\underbrace{\frac{\underbrace{|h_{i,1,0,2}(t)|^2+|h_{i,1,0,2}(t)|^2+\cdots+|h_{i,1,L-1,2}(t)|^2}_{L\text{signal terms}} + \underbrace{|h_{i,3,0,2}(t)|^2+\cdots+|h_{i,3,L-1,2}(t)|^2}_{L\text{signal terms}}}{\sqrt{h_{i,0,0,0}^2(t)+h_{i,0,1,0}^2(t-1)+\cdots+h_{i,0,L-1,0}^2(t-L+1)}}}_{\text{Signal term of interest at user } s_2}\right.}_{L\times 1}$$

$$\left.\begin{array}{c}0 \\ \vdots \\ \Big\} (L-3) \text{ zeros} \\ 0\end{array}\right] \tag{5.17}$$

As shown in the Fig. 5.2, in order to implement this scenario, $S = 3$ orthogonal time slots from the i-th symbol stream corresponding to the i-th RF chain will be selected to create 3 continuous symbol-streams for each of the s-th user. LC-SC space-time A-BF $\boldsymbol{a}_{i,SC}(t)$ is then performed over each of the M antennas over L time slots, whereas MUI suppression, as stated previously, is accomplished by the combination of analog-preprocessing, mm-Wave SV channel effects and the Rx BF weights $\boldsymbol{w}$ at the s-th user. The LC-SC space-time A-BF matrix $\boldsymbol{a}_{i,SC}(t)$, specific to the system scenario depicted in Fig. 2, can be derived using a similar approach as previously applied in (8). It is given by (13), where $h_{i,m,l,s}^*(t)$ is the conjugate of the complex channel coefficient connecting the m-th Tx antenna element in the i-th RF chain via the l-th multi-path to the s-th user. It can be seen that $\boldsymbol{a}_{i,SC}(t)$

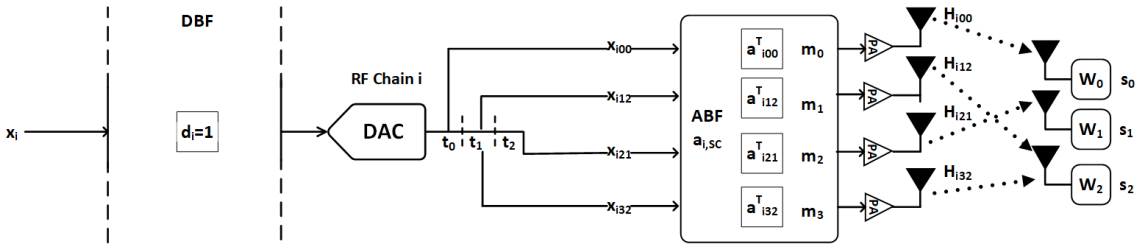

FIGURE 5.2: LC-SC Antenna Allocation for the i-th RF chain. t_0, t_1, t_2 and t_3 indicates the 0-th, 1-st, 2-nd and the 3-rd orthogonal time slots, or any 4 contiguous orthogonal time slots of the data stream $\boldsymbol{x}_i$ which maps the i-th symbol stream onto the i-th RF chain. $\boldsymbol{x}_{ims}$ represents the symbol vector selected for the m-th ANT and the s-th user from the s-th time-slot in the i-th data stream $\boldsymbol{x}_i$

is a $4(2L-1)$ vector for the scenario depicted in Fig. 4.2.

Now, let us investigate the case for the $s = 2$-nd user . The received symbol samples after MUI cancellation at the $s = 2$-nd user can be represented as given by (4.16), where $\boldsymbol{H}_{i,m,s}(t)$ is the $L \times (2L-1)$ dimensional CIR from the m-th Tx antenna in the i-th RF chain connecting the $s = 2$-nd user. $x_{i,s}(t)$ is the Tx symbol from the i-th RF chain chosen for the s-th user from the 3 available orthogonal (in time) symbol streams, as shown in Fig. 2. $\boldsymbol{n}_{i,2}(t)$ is the $L \times 1$ iid complex Gaussian random noise for the user s_2 with a variance of $\sigma^2_{i,2}$. The complete $L \times M(2L-1) = L \times 4(2L-1)$ CIR, $\boldsymbol{H}_{i,2}$, connecting the i-th RF chain to the 2-nd user is given in (4.14).

Similar to the discussion in Section II, the L symbol vectors, where each vector is received at the l-th time-slot ($0 < l \leq L-1$) at $s = 2$-nd user after analog pre-processing and mm-Wave SV channel conditioning, denoted by $\{\boldsymbol{H}_{i,2}(t)\boldsymbol{a}_{i,SC}(t)\}$ is given by (4.16). In (4.16), it can be observed that there are several MUI components received at user s_2 over the entire L time-slots. Additionally, in-order to eliminate any unwanted signal over the remaining $L-1$ time-slots, L Rx weights given in (4.15) given by $\boldsymbol{w} = [1, 0, \cdots, 0]$ can be applied. Therefore, in the $L \times 1$ received signal vector given in (4.17), the signal of interest will be received at s_2 at the $l = 0$-th time-slot. This analysis can be extended for any other LC-SC antenna allocation. In this way, the receiver complexity can be reduced significantly because processing is moved to the Tx side. To satisfy the total power constraint the signal power of the i-th RF chain is:

$$\frac{1}{M}\sum_{m=1}^{M}\sum_{s=0}^{S-1} p_{i,m,s} \leq \sigma_i^2 \gamma_i \tag{5.18}$$

The SNR for the i-th RF chain and the s-th user for the LC-SC algorithm is calculated as follows [71]:

$$\gamma_{i,SC}(\boldsymbol{w}, d_i, \boldsymbol{a}_{i,SC}(t), \boldsymbol{H}_{i,s}(t)) = \frac{M_s \gamma_0}{SM} \sum_{l=0}^{L-1} \Big|\Big|(\sigma_{i,s}^2 \boldsymbol{w}^H)^{-1} \times \boldsymbol{w}^H \boldsymbol{H}_{i,s}^H(t) \boldsymbol{a}_{i,SC}^H(t) d_i^H \times d_i \boldsymbol{a}_{i,SC}(t) \boldsymbol{H}_{i,s}(t) \boldsymbol{w}\Big|\Big|, \quad (19)$$

where M_s is the number of antennas allocated to the s-th user and $\sigma_{i,s}^2$ is the corresponding iid noise variance. The SE of the $s-th$ user is given by:

$$\eta_{i,s,SC} = \log_2\left[1 + \gamma_i\left(\boldsymbol{a}_{i,SC}(t), \boldsymbol{H}_{i,s}(t)\right)\right] \quad (5.20)$$

Lastly the overall sum-rate for the i-th RF chain supporting S users will be:

$$S_{i,SC} = \sum_{s=0}^{S-1} \eta_{i,s} \quad (5.21)$$

5.2.2 Hybrid D-A BF using Principal Component (LC-PC)

In the SC algorithm, $(K-S)$ users had to be discarded because of the power constraint at the i-th RF chain. Furthermore, the D-BF matrix was unchanged as it remained identity. To support maximum number of users, the LC-PC algorithm was proposed. First, the CIR matrix for the K users, where $K \leq M$, is obtained, and is given by:

$$\boldsymbol{H}_{i,LC-PC}(t) = \left[\boldsymbol{H}_{i,0}(t), \boldsymbol{H}_{i,1}(t), \cdots, \boldsymbol{H}_{i,K-1}(t)\right], \quad (5.22)$$

where $\boldsymbol{H}_{i,k}$ is the 3D mm-Wave modified SV CIR experienced by the k-th user at the i-th RF chain as explained in (4.6). Then, the normalized instantaneous channel realization matrix $\boldsymbol{R}_{i,LC-PC}$, is calculated as:

$$\boldsymbol{R}_{i,LC-PC}(t) = \frac{\left(\boldsymbol{H}_{i,LC-PC}(t)\right)^H \boldsymbol{H}_{i,LC-PC}(t)}{||\left(\boldsymbol{H}_{i,LC-PC}(t)\right)^H \boldsymbol{H}_{i,LC-PC}(t)||_F}, \quad (5.23)$$

where $||\cdot||_F$ denotes the Frobenius norm. The EVD of $\boldsymbol{R}_{i,LC-PC}(t)$ is then performed to obtain the eigenvalues and the eigenvectors. Then, the dominant eigenvalue $\boldsymbol{\lambda}_{k,i,LC-PC}$, and its corresponding eigenvectors $\boldsymbol{\Phi}_{k,i,LC-PC}$, are selected to compute the normalized joint hybrid D-A BF beamformer $\boldsymbol{g}_{i,LC-PC}$ for the i-th RF chain, given in (4.24) at the bottom of this page. In order to allocate the M Tx antennas

$$\boldsymbol{g}_{i,LC-PC} = \underbrace{\left[\lambda_{i,LC-PC}\right]}_{d_{i,LC-PC}} \underbrace{\left[\underbrace{\left[\Phi_{0,i,0}, \cdots, \Phi_{m_0-1,i,0}\right]^T}_{\boldsymbol{\Phi}_{0,i,0,LC-PC}}, \underbrace{\left[\Phi_{0,i,1}, \cdots, \Phi_{m_1-1,i,1}\right]^T}_{\boldsymbol{\Phi}_{1,i,LC-PC}}, \cdots, \underbrace{\left[\Phi_{0,i,K-1}, \cdots, \Phi_{m_K-1,i,K-1}\right]^T}_{\boldsymbol{\Phi}_{K-1,i,LC-PC}}\right]^T}_{\boldsymbol{a}_{i,LC-PC} \equiv M(2L-1)\times 1} \quad (5.24)$$

among all the K users, it is ensured that $\sum_{k=0}^{K-1} m_k = M(2L-1)$. Therefore, the k-th user is allocated m_k antenna elements from the i-th RF chain. To satisfy the total power constraint the signal power of the ith RF chain should satisfy:

$$\begin{aligned} ||\boldsymbol{g}_{i,LC-PC}||^2 &= ||d_{i,LC-PC}\boldsymbol{a}_{i,LC-PC}||^2 \\ &= \mathrm{Tr}(d_{i,LC-PC}\boldsymbol{a}_{i,LC-PC}\left(\boldsymbol{a}_i^{LC-PC}\right)^H (d_{i,LC-PC})^H) \\ &\leq \sigma_i^2\gamma_i \end{aligned} \tag{5.25}$$

The SNR for the i-th RF chain with K users for the LC-PC algorithm is derived as:

$$\begin{aligned} &\gamma_{i,LC-PC}(d_{i,LC-PC}, \boldsymbol{a}_{i,LC-PC}, \boldsymbol{H}_{i,LC-PC}(t)) \\ &= \frac{\gamma_0}{\sigma_i^2}\sum_{l=0}^{L-1} \left|\left|\boldsymbol{H}_{i,LC-PC}(t)\boldsymbol{a}_{i,LC-PC}d_{i,LC-PC}\right|\right|^2 \end{aligned} \tag{5.26}$$

The k-th user SE for the LC-PC algorithm is given by:

$$\eta_{i,k,LC-PC} = \log_2\left[1+\gamma_{i,LC-PC}\left(d_{i,LC-PC}, \boldsymbol{a}_{i,LC-PC}(t), \boldsymbol{H}_{i,k}(t)\right)\right] \tag{5.27}$$

Lastly, the complete system sum-rate for the i-th RF chain will be:

$$S_{i,LC-PC} = \sum_{k=0}^{K-1} \eta_{i,k} \tag{5.28}$$

5.3 Beamformer Complexity Analysis

Now, the computational complexity of the LC-SC and LC-PC based hybrid D-A BF algorithms is compared to the current known hybrid D-A BF which has been proposed in [77],[144]. In [77],[144], the A-BF matrix is taken as the hermitian of the CIR. Hence, for the hybrid D-A BF preprocessing of a Tx symbol in [77],[144], for a particular k-th user from the i-th RF chain, $M(4L-1)$ scalar multiplications and $M(4L-1)-2$ scalar additions need to be performed[50]. On the other hand, in the LC-SC algorithm, the number of scalar multiplications and additions are $\sum_{s=0}^{S-1} M_s(2L-1)+2$ and $\sum_{s=0}^{S-1} M_s(2L-1)-1$ receptively, where M_k is the number of antenna elements allocated to the k-th user. In the context of LC-PC algorithm, it takes about $N_\tau + L - 1$ multiplications to calculate the eigenvalue from the normalized instantaneous channel realization matrix $\boldsymbol{R}_{i,LC-PC}$ given by (24), where N_τ is the number of time slots per symbol as discussed in Section II [51]. When the eigenvectors are calculated, it takes $(N_\tau + L - 1)^3$ number of additions and $(N_\tau + L - 1)^3$ number of multiplications to determine the required eigenvectors [51]. Furthermore, the number of multiplications and additions that are performed will be analytically identical to LC-SC, albeit the number of users supported will now be K, with $S \leq K$ as stated previously.Moreover, the number of users supported per RF chain has been scaled-up to S and K respectively in LC-LC-PC and LC-PC, as compared to a particular user in [77],[144]. Table 4.I summarizes the number of computations required.

TABLE 5.1: Computational complexity

Algorithm	Number of operations per Tx symbol	
	Scalar Additions	Scalar Multiplications
Complete SC Algorithm	$\sum_{s=0}^{S-1} M_s(4L-1)-2$	$\sum_{s=0}^{S-1} M_s(4L-1)$
LC-SC Algorithm	$\sum_{s=0}^{S-1} M_s(2L-1)-1$	$\sum_{s=0}^{S-1} M_s(2L-1)+2$
LC-PC Algorithm	$(N_\tau+L-1)^3+\sum_{k=0}^{K-1} M_k(2L-1)-1$	$(N_\tau+L-1)^3+\sum_{k=0}^{K-1} M_k(2L-1)+2$

5.4 Simulation Results and Discussion

In this section, beam pattern, sum-rate performance and the complexity analysis of four different kinds of hybrid D-A BF algorithms are investigated. The LC-SC and LC-PC based hybrid D-A BF are compared with the complete SC hybrid D-A BF algorithm and the separate hybrid D-A BF[77],[144]. The parameters for generating the 3D mm-Wave modified SV channel model are mentioned in Table-II[187]. Perfect channel knowledge or CSI is assumed between the Tx antennas and Rx antenna. Two different environments are considered in the simulations. In the first environment perfect line-of-sight (LoS) is available. While, in the second environment, multi-path are present, and the number of resolvable multi-path is assumed to be 100. A uniform planar array of $M = 16 \times 16$ antennas is considered.

Fig. 5.3 shows the sum-rate of this hybrid D-A BF system when using i-th RF chain. In this figure, it can be observed that the LC-PC based algorithm achieves the upper bound of SE for all the simulated environments. This is because the LC-PC algorithm accomplishes the joint design of the A-BF and D-BF matrices, and assigns diagonal weights to the D-BF matrix, as compared to identity weights in LC-SC or the benchmark separate hybrid D-A BFs as proposed in[77],[144]. Furthermore, Fig. 8.3 also indicates that by using the LC-SC and LC-PC algorithms to design the hybrid D-A BF system, the SE increases when the number of users per RF chain increases. This is because with a larger number of users, the number of resolvable multi-path in the mm-Wave channel increases which are combined using A-BF to improve the SNR at the respective users. In this way, multi-path diversity has been exploited in the mm-Wave system. This is observed in the curves with $K = 16$ users and $L = 100$ resolvable multi-path per Tx antenna cluster attaining the upper bound as compared to the single user line-of-sight (LoS) case. $K = 16$ users per RF chain in a BS is chosen to represent a high user density scenario in mm-Wave systems. However, SE gains from multi-path diversity will be offset by the power

TABLE 5.2: 3D mm-Wave Modified SV Channel Parameters

Description	Unit	Value
Inter-cluster inter-arrival rate	1/ns	0.21
Intra-cluster inter-arrival rate	1/ns	0.77
Inter-cluster decay factor	ns	4.19
Intra-cluster decay factor	ns	1.07
Small-scale fading RMS	dB	1.26
Inter-cluster Rician K-factor	dB	-10
Intra-cluster Rician K-factor	dB	-10

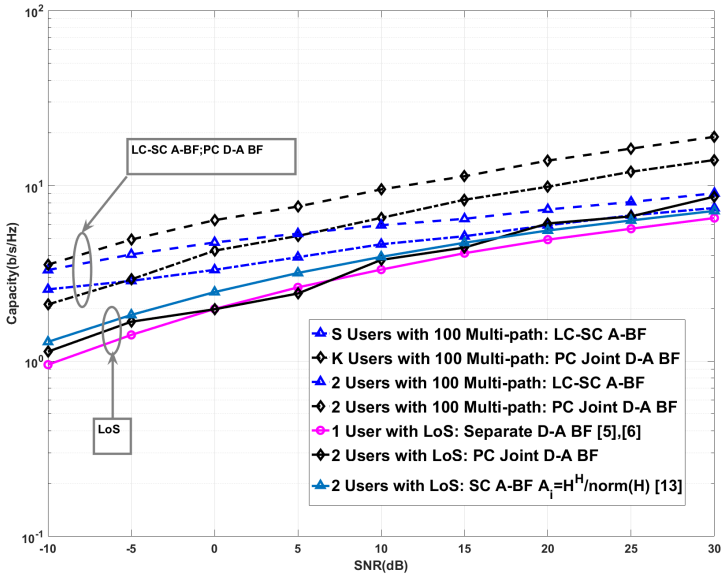

FIGURE 5.3: Sum-rate of the proposed hybrid D-A BF systems. Results are reported for a downlink mm-Wave system with $M = 16 \times 16$ BS antennas from SNR of -30dB to 30dB. The simulated environment includes both a single LoS channel and $L = 100$ multi-path.

constraint in the i-th RF chain, and it will tend to saturate. From this figure, it can

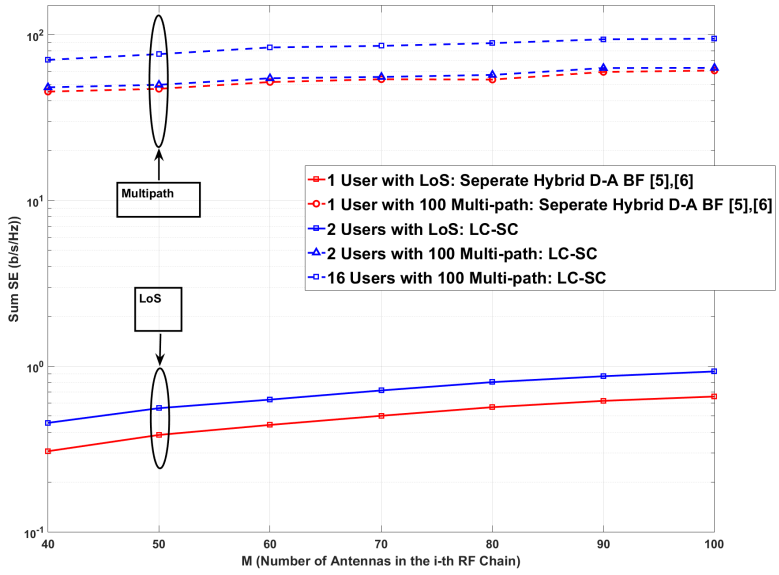

FIGURE 5.4: Sum-rate of the proposed hybrid D-A BF systems as a function of number of antenna elements. Results are reported for a downlink mm-Wave system with $M = 16 \times 16$ BS antennas for an SNR of -30dB. The simulated environment includes both a single LoS channel and $L = 100$ multi-path.

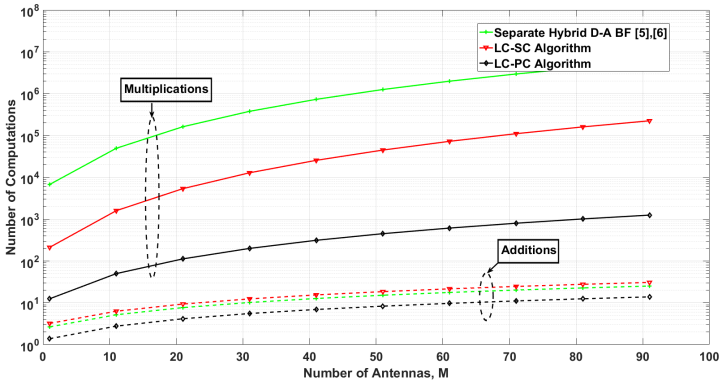

FIGURE 5.5: Number of computations of the proposed hybrid D-A BF systems as a function of the number of antennas. Results are reported for $L = 100$ multi-path per cluster for up-to $M = 10 \times 10$ antenna array.

also be observed that LC-PC and LC-SC algorithms outperform the benchmark separate hybrid D-A BF design in[77],[144]. Substantial gains in terms of performance are achieved by using these algorithms.

Fig. 5.4 shows the sum-rate of this hybrid D-A BF system when using i-th RF chain versus the number of antenna elements for an SNR of -10dB. It can be observed that the SE of all the hybrid D-ABF system saturates. This is because of the power constraint imposed on the i-th RF chain, adding antenna elements and thus increasing the number of multi-path clusters does not improve the diversity order at the user.

Now, the plots for complexity analysis of the proposed hybrid D-A BF systems based on the analysis in Section IV is discussed. Fig. 4.5 plots number of matrix multiplications and matrix additions for the separate hybrid D-A BF design in [77],[144], LC-SC and LC-PC algorithms as a function of the number of antennas. As predicted in Section IV, the computational complexity of the LC-PC technique in the case of multiplications is lower than the separate design and the LC-SC technique by at least an order of 2 and 4 respectively. Furthermore, the number of additions and multiplications is reduced substantially, as compared to the SC and PC proposed in the previous chapter. No special algorithms for improving the speed of matrix computations is assumed in the results.

Therefore, it has been proven that the proposed hybrid D-A BF techniques based on the LC-SC and LC-PC algorithm provide an alternative for supporting more than a particular user per RF chain as compared to the current known separate hybrid D-A BF system in [77],[144].

5.5 Summary

In this chapter, two novel algorithms which operate on the principles of LC-SC and LC-PC have been proposed for hybrid D-A BF based mm-Wave system. From the algorithms, it was possible to support more than a single user per RF chain. These

algorithms have a significant impact when higher density of users were present and the particular RF chain had to support multiple users. From the simulations, it was observed that the proposed hybrid D-A BF using LC-SC and LC-PC achieves higher SE as compared to the known hybrid D-A BF and supports higher density of users per RF chain. Lastly, it has also been proved that the LC-PC algorithm which jointly designed the hybrid D-A BF beamformer attained lower computational complexity.

Chapter 6

Performance Improvement for Experimental 60 GHz Systems with Millimetre Wave Beamforming

6.1 Introduction

The meteoric rise in demand for ever higher data-rates along with lower latencies has created new challenges in existing communication networks [4] which has led to research and development of fifth generation (5G) cellular networks. For new systems, the severe scarcity of spectrum in the current cellular bands has led to proposals for use of millimeter waves (mmWave), where larger bands of frequency are available to offer high data rates, and in particular, the 60GHz band, which has attracted substantial interest in recent research due to its unlicensed 7GHz bandwidth [93].

When adopting 60GHz in indoor environments, the integration of mmWave front end wireless links with Radio-over-fiber transmission is an attractive approach [205]. Properties of optical fiber communication such as ultra-high capacity and low loss propagation make it easy to realize a robust architecture for data transport between the Central Unit (CU) and the Remote Antenna Unit (RAU). The RoF part serves as a backbone for the whole network and provides centralized control [39]. RAU communication with the mobile user (MU) at 60GHz can then be achieved using compact integrated transmitter and receiver units. Since 60GHz wireless links rely on line-of-sight (LoS) conditions with narrow-beam antennas to compensate for the high path-loss [73], the coverage for multiple MU locations is still a challenge for 60 GHz communication systems that needs to be addressed, and has been highlighted in recent research [113]. Theoretical analysis has been presented for the indoor coverage of 60GHz systems [110] and the use of repeaters has been proposed to address the coverage issue [153]. However experimental implementations for 60GHz transmission which show coverage improvement are lacking. Spatial diversity and spatial multiplexing techniques have been widely deployed in lower-frequency systems, such as IEEE 802.11n/ac and LTE 4G standards, to improve the reliability and/or increase the data rate of the system [92]. These can provide coverage improvement for a mmWave communication system by making use of the decorrelation of different channel paths from spatially distributed transmitting units. We have previously shown that for a communication system based on photonic generation of a 25GHz

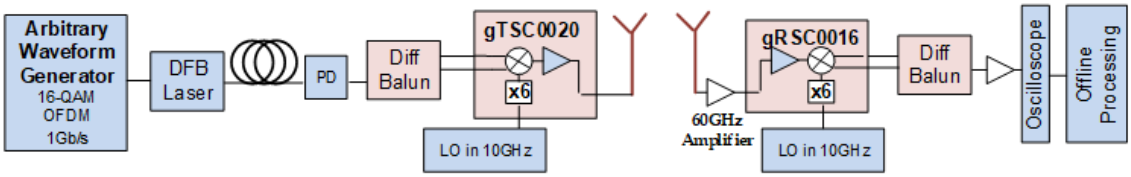

FIGURE 6.1: System model for OFDM-RoF based 60GHz Transmission using Integrated Transmitter/Receiver.

carrier, the use of Alamouti Space Time Block Coding STBC can provide improvement in Error Vector Magnitude (EVM) performance, while higher data rates through multiplexing can be achieved with the use of the Zero Forcing algorithm [74].

In this chapter, a proof of concept to improve the performance of 60 GHz transmission to multiple user locations in indoor environments by using spatial diversity and spatial multiplexing is demonstrated by extending this previous work [74]. The experimental setup consists of OFDM-RoF transport and upconversion to 60 GHz using an integrated transmitter unit. Wireless transmission through 0.5m, 1m and 1.5m channels and performance analysis has been conducted at different user locations. The results have been extended to longer distances through simulations by modelling the experimental mmWave environment. To perform theoretical analysis for mmWave transmission systems, channel modeling at 60GHz has always been a challenge due to high path-loss and larger bandwidth; conventional channel models cannot be applied since they are based on assumptions of narrow bandwidth. The propagation model presented here uses a modified Saleh Valenzuela (SV) [64] channel which accurately models a wide bandwidth channel and is used to analyze the system performance at longer distances. Furthermore, in order to experimentally analyze the performance of Alamouti STBC and Zero Forcing algorithms, the channel estimation at various transmitter and receiver locations is performed. To accomplish this, OFDM preambles (for channel estimation) and pilot tones (for phase tracking) were used to calculate channel coefficients for two transmitter positions and two receiver positions. From these experiments, it has been shown that performance at different user locations can be improved by reducing the EVM to below the threshold value (i.e. 12.5% for LTE) through spatial diversity using STBC processing. Moreover, it has also been demonstrated that multiple user data streams transmitted from different transmitter locations can be combined to obtain twice the data rate using spatial multiplexing through the Zero Forcing (ZF) algorithm.

The chapter is organized as follows. Section II presents the experimental setup and its performance. The results have been extended for larger coverage areas using a simulation model in Section III. The geometrical arrangement of the experimental setup to achieve spatial diversity and multiplexing is explained in Section IV along with the results. The chapter is concluded in Section V.

TABLE 6.1: System Parameters for the Experimental Setup

Description	Unit	Value
Operating Frequency	GHz	60
OFDM Signal Bandwidth	MHz	305
Modulation	QAM	16
Tx-Sampling Rate	Msps	390.625
Tx-Rx Separation	m	1.5
E_b/N_0 Tx SNR	dB	30

6.2 Experimental Set Up

Fig. 6.1 shows the experimental setup in which a Distributed Feedback (DFB) Laser (Emcore 1935F) is modulated by an OFDM signal (at an IF of 1.5GHz and data rate of 1Gb/s) generated through a Tektronix 7122C Arbitrary Waveform Generator. The resultant signal is transmitted through a single mode optical fiber to the Central Unit CU where a photodiode (Appointech, 2.5Gbps InGaAs PIN, 0.7A/W) at the other end of the fiber converts the optically modulated signal to an IF signal at the RAU. The system parameters for the experiment can be summarized as in Table 6.1.

The IF signal from the photodiode is passed through a differential balun and DC blocker to be upconverted to 61.5GHz using a gTSC0020 integrated transmitter with an LO of 10GHz. The 61.5GHz data modulated signal is transmitted over 1.5m wireless distance using an 18dBi gain horn antenna. At the other end, the mmWave signal is received by a 16.8dBi slot antenna [140] and is downconverted to IF using a gRSC0016 integrated receiver using an LO of 10GHz. The signal is captured using a Tektronix Digital Oscilloscope DPO72304DX for offline processing which includes carrier synchronization and demodulation for EVM analysis. Fig. 6.2 shows the performance of the experimental RoF transport from the central unit to RAU (without wireless transmission or 60GHz upconversion) for different input IF power levels which indicates the input power levels for which optimum performance can be achieved through the initial RoF transport of the setup. The performance of the com-

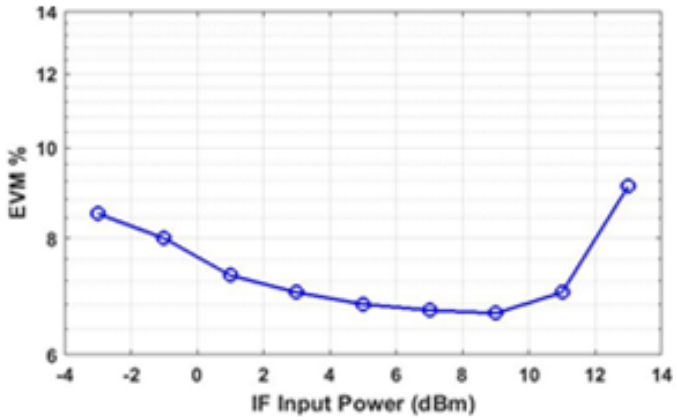

FIGURE 6.2: Performance of RoF transport for different IF input power levels.

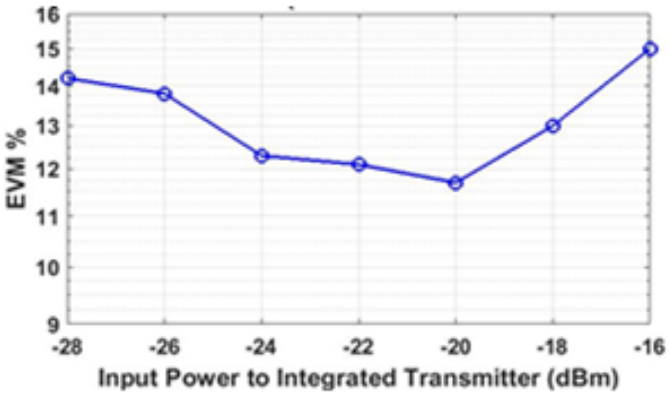

FIGURE 6.3: System Performance of the RoF based 60 GHz Transmission for different IF power levels.

plete system including 60GHz wireless transmission versus the power of the data signal from the photodiode after RoF transport is shown in Fig. 6.3. This shows that the EVM was found to be less than the 12.5% limit of LTE (for 16-QAM) for the overall system when the receiver was in LoS and in front of the transmitter as indicated by position C in geometric arrangement of the experimental setup in Fig. 6.4. Then, the measurements were performed for five receiver locations (A to E) as shown in Fig. 6.4 which correspond to angular locations of approximately $-15\circ$, $-7.5\circ$, $0\circ$, $7.5\circ$ and $15\circ$ from geometrical measurements. The transmission distance in the experimental analysis was constrained to 1.5m due to limitations of the transmit power and the 16.8dBi gain of the receiving antenna.

A simulation model was developed based on the experimental results through the modelling of the 60GHz indoor experimental environment. The simulation results showed a high degree of agreement with the experimental results for multiple transmission distances of 0.7m, 1m and 1.5m and for the five receiver locations. Further simulations were performed to show the feasibility of the system for longer distances, which are presented in the next section.

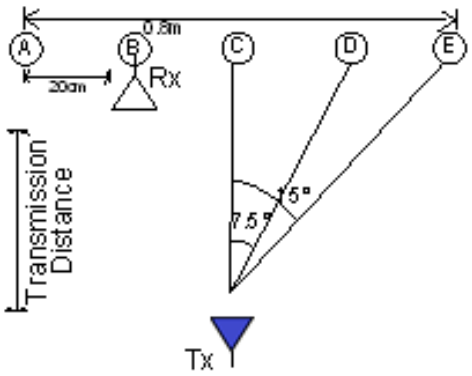

FIGURE 6.4: Geometric orientation of the Experimental Setup and slot antenna array.

6.3 Extension of Experimental Results Using Wideband mmWave Channel Model Simulations

In order to extend the experimental results of the 60GHz transmission in the previous section to longer transmission distances, simulation of the indoor experimental environment by applying a LoS extension to the wideband modified Saleh Valenzuela (SV) channel impulse response (CIR) [7] has been considered. The modified SV channel model accurately represents wideband fading in terms of clustered multi-paths, and hence has been chosen over other channel models, such as Rayleigh or Rician channel which are valid only for narrowband propagation environments [64],[7]. Furthermore, other channel models such as WINNER 2, which have been previously used at mmWave, are also narrowband and hence cannot be applied to this 305MHz bandwidth system. Firstly, the coefficients of the wideband modified SV channel, for vth cluster and uth multipath of that cluster, are given by

$$\begin{aligned} \alpha_l(t) &= \sum_{v=0}^{V-1}\sum_{u=0}^{U-1}\sqrt{P_{uv}}\alpha_{u,v}\delta(t-\tau_v-\tau_{uv}) \\ &= \sum_{l=0}^{L-1}\sqrt{P_l}\alpha_l\delta(t-l\tau) \end{aligned} \tag{6.1}$$

where α_l is the receiver CIR of the l-th resolvable multi-path signal component from the transmit antenna and $P_{l=uv}$ is the power of the u-th multipath in the v-th cluster. Here, where L is the total number of resolvable multipath components, V denotes the number of clusters, U the number of resolvable multi-paths in one cluster, and $L = UV$ is the total number of resolvable multi-paths at the receiver [11]. l is related to u and v by $l = vU + u$. In (6.1) $\alpha_{u,v} = |\alpha_{u,v}|e^{j\theta_{uv}}$ represents the fading of the u-th resolvable path in the v-th multipath cluster connecting the transmit antenna to the receiver. τ_v is the time-of-arrival (ToA) of the v-th cluster and denotes the ToA of the u-th resolvable multi-path in the v-th cluster. In this mmWave channel, it is assumed that the average power of a multi-path at a given delay is related to the power of the first resolvable multi-path of the first cluster through the following relationship

$$P_{uv}^k = P_{00}^k \exp^{(-\frac{T_v}{\Psi})} \exp^{(-\frac{T_{uv}}{\psi})} \tag{6.2}$$

where $P_{uv,k} = P_l = |\alpha_{uv}|^2$ represents the expected power of the u-th resolvable path in the v-th multipath cluster connecting the user to the transmit antenna. Ψ and ψ are the corresponding power delay constants of the cluster and the resolvable multi-path respectively. For the channel model to be generic, it is assumed that the delay spread, which is $(L-1)\tau$ of the mmWave channel spans $g \geq 1$ data bits, satisfying $(g-1)N_\tau \leq (L-1)\tau \leq gN_\tau$, where is the number of time slots per symbol. Secondly, it is assumed that the L resolvable multi-path components are randomly distributed and does not change over each symbol. Due to the wide bandwidth at mmWave, all the L multi-path components can be resolved at the receiver (Rx) [7]. In the LoS extension for modeling directional antennas, it can be assumed that the first multi-path is the dominant component. A high rate of power decay in (6.2) will make all the other multi-path coefficients of the wideband SV channel close to zero. The parameters

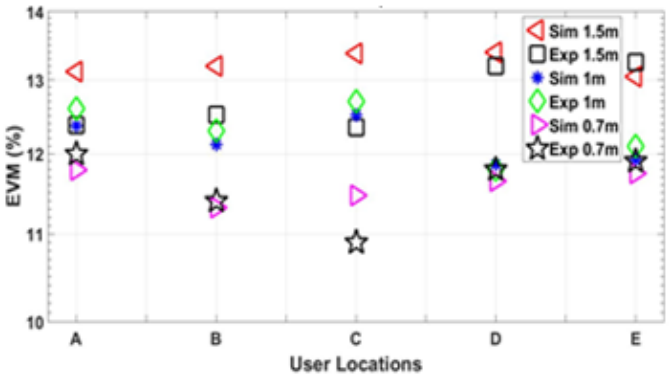

FIGURE 6.5: EVM of simulated and experimental analysis at different angular locations of the user.

for generating the 3D mmWave modified SV channel model at 60GHz are given in Table 6.2 [187]. The comparison between experimental results and simulations is

TABLE 6.2: 3D mmWave Modified SV Channel Parameters

Description	Unit	Value
Inter-cluster inter-arrival rate	1/ns	0.21
Inra-cluster inter-arrival rate	1/ns	0.77
Inter-cluster decay factor	ns	4.19
Intra-cluster decay factor	ns	1.07
Small-scale fading RMS	dB	1.26
Inter-cluster Rician K-factor	dB	-10
Intra-cluster Rician K-factor	dB	-10

presented in Fig. 6.5 and shows agreement for various transmission distances and receiver locations which demonstrates the accuracy of the modelling. Based on this observed agreement between the simulated and measured results, the EVM at various angular locations for longer transmission distances is shown in Fig. 6.6. The results were obtained by assuming 6dB amplification for 4.5m and 10dB amplification for 10m distance (with 2dB noise figure for both cases) of the transmit powe . The simulation for 4.5m distance indicates the practicability of the system in rooms, and at 10m for larger transmission distances such as in shopping malls or airports where access points are usually installed on higher structures. From these results, the mean spectral efficiency (in b/s/Hz) at 10m Tx-Rx separation distance has been calculated and plotted in Fig. 6.7 at five user locations. In order to obtain the mean spectral efficiency, the Rx SNR has been first calculated using

$$\mathrm{SNR}_{\mathrm{Rx}} = \frac{(\frac{E_b}{N_0} + \mathrm{SINR}_i) \cdot \frac{C}{B} \cdot K}{P_l} \tag{6.3}$$

where the free space path loss P_l at 60GHz, given by

$$P_l = d \cdot f_c \cdot \frac{4\pi}{c} = 66\mathrm{dB} \text{ at} f_c = 60\mathrm{GHz}. \tag{6.4}$$

In (6.3), $\frac{E_b}{N_0}$ is the Tx SNR, SINR_i is the SINR of the i-th beam obtained from modelling the system along with the wideband mmWave modified SV channel, C is the Tx sampling rate, B is the channel bandwidth (both are indicated in Table 6.1), $K = 4$ is the modulation index for 16-QAM. In (6.4), $d = 10$m is the Tx-Rx separation, $f_c = 60$GHz is the carrier frequency, and c is the velocity of electromagetic radiation in free space. Spectral efficiency (SE) is then calculated as

$$\text{SE} = \log_2(1 + \text{SINR}_i) \tag{6.5}$$

The mean spectral efficiency in Fig. 6.7 has been obtained over 15 simulation runs to characterize the effect of the randomized Additive White Gaussian Noise (AWGN). It can be observed in Fig. 6.7 that the mean spectral efficiency obtained is just over 5b/s/Hz, when the system parameters in Table 6.1 have been applied. The standard deviation was found to be 0.1 for the peak values of the spectral efficiency at these particular user locations.

6.4 Experimental Achievement of Spatial Diversity and Spatial Multiplexing

In this section, it is demonstrated that performance improvement at the previously discussed user locations and transmission distances through spatial diversity and spatial multiplexing. This can be achieved by measuring the channel transfer function for spatially distributed N transmit and M receive units and combining it with the transmitted symbols using STBC Alamouti or Zero Forcing algorithms. This arrangement can be represented as

$$\begin{bmatrix} y_1 \\ y_2 \end{bmatrix} = \begin{bmatrix} h_{11} & h_{12} \\ h_{21} & h_{22} \end{bmatrix} \begin{bmatrix} x_1 \\ x_2 \end{bmatrix} + \begin{bmatrix} n_1 \\ n_2 \end{bmatrix} \tag{6.6}$$

where y_1 and y_2 are the received OFDM symbols for Rx1 and Rx2, x_1 and x_2 are the transmitted symbols from Tx1 and Tx2, h_{11}, h_{21}, h_{12}, h_{22} are the measured channel transfer functions and n_1, n_2 represent the noise. In the first scenario, in order to achieve spatial diversity using the Alamouti STBC algorithm, the encoded signals

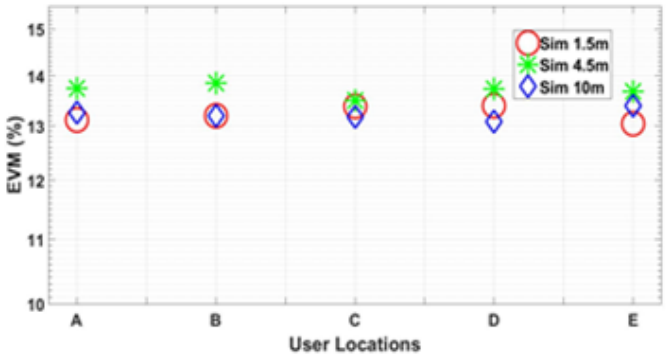

FIGURE 6.6: Simulated EVMs at Different User Locations.

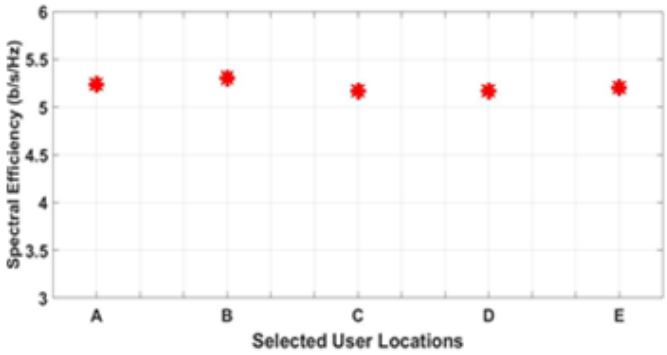

FIGURE 6.7: Mean Spectral Efficiency at user locations for Tx-Rx separation of 10m.

are transmitted from two transmit locations over two symbol periods. The first period consists of two symbols x_1 and x_2, simultaneously transmitted, while during the second period, these symbols are transmitted again in the form of $-x_2^*$ from the first antenna and x_1^* from the second antenna. The Alamouti STBC decoder restores the transmitted symbol periods using (6.7) and (6.8)

$$x_1 = h_{11}y_1 + h_{12}y_2^* + h_{21}y_1 + h_{22}y_2^* \tag{6.7}$$

$$x_2 = -h_{11}y_2^* + h_{12}^*y_1 - h_{22}y_2^* + h_{21}y_1^* \tag{6.8}$$

where y_1 and y_2 are the received signals over two symbol periods and h_{11}, h_{21}, h_{12}, h_{22} represent the measured channel co-efficient estimated from the transmitted preamble symbols. In the second case, to achieve multiplexing gain using the zero-forcing algorithm, two different symbols x_1 and x_2 are simultaneously transmitted on two different antennas and the symbols are multiplexed using the zero-forcing algorithm. The zero-forcing algorithm uses (6.9) to restore the separate data where the weight matrix treats all transmitted signals as interference except for the desired signals from the target transmit antennas.

$$\boldsymbol{W}_{\mathrm{ZF}} = (\boldsymbol{HH})^{-1}\boldsymbol{H}^H \tag{6.9}$$

The complex channel transfer matrix measurements can be obtained by placing transmit antennas at two distributed locations and capturing the data at two receiver location. In order to achieve improvement in performance, the channel transfer function matrix $\begin{bmatrix} h_{11} & h_{12} \\ h_{21} & h_{22} \end{bmatrix}$ was experimentally obtained by selecting two positions for the transmit antenna and marking them with a tape according to the layout shown in Fig 6.8. The coefficient h_{11} was measured by placing the transmit antenna in position Tx1 and receive antenna in position Rx1 while h_{12} was measured by moving the receive antenna to Rx2 (while keeping the transmit antenna at the same position of Tx1). Subsequently, to measure h_{21}, the transmit antenna was moved to Tx2 with receiving antenna at Rx1 and lastly, h_{22} was measured by moving the received antenna to Rx2 while keeping the transmit antenna at Tx2. These measurements were repeated for different user locations (A-E) over a span of 0.8m at wireless distance of 1.5m (Fig. 6.8). The experiment was conducted for different separation of 20cm, 30cm and 40cm between Tx1 and Tx2 points as shown in Fig. 6.9.

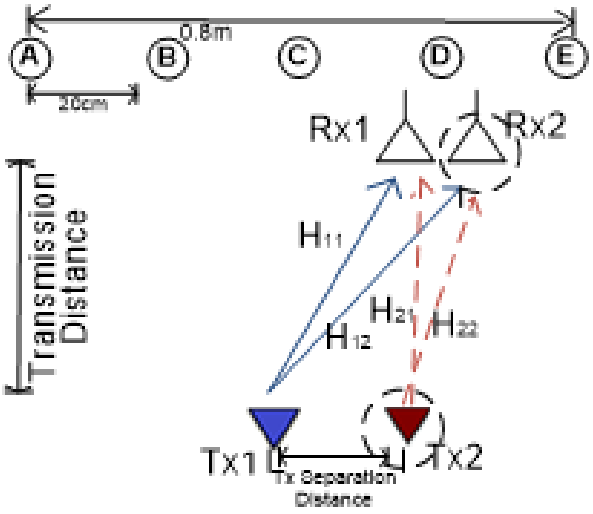

FIGURE 6.8: Experimental Arrangement of Tx and Rx at Different Positions to achieve Spatial Diversity and Multiplexing.

The values of h_{11}, h_{21}, h_{12}, h_{22} are used by (6.7) and 6.(8) in MATLAB/Simulink software for offline processing using the Alamouti STBC algorithm. The EVM obtained at the five user locations (A to E) was improved using the STBC Alamouti signal processing algorithm for the received OFDM symbols (y_1 and y_2). The achieved spatial diversity results in enhancement of coverage at multiple user locations. Additionally, the setup was used to realize multiplexing gains by combining the signals from two transmitter locations. One data stream with 0.5Gb/s data rate is transmitted through location Tx1 in the first step and the data is captured at points Rx1 and Rx2 by moving the receiving antenna to the respective positions. Then, a second (different) data stream is transmitted through the same transmit antenna from location Tx2 and data was captured again at positions Rx1 and Rx2 as given by (6.9). The captured data is processed using the Zero Forcing algorithm to achieve an aggregate 1Gb/s data rate.

6.5 Summary

In this chapter, the feasibility and analysis of an OFDM-RoF transported 60GHz system was presented and experimentally demonstrated for up to 1.5m transmission distance. A simulation model using a mmWave modified SV channel was presented, that accurately modelled the 60 GHz experimental EVM results. The feasibility of the experimental setup for longer wireless distances was shown by extension of simulation results. Experimental results using offline processing, in order to achieve improvement in performance and data rate, show that the channel estimation and use of the channel transfer function at different transmitter and receiver locations provided spatial diversity and multiplexing gain with Alamouti STBC and Zero-Forcing algorithms, respectively.

Chapter 7

Exploiting Low Complexity Beam Allocation in Multi-User Switched Beam Millimeter Wave Systems

7.1 Introduction

The demand for ever higher data-rates along with the scarcity of spectrum in current cellular bands is leading to the adoption of millimeter-wave (mmWave) bands in new generations of cellular networks [60],[9]. The short mmWave wavelength, combined with advances in analog integrated circuit design and radio frequency (RF) semiconductor technology, has enabled the realization of beamforming hardware in which highly directive antenna arrays with small form factors are integrated with compact RF transceiver modules [44],[127]. Beamforming is crucial for facilitating high data-rate transmission at mmWave frequencies to overcome high propagation loss [136],[10].

In multi-user mmWave systems, adaptive-beam and switched-beam based beamforming have been investigated [130][7],[83]. In adaptive beamforming, sophisticated codebook-based signal processing algorithms are utilized for generating beamforming weights at the base station (BS), which are continuously adjusted to simultaneously generate and steer several directional beams towards the respective mobile users [65],[138]. However, such a strategy requires obtaining and continual updating of the direction-of-arrival (DoA) of signals from all mobile users, along with full channel state information (CSI). Furthermore, the generation and update of the beamforming codebook involves computationally intensive matrix operations such as a pseudo-inverse [82]. [36] proposes a codebook of beamforming vectors over an initial beam alignment phase, followed by a learning phase where each mobile user estimates the "top-P" beams, and reports the beam indices as well as the received signal-to-interference plus noise ratios (SINR) to the BS. However, such an approach can incur considerable feedback overhead between the mobile users and the BS. In [141], a combination of generalized eigenvector codebook and SINR based codeword selection metric with limited feedback is shown to lead to improved ergodic sum data-rates. However, this cannot be adopted into switched beam based beamforming systems. This is because, by contrast, switched-beam based beamforming systems have to choose from one of several predefined directional spatial beams within a cell

in order to enhance the received SINR at the mobile user [136]. The BS determines the beam that is best aligned to the user signal's DoA, and switches to that beam to communicate with the user. The cell is sectorized by many narrow beams with each beam serving an individual user or a group of users. The spatially separated directional beams lead not just to an increase in the possible reuse of frequency channels by reducing potential inter-beam-interference, but also to an increase in transmission range [85],[107]. A particular limitation in switched-beam systems is the frequent hand-offs when the user moves from the sector of one beam to another, as the flexibility of continuous steering is not provided [192]. Although codebook based beamforming systems [82, 36, 141] have addressed the hand-off issue by beam-training and beam-alignment, however, as indicated earlier, they cannot be directly adopted into switched-beam systems. Moreover, in mmWave systems, the beams have narrow beamwidths, and together with a large number of predefined beams, codebooks cause very high frequency hand-off having a huge signaling overhead. Nevertheless, despite these disadvantages, the switched-beam approach is economically expedient, easy to deploy and maintain (than the completely adaptive systems), thus simplifying practical hardware design.

In switched-beam scenarios where the number of possible beams N is much larger than the number of users K, the low complexity beam allocation (LBA) algorithm, proposed in [175], offers a low computational complexity beam-user search approach to what could be a significant algorithmic problem of maximizing sum data-rates [45, 43, 183, 172]. For example, the simplest greedy algorithm in [172] has a complexity of $\mathcal{O}(KN^2)$, which is too high when the number of beams is large. By contrast, LBA algorithm attains nearly the same sum-data rate as compared to an optimal brute-force search based beam allocation, albeit with a much lower complexity of $\mathcal{O}(K \log N)$. In LBA, only those beams with the highest user directivity, known as active beams, are selected for data transmission, and then, to maximize sum data rate, only those users which have the highest receive SINR are selected. The remaining users are discarded and the unselected beams are turned off, focusing transmit power only onto the selected beams/users, and reducing inter-beam interference through having fewer beams. However, in [175], practical limitations, including the number of available RF chains and higher and non-uniform sidelobe levels, were not considered.

In this chapter, after describing application scenarios for switched-beam mmWave systems in Section II, LBA is applied to a switched-beam mmWave system with a limited number of RF chains. In Section III, generalized, theoretical beam patterns based on element fed arrays are developed, which have an idealized main lobe with fixed beam gain and angular resolution, along with exponentially decaying sidelobes [27]. Using these theoretical beam patterns, it is shown that the performance benefit of switched-beam systems, using the LBA, over comparable fixed-beam mmWave systems, which are practically simple but constantly generate fixed numbers of beams. Fixed-beam networks along with beam selection has emerged as a popular technique in hybrid analog-digital beamforming systems due to its simplicity [34, 20, 84, 68]. By applying this fixed-beam network in hybrid analog-digital beamforming systems, a number of analog beams are first selected (which produce a high array gain) and a digital beamformer is then adopted based on the selected

analog beams [64, 14, 111, 156]. The design of the digital beamformer serves to attain certain objective functions such as maximization of sum capacity, minimization of SINR, optimization of energy efficiency etc. However, digital beamformer design entails sparse mmWave channel estimation along with (at least) partial channel feedback, again incurring feedback and signaling overhead [64, 14, 111, 156]. LBA avoids these whilst achieving near optimal sum data-rates, subject to saturation due to inter-beam interference at higher transmit powers. Subsequently, in Section IV, measured beam patterns of a practical lens antenna system is used to show that improved performance can be obtained despite high and non-uniform sidelobe levels. Finally, in Section V, the level of sidelobe interference that can be tolerated before system performance is degraded to the level of a fixed beam system is determined, thereby providing guidance for future antenna and wireless system designers. The chapter is concluded in Section VI.

7.2 Application Scenario Description

The switched-beam mmWave system in Fig. 7.1 shows remote antenna units (RAUs) [204],[174], which might be mounted on a ceiling, capable of generating beams in N distinct directions. Several ceiling mounted RAUs can be connected by optical fiber, as indicated in Fig. 7.1, and coordinated by a central BS unit (not shown in the figure). Each beam is able to transmit independent data-streams, and every RAU can serve multiple mobile users simultaneously. Assuming that there are generally no obstacles between RAUs and users, ceiling mounted RAUs communicate with users by line-of-sight (LoS) communication. In this chapter, although application scenario is restricted to LoS, it could be easily extended for non-line-of-sight (NLoS) as well. An analysis of NLoS transmission at mmWave would have to apply the modified Saleh-Valenzuela (SV) channel with clustered ray multi-path propagation as investigated in [64]. The AoDs would then correspond to the dominant ray multi-path cluster of the mmWave channel, not the initial beam AoD from the RAU. Moreover, in a mmWave channel, it is the LoS path that is dominant, and the NLoS paths are weak due to the high propagation loss, scattering and blockage in mmWave environments. Nevertheless, this work is generalizable for NLoS cases also. The inter-RAU

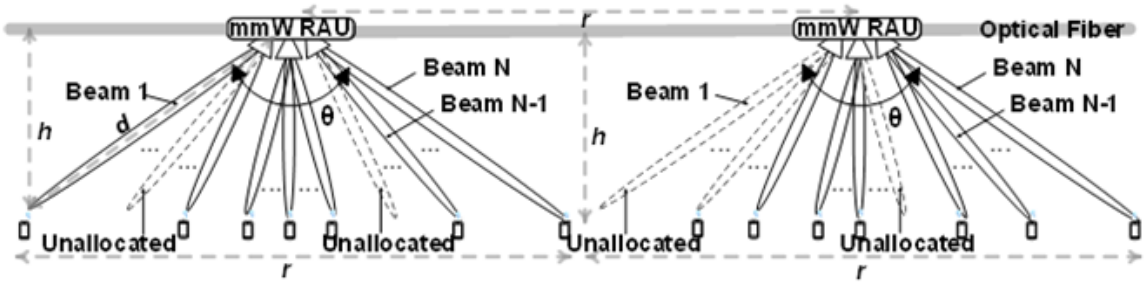

FIGURE 7.1: Application scenario showing ceiling mounted mmWave RAUs generating N beams communicating simultaneously with different mobile users. The inter-RAU distance r depends on the angle of coverage θ and height h of the mmWave RAU.

distance, denoted by r, is the distance between two successive ceiling mounted RAUs providing contiguous coverage. For the system to provide geographical coverage, the inter-RAU distance will depend on the height of the ceiling mount h, here assumed to be the minimum user-antenna distance, the overall coverage angle of the beams denoted by θ, and the maximum user-antenna distance, denoted by d in Fig. 7.1. The dependence of inter-RAU distance r on h, d and θ can be derived based on the simple geometric relationships: $\tan(\theta/2) = r/2h$, and $\cos(\theta/2) = h/d$. Examples are provided in Table 7.1. From Table 7.1, it can be observed that for narrower coverage angles θ and larger ceiling mount heights h, the maximum and minimum user-RAU distances d are similar to the ceiling mount height h. This assumption of constant distance $h \approx d$ is applied later in the chapter.

In a switched-beam system, the angular coverage of each beam is generally much less than the angular coverage of the RAU. Moreover, coverage is generally non-contiguous as only beams with users currently in their coverage would be switched on. In the RAU, RF chains are needed for each beam that is switched on. Thus, in a real system, the number of RF chains present in a RAU limits the number of beams that can be simultaneously switched on. By contrast, a fixed beam system needs to provide complete angular coverage for the RAU. For a fixed beam system with the same number of RF chains as the switched beam system, the beams would be less directional. In the extreme case, a single beam system employs a much less directional beam, with much lower antenna gain, but requires only one RF chain.

7.3 Serving Multiple Users with Limited RF Chains

A downlink model of a switched-beam mmWave system is considered. Denote $\mathcal{K}$ as the set of users and $\mathcal{N}$ as the set of available beams, where $|K| = K$ and $|N| = N$. It is assumed that a limited number of RF chains can select a certain number of beams from the set of N available beams in order to serve up to N_{RF} users. It is also

TABLE 7.1: Variation of Angle of Coverage θ and inter-RAU distance d of mobile users with height h of ceiling mounted RAU.

mmWave RAU Ceiling Mount Height: $h = 5$**m**		
$\theta = 15\circ$	$r \approx 1.4$m	$d \approx 5$m
$\theta = 45\circ$	$r \approx 3.8$m	$d \approx 5.4$m
$\theta = 120\circ$	$r \approx 10.6$m	$d \approx 10$m
mmWave RAU Ceiling Mount Height: $h = 10$**m**		
$\theta = 15\circ$	$r \approx 2.6$m	$d \approx 10$m
$\theta = 45\circ$	$r \approx 7.7$m	$d \approx 10.8$m
$\theta = 120\circ$	$r \approx 17.3$m	$d \approx 20$m
mmWave RAU Ceiling Mount Height: $h = 20$**m**		
$\theta = 15\circ$	$r \approx 5.2$m	$d \approx 20.2$m
$\theta = 45\circ$	$r \approx 1.3$m	$d \approx 21.6$m
$\theta = 120\circ$	$r \approx 36.6$m	$d \approx 40$m

assumed every RF chain is fed by independent data-streams. Hence, $N_{RF} \leq K \leq N$. Beam-allocation and user-selection are decided by the two-step, low complexity beam allocation (LBA) algorithm [175].

7.3.1 Low Complexity Beam Allocation (LBA) Algorithm

The LBA algorithm consists of beam-user association and user-selection.

Beam User Association

In the beam-user association step, each user k is associated with the beam n_k^* which has the largest directivity at the k-th user, given by

$$n_k^* = \arg\max_{n \in \mathcal{N}} D_n(\theta_k), \forall k, \tag{7.1}$$

where $D_n(\theta_k)$ is the beam-directivity of the k-th user associated with the n-th beam and located at θ_k.

User Selection

Based on the assumption that a limited number of RF chains, it is imperative to select users from the set of associated users for each beam. The set of associated users for beam n is defined as

$$\mathcal{K}_n^* = \{k | n_K^*, \forall k\}. \tag{7.2}$$

Let $\mathcal{N}_a^*$ denote the set of all the associated beams. The user selection step is then given by

$$k^* = \arg\max_{k \in \mathcal{K}_n^*} D_n(\theta_k), \forall n \in \mathcal{N}_a^*. \tag{7.3}$$

In the user-selection step, only one user which has the highest directivity is selected from the set of associated users $\mathcal{N}_n^*$ for the n-th beam, where $n \in \mathcal{N}_a^*$. This process is repeated for every associated beam and results in the highest sum data rate.

In [175], for the LBA algorithm, there was no limit to the number of possible beams and there could be as many as required according to the number of users. In this work, when the further limitation of number of RF chains is added, a selection is made of the best N_{RF} beams from the set of associated beams $\mathcal{N}_a^*$ obtained in the beam-user association step of the LBA. After the beam-user association and user-selection steps, any unallocated beams are turned off by turning off the associated RF chains, and any unselected users are discarded. Let $\mathcal{N}^*$ be the final set of allocated beams, and $\mathcal{K}^*$ denote the set of served users, respectively. Assuming that the total transmit power of the switched-beam mmWave system is fixed at P and is equally

allocated among active beams, the transmit power allocated to any active beam n is given by

$$P_n = \begin{cases} \frac{P}{N^*}, & n \in \mathcal{N}^*, \\ 0, & n \notin \mathcal{N}*. \end{cases} \tag{7.4}$$

Since the number of users that can be served is limited by the number of RF chains, $K^* \leq N_{RF}$. The assumption of a limited number of RF chains was made in order to obtain the sum data-rate in a practical switched-beam mmWave system. A single beam could serve multiple users through common multiple access techniques, e.g., time division multiple access (TDMA), orthogonal frequency division multiple access (OFDMA), or, non-orthogonal multiple access (NOMA) [56]. The principle of NOMA can effectively double the number of served users, keeping the number of RF chains constant. In NOMA, each allocated beam N^* and the associated RF chain can serve two users instead of one. The two served users are known as the strong-user and the weak-user, respectively. Strong-user selection can proceed as explained in (7.3). Denote this selected strong-user as k_s^*. Having selected the strong user, the selection of the weak-user pair can be given by

$$k_w^* = \underset{k \in \mathcal{K}_n^* \setminus k_s^*}{\arg\min} D_n(\theta_k), \forall n \in \mathcal{N}_a^*. \tag{7.5}$$

In the weak user selection step, only that user which has the least directivity is selected from the set of associated users $\mathcal{N}_n^*$ for the n-th beam, where $n \in \mathcal{N}_a^*$. This is because the selection of two served users per beam results in intra-beam interference from the strong user k_s^*, experienced by its weak-user pair k_w^*. The LBA algorithm can be suitably modified to apply the principle of NOMA. However, such an investigation has been left for a future work.

Sum Data-Rate Calculation

The SINR for the k-th user which is served by the n_k^*-th beam is given by

$$\text{SINR}_{k,n_k^*} = \frac{P_n D_{n_k^*}(\theta_k) L(\rho_k)}{\mathcal{F}_k + \kappa\tau B + \sum_{l \in \mathcal{N}^*, l \neq n_k^*} P_l D_l(\theta_k) L(\rho_k)}, \forall k \in \mathcal{K}^* \tag{7.6}$$

where $\mathcal{F}_k$ is the cascaded noise power of the mmWave receiver components at the k-th user and $\kappa\tau B$ is the thermal noise power at the user for the mmWave downlink system. $L(\rho_k) = (\frac{4\pi\rho_k f_c}{c})^{-2}$ is the LoS path loss, $f_c = 60$GHz is the mmWave operating frequency, $\rho_k = 10$m is the distance of the k-th user from the antenna elements (RAU), and $c = 3 \times 10^8$m/s is the velocity of electromagnetic radiation in free space. The sum data-rate is given by

$$R_s = \sum_{k \in \mathcal{K}^*} \log_2(1 + \text{SINR}_{k,n_k^*}). \tag{7.7}$$

It is expected that in the high transmit power regime, inter-beam interference, represented by the summation term in the denominator of (7.6), will also be high, causing the sum data-rates to saturate.

User Scheduling and SINR Constraints

In switched beam systems, since the beams are predefined (as the set of available beams N), the beam-user association step can be accomplished simultaneously for the set of available beams N within a single time-slot. User selection step can also be accommodated within the same time-slot.

LBA already accounts for SINR constraints because, (i) each user can only be associated with one beam (Equation (7.1)), and, (ii) an associated beam only select one user (Equation (7.3)). Although these constraints avoid severe inter-beam interference and enhances the received SINR, the scheduled/selected users will nonetheless experience interference from the beams that are allocated to other users, because of which the sum data-rates saturate.

Sum Data-Rate and User Fairness

Since LBA maximizes the sum-data rate, not all users can be simultaneously served. The application of LBA to a practical switched-beam mmWave system with limited number of RF chain hence produces an upper bound for the sum-data rate performance in such systems. To ensure fairness among users with varying locations, individual data rate constraints for users can be added into the sum data rate maximization problem, which would be carefully investigated in a future work.

7.3.2 Switched Beam and Fixed Beam Coverage

Fig. 7.2 illustrates an example switched-beam mmWave system, in one plane of operation, where $N = 9$ potential beams provide a coverage of $-7.5^\circ \leq \theta \leq 7.5^\circ$, meaning that each beam has a coverage approximately equal to 1.6°. It is assumed that there are $N_{RF} = 4$ RF chains, so up to $N^* = 4$ beams out of the potential set of $N = 9$ beams can be selected by implementing LBA. Thus, the system (in this plane) can provide coverage for up to $K = 4$ users, assuming that a beam is allocated to each user. If 2 users (out of the $K = 4$) are associated to the same beam, then in the user selection step of LBA, only the user with the higher directivity, as defined in (7.3) is selected, while the other is discarded. Hence, only 3 users are served in such a case. The switched-beam system is benchmarked against a fixed-beam system, with two cases considered.

Fixed Beam: All Beams On

Here, the set of beams providing contiguous coverage are always active, i.e. $N^* = N$. The beams are equivalent to sectors in a standard antenna system. A greedy

algorithm can be implemented, whereby for the set of N beams and K users, beams are allocated to users greedily, based on the achievable SINR, to maximize sum data rate. This can be mathematically represented as

$$(k^*, n_k^*) = \underset{k \in \mathcal{K}, n_k \in \mathcal{N}}{\arg\max}\ \text{SINR}_{k,n_{k^*}}. \tag{7.8}$$

Fixed Beam: Unallocated Beams Off

In this case, there is an additional step that if there are no users in the coverage area of a beam, it is switched off and the power is reallocated to other beams. The maximum sum data-rate for the fixed-beam systems is then derived as previously in (7.7). In reality, in both switched-beam and fixed-beam systems, fairness, for example by sharing beams, may be taken into account, but this would not give the maximum sum data-rate.

To benchmark the switched-beam system with $N_{RF} = 4$ RF chains, the fixed-beam system is assumed to have N=4 beams over the same coverage range, hence requiring each beam to have a beam width of $\approx 3.75°$. A beam gain of 35dB is assumed, as high as in the switched-beam system, as technologically it is likely to be easier to manufacture high gain fixed antennas [37]. As a further comparison, a system with a single beam covering the angular range $-7.5° \leq \theta \leq 7.5°$ can be considered. An antenna for such a system (when a standard gain horn) is likely to have a gain of 22dB [3].

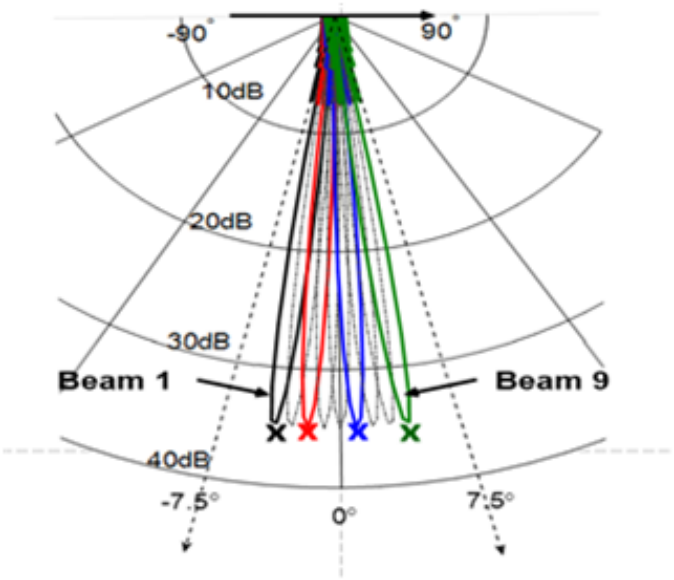

FIGURE 7.2: An example switched-beam mmW system having up to 9 idealized beams in one plane and a set of 4 users in that plane, each user represented by the "x".

Sum Data Rates With Idealized Beams

In this subsection, the estimated sum data-rates of the switched-beam and fixed-beam mmWave systems with idealized beam patterns are compared for different cases.

The estimated sum data-rates vs. total system transmit power for $10,000$ realizations of uniformly distributed mobile user locations are shown in Fig. 7.3 (a), (b), and (c), for $K = 6$, $K = 4$ and $K = 2$ users, respectively, for a bandwidth $B = 1$GHz. Although both switched-beam and fixed-beam systems have the same beam gain of 35dB, the switched-beam achieves higher estimated sum-data rates. This is because: (i) there are more potential beams for the switched-beam system giving a higher likelihood that the user is nearer a maximum gain angle of a beam, and, (ii) there will generally be higher inter-beam interference in the fixed-beam system. Low transmit power data-rates are limited by thermal noise, while the saturation at high powers is caused by the inter-beam interference. When unallocated beams are turned off, there is a small improvement in the average fixed-beam performance at lower transmit powers. This is because there occurs an improvement in the received SINRs when the unallocated beams are turned off. However at higher transmit powers, the inter-beam interference (which saturates the sum data-rates) dominates over any improvement in the received SINR (observed at lower transmit powers with unallocated beams turned off). This results in similar saturated sum data-performance in both the fixed-beam cases.

Comparing the cases for different number of users in the coverage plane, it can be seen that the switched-beam case shows increasingly enhanced performance for more users, as the users that are allocated beams are more likely to be at positions with high beam gain. On the other hand, as the maximum sum data-rate is being calculated, the assumption is that in all cases, there may be users who are not served, increasingly so for larger numbers of users (an investigation including fairness is left for future work).

Finally, Fig. 7.3(c) shows the sum data-rate when only a single beam of 22dB gain provides coverage for the whole angular range; as expected, much reduced sum data-rates at reasonable power levels are observed. This system is not limited by inter-beam interference, at least not by beams from the same RAU.

7.4 Millimeter Wave Beam Generation with Lens Antenna

A research and development (R&D) prototype lens antenna is considered as a practical example of a mmWave switched-beam system [108]. Fig. 7.4 illustrates its principle of operation; it is constituted by a convex dielectric lens and radiating antenna elements arrayed on its focal plane. A switching matrix would enable the selection of beams out of the total number available, with a requirement for RF chains in order to distribute different signals using the selected beams. The number of beams available is defined by the number of radiating elements. A lens antenna avoids phase shifting of each radiating element as would be required by an array antenna.

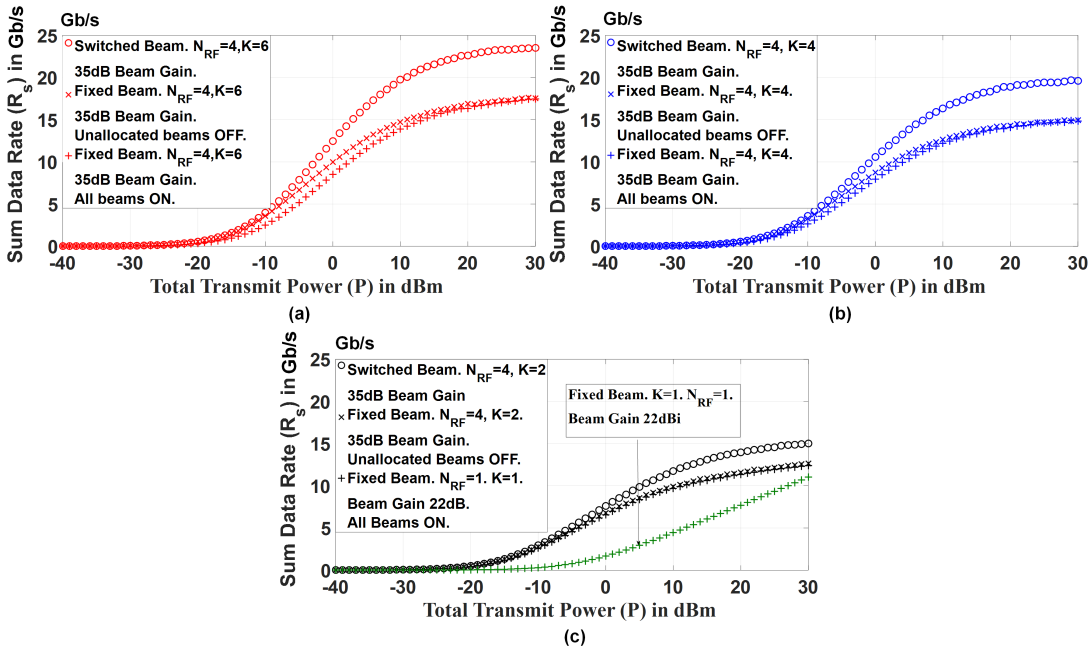

FIGURE 7.3: Estimated sum data-rates in b/s for switched-beam and the two adaptations of fixed-beam mmWave systems, for (a) $K = 6$ (red), (b) $K = 4$ (blue), and (c) $K = 2$ (black) as well as $K = 1$ (green) user scenarios. There are $N_{RF} = 4$ RF chains able to transmit independent data-streams through up to 4 active beams. Center frequency $f_c = 60$GHz, system bandwidth $B = 1$GHz. The distance of the users from the antenna elements is 10m.

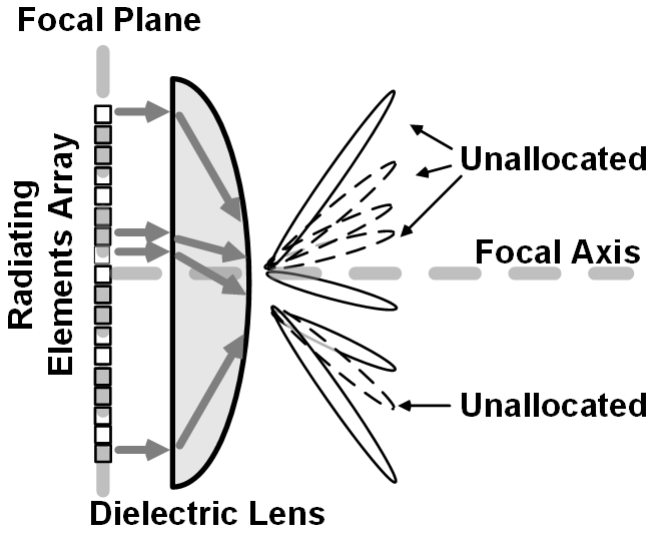

FIGURE 7.4: Schematic diagram illustrating the concept of SIKLU lens antenna.

Fig. 7.5. shows overlaid measured beam patterns from 4 radiating elements in the SIKLU lens-antenna with 4 beams from the switched-beam system model that were

generated in MATLAB for the results of Section III. Fig. 7.5(a) and Fig. 7.5(d) represent the extreme edges of coverage, where as Fig. 7.5(b) and Fig. 7.5(c) represent those nearer the center. It can be observed that the beam angles are well aligned to each other, and the mainlobe beam gain levels are closely matched. However, the practical lens antenna produces generally higher and non-uniform sidelobes. The high sidelobe measurements in the lens antenna can attributed to: (i) any unevenness in the density of the glass lens, (ii) surface smoothness of the fabricated lens, (iii) any impedance mismatch between the passive radiating elements array (Fig. 7.4) mounted on a printed circuit board (not shown in the figure) and the respective RF chain, or, (iii) system integration issues. Lastly, these measurements were conducted on the very first R&D prototype, and improvements can be expected in the later prototypes.

The simulations performed in Section III were repeated, this time using the measured beam patterns. The results in Fig. 7.6. demonstrate the impact of the higher and non-uniform sidelobes on the achievable sum data rates. As before, results in Fig. 7.6(a), Fig. 7.6(b) and Fig. 7.6(c) are for the $K = 6$, $K = 4$ and $K = 2$ user scenarios, respectively. It is observed that the data-rate performance of the lens-antenna switched-beam system (with the SIKLU lens-antenna beams) has reduced to approximately that of the fixed-beam system. It should be noted that the fixed-beam system is idealized, of course, and practical antennas will exhibit at least some non-uniformity. The higher sidelobes in the lens-antenna (Fig. 7.5) cause a general reduction in the saturated (interference-limited) sum data-rate performance in

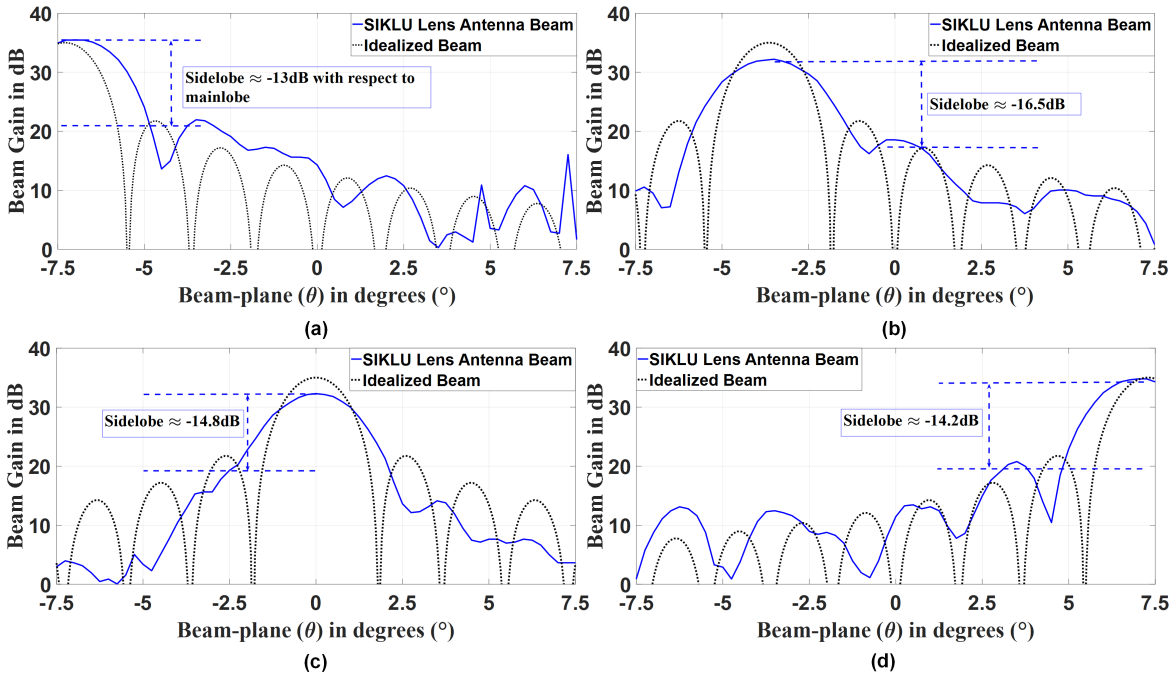

FIGURE 7.5: Measured beam patterns from 4 of the radiating elements in a SIKLU lens antenna, overlaid with 4 idealized beams. (a) Overlay of SIKLU lens antenna beam and idealized beam at $\theta = -7.5°$, (b) Overlay at $\theta = -1.25°$, (c) at $\theta = 0°$, and (d) $\theta = +7.5°$.

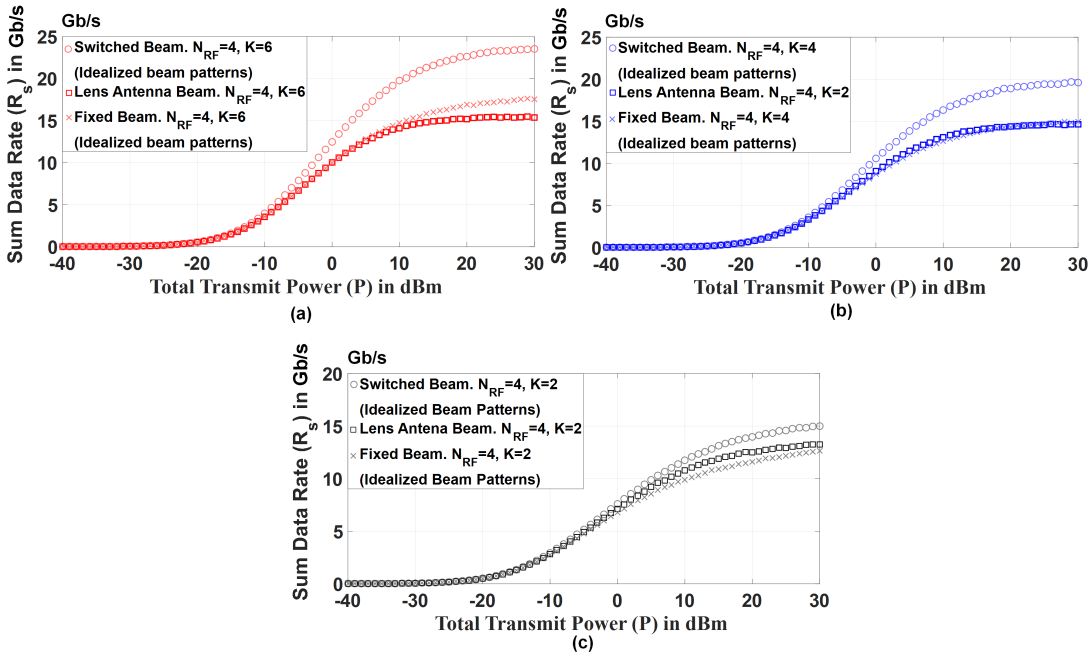

FIGURE 7.6: mmWave sum data-rates for SIKLU lens antenna switched-beam system: (a) $K = 6$ user scenario, (b) $K = 4$ user scenario, and, (c) $K = 2$ user case. Also shown for comparison are the idealized switched-beam and fixed-beam results as presented in Fig. 7.3. The fixed-beam system corresponds to the adaptation when all beams are active.

the lens-antenna switched-beam system as compared to the idealized switched-beam system (Fig. 7.6). While the received signal power at the user is proportional only to the directivity of the mainlobe of the allocated beam (see SINR Equation (6)), high sidelobes add to the received interference power at the user (not the received signal power). Lower mainlobe gain in the lens-antenna system are also a factor.

In [87], the Taylor-synthesis method was applied to 2×2 uniformly-fed subarrays of a 16×16 slot antenna array to design an efficient amplitude tapering antenna-feed network, which provided amplitude and phase control for selecting specific sidelobe levels. A similar approach could be incorporated into the design of future R&D prototypes of the SIKLU lens-antenna array for attaining sidelobe reduction. The effect of high sidelobe interference in the saturated sum-data rate performance is investigated in detail in the next Section. Lastly, inter-beam interference becomes significant for increased numbers of users as there will typically be more beams switched on.

7.5 Sidelobe Interference Impact on Sum Data-Rates

In the previous section, it was observed that high sidelobe interference in the SIKLU lens antenna beams resulted in a reduction in sum data-rates for a switched-beam system. In this section, the reduction in sum data-rates in a switched-beam system

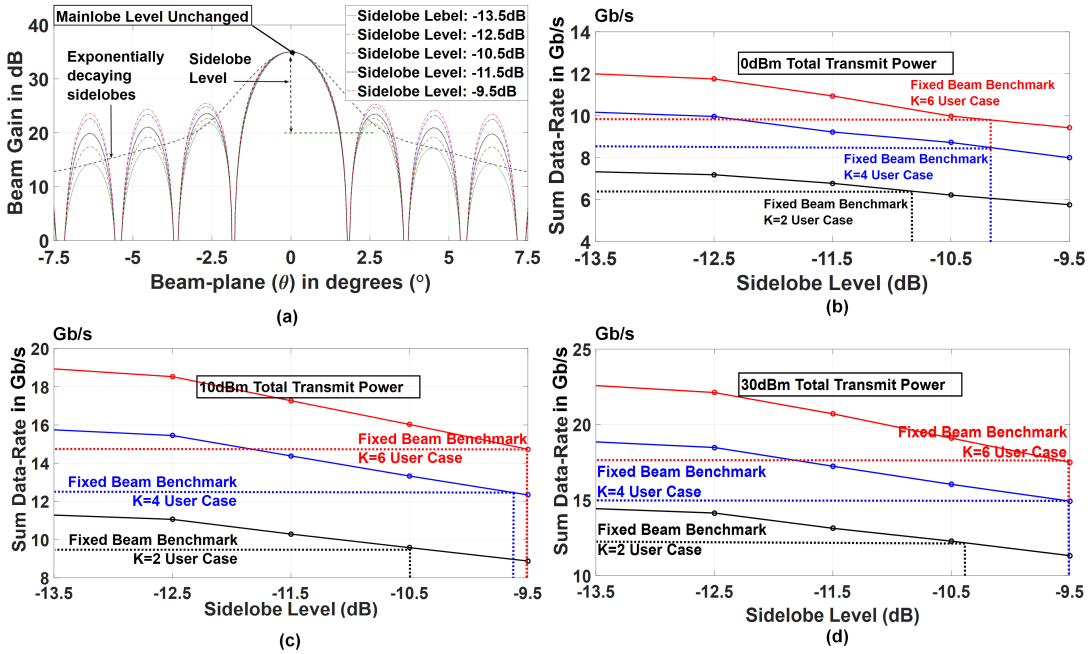

FIGURE 7.7: mmWave sum data-rates for varying sidelobe levels. (a) Beam pattern indicating exponentially decaying sidelobe levels. Different relative sidelobe levels are simulated for fixed transmit powers, (b) Sum data-rates vs. change in relative sidelobe level for 0dBm total transmit power, (c) for 10dBm total transmit power, and, (c) for 30dBm total transmit power.

is calibrated against the sidelobe level for idealized beam-patterns based on element-fed linear arrays, which can be considered as a generalized discrete spatial Fourier transform [174]. These result in exponentially decaying sidelobes, as shown in Fig. 7.7(a).

The sidelobe level is defined as ratio of the first sidelobe to mainlobe, as shown in Fig. 7.7(a). In this investigation, the sidelobe level is decremented from -13.5dB to -9.5dB in steps of 1dB for the total transmit power levels of 0dBm, 10dBm and 30dBm. The sum data-rates are obtained for $K = 6$, $K = 4$ and $K = 2$ users. The results are shown in Figs. 7.7(b)-(d). In general, it can be observed that as the relative sidelobe level increases, higher interference causes the sum data-rates of the switched-beam system to fall, eventually to below that of the fixed-beam systems, which are shown in Figs. 7.7(b)-(d) as benchmarks for their respective user scenarios.

Fig. 7.7(b) shows that for a system with 0dBm total transmit power, in order to provide improved performance, the sidelobe level in a multi-user switched-beam mmWave system should be lower than -10dB in the $K = 6$ user case. For $K = 2$ users, the required sidelobe level reduces to -11dB. Fig. 7.7(c) shows that for total transmit power of 10dBm, improved performance is obtained for sidelobe levels lower than -9.5dB for $K = 6$ users. It reduces to approximately -9.8dB and -10.5dB for $K = 4$ and $K = 2$ users respectively. The results are similar in Fig. 7.7(d) for the total transmit power level of 30dBm, except for $K = 2$ users for which the benchmark is at approximately -10.3dB.

In general, the sum data-rate for $K = 2$ falls to the fixed-beam benchmark at lower sidelobe levels than for $K = 4$ or $K = 6$. This occurs because as the number of users decreases when the number of possible beams remains the same, the received power per user increases, improving the received SINR. Hence, $K = 2$ user is more robust to sidelobe interference. Based on these observations, it can be inferred that multi-user switched-beam mmWave systems are sensitive to sidelobe interference. The results in Fig. 7.7 therefore provide guidance to antenna system engineers for beam pattern requirements in multi-user switched beam mmWave systems.

7.6 Summary

In this chapter, the maximum sum data-rate performance of a multi-user switched-beam mmWave system with a limited number of RF chains has been studied. The LBA has been applied to both theoretical and practical beam patterns (the latter for a lens-antenna) and benchmarked against an ideal fixed-beam mmWave system. Simulation results show that the switched-beam system outperforms the fixed-beam system in mmWave systems. The sensitivity of switched-beam performance to relative sidelobe level was investigated. Guidance for the required sidelobe level suppression for generalized antenna beam patterns has been given for systems that will employ switched-beams.

Chapter 8

Exploiting NOMA Relay with Hybrid Precoding for Supporting High User Densities in Overloaded Millimeter Wave Systems

In order to support more than one user per RF chain, the concept of NOMA relays can be employed which have been proposed for fifth generation (5G) cellular networks[38]. In a 2 user downlink system, a superposed signal is transmitted to both the relay and destination users through superposition coding in the direct-transmission phase. The user with the better channel conditions known as the relay-user, is assigned less transmit power than the user with poorer channel conditions, known as the destination user[38]. The relay-user applies successive-interference-cancellation (SIC), i.e., it first decodes the destination-user's signal, then subtracts it from the received signal, and decodes its own signal next. The destination-user decodes its own signal directly. Then, in the relay-transmission phase, the relay-user forwards the destination-user's message, and the destination-user combines this with the message received earlier, using maximum ratio combining (MRC). MRC significantly improves the diversity order at the destination-user as compared to previously proposed relay systems. In this chapter, it is also assumed that the amplify-and-forward (AF) protocol at the relay-user performs the relaying operation without draining the relay-users' batteries in the relay-transmission phase.

However, such systems have not explicitly considered high user density that will be prevalent in future mmWave scenarios. Whereas massive MIMO can drastically increase the spectral efficiency of mmWave systems through aggressive spatial multiplexing, specifically MRC and zero-forcing (ZF) combining attain the highest spectral efficiency when the number of users are 2-to5 times less than the number of antennas per RF chain[31]: hence massive MIMO cannot support overloaded systems, i.e. when the number of users exceed the number of antennas at the BS. Motivated by this issue, in this paper, to support high user density in current mmWave systems having M antennas per RF chain, firstly, two methods of designing hybrid D-A P based on selection combining (SC) and a novel low complexity principal component (PC) are considered, both of which can initially support up to K users per RF chain.

- The SC algorithm was initially proposed by the authors in [105] in order to support K users per RF chain. SC designs the analog precoder (AP) by extracting the phase information from the instantaneous channel state information (CSI). It designates a set of antenna elements to every user while keeping the digital precoding (DP) matrix identity.
- PC is a novel low complexity method where the joint design of the AP and DP matrices is carried out by implementing the eigenvalue decomposition (EVD) of the normalized expected channel realization matrix. The dominant eigenvalues are assigned to the digital precoding (DP) matrix, and the phases of corresponding eigenvectors are assigned to design the AP matrix.

Secondly, a relay NOMA mmWave system is proposed, which enhances the number of users supported per RF chain from K to $2K$. The K initially selected users, henceforth called the relay-users, selected either via hybrid SC AP or PC joint D-A P, in turn, select their corresponding K destination user-pairs, thus enhancing the number of users supported per RF chain from K to $2K$. Furthermore, the relay-users experience multi-user interference (MUI) due to beamformed signals from base station (BS) antennas allocated to other relay-users. Likewise, the destination-users experience inter-cluster interference (ICI) from neighboring relay-destination clusters. Therefore, a joint (i.e., relay-destination) zero-forcing (JZF) interference cancellation scheme has been proposed at both relay and destination user-pairs to mitigate MUI and ICI. The computational complexity of the hybrid SC AP and PC joint D-A P systems, the energy-efficiency (EE) of the system has also been analyzed for obtaining the green point.

Simulation results corroborate that the proposed mmWave relay NOMA system with hybrid D-A P based SC and joint D-A P based PC have accomplished superior sum-rates for the relay and destination-users compared to the hybrid D-A precoding systems proposed in [77],[144] and[105], as well as current NOMA systems as proposed in [100]. For a given green point, our proposed systems also attain superior sum data-rate. Lastly, the joint hybrid D-A P based PC attains low computational complexity. Throughout this paper, upper case and lower case boldfaces are used for matrices and vectors, respectively. $\arg[\mathbf{X}]$ generates a matrix containing the phases of the entries. $\mathbf{X}^H$, $\mathbf{X}^T$ and $||\cdot||$ denotes a matrix hermitian, transpose and norm respectively.

8.1 An Example Hybrid D-A P Relay NOMA System for supporting 2 Users per RF Chain

The block diagram of relay NOMA hybrid D-A P system which supports 2-users per RF chain is shown in Fig. 8.1. Each of N RF chains is connected to a large-scale array of M identical antennas. In this paper, the analysis is initially carried out considering a downlink scenario for an i-th RF chain, where $1 \leq i \leq N$. The i-th RF chain co-operatively supports a particular single antenna relay-user k_r and its corresponding single antenna destination-user pair k_d respectively, through hybrid D-A P and relaying, where $1 < k_r, k_d \leq 2K$. In the i-th RF chain source, x_{k_r} and x_{k_d} are the symbols for the k_r-th relay-user and the k_d-th destination-user respectively. x_{k_r}

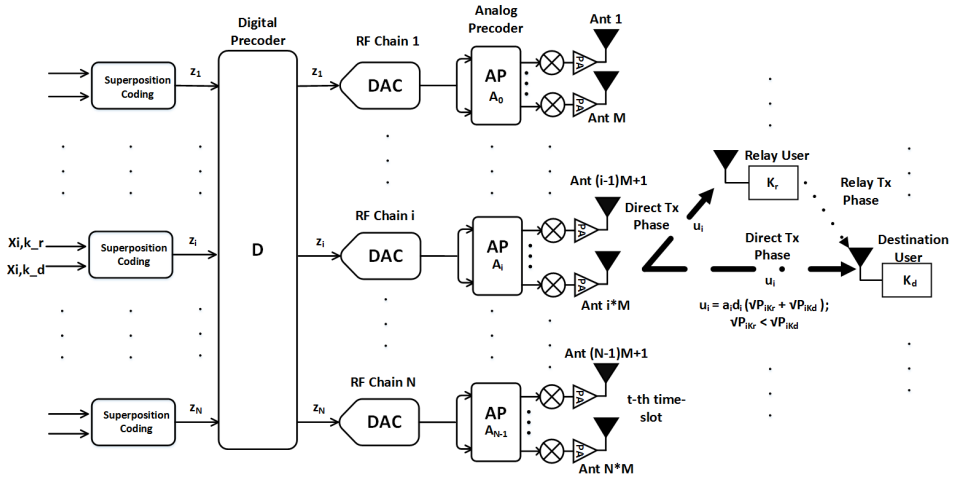

FIGURE 8.1: Hybrid D-A P for supporting 2-users per RF chain in relay NOMA downlink scenario.

and x_{k_d} are allocated unequal powers P_{i,k_r} and P_{i,k_d} respectively, where $P_{i,k_r} \leq P_{i,k_d}$ by the superposition coding block to generate the i-th superposed symbol z_i. At the k_r-th relay-user, a power splitting (PS) receiver is considered as proposed in [197]. It is further assumed that the PS receiver only utilizes the signal power and not the antenna noise power as in [112]. In the direct transmission phase, downlink transmission of the superposed symbol occurs from the i-th RF chain to the k_r-th relay-user and k_d-th destination-user. In the same phase, k_r-th relay-user harvests energy from the received signal by adopting power splitting. The k_r-th relay-user then applies SIC, i.e., it decodes the k_d-th destination-user's message x_{k_d}, subtracts it from the received signal, and decodes its own message x_{k_r} next. The k_d-th destination-user decodes its own message x_{k_d} in this phase. The k_d-th destination user can distinguish and decode its own symbol x_{k_d} from x_{k_r} due to unequal power allocation at the i-th RF chain source. In the cooperative phase, the k_r-th relay-user forwards the k_d-th destination-user's message x_{k_d} by adopting the AF protocol. The k_d-th destination-user decodes the relayed message and combines it with the message received in the previous direct transmission phase from the i-th RF chain, using MRC. These assumptions are described further in Subsection D.

8.1.1 3D Channel Gain

The k_r-th relay-user's 3D channel gain β_{i,m,k_r} for the m-th Tx antenna of the i-th RF chain can be given by[105]

$$\beta_{i,m,k_r} \sqrt{P_{m,k_r}} \sum_{m=1}^{M} \begin{bmatrix} F_{Rx,V}(\varphi,\vartheta) \\ F_{Rx,H}(\varphi,\vartheta) \end{bmatrix}^T \begin{bmatrix} e^{j\phi^{VV}} & \sqrt{\kappa_m^{-1}} e^{j\phi^{VH}} \\ \sqrt{\kappa_m^{-1}} e^{j\phi^{HV}} & e^{j\phi^{HH}} \end{bmatrix} \begin{bmatrix} F_{Tx,i,V}(\phi_m,\theta_m) \\ F_{Tx,i,H}(\phi_m,\theta_m) \end{bmatrix}, \tag{8.1}$$

where, $\sqrt{P_{m,k_r}}$ is the transmit power at the m-th Tx antenna associated with the k_r-th relay-destination user-pair. $F_{Rx,V}$ and $F_{Rx,H}$ are the Rx antenna radiation patterns for the vertical (V) and horizontal (H) polarizations, respectively. $F_{Tx,i,V}$ and $F_{Tx,i,H}$

are the corresponding vertical (V) and horizontal (H) polarizations for the i-th RF chain. $\phi^{VV}, \phi^{VH}, \phi^{HV}, \phi^{HH}$ are the initial random phases for vertical (VV), cross (VH, HV), and horizontal polarizations (HH). κ_m is the intra-cluster Rician K-factor associated with the m-th Tx antenna cluster. ϑ and φ are the elevation and azimuth angle-of-arrival (AoA), respectively at the k_r-th relay-user. θ_m and ϕ_m are the elevation and azimuth angle-of-departure (AoD) from the m-th Tx antenna in the i-th RF chain.

8.1.2 Relay and Destination User Selection

We assume a pool of $2K$ available users for selection as a potential relay-user. The i-th RF chain source selects a particular k_r-th relay-user from this pool of available $2K$ users where $K \leq M$, by allocating its M antennas based on the 3D channel gain. Initially, the gain of the M antennas is calculated for a particular k_r-th potential relay-user as shown below

$$P_{i,M,k_r} = \sum_{m=1}^{M} |\beta_{i,m,k_r} h_{i,m,k_r}|^2, k_r = 1, \cdots, 2K, \tag{8.2}$$

where h_{i,m,k_r} is the Rayleigh channel connecting the m-th TX antenna in the i-th RF chain to the k_r-th relay user. This process is then repeated for all available pool of $2K$ users, and the M antennas are then assigned to that user which has the maximum gain, i.e.,

$$k_M = \underset{k_r}{\operatorname{argmax}} \left\{ P_{i,M,1}, P_{i,M,2}, \cdots, P_{i,M,2K} \right\}. \tag{8.3}$$

This becomes the k_r-th relay-user for the i-th RF chain source. The group of unselected users become the candidates for selecting the destination-user. The selected k_r-th relay-user associated with the i-th RF chain source acquires its corresponding k_d-th destination-user based on minimum angular separation. This process can be represented for any k_r-th k_d-th relay-destination user-pair as follows

$$k_{r,d} = \underset{k_d}{\operatorname{argmin}} \left\{ \angle_{k_r,k_{d_1}}, \angle_{k_r,k_{d_2}}, \cdots, \angle_{k_r,k_{2K}} \right\}, \tag{8.4}$$

where $\angle_{k_r,k_{d_k}}$ is the angular separation of k_r-th relay-user and a potential k_{d_k}-th destination-user in the pool of remaining $2K-1$ users. For a sufficiently high density of users in the mmWave environment, selecting the k_d-th destination-user having the minimum angular separation from its associated k_r-th relay-user ensures that the 3D mmWave channel remains constant, albeit with additional fading-loss which is compensated by unequal power allocation in the superposed symbols.

8.1.3 Direct Transmission form the i-th RF Chain to the Relay and Destination Users

In the direct transmission phase, the precoded transmit signal vector $\mathbf{u}_i \in \mathbb{C}^{M\times 1}$ generated by superposition coding at the i-th RF chain is represented by

$$\begin{aligned}\mathbf{u}_i &= \mathbf{a}_i d_i z_i \\ &= \mathbf{a}_i d_i \big(\sqrt{P_{i,k_r}} x_{k_r} + \sqrt{P_{i,k_d}} x_{k_d}\big)\end{aligned} \tag{8.5}$$

$\mathbf{a}_i \in \mathbb{C}^{M\times 1}$ is the AP vector operating over the superposed symbol z_i. $\mathbf{a}_i$ is implemented by phase-shifters. Therefore, a non-convexity constant modulus constraint is applied in the AP $\mathbf{a}_i$. z_i is generated at the superpostion coding block at the i-th RF chain, by allocating the power P_{i,k_r} and P_{i,k_d} to the k_r-th relay-user's and the k_d-th destination-user's information symbols x_{k_r} and x_{k_d} respectively. $P_{i,k_r} < P_{i,k_d}$ enables SIC of the k_d-th destination-user symbols at the k_r-th relay-user. Further, $\mathrm{E}\big[z_{i,k} z_{i,k}^H\big] = \gamma_0$, where γ_0 is the expected transmitted symbol power. $\mathbf{a}_i$ is expressed as

$$\mathbf{a}_i = \underbrace{\big[a_{i,0}, a_{i,1}, \cdots, a_{i,M-1}\big]}_{M\times 1} \tag{8.6}$$

In (5) d_i is the DP element. Since the digital precoder $\mathbf{D}$ is kept identity, i.e., $\mathbf{D} = \mathbf{I}$, $d_i = 1$. The k_r-th relay-user's received signal from the i-th RF chain, denoted by the vector $\mathbf{h}_{i,k_r}\mathbf{a}_i$ can be formulated as

$$\mathbf{h}_{i,k_r}(t)\mathbf{a}_i(t) = \sum_{m=0}^{M-1} h_{i,m,k_r} a_{i,m}, \tag{8.7}$$

at the k_d-th destination user, the received signal is

$$\begin{aligned} y_{i,k_d} &= \mathbf{h}_{i,k_r}\mathbf{u}_i + n_{i,k_d} \\ &= \underbrace{\mathbf{h}_{i,k_r}\mathbf{a}_i d_i \sqrt{P_{i,k_r}} x_{k_r}}_{\text{Interference from } k_r\text{-th relay-user}} \\ &\quad + \underbrace{\mathbf{h}_{i,k_d}\mathbf{a}_i d_i \sqrt{P_{i,k_d}} x_{k_d}}_{\text{Desired } k_d\text{-th destination-user symbols}} + n_{i,k_d}, \end{aligned} \tag{8.8}$$

where $\mathbf{h}_{i,k_r}\mathbf{a}_i d_i \sqrt{P_{i,k_r}} x_{k_r}$ is the interference at k_d-th destination-user from the k_r-th relay-user symbols due to superposition coding at the i-th RF chain source. n_{i,k_d} is the complex Gaussian noise at the k_d-th destination user with variance σ^2_{i,k_d}. $\mathbf{h}_{i,k_r} \in \mathbb{C}^{1\times M}$ is the Rayleigh channel from the k_r-th relay-user to the i-th RF chain. As aforesaid in Subsection C, a low angular separation between the k_r-th relay-user and its associated k_d-th destination-user in our high user density mmWave environment ensures that the 3D mmWave channel remains unchanged for the k_d-th destination user, except with additional path-loss. Therefore, in our paper, $\mathbf{h}_{i,k_d} = \epsilon \mathbf{h}_{i,k_r}$, where

$0 < \epsilon < 1$. The received signal-to-interference-plus-noise ratio (SINR) at the k_d-th destination user to detect x_{k_d} from $\mathbf{u}_i$ (generated at the i-th RF chain) will be

$$\gamma_{k_d} = \frac{\frac{P_{i,k_d}\gamma_0}{\sigma^2_{i,r}}\left|\left|\mathbf{h}_{i,k_d}\mathbf{a}_i d_i\right|\right|^2}{\sigma^2_{i,k_d} + \frac{P_{i,k_r}\gamma_0}{\sigma^2_{i,r}}\left|\left|\mathbf{h}_{i,k_r}\mathbf{a}_i d_i\right|\right|^2}, \tag{8.9}$$

At the k_r-th relay-user, as aforesaid, a power splitting (PS) receiver is considered[197]. It is also assumed that the PS receiver only utilizes the signal power and not the antenna noise power as in [112]. Then, the energy harvested by the k_r-th relay-user will be $\rho\eta P_{i,k_r}||\mathbf{h}_{i,k_r}\mathbf{a}_i d_i||^2$[58], where $0 < \rho < 1$ is the power splitting ratio, $0 < \eta < 1$ denotes the energy conservation efficiency, The k_r-th relay-user's received signal is derived as

$$y_{i,k_r} = \sqrt{1-\rho}\mathbf{h}_{i,k_r}\mathbf{u}_i + n_{i,k_r}, \tag{8.10}$$

where $\mathbf{h}_{i,k_r}$ is the $1 \times M$ Rayleigh channel associating the k_r-th relay-user to the i-th RF chain having M Tx antennas as mentioned previously. n_{i,k_r} is the complex Gaussian noise at the k_r-th relay-user with variance σ^2_{i,k_r}. The received SINR at the k_r-th relay-user to detect x_{k_d} can be obtained as

$$\gamma^{x_{k_d}}_{k_r} = (1-\rho)\frac{P_{i,k_d}\gamma_0\left|\left|\mathbf{h}_{i,k_r}\mathbf{a}_i d_i\right|\right|^2}{\sigma^2_{i,k_r} + (1-\rho)P_{i,k_r}\gamma_0\left|\left|\mathbf{h}_{i,k_d}\mathbf{a}_i d_i\right|\right|^2} \tag{8.11}$$

Lastly, the received SINR at the k_r-th relay-user to detect its own message symbol x_{k_r} will be

$$\gamma^{x_{k_r}}_{k_r} = \frac{(1-\rho)P_{i,k_r}\gamma_0\left|\left|\mathbf{h}_{i,k_r}\mathbf{a}_i d_i\right|\right|^2}{\sigma^2_{i,k_r} + P_{i,k_d}\gamma_0\left|\left|\mathbf{h}_{i,k_d}\mathbf{a}_i d_i\right|\right|^2} \tag{8.12}$$

8.1.4 Relay Transmission from the Relay User to the Destination User with Amplify and Forward (AF)

Assuming that all the harvested energy in the direct transmission phase is used, the transmit power at the k_r-th relay-user can be presented as

$$P_{k_r} = \rho\eta\gamma_0 P_i||\mathbf{h}_{i,k_r}\mathbf{a}_i d_i||^2|h_{k_r,k_d}|^2, \tag{8.13}$$

$$\gamma_{k_r k_d}^{AF} = \frac{\rho(1-\rho)\eta\gamma_0^2 P_{i,k_d}\left|\left|\mathbf{h}_{i,k_r}\mathbf{a}_i d_i\right|\right|^4 \left|h_{k_r,k_d}\right|^2}{\rho(1-\rho)\eta\gamma_0^2 P_{i,k_r}\left|\left|\mathbf{h}_{i,k_d}\mathbf{a}_i d_i\right|\right|^4 \left|h_{k_r,k_d}\right|^2 + \rho\eta\gamma_0\left|\left|\mathbf{h}_{i,k_d}\mathbf{a}_i d_i\right|\right|^2 \left|h_{k_r,k_d}\right|^2 + \sigma_{k_r,k_d}^2} \tag{8.15}$$

where h_{k_r,k_d} is the line-of-sight (LoS) channel connecting the k_r-th-k_d-th relay-destination user-pair. Furthermore, assuming the amplify-and-forward (AF) protocol, the amplification factor is represented by

$$\begin{aligned} G^2 &= \frac{P_{k_r}}{(P_{i_{k_r}} + P_{i_{k_d}})\left|\left|\mathbf{h}_{i,k_d}\mathbf{a}_i d_i\right|\right|^2 + \sigma_{i,k_d}^2} \\ &= \frac{\rho\eta\gamma_0 P_{i,k_r}\left|\left|\mathbf{h}_{i,k_r}\mathbf{a}_i d_i\right|\right|^2 \left|h_{k_r,k_d}\right|^2}{(P_{i,k_r} + P_{i,k_d})\left|\left|\mathbf{h}_{i,k_d}\mathbf{a}_i d_i\right|\right|^2 + \sigma_{i,k_d}^2} \end{aligned} \tag{8.14}$$

Then, the received SINR at the k_d-th destination-user to detect x_{k_d} transmitted from the k_r-th relay-user using the AF protocol can be given by (8.15), where σ_{k_r,k_d}^2 is variance of the complex Gaussian noise for the channel h_{k_r,k_d}.

8.2 Sum Data-Rate of the Relay and Destination-Users

From (8.13), the decoded symbol at the k_r-th relay-user after SIC will be

$$R_{k_r} = \log_2\left(1 + (1-\rho)P_{i,k_r}\gamma_0\left|\left|\mathbf{h}_{i,k_r}\mathbf{a}_i d_i\right|\right|^2\right), \tag{8.16}$$

the k_d-th destination-user combines the direct signal from the i-th RF chain received in the direct transmission phase and the relayed signal from the k_r-th relay-user received in the relay transmission phase using maximum ratio combining (MRC). The sum data-rate achieved at the k_d-th destination-user over both these phases after applying MRC is evaluated as

$$R_{k_d} = \log_2\left(1 + \gamma_{k_d}\gamma_{k_r k_d}^{AF}\right), \tag{8.17}$$

where γ_{k_d} and $\gamma_{k_r k_d}^{AF}$ were derived in (8.9) and (8.15) respectively.

8.3 Hybrid D-A based SC AP System with NOMA Relay

In the previous section, an example hybrid D-A P system for supporting 2 users per RF chain was proposed. Now, our focus is to extend the users per RF chain from 2 up to $2K$. Suppose $2K$ users are to be supported by the i-th RF chain with M Tx antennas, where $K \leq M$. The allocation of antennas is based on the calculation

of instantaneous power of the 3D channel for every k_r-th relay-user. For the m-th antenna in the i-th RF chain, the channel power associated with the k_r-th relay-user is calculated as

$$P_{i,m,k_r} = |\beta_{i,m,k_r} h_{i,m,k_r}|^2, k_r = 1, \cdots, 2K, \tag{8.18}$$

where $1 < k_r \leq 2K$. The m-th antenna is then assigned to that user which has the maximum power, i.e.,

$$k_m = \underset{k_r}{\operatorname{argmax}} \left\{ P_{i,m,1}, P_{i,m,2}, \cdots, P_{i,m,2K} \right\}. \tag{8.19}$$

This process is repeated M times until all the M antennas are allocated to the S users where $S \leq K \leq M$. In this way, the S relay-users associated with the i-th RF chain have been selected. The remaining $(2K - S)$ users are the candidates for choosing the destination-users. S destination-users will now be acquired from the pool of remaining $2K - S$ available candidates by each of the selected s_r-th relay-user based on minimum angular separation, where $0 \leq s_r \leq S$. This process can be enumerated for each of the s-th relay-user as follows

$$s_r, s_d = \underset{s_{d_k}}{\operatorname{argmin}} \left\{ \angle_{s_r, s_{d_1}}, \angle_{s_r, s_{d_2}}, \cdots, \angle_{s_r, s_{2K-S}} \right\}, \tag{8.20}$$

where $\angle_{s_r, s_{d_k}}$ is the angular separation of s_r-th relay-user and the s_d-th destination-user in the pool of $2K - S$ available candidates for the destination user. In this way, $2S$ users are selected from the pool of $2K$ users where $S \leq K$, and remaining $(2K - 2S)$ users are not supported.

Since a total of S relay-destination user-pairs are selected for the i-th RF chain, S continuous symbols from the i-th symbol stream have to be superposed and multiplexed onto the i-th RF chain. In this chapter, using S orthogonal time-slots from the i-th symbol stream is proposed, to create S continuous symbol-streams for the selected s-th relay-destination user-pair.

8.3.1 Joint Zero Forcing (JZF) at Relay-Destination User-Pair

The s-th relay-destination user-pair will experience multi-user interference (MUI) from the beamformed signals generated from antenna elements that are allocated to other user-pairs. The destination-users experience inter-cluster interference (ICI) from the neighboring clusters. MUI and ICI at any s-th relay-destination user-pair can be removed by applying JZF. It is assumed that the SC antenna allocation information is available at every relay-user.

For example, consider a scenario depicted in Fig. 8.2 in the following page, where, (i) the number of antenna elements in the i-th RF chain is $M = 4$; (ii) The total number of single antenna relay-destination user-pairs to be supported by this i-th RF chain is $S = 3$; and, (iii) the SC antenna allocation for the i-th RF chain that follows the pattern as shown in Fig. 2. In this scenario, antenna m_0 is allocated to the relay-user s_{r_0}; m_1 and m_3 to s_{r_2}; and m_2 to s_{r_1}. The corresponding destination-users are denoted

as s_{d_0}, s_{d_2} and s_{d_1} respectively. As shown in the Fig. 2, in order to implement this scenario, $S = 3$ orthogonal time-slots from the i-th symbol stream corresponding to the i-th RF chain will be selected to create 3 continuous symbol -streams for each of the selected s-th relay-destination user-pairs. Hybrid D-A P based SC is then performed over each of the M antennas. The SC AP vector $\mathbf{a}_{i,SC}$, specific to the system scenario depicted in Fig. 8.2, is derived using a similar approach as previously in (8.6). It is given by (8.21) at the bottom of this page, where $h^*_{i,m,s_r}(t)$ is the conjugate of the complex channel coefficient connecting the m-th Tx antenna element in the i-th RF chain to the s_r-th relay-user. It can be seen that $\mathbf{a}_{i,SC}$ is a 4×1 vector for the scenario depicted in Fig. 2, and satisfies the non-convexity constant modulus constraint $\mathbf{a}_{i,SC} = 1/\sqrt{M} e^{j \arg[\mathbf{h}^*_{i,s_r}]}$[19]. The DP matrix is kept identity.

For the purpose of analysis, let us examine specific the case for the s_{r_2}-s_{d_2} relay-destination user-pair in Fig. 8.2, i.e., the 2-nd relay-destination user-pair. The received symbol samples at the s_{r_2}-th relay-user is given by

$$\begin{aligned}
\mathbf{y}_{i,s_{r_2}} = & \underbrace{\mathbf{w}^H_{s_{r_2}} h_{i,0,s_{r_2}} a_{i,0,s_{r_0}} (\sqrt{P_{i,0,s_{r_0}}} x_{s_{r_0}}}_{\text{MUI at } s_{r_2} \text{ from relay } s_{r_0}} + \underbrace{\sqrt{P_{i,0,s_{d_0}}} x_{s_{d_0}})}_{\text{residual from } s_{d_0}} \\
& + \mathbf{w}^H_{s_{r_2}} h_{i,1,s_{r_2}} a_{i,s_{r_2}} (\sqrt{P_{i,1,s_{r_2}}} x_{s_{r_2}} + \sqrt{P_{i,1,s_{d_2}}} x_{s_{d_2}}) \\
& + \underbrace{\mathbf{w}^H_{s_{r_2}} h_{i,2,s_{r_2}} a_{i,1,s_{r_1}} (\sqrt{P_{i,2,s_{r_1}}} x_{s_{r_1}}}_{\text{MUI at } s_{r_2} \text{ from relay } s_{r_1}} + \underbrace{\sqrt{P_{i,2,s_{d_1}}} x_{s_{d_1}})}_{\text{residual from } s_{d_1}} \\
& + \mathbf{w}^H_{s_{r_2}} h_{i,3,s_{r_2}} a_{i,s_{r_2}} (\sqrt{P_{i,1,s_{r_2}}} x_{s_{r_2}} + \sqrt{P_{i,1,s_{d_2}}} x_{s_{d_2}}) \\
& + \mathbf{w}^H_{s_{r_2}} \mathbf{n}_{i,s_{r_2}}, \qquad (8.22)
\end{aligned}$$

where $h_{i,m,s_{r_2}}$ is the Rayleigh channel connecting the m-th Tx antenna in the i-th RF chain to the s_{r_2}-th relay-user. Additionally, in (8.22), the $M \times 1 = 4 \times 1$ JZF weights

$$\mathbf{w}_{s_{r_2}} = (\mathbf{h}^H_{i,s_{r_2}} \mathbf{h}_{i,s_{r_2}})^{-1} \mathbf{h}_{i,s_{r_2}} \qquad (8.23)$$

operating on $\mathbf{h}_{i,s_{r_2}} \mathbf{a}_{i,SC}$ will cancel the MUI from unwanted beamformed signals that are generated by antenna elements allocated to the other users by the hybrid D-A P based SC. $x_{i,s_{d_v}}, v \in \{0,1,2,3\}$, is the superposed Tx symbol from the i-th RF chain chosen for the s_r-s_d-th relay-destination user-pair from the 3 available orthogonal (in time) symbol streams, as shown in Fig. 8.2. The complete $1 \times M = 1 \times 4$ channel

$$\mathbf{a}_{i,SC} = \Big[\overbrace{a^T_{i,0,s_{r_0}}}^{\text{A-BF for 0-th ANT } m_0} , \overbrace{a^T_{i,1,s_{r_2}}}^{\text{A-BF for 1-st ANT } m_1} , \overbrace{a^T_{i,2,s_{r_1}}}^{\text{A-BF for 2-nd ANT } m_2} , \overbrace{a^T_{i,3,s_{r_2}}}^{\text{A-BF for 3-rd ANT } m_3} \Big] \qquad (8.21)$$

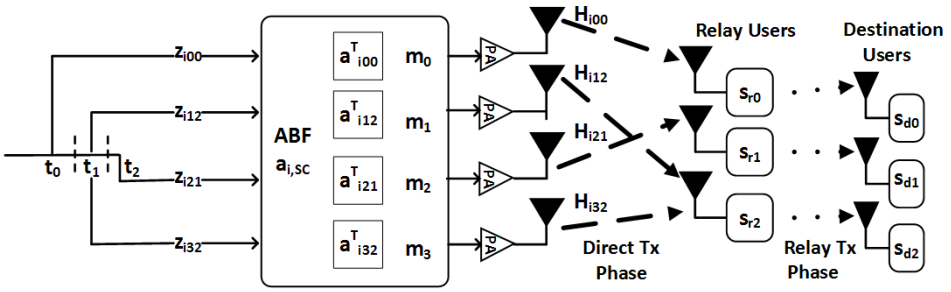

FIGURE 8.2: hybrid D-A based SC AP for the i-th RF chain. t_0, t_1, t_2 and t_3 indicates the 0-th, 1-st, 2-nd and the 3-rd orthogonal time-slots of the symbol stream $\mathbf{z}_i$ which maps the i-th symbol stream onto the i-th RF chain.

vector, $\mathbf{h}_{i,s_{r_2}}$, connecting the i-th RF chain to the s_{r_2}-th relay-user is given by

$$\mathbf{h}_{i,s_{r_2}} = \underbrace{\left[h_{i,0,s_{r_2}}, h_{i,1,s_{r_2}}, h_{i,2,s_{r_2}}, h_{i,3,s_{r_2}}\right]}_{1\times M=1\times 4} \tag{8.24}$$

The interference from the destination user-pair s_{d_v} is removed by SIC, and the residual interference from other destination users $s_{d_w}, w \in \{0,1,3\}$ has been neglected. Similarly the s_{d_2}-th destination user's received symbols during the direct transmission phase will be

$$\begin{aligned}
\mathbf{y}_{i,s_{d_2}} = {} & \underbrace{\mathbf{w}^H_{s_{d_2}} a_{i,0,s_{r_0}} (h_{i,0,s_{r_2}} \sqrt{P_{i,0,s_{r_0}}} x_{s_{r_0}}}_{\text{MUI at } s_{r_2} \text{ from relay } s_{r_0}} + \underbrace{h_{i,0,s_{d_2}} \sqrt{P_{i,0,s_{d_0}}} x_{s_{d_0}})}_{\text{ICI from } s_{d_0}} \\
& + \mathbf{w}^H_{s_{d_2}} a_{i,s_{r_2}} (h_{i,1,s_{r_2}} \sqrt{P_{i,1,s_{r_2}}} x_{s_{r_2}} + h_{i,1,s_{d_2}} \sqrt{P_{i,1,s_{d_2}}} x_{s_{d_2}}) \\
& + \underbrace{\mathbf{w}^H_{s_{r_2}} a_{i,1,s_{r_1}} (h_{i,2,s_{r_2}} \sqrt{P_{i,2,s_{r_1}}} x_{s_{r_1}}}_{\text{MUI at } s_{r_2} \text{ from relay } s_{r_1}} + \underbrace{h_{i,2,s_{d_2}} \sqrt{P_{i,2,s_{d_1}}} x_{s_{d_1}})}_{\text{ICI from } s_{d_1}} \\
& + \mathbf{w}^H_{s_{d_2}} a_{i,s_{r_2}} (h_{i,3,s_{r_2}} \sqrt{P_{i,1,s_{r_2}}} x_{s_{r_2}} + h_{i,3,s_{d_2}} \sqrt{P_{i,1,s_{d_2}}} x_{s_{d_2}}) \\
& + \mathbf{w}^H_{s_{d_2}} \mathbf{n}_{i,s_{d_2}},
\end{aligned} \tag{8.26}$$

where $\mathbf{w}_{s_{d_2}} = (\mathbf{h}^H_{i,s_{d_2}} \mathbf{h}_{i,s_{d_2}})^{-1} \mathbf{h}_{i,s_{d_2}}$ are the 4×1 JZF weights which, when operating on $\mathbf{h}_{i,d_{r_2}} \mathbf{a}_{i,SC}$, where $\mathbf{h}_{i,s_{d_2}} = [h_{i,0,s_{d_2}}, h_{i,1,s_{d_2}}, h_{i,2,s_{d_2}}, h_{i,3,s_{d_2}}]$ will null the ICI from the destination-users of the neighboring clusters. However, the MUI due to relay-users in the neighboring clusters, as well as interference from its own relay-pair s_{r_2} would linger, and is treated as noise: it should further be noted, similar to as was explained previously in Section II D, $\mathbf{h}_{i,s_{d_2}} = \epsilon' \mathbf{h}_{i,s_{r_2}}$, where $0 < \epsilon' < 1$. Therefore, the interference from the relay-users in the neighboring clusters relay-pair s_{r_2} would be mitigated to some extent, but not entirely. It is in such a scenario that relay transmission and MRC combining at the destination-user becomes vital,

since it enhances the destination user's receive SINR (derived in (8.29) and (8.30)).

The above analysis can be extended for any other SC antenna allocation for all the M antennas, which can then support S relay-destination user pairs per RF chain, where $S \leq K \leq M$, i.e., a total number of $2S$ users. To satisfy the total power constraint, the total signal power from the i-th RF chain to all the S supported relay-destination user pairs needs to satisfy the power constraint

$$1/M \sum_{m=1}^{M} \sum_{s_r=1}^{S} p_{i,m,s_r} \leq \sigma_i^2 \gamma_i, \tag{8.27}$$

where $1/M$ normalizes the i-th RF chain to unity, γ_i is the total Tx signal-to-noise-ratio (SNR) at the i-th RF chain, and σ_i is the noise variance. Based on these discussions, the maximum achievable sum data-rate for any s_r-th relay-user R_{s_r} associated with the i-th RF chain can be as derived as in (8.28) at the bottom of this page, where M_{s_r} is the number of antennas allocated to the s_r-th relay-user, σ^2_{i,s_r} is the corresponding noise variance, and S is the number of orthogonal time slots allocated to the S supported relay-user by the hybrid D-A based SC AP algorithm, where $S \leq K$. Ultimately, for each of the s_d-th destination-user that is associated with the corresponding s_r-th relay-user, the analysis will proceed in a similar manner as just explained for the s_r-th relay-user, and the maximum achievable sum data-rate due to MRC combining over two orthogonal phases for the s_d-th destination-user can be derived as follows. The SINR γ^{AF}_{SC,s_r,s_d} at the s_d-th destination-user for the relay phase can be given by (8.29), where $\mathbf{w}_{s_d}$ are the ICI canceling JZF weights for the s_d-th destination-user. The SINR $\gamma^{x_{k_d}}_{SC,s_d}$ at the s_d-th destination-user for the direct transmission phase can be similarly derived as given by (8.30). Using (8.29) and (8.30), the s_d-th destination user sum data-rate over the two orthogonal phases attained due to MRC combining can be given by

$$R_{k_d,SC} = \log_2 \left(1 + \gamma^{AF}_{SC,s_r,s_d} \gamma^{x_{k_d}}_{SC,s_d}\right) \tag{8.31}$$

In this way, by applying the hybrid D-A P based SC, it has been proven that the number of users that can be supported by the i-th RF chain having M antennas can be scaled to $2S$, where $S \leq K \leq M$.

$$R_{s_r} = \log_2 \left(1 + \frac{M_{s_r}}{SM} P_{i,s_r} \gamma_0 (1-\rho) (\sigma^2_{i,s_r} \mathbf{w}^H_{s_r})^{-1} \left|\left| \mathbf{w}_{s_r} \mathbf{h}_{i,k_{s_r}} \mathbf{a}_{i,SC} d_i \right|\right|^2 \right) \tag{8.28}$$

$$\gamma^{AF}_{SC,s_r,s_d} = \frac{\rho(1-\rho)\eta\gamma_0^2 P_{i,s_d} (\sigma^2_{i,s_d} \mathbf{w}^H_{s_d})^{-1} \left|\left| \mathbf{w}_{s_d} \mathbf{h}_{i,s_r} \mathbf{a}_{i,SC} d_i \right|\right|^4 \left|h_{s_r,s_d}\right|^2}{\begin{array}{r}\rho(1-\rho)\eta\gamma_0^2 P_{i,s_r} (\sigma^2_{i,s_d} \mathbf{w}^H_{s_d})^{-1} \left|\left| \mathbf{w}_{s_d} \mathbf{h}_{i,s_r} \mathbf{a}_{i,SC} d_i \right|\right|^4 \left|h_{s_r,s_d}\right|^2 + \\ \rho\eta\gamma_0 (\sigma^2_{i,s_d} \mathbf{w}^H_{s_d})^{-1} \left|\left| \mathbf{w}_{s_d} \mathbf{h}_{i,s_r} \mathbf{a}_{i,SC} d_i \right|\right|^2 \left|h_{s_r,s_d}\right|^2 + \sigma^2_{s_r,s_d}\end{array}} \tag{8.29}$$

$$\gamma^{x_{k_d}}_{SC,s_d} = (1-\rho) \frac{P_{i,s_d} \gamma_0 (\sigma^2_{i,s_d} \mathbf{w}^H_{s_d})^{-1} \left|\left| \mathbf{w}_{s_d} \mathbf{h}_{i,s_r} \mathbf{a}_{i,SC} d_i \right|\right|^2}{\sigma^2_{i,s_r} + (1-\rho) P_{i,s_r} \gamma_0 (\sigma^2_{i,s_d} \mathbf{w}^H_{s_d})^{-1} \left|\left| \mathbf{w}_{s_d} \mathbf{h}_{i,s_r} \mathbf{a}_{i,SC} d_i \right|\right|^2} \tag{8.30}$$

8.4 Joint D-A P using Low Complexity Principal Component (PC)

Although the hybrid D-A P based SC system could support $2S$ users per RF chain, $(2K - 2S)$ users had to be discarded because of the power constraint at the i-th RF chain. Hence, D-A P based SC system cannot support all the users in the system. Moreover, as SC has to evaluate the energy from each Tx antenna to every user, a dense user environment with massive MIMO in base station results in a high complexity in SC. These reasons motivates us to propose a low complexity joint hybrid D-A P based principal component (PC)[105]. First, the Rayleigh channel for the K relay-users, where $K \leq M$, is given by

$$\mathbf{h}_{i,r,PC} = \left[\mathbf{h}_{i,0}, \mathbf{h}_{i,1}, \cdots, \mathbf{h}_{i,K-1}\right], \tag{8.32}$$

where $\mathbf{h}_{i,k_r}$ is the $1 \times M$ Rayleigh channel experienced by the k_r-th relay-user from the M antennas in the i-th RF chain. Then, the normalized instantaneous channel realization matrix $\mathbf{G}_{i,r,PC}$, is calculated as

$$\mathbf{G}_{i,r,PC} = \frac{\left(\mathbf{h}_{i,r,PC}\right)^H \mathbf{h}_{i,r,PC}}{|| \left(\mathbf{h}_{i,r,PC}\right)^H \mathbf{h}_{i,r,PC} ||}. \tag{8.33}$$

The eigenvalue decomposition (EVD) of $\mathbf{G}_{i,r,PC}$ is then performed to obtain the eigenvalues and the eigenvectors. Then, the dominant eigenvalue $\breve{}_{k_r,i,PC}$, and the phases of their corresponding eigenvectors $\mathbf{\Phi}_{k_r,i,PC}$, are extracted to compute the normalized joint hybrid precoder $\mathbf{g}_{i,r,PC}$ for the i-th RF chain, given in (31) at the top of the page. In order to allocate the M Tx antennas among all the K relay-destination user-pairs, it is ensured that $\sum_{k_r=0}^{K-1} m_{k_r} = M$. Therefore, the k_r-th relay-user is allocated m_{k_r} antenna elements from the i-th RF chain. To satisfy the total power constraint the signal power of the ith RF chain should satisfy

$$\begin{aligned} ||\mathbf{g}_{i,r,PC}||^2 &= ||d_{i,PC}\mathbf{a}_{i,PC}||^2 \\ &= \mathrm{Tr}(d_{i,PC}\mathbf{a}_{i,PC} \left(\mathbf{a}_{i,PC}\right)^H \left(d_{i,PC}\right)^H) \\ &\leq \sigma_i^2 \gamma_i. \end{aligned} \tag{8.34}$$

To overcome the proposed SC algorithm limits, (i) $\mathbf{G}_{i,r,PC}$ is computed based on instantaneous CSI instead of allocating TX antennas to every user based on channel power, (ii) as $\mathbf{G}_{i,r,PC}$ does not require any evaluation of energy from each Tx antenna to every user, it intrinsically results in reducing the complexity of SC algorithm. Ultimately, In this way, all K relay-destination user-pairs, i.e., a total of $2K$ users, are supported, where $K \leq M$. Finally, the SINR and sum-rates can be derived as analyzed in the previous section.

$$\mathbf{g}_{i,r,PC} = \underbrace{\left[\lambda_{i,PC}\right]}_{d_{i,PC}} \underbrace{\left[\underbrace{\left[\Phi_{0,i,0},\cdots,\Phi_{m_0-1,i,0}\right]^T}_{\mathbf{\Phi}_{0,i,0,PC}}, \underbrace{\left[\Phi_{0,i,1},\cdots,\Phi_{m_1-1,i,1}\right]^T}_{\mathbf{\Phi}_{1,i,PC}},\cdots, \underbrace{\left[\Phi_{0,i,K-1},\cdots,\Phi_{m_K-1,i,K-1}\right]^T}_{\mathbf{\Phi}_{K-1,i,PC}}\right]^T}_{\mathbf{a}_{i,PC}\in\mathbb{C}^{M\times 1}=1/\sqrt{M}e^{j\arg[\mathbf{\Phi}_{k_r,i}]}} \quad (8.35)$$

8.5 Simulation Results and Discussion

In this section, the sum data-rate, computational complexity and energy-efficiency of the hybrid D-A P based SC and the low complexity joint D-A P based PC with NOMA relay which can support $2S$ and $2K$ users per RF chain respectively, are compared with (i) separate hybrid D-A P in [77],[144] that supports a single user, (ii) current NOMA system in [100] which supports 2 users, and, (iii) hybrid SC AP system in [105] which supports S users, for a downlink mmWave system. A uniform planar array of $M = 8 \times 8 = 64$ antennas for the i-th RF chain is considered which models a massive MIMO system. Fig. 8.3 shows the sum data-rate of $K =$

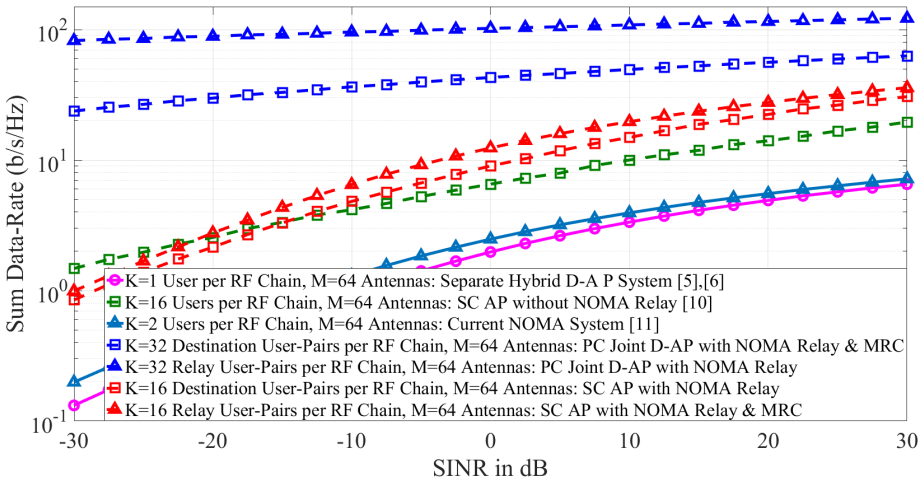

FIGURE 8.3: sum data-rate of 16 destination-users.

16 destination-users in the proposed hybrid D-A P based SC and joint hybrid D-A P based PC systems when using i-th RF chain. Results are reported for an SNR of up to 30dB. In this figure, it can be observed that for all the destination-users, hybrid D-A P based SC and joint D-A P based PC attain higher sum data-rate. This is because the destination-users combine the received signals using MRC that are received over two transmission phases, which improves the their diversity order. Moreover, the joint hybrid D-A P based PC attains the highest sum data-rate as it jointly designs the analog and digital precoder by assigning normalized diagonal weights to the DP matrix, as compared to identity matrix in SC.

Fig. 8.4 compares the sum data-rate of the hybrid D-A P based SC and joint hybrid D-A P based PC systems for all the $K = 16$ relay-users and $K = 16$ destination-users. It can be observed from this figure that the sum data-rate of the relay-users in both hybrid D-A P based SC and joint hybrid D-A P based PC achieve significantly higher

sum data-rate than separate hybrid D-A P systems in [77] and [144]. The higher sum data-rate of the relay-users is due to lower mmWave channel path-loss as compared to the destination-users. The sum data-rate of SC and PC eventually saturate. This is because of the power constraint imposed on the i-th RF chain, whereby adding antenna elements yields diminishing improvement in diversity order at both the relay and destination users.

Fig. 8.4 plots the curves which relate the sum data-rate in the proposed hybrid D-A P based SC and joint hybrid D-A P based PC systems, to their respective energy efficiencies (measured in micro-Watts/bits/s). Separate hybrid D-A P system proposed in [77] and [144] is also plotted for comparison. The objective is to obtain an optimum green-point, i.e., an optimum value of energy efficiency that yields the best achievable sum data-rate in the all the systems. This optimum value of energy efficiency, which is also known as the green point, is located at 0.9 micro-watts/bits/s, for a system having a bandwidth of $W = 1$GHz at 60GHz. These curves were modeled using the relationship given below[77]

$$\begin{aligned} \eta_{EE} &= Rate_{sum} / P_{total} \\ &= \frac{R_s}{NP_0 + P_{common} \left(2^{\frac{\eta_{SE}}{N}} - 1\right) \frac{N_0}{\eta_{PA}} \frac{N}{M} + \frac{NMP_{RF_{circuit}}}{W}}, \end{aligned} \tag{8.36}$$

where the parameters in this relationship were $N_0 = 10^{-17}$dBm/Hz (noise power spectral density), $M = 16 \times 16$ (antennas in the i-th RF chain), $P_{RF_{circuit}} = 1$W (power of the RF front end components such as power amplifier), $P_{common} = 100$W (power of the i-th RF chain represented by the DAC in Fig.1), and, $P_0 = 1$W (power

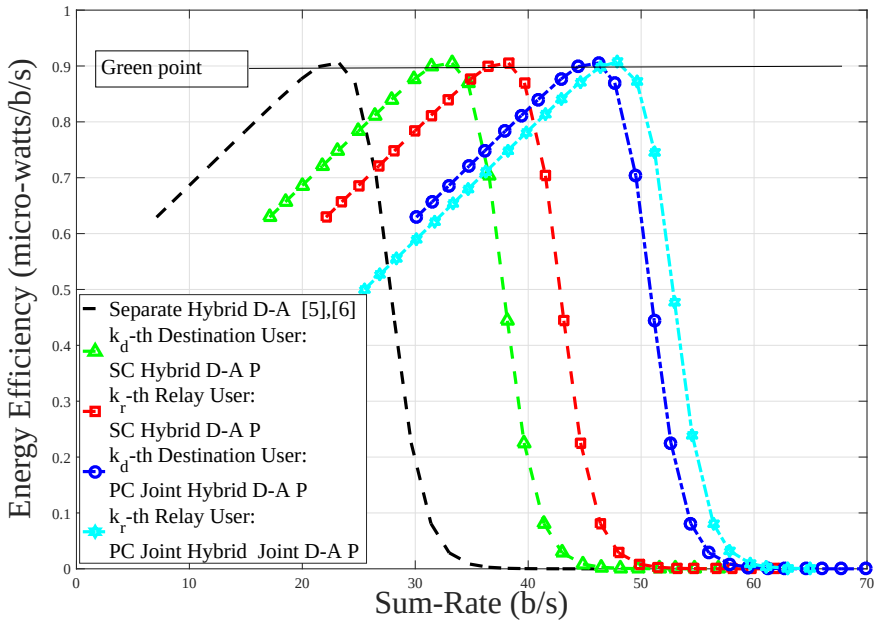

FIGURE 8.4: Energy efficiency vs sum data-rate

of DP corresponding to the i-th RF chain). In Fig. 6, it can be also observed that all the curves attain the same green point of energy efficiency i.e., 0.9 micro-watts/bits/s. This is because the power constraint described earlier by equations (25) and (34) normalizes the energy efficiency of the proposed system to the systems in[77] and [144] for fair comparison.

8.6 Summary

In this paper, novel methods for supporting high user densities in overloaded mmWave systems based on the concept of exploiting NOMA relays along with hybrid D-A P was proposed. Two methods, the hybrid D-A P based SC, and the joint hybrid D-A P based PC, were proposed to design the hybrid D-A P, which could select upto S and K users respectively. When combined with NOMA relay, they could support up to $2S$ and $2K$ user-pairs respectively ($2S, 2K \geq M$), where M is the number of antennas at the RF chain, and hence suited for overloaded systems where the number of users exceed the number of antennas at the BS. This is significantly higher user density when compared to the existing mmWave systems which can support only one user per RF chain, or current NOMA systems which can support only 2 users. From the simulations, it was also observed that the proposed hybrid D-A P based SC and the low complexity joint hybrid D-A P based PC attained higher sum data-rates. Moreover, for a given green point, the proposed methods gained higher sum data-rate as compared to the existing hybrid D-A P massive MIMO mmWave systems.

Chapter 9

Conclusions and Future Work

9.1 Introduction

In this concluding chapter of the thesis, the conclusions have been summarized, and future research which are under active investigation, has been introduced.

9.2 Conclusions

Meteoric rise in the demand for ever higher data-rates along with lower latencies has resulted in the development of fifth generation (5G) cellular networks. Millimeter-wave (mmWave) bands have been adopted to provide wide spectrum for wireless communications[161]. It has been projected that mmWave, operating in the 30 ˘ 300 GHz spectrum, offers a promising approach for meeting spectrum scarcity by providing larger bandwidths[20]. Moreover, short wavelength at mmWave enables packing a large number of antennas in a small aperture area to support massive multiple input and multiple output (MIMO) systems[8]. However, these systems have not explicitly considered high user density that will be prevalent in mmWave environments.

Motivated by this issue, in this thesis, to support high user density in current mmWave systems having M antennas per RF chain, two methods of designing hybrid D-A P based on selection combining (SC) and a low complexity principal component (PC) are proposed, which can support up to $2K$ users per RF chain in the proposed relay mmWave relay system[105].

- Two new hybrid D-A BF algorithms for supporting multiple users at mmWave were proposed. With these employed techniques, each user has its own separate 3D beam assisting in supporting multiple users simultaneously. These algorithms were implemented with the help of selection combining (SC) and principal component (PC).
- The SC algorithm was an analog beamforming (A-BF) technique which modifies the A-BF matrix by designating each and every antenna element to the selected users. The users and antennas are selected depending upon their instantaneous channel state information (CSI). However, the users experienced

multi-user interference (MUI) from the beamformed signals. Therefore, a low complexity MUI cancelling technique was proposed at the receiver (Rx).

- From the simulations, it was be observed that the proposed hybrid D-A BFs using SC and PC algorithms achieved superior capacity gains to other hybrid D-A algorithms as proposed in [77],[144]. Furthermore, the complexities of the SC and the PC algorithms in terms of the number of matrix computations per symbol vectors has been analyzed, and compared it with the existing hybrid D-A BF in [77],[144]. Our proposed hybrid D-A BF algorithms also accounted for the 3D mm-Wave channel for a multi-user system which was generated when planar antenna arrays were deployed.

- A low-complexity adpatation of SC, known as low-complexity selection combining (LC-SC), had been proposed. LC-SC was a space-time A-BF technique which attained lower computational complexity as compared to the SC, yet the reduction in capacity gains were not much.

- Two 3D beamforming algorithms with aim of tracking users in both the azimuth and elevation planes had been proposed. Our proposed beamforming algorithms operated based on the principles of singular value decomposition (SVD) and particle swarm optimization (PSO). Furthermore, these beamforming algorithms were designed to have limited or negligible side lobes, which caused less interference to the other users operating in the same cell. In order to achieve this objective, Kaiser Bessel (KB) filter was adopted which helped in mitigating side lobes in the synthesized beampattern. The proposed algorithms were shown to perform well in achieving high capacity and considerably lower sidelobes.

- In Radio-over-Fiber systems, in order to extend the experimental results of the 60GHz transmission to longer transmission distances, simulation of the indoor experimental environment by applying a LoS extension to the wideband modified Saleh Valenzuela (SV) channel impulse response (CIR) had been successfully considered. The modified SV channel model accurately represents wideband fading in terms of clustered multi-paths, and hence had been chosen over other channel models, such as Rayleigh or Rician channel which are valid only for narrowband propagation environments [64],[7]. Furthermore, other channel models such as WINNER 2, which have been previously used at mmWave, were also narrowband and hence cannot be applied to the 305MHz bandwidth system.

- A low complexity beam allocation (LBA) algorithm had been applied to a switched-beam mmWave system with a limited number of RF chains. Generalized, theoretical beam patterns based on element fed arrays, having an idealized main lobe with fixed beam gain and angular resolution, along with exponentially decaying sidelobes, had been developed. Using these theoretical beam patterns, the performance benefit of switched-beam systems, using the LBA, over comparable fixed-beammmWave systems, which were practically simple but constantly generate fixed numbers of beams, were shown. LBA achieved near optimal sum data-rates, subject to saturation due to interbeam interference at higher transmit powers. Subsequently, measured beam patterns

of a practical mmWave lens antenna system had been applied to show that improved performance was obtained despite high and non-uniform sidelobe levels. The level of sidelobe interference that can be tolerated before system performance is degraded to the level of a fixed beam systems were determined, thereby providing guidance for future antenna and wireless system designers.

9.3 Performance Impairments in Beamforming Assisted Millimeter-Wave Non-Orthogonal Multiple Access Systems due to Far-User AoA Divergence

9.3.1 Network Model

In the proposed downlink network, a centralized mmWave massive MIMO NOMA base station (BS) selects U non-orthogonal groups of mobile-users, as illustrated in Fig. 9.1. User selection and grouping is to be discussed in detail in Section II. Each group is comprised of not more than two mobile-users. The two mobile-users are classified as near-user and far-user respectively, depending upon their radial distance from the BS. Every near-far user-pair within a group are initially assumed to be perfectly spatially (in azimuth) aligned, i.e., having the same azimuth angle-of-departures (AoDs), represented by $\phi_1, \phi_2, \cdots, \phi_u, \cdots, \phi_U$.

It is assumed U_N near-users and U_F far-users, denoted by the sets $\mathcal{U}_\mathcal{N} = \{1_n, \cdots, u_n, \cdots, U_n\}$ and $\mathcal{U}_\mathcal{F} = \{1_f, \cdots, u_f, \cdots, U_f\}$ respectively, are selected from a set of $\mathcal{K} = \{1, \cdots, k, \cdots, K\}$ available users. $|\mathcal{U}_\mathcal{N}| = U_N$, $|\mathcal{U}_\mathcal{F}| = U_F$, $|\mathcal{K}| = K$, $U = 2U_N = 2U_F$, $U_N + U_F < K$, and $\mathcal{U}_\mathcal{N}, \mathcal{U}_\mathcal{F} \subseteq \mathcal{U} \subset K$.

It is further assumed that the near users are radially spread out from the BS. This is represented by the vectors $r_1, r_2, \cdots, r_u, \cdots, r_U$. The near-far user pair separations within the clusters are given by the vectors $r_{1_{n,f}}, r_{2_{n,f}}, \cdots r_{u_{n,f}}, \cdots, r_{U_{n,f}}$.

Since every near-far user-pair within a group has the same AoD, $\angle r_1 = \angle r_{1_{n,f}} = \phi_1; \angle r_2 = \angle r_{2_{n,f}} = \phi_2; \cdots; \angle r_u = \angle r_{u_{n,f}} = \phi_u; \cdots; \angle r_U = \angle r_{U_{n,f}} = \phi_U$. However, $r_1 \neq r_2 \neq \cdots \neq r_u \neq \cdots \neq r_U$ and $r_{1_{n,f}} \neq r_{2_{n,f}} \neq \cdots r_{u_{n,f}} \neq \cdots \neq r_{U_{n,f}}$, i.e., the radial separation of the near-users from the BS, as well as the near-far user-pair separation, need not be equal.

The U groups are initially served by a single beam, each having the same beam-gain G and beam-width ψ. Each beam is able to transmit independent superposed data-streams for two mobile-users per group simultaneously. Therefore, in the u-th group, the u-th beam, will transmit the superposed information given by $w_{N_u} s^n_{N_u} + v_{N_u} s^f_{N_u}$, where w_{N_u},w_{N_u} are the square root of the power allocations for the $s^n_{N_u}$-th data stream (for the near user) and the $s^f_{N_u}$-th data stream (for the far user). Since every beam has the same gain G but serves two users within a group (the corresponding near-far user-pair), initially having the same AoD but separated radially, the near user is assigned less symbol power, and its far user pair is assigned more symbol power

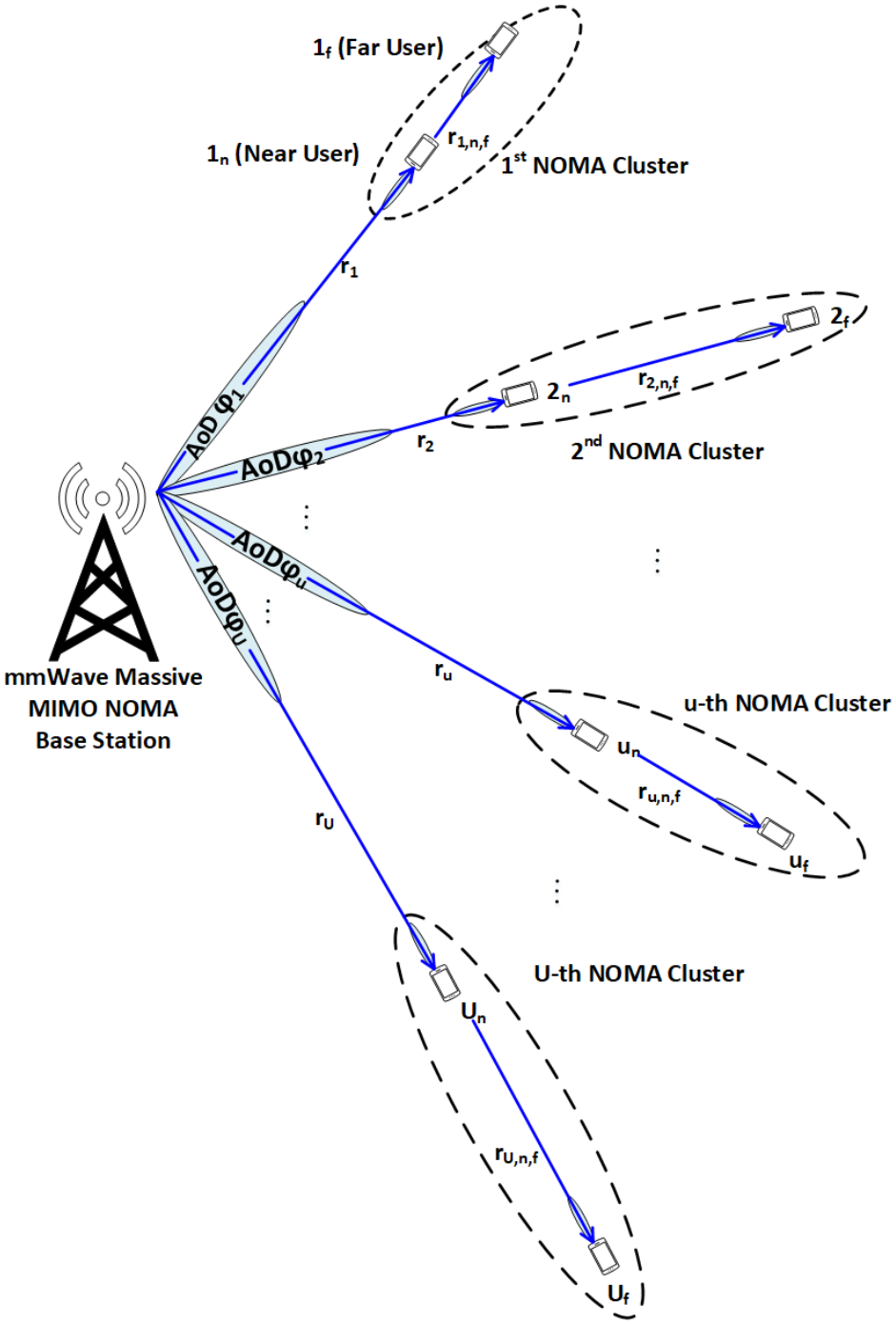

FIGURE 9.1: Network Model for the mmWave Massive MIMO NOMA System. The radial separation of groups from the BS is not constant. Also, the near-far user pair separation is different for different groups.

during superposition coding at the BS. Therefore in the u-th cluster, $w_{N_u} \leq v_{N_u}$. These issues will be addressed in future investigation.

9.3.2 Full-Array BS Structure

The block diagram of the mmWave massive MIMO NOMA base station (BS) is having the full-array structure is shown in Fig. 9.2. At the BS, N_u independent data-symbols for the near-users and far-users, denoted by $\boldsymbol{s}_i^n = [s_1^n, \cdots, s_{N_u}^n]$ and $\boldsymbol{s}_j^f = [s_1^f, \cdots, s_{N_u}^f]$ respectively, are weighted by their respective power allocation vectors $\boldsymbol{w}_i$ and $\boldsymbol{v}_j$, where $\boldsymbol{w}_i \in \mathbb{C}^{N_u \times 1}$ and $\boldsymbol{v}_j \in \mathbb{C}^{N_u \times 1}$. The weighted symbols are then combined by vector addition to form N_u streams of $\boldsymbol{s}$, which can be represented as

$$\boldsymbol{s} = \sum_{i \in \mathcal{U}_\mathcal{N}} \boldsymbol{w}_i \boldsymbol{s}_i + \sum_{j \in \mathcal{U}_\mathcal{F}} \boldsymbol{v}_j \boldsymbol{s}_j. \tag{9.1}$$

(9.1) is a linear operation representing superposition coding, where the two sets of data symbols weighted by their respective powers are combined. For both sets of data symbols, Gaussian inputs are assumed, i.e. $\boldsymbol{s}_i^n, i \in \mathcal{U}_\mathcal{N}$ and $\boldsymbol{s}_j^f, j \in \mathcal{U}_\mathcal{F}$ are independent and identically distributed (i.i.d.) circularly symmetric complex Gaussian (CSCG) random variables which satisfy $\mathbb{E}[|\boldsymbol{s}_i^n|^2], \mathbb{E}[|\boldsymbol{s}_j^f|^2] = \frac{1}{N_u}\boldsymbol{I}_{N_u}$, respectively. Furthermore, assuming that the power allocation vectors at the BS have the symbol transmit power constraint of P_s, then from (8.36), since $\boldsymbol{x}$ is linear,

$$\mathbb{E}\left[\boldsymbol{s}^H \boldsymbol{s}\right] = \left(\sum_{i \in U_N} \|\boldsymbol{w}_i^2\| + \sum_{j \in U_F} \|\boldsymbol{v}_j^2\| \right) \leq P_s = \sum_{u=1}^{U} \left(r_u^{-\gamma} + r_{u_{n,f}}^{-\gamma} \right), \tag{9.2}$$

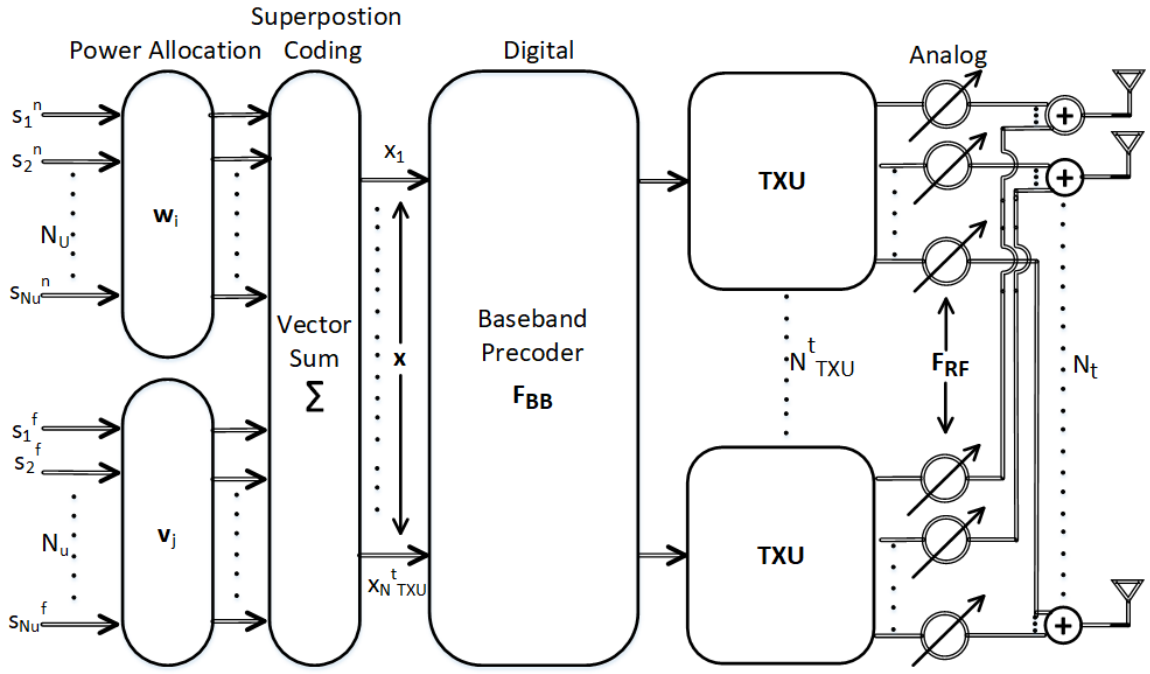

FIGURE 9.2: mmWave Massive MIMO NOMA BS: Full-Array Structure.

where γ is the distance dependent path-loss at mmWave. As stated earlier, $r_u^{-\gamma}$ and $r_{u_{n,f}}$ are the radial separation of the u-th near user in the u-th group to the BS, and the separation between the u-th near-far user pair, respectively. (8.37) implies that symbol powers $\boldsymbol{w}_i^2$ and $\boldsymbol{v}_j^2$ are allocated adaptively, depending upon the radial distance of the near user as well as near-far user-pair separation within a group, which is in-turn served by a single beam. Power management is also a subject of active investigation in a future work.

The BS is equipped with T downlink transmit units (TXU's) and a massive MIMO uniform linear array (ULA) of N_t transmit antennas. As employing TXUs is considered expensive, the number of TXUs T is not large and is assumed to be smaller than the number of available users K. Furthermore, the number of symbol-streams, N_u, for both the near-users and their far-user pairs, will be equal to the number of selected user-groups. Consolidating these assumptions

$$T \leq N_u = U = 2U_N = 2U_F < K \ll N_t. \tag{9.3}$$

Such a full-array BS enables simultaneous multi-stream communication to U groups of users via U beams. The full-array structure also allows the BS to apply a block diagonalizing baseband precoder $\boldsymbol{F}_{BB} = [\boldsymbol{f}_{BB,1}, \boldsymbol{f}_{BB,2}, \cdots, \boldsymbol{f}_{BB,N_u}]$ using its T TXU's, where $\boldsymbol{F}_{BB} \in \mathbb{C}^{T \times N_u}$ and $\boldsymbol{f}_{BB,u} \in \mathbb{C}^{T \times 1}$. This is followed by an RF precoder $\boldsymbol{F}_{RF} = [\boldsymbol{f}_{RF,1}, \boldsymbol{f}_{RF,2}, \cdots, \boldsymbol{f}_{RF,N_t}]$ which is implemented using analog phase shifters, where $\boldsymbol{F}_{RF} \in \mathbb{C}^{N_t \times T}$ and $\boldsymbol{f}_{RF,u} \in \mathbb{C}^{N^t \times 1}$. Since $\boldsymbol{F}_{RF}$ is implemented using analog phase shifters, its elements are constrained to satisfy the non-convex constant modulus constraint

$$\|\boldsymbol{F}_{RF}\|_F = \sqrt{\sum_{m,n} |[\boldsymbol{F}]_{m,n}|^2} = \sqrt{\mathrm{Tr}\big(\boldsymbol{F}_{RF}\boldsymbol{F}_{RF}^H\big)} = \frac{1}{N_t} \tag{9.4}$$

This implies that all the elements of $\boldsymbol{F}_{RF}$ have equal norm. Representing $\boldsymbol{x} = \boldsymbol{F}_{RF}\boldsymbol{F}_{BB}$ as the linear BF signal of N_u symbol streams, the BS's total power constraint is enforced by normalizing $\boldsymbol{F}_{BB}$ such that $\mathrm{Tr}\big(\mathbb{E}\big[\boldsymbol{x}\boldsymbol{x}^H\big]\big) = \|\boldsymbol{F}_{RF}\boldsymbol{F}_{BB}\|_F^2 = N_u$.

$$\|\boldsymbol{F}_{RF}\boldsymbol{F}_{BB}\|_F^2 \cdot \left(\sum_{i \in U_N} \|\boldsymbol{w}_i^2\| + \sum_{j \in U_F} \|\boldsymbol{v}_j^2\| \right) = N_u \cdot P_{BB}^t, \text{ where } \|\boldsymbol{F}_{RF}\boldsymbol{F}_{BB}\|^2 = N_u \tag{9.5}$$

Fig. 9.3 shows the u_n-th near user and the u_f-th far user in the u-th group, where $1 \leq u \leq U$, each having a massive MIMO linear array of N_r receive antennas, $N_r < N_t$, followed by constant modulus analog precoders $\boldsymbol{f}_{MS_{u,n}}$ and $\boldsymbol{f}_{MS_{u,f}}$ respectively. Each user has a single receive unit (RXU). $\boldsymbol{f}_{MSu,n}, \boldsymbol{f}_{MSu,f} \in \mathbb{C}^{N_r \times 1}$. The constant modulus constraints are enforced as $\|\boldsymbol{f}_{MS_{u,n}}\|, \|\boldsymbol{f}_{MSu,f}\| = N_r^{-1}$. In the u-th group,

the received signal of the near user u_n after analog precoding can be represented as

$$
\begin{aligned}
\boldsymbol{y}_{u,n} &= \boldsymbol{f}_{MS_{u,n}}^{H}\boldsymbol{H}_{u,n}(\phi_u)\boldsymbol{F}_{RF}\boldsymbol{F}_{BB}\left(\sum_{i\in\mathcal{U}_{\mathcal{N}}}\boldsymbol{w}_i^{H}+\sum_{j\in\mathcal{U}_{\mathcal{F}}}\boldsymbol{v}_j^{H}\right)+\boldsymbol{f}_{MS_{u,n}}^{H}\boldsymbol{n}_{u,n}\\
&= \boldsymbol{f}_{MS_{u,n}}^{H}\boldsymbol{H}_{u,n}(\phi_u)\sum_{u=1}^{U}\boldsymbol{F}_{RF}\boldsymbol{f}_{BB,u}\left(\sum_{i\in\mathcal{U}_{\mathcal{N}}}\boldsymbol{w}_i^{H}+\sum_{j\in\mathcal{U}_{\mathcal{F}}}\boldsymbol{v}_j^{H}\right)+\boldsymbol{f}_{MS_{u,n}}^{H}\boldsymbol{n}_{u,n}\\
&= \underbrace{\boldsymbol{f}_{MS_{u,n}}^{H}\boldsymbol{H}_{u,n}(\phi_u)\boldsymbol{F}_{RF}\boldsymbol{f}_{BB,u}\boldsymbol{w}_{u_n}^{H}}_{\text{desired signal at near-user } u_n}+\underbrace{\boldsymbol{f}_{MS_{u,n}}^{H}\boldsymbol{H}_{u,n}(\phi_u)\boldsymbol{F}_{RF}\boldsymbol{f}_{BB,u}\boldsymbol{v}_{u_f}^{H}}_{\text{interference due to far-user pair } u_f}\\
&\quad+\underbrace{\boldsymbol{f}_{MS_{u,n}}^{H}\boldsymbol{H}_{u,n}(\phi_u)\sum_{q=1,q\neq u}^{U}\boldsymbol{F}_{RF}\boldsymbol{f}_{BB,q}\left(\sum_{g\in\mathcal{U}_{\mathcal{N}}\setminus u_n}\boldsymbol{w}_g^{H}+\sum_{h\in\mathcal{U}_{\mathcal{F}}\setminus u_f}\boldsymbol{v}_h^{H}\right)}_{\text{total inter-beam-interference}}+\underbrace{\boldsymbol{f}_{MS_{u,n}}^{H}\boldsymbol{n}_{u,n}}_{\text{noise}}\\
&= \underbrace{\boldsymbol{f}_{MS_{u,n}}^{H}\boldsymbol{H}_{u,n}(\phi_u)\boldsymbol{F}_{RF}\boldsymbol{f}_{BB,u}\boldsymbol{w}_{u_n}^{H}}_{\text{desired signal at near-user } u_n}+\underbrace{\boldsymbol{f}_{MS_{u,n}}^{H}\boldsymbol{H}_{u,n}(\phi_u)\boldsymbol{F}_{RF}\boldsymbol{f}_{BB,u}\boldsymbol{v}_{u_f}^{H}}_{\text{interference due to far-user pair } u_f}\\
&\quad+\underbrace{\boldsymbol{f}_{MS_{u,n}}^{H}\boldsymbol{H}_{u,n}(\phi_u)\sum_{q=1,q\neq u}^{U}\boldsymbol{F}_{RF}\boldsymbol{f}_{BB,q}\left(\sum_{g\in\mathcal{U}_{\mathcal{N}}\setminus u_n}\boldsymbol{w}_g^{H}\right)}_{\text{inter-beam-interference due to remaining near-users}}\\
&\quad+\underbrace{\boldsymbol{f}_{MS_{u,n}}^{H}\boldsymbol{H}_{u,n}(\phi_u)\sum_{q=1,q\neq u}^{U}\boldsymbol{F}_{RF}\boldsymbol{f}_{BB,q}\left(\sum_{h\in\mathcal{U}_{\mathcal{F}}\setminus u_f}\boldsymbol{v}_h^{H}\right)}_{\text{inter-beam-interference due to all the far-users}}+\underbrace{\boldsymbol{f}_{MS_{u,n}}^{H}\boldsymbol{n}_{u,n}}_{\text{noise}}.
\end{aligned}
\tag{9.6}
$$

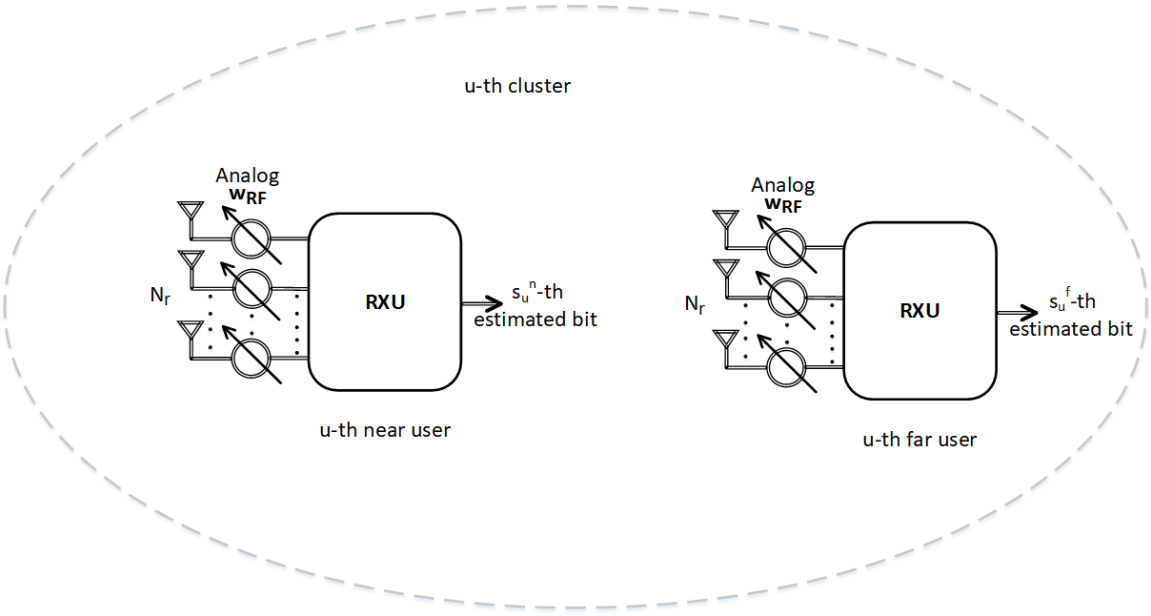

FIGURE 9.3: u_n-th near-user and u_f-th far-user within the u-th group.

In (9.6), $\boldsymbol{n}_{u,n} \sim \mathcal{CN}(0, \sigma_n^2)$ is the i.i.d Gaussian noise vectors at the near user in the u-th group. $\boldsymbol{H}_{u,n}(\phi)$ is the beam-domain 2D mmWave channel given by [64]

$$\boldsymbol{H}_{u,n}(\phi_u) = \sqrt{N_t N_r} r_u^{-\gamma} \boldsymbol{a}_{MS,n}(\phi_{u,n}) \boldsymbol{a}_{BS}^H(\phi_u), \tag{9.7}$$

where ϕ_u denotes the angle-of-departure (AoD) of u-th beam to the u_n-th near user user and $r_u^{-\gamma}$, as stated earlier, is the radial distance vector from the BS to to the u_n-th user. $\phi_{u,n} \in \{-\pi/2, \pi/2\}$ is the beam-angle of the u_n-th near-user user. Since it is assumed that initially, every near-far user-pair is perfectly aligned in azimuth, $\phi_u = \phi_{u,n}$.

$\boldsymbol{a}_{MS,n}(\phi_{u,n})$ and $\boldsymbol{a}_{BS}(\phi_u)$ are the uniform linear antenna array (ULA) response vectors of the u,n-th near user in the u-th group and the BS respectively, generating 2D beams. The array response vector at the BS $\boldsymbol{a}_{BS}(\phi_u)$ is given as

$$\boldsymbol{a}_{BS}(\phi_u) = \frac{1}{\sqrt{N_t}} [1, e^{j\frac{2\pi}{\lambda} d \sin(\phi_u)}, \cdots, e^{j\frac{2\pi}{\lambda}(N_t-1)\sin(\phi_u)}]^H, \tag{9.8}$$

where λ is the wavelength at mmWave frequency of operation and $d = 0.5\lambda$ is the decorrelated antenna element spacing. Similarly,

$$\boldsymbol{a}_{MS,n}(\phi_{u,n}) = \frac{1}{\sqrt{N_r}} [1, e^{j\frac{2\pi}{\lambda} d \sin(\phi_{u,n})}, \cdots, e^{j\frac{2\pi}{\lambda}(N_t-1)\sin(\phi_{u,n})}]^H. \tag{9.9}$$

By following a similar procedure as above, the received signals of the far user u_f in the u-th group after analog precoding can be derived as

$$\begin{aligned}
\boldsymbol{y}_{u,f} = & \underbrace{\boldsymbol{f}_{MS_{u,f}}^H \boldsymbol{H}_{u,f}(\phi_u) \boldsymbol{F}_{RF} \boldsymbol{f}_{BB,u} \boldsymbol{w}_{u_n}^H}_{\text{interference from near-user pair } u_n} + \underbrace{\boldsymbol{f}_{MS_{u,f}}^H \boldsymbol{H}_{u,f}(\phi_u) \boldsymbol{F}_{RF} \boldsymbol{f}_{BB,u} \boldsymbol{v}_{u_f}^H}_{\text{desired signal at far-user } u_f} \\
& + \underbrace{\boldsymbol{f}_{MS_{u,f}}^H \boldsymbol{H}_{u,f}(\phi_u) \sum_{q=1, q\neq u}^{U} \boldsymbol{F}_{RF} \boldsymbol{f}_{BB,q} \left(\sum_{g \in \mathcal{U}_{\mathcal{N}} \setminus u_n} \boldsymbol{w}_g^H \right)}_{\text{inter-beam-interference from remaining near-users}} \\
& + \underbrace{\boldsymbol{f}_{MS_{u,f}}^H \boldsymbol{H}_{u,f}(\phi_u) \sum_{q=1, q\neq u}^{U} \boldsymbol{F}_{RF} \boldsymbol{f}_{BB,q} \left(\sum_{h \in \mathcal{U}_{\mathcal{F}} \setminus u_f} \boldsymbol{v}_h^H \right)}_{\text{inter-beam-interference from remaining far-users}} + \underbrace{\boldsymbol{f}_{MS_{u,f}}^H \boldsymbol{n}_{u,f}}_{\text{noise}}.
\end{aligned} \tag{9.10}$$

where $\boldsymbol{n}_{u,f} \sim \mathcal{CN}(0, \sigma_f^2)$ is the i.i.d Gaussian noise vectors at the far user in the u-th group. The beam domain 2D mmWave channel for the far-user $\boldsymbol{H}_{u,f}(\phi)$ is given by

$$\boldsymbol{H}_{u,f}(\phi_u) = \sqrt{N_t N_r} \left(r_u^{-\gamma} + r_{u_{n,f}}^{-\gamma} \right) \boldsymbol{a}_{MS,f}(\phi_{u,f}) \boldsymbol{a}_{BS}^H(\phi_u), \tag{9.11}$$

where $r_{u_{n,f}}^{-\gamma}$ is the radial distance vector from the u_n-th near-user to its far-user pair u_f in the u-th group. It should be noted that because of the assumption of AoD alignment between the near-far user-pairs in all the U groups, initially, in the u-th group, $\phi_u = \phi_{u,n} = \phi_{u,f}$. Hence, $\angle r_u^{-\gamma} = r_{u_{n,f}}^{-\gamma} = \phi_u$, and therefore, $r_u^{-\gamma} + r_{u_{n,f}}^{-\gamma}$ represents a scalar addition of radial distances, as shown in Fig. 9.4. Lastly, it is clear

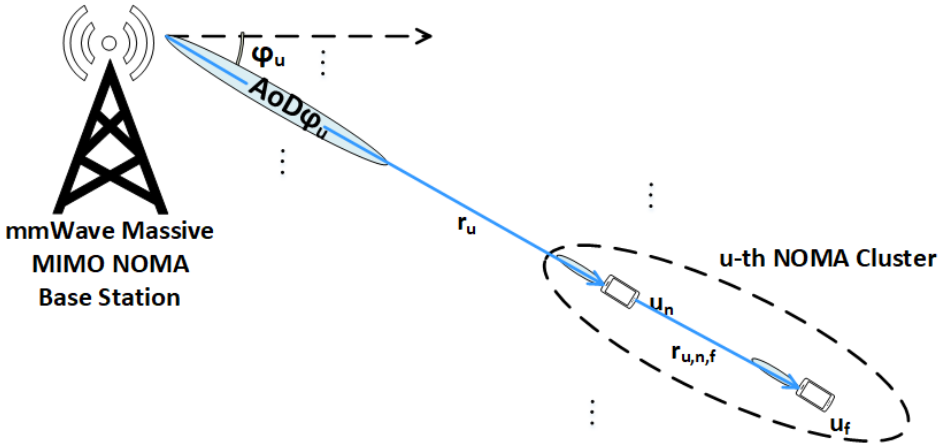

FIGURE 9.4: Assumption of initial AoA alignment between the u_n-th near-user and its u_f-th far-user pair in the u-th group. The vectors $r_u^{-\gamma}$ and $r_{u_{n,f}}^{-\gamma}$ have the same AoD ϕ_u, producing a scalar addition $r_u^{-\gamma} + r_{u_{n,f}}^{-\gamma}$.

from (9.7) and (9.11) that

$$\frac{|\boldsymbol{H}_{u,f}(\phi_u)|}{|\boldsymbol{H}_{u,n}(\phi_u)|} = 1 + \frac{r_{u_{n,f}}^{-\gamma}}{r_u^{-\gamma}}, \text{ if } \phi_{u,n} = \phi_{u,f} = \phi_u; \forall u \in \mathcal{U}, u_i n \in \mathcal{U}_{\mathcal{N}}, u_f \in \mathcal{U}_{\mathcal{F}}. \tag{9.12}$$

This proves that channel for the u_n-th near-user $\boldsymbol{H}_{u,n}(\phi_u)$, and the channel for it's far-user pair u_f, in any group $u \in \mathcal{U}$, are not linearly independent. This is an important result which will be used in a future investigation.

Further research efforts being investigaed include hybrid D-A BF design for mmWave massive MIMO NOMA dwonlink, implementing successive interference cancellation (SIC) in this system, user selection and pairing, beam search-angle user-association, near-user selection, far-user pairing, hybrid D-A BF design, developing the zero-interference constraint (ZIC), interference nulling, far-user angle-of-departure (AoD) divergence with respect to its near user pair, the resulting performance impairments (due to far user's AoD divergence), and last but not the least, adaptive power management and compensation in such a system.

Bibliography

[1] In: *Part 15.3: Wireless MAC and PHY Specifications for High Rate WPANs. Amendment 2: Millimeter-Wave-Based Alternative Physical Layer Extension* (2009).

[2] In: *Part 11: Wireless LAN Medium Access Control (MAC) and Physical Layer (PHY) Specifications. Amendment 3: Enhancements for Very High Throughput in the 60 GHz Band* (2012).

[3] A. Matlshev et al. "Channel Models for IEEE 802.11a". In: *IEEE 802.11-15/1150r9* (2016).

[4] M. Agiwal, A. Roy, and N. Saxena. "Next Generation 5G Wireless Networks: A Comprehensive Survey". In: *IEEE Communications Surveys Tutorials* 18.3 (2016), pp. 1617–1655. ISSN: 1553-877X. DOI: 10.1109/COMST.2016.2532458.

[5] Q. Z. Ahmed and L. L. Yang. "Reduced-rank adaptive multiuser detection in hybrid direct-sequence time-hopping ultrawide bandwidth systems". In: *IEEE Transactions on Wireless Communications* 9.1 (2010), pp. 156–167. ISSN: 1536-1276. DOI: 10.1109/TWC.2010.01.081172.

[6] Q. Z. Ahmed et al. "Compression and Combining Based on Channel Shortening and Reduced-Rank Techniques for Cooperative Wireless Sensor Networks". In: *IEEE Transactions on Vehicular Technology* 63.1 (2014), pp. 72–81. ISSN: 0018-9545. DOI: 10.1109/TVT.2013.2272061.

[7] Q.Z. Ahmed and Lie-Liang Yang. "Reduced-rank adaptive multiuser detection in hybrid direct-sequence time-hopping ultrawide bandwidth systems". In: *IEEE Transactions on Wireless Communications* 9.1 (2010), pp. 156–167. ISSN: 1536-1276. DOI: 10.1109/TWC.2010.01.081172.

[8] M. R. Akdeniz et al. "Millimeter Wave Channel Modeling and Cellular Capacity Evaluation". In: *IEEE Journal on Selected Areas in Communications* 32.6 (2014), pp. 1164–1179. ISSN: 0733-8716.

[9] C. Jiannong et al. "5G new radio (NR): Standard and technology". In: *Int. ICT R&D J.* 15 (2017), pp. 1–72.

[10] J. Ala-Laurinaho et al. "2-D Beam-Steerable Integrated Lens Antenna System for 5G*E*-Band Access and Backhaul". In: *IEEE Transactions on Microwave Theory and Techniques* 64.7 (2016), pp. 2244–2255. ISSN: 0018-9480. DOI: 10.1109/TMTT.2016.2574317.

[11] A. Alkhateeb and R. W. Heath. "Frequency Selective Hybrid Precoding for Limited Feedback Millimeter Wave Systems". In: *IEEE Transactions on Communications* PP.99 (2016), pp. 1–1. ISSN: 0090-6778. DOI: 10.1109/TCOMM.2016.2549517.

[12] A. Alkhateeb, G. Leus, and R. W. Heath. "Limited Feedback Hybrid Precoding for Multi-User Millimeter Wave Systems". In: *IEEE Transactions on*

Wireless Communications 14.11 (2015), pp. 6481–6494. ISSN: 1536-1276. DOI: 10.1109/TWC.2015.2455980.

[13] A. Alkhateeb, G. Leus, and R. W. Heath. "Multi-Layer Precoding: A Potential Solution for Full-Dimensional Massive MIMO Systems". In: *IEEE Transactions on Wireless Communications* 16.9 (2017), pp. 5810–5824. ISSN: 1536-1276. DOI: 10.1109/TWC.2017.2716362.

[14] A. Alkhateeb et al. "Channel Estimation and Hybrid Precoding for Millimeter Wave Cellular Systems". In: *IEEE Journal of Selected Topics in Signal Processing* 8.5 (2014), pp. 831–846. ISSN: 1932-4553. DOI: 10.1109/JSTSP.2014.2334278.

[15] A. Alkhateeb et al. "Hybrid Precoding for Millimeter Wave Cellular Systems with Partial Channel Knowledge". In: (2013), pp. 1–5. DOI: 10.1109/ITA.2013.6522603.

[16] A. Alkhateeb et al. "MIMO Precoding and Combining Solutions for Millimeter-Wave Systems". In: *IEEE Communications Magazine* 52.12 (2014), pp. 122–131. ISSN: 0163-6804. DOI: 10.1109/MCOM.2014.6979963.

[17] A. Alkhateeb et al. "MIMO Precoding and Combining Solutions for Millimeter-Wave Systems". In: *IEEE Communications Magazine* 52.12 (2014), pp. 122–131. ISSN: 0163-6804. DOI: 10.1109/MCOM.2014.6979963.

[18] A. Alkhateeb et al. "Single-sided adaptive estimation of multi-path millimeter wave channels". In: (2014), pp. 125–129. ISSN: 1948-3244. DOI: 10.1109/SPAWC.2014.6941330.

[19] O. Alluhaibi et al. "Hybrid Digital-to-Analog Precoding Design for mm-Wave Systems". In: *to appear in IEEE International Conference on Communications (ICC)* (2017). ISSN: 1053-587X. DOI: 10.1109/TSP.2011.2140112.

[20] P. V. Amadori and C. Masouros. "Low RF-Complexity Millimeter-Wave Beamspace-MIMO Systems by Beam Selection". In: *IEEE Transactions on Communications* 63.6 (2015), pp. 2212–2223. ISSN: 0090-6778. DOI: 10.1109/TCOMM.2015.2431266.

[21] X. An et al. "Beam switching support to resolve link-blockage problem in 60 GHz WPANs". In: (2009), pp. 390–394. ISSN: 2166-9570. DOI: 10.1109/PIMRC.2009.5449837.

[22] "Applications Of Antenna Arrays To Mobile Communications, Part I: Performance Improvement, Feasibility, And System Considerations". In: *Proceedings of the IEEE* 85.7 (1997), pp. 1029–1030. ISSN: 0018-9219. DOI: 10.1109/JPROC.1997.611114.

[23] D. C. Araújo et al. "Channel estimation for millimeter-wave Very-Large MIMO systems". In: (2014), pp. 81–85. ISSN: 2076-1465.

[24] O. E. Ayach et al. "Low complexity precoding for large millimeter wave MIMO systems". In: (2012), pp. 3724–3729. ISSN: 1938-1883. DOI: 10.1109/ICC.2012.6363634.

[25] O. E. Ayach et al. "The capacity optimality of beam steering in large millimeter wave MIMO systems". In: (2012), pp. 100–104. ISSN: 1948-3252. DOI: 10.1109/SPAWC.2012.6292865.

[26] O. El Ayach et al. “Multimode precoding in millimeter wave MIMO transmitters with multiple antenna sub-arrays”. In: (2013), pp. 3476–3480. ISSN: 1930-529X. DOI: 10.1109/GLOCOM.2013.6831611.

[27] D. Bai et al. “Beam Selection Gain from Butler Matrices”. In: (2008), pp. 1–5. ISSN: 1090-3038. DOI: 10.1109/VETECF.2008.107.

[28] W. U. Bajwa et al. “Compressed Channel Sensing: A New Approach to Estimating Sparse Multipath Channels”. In: *Proceedings of the IEEE* 98.6 (2010), pp. 1058–1076. ISSN: 0018-9219. DOI: 10.1109/JPROC.2010.2042415.

[29] C. Balanis. “Antenna Theory: Analysis and Design”. In: *Hoboken, NJ, USA: Wiley* (2007).

[30] R. Baldemair et al. “Ultra-dense networks in millimeter-wave frequencies”. In: *IEEE Communications Magazine* 53.1 (2015), pp. 202–208. ISSN: 0163-6804. DOI: 10.1109/MCOM.2015.7010535.

[31] E. Björnson, E. G. Larsson, and T. L. Marzetta. “Massive MIMO: ten myths and one critical question”. In: *IEEE Communications Magazine* 54.2 (2016), pp. 114–123. ISSN: 0163-6804. DOI: 10.1109/MCOM.2016.7402270.

[32] T. E. Bogale and L. B. Le. “Beamforming for multiuser massive MIMO systems: Digital versus hybrid analog-digital”. In: (2014), pp. 4066–4071. ISSN: 1930-529X. DOI: 10.1109/GLOCOM.2014.7037444.

[33] J. Brady, N. Behdad, and A. M. Sayeed. “Beamspace MIMO for Millimeter-Wave Communications: System Architecture, Modeling, Analysis, and Measurements”. In: *IEEE Transactions on Antennas and Propagation* 61.7 (2013), pp. 3814–3827. ISSN: 0018-926X. DOI: 10.1109/TAP.2013.2254442.

[34] J. Brady and A. Sayeed. “Beamspace MU-MIMO for high-density gigabit small cell access at millimeter-wave frequencies”. In: (2014), pp. 80–84. ISSN: 1948-3244. DOI: 10.1109/SPAWC.2014.6941321.

[35] J. Capon. “High-resolution frequency-wave number spectrum analysis”. In: *Proc. IEEE* 57.8 (1997), pp. 1408–1418.

[36] M. R. Castellanos et al. “Channel-Reconstruction-Based Hybrid Precoding for Millimeter-Wave Multi-User MIMO Systems”. In: *IEEE Journal of Selected Topics in Signal Processing* 12.2 (2018), pp. 383–398. ISSN: 1932-4553. DOI: 10.1109/JSTSP.2018.2819135.

[37] L. Chang et al. “Low-Sidelobe Air-Filled Slot Array Fabricated Using Silicon Micromachining Technology for Millimeter-Wave Application”. In: *IEEE Transactions on Antennas and Propagation* 65.8 (2017), pp. 4067–4074. ISSN: 0018-926X. DOI: 10.1109/TAP.2017.2717971.

[38] Z. Chen et al. “Cooperation in 5G Heterogeneous Networking: Relay Scheme Combination and Resource Allocation”. In: *IEEE Transactions on Communications* 64.8 (2016), pp. 3430–3443. ISSN: 0090-6778. DOI: 10.1109/TCOMM.2016.2584044.

[39] L. Cheng et al. “Coordinated Multipoint Transmissions in Millimeter-Wave Radio-Over-Fiber Systems”. In: *Journal of Lightwave Technology* 34.2 (2016), pp. 653–660. ISSN: 0733-8724. DOI: 10.1109/JLT.2015.2480786.

[40] L. Chiu and S. Wu. “Hybrid radio frequency beamforming and baseband precoding for downlink MU-MIMO mmWave channels”. In: (2015), pp. 1346–1351. ISSN: 1550-3607. DOI: 10.1109/ICC.2015.7248510.

[41] J. Choi. "Beam Selection in mm-Wave Multiuser MIMO Systems Using Compressive Sensing". In: *IEEE Transactions on Communications* 63.8 (2015), pp. 2936–2947. ISSN: 0090-6778. DOI: 10.1109/TCOMM.2015.2449860.

[42] J. Choi. "Minimum Power Multicast Beamforming With Superposition Coding for Multiresolution Broadcast and Application to NOMA Systems". In: *IEEE Transactions on Communications* 63.3 (2015), pp. 791–800. ISSN: 0090-6778. DOI: 10.1109/TCOMM.2015.2394393.

[43] J. Choi. "Opportunistic Beamforming With Single Beamforming Matrix for Virtual Antenna Arrays". In: *IEEE Transactions on Vehicular Technology* 60.3 (2011), pp. 872–881. ISSN: 0018-9545. DOI: 10.1109/TVT.2011.2113197.

[44] W. Choi et al. "AV-Band Switched Beam-Forming Antenna Module Using Absorptive Switch Integrated With 4×4 Butler Matrix in 0.13-μmCMOS". In: *IEEE Transactions on Microwave Theory and Techniques* 58.12 (2010), pp. 4052–4059. ISSN: 0018-9480. DOI: 10.1109/TMTT.2010.2086472.

[45] W. Choi et al. "Opportunistic Space-Division Multiple Access With Beam Selection". In: *IEEE Transactions on Communications* 55.12 (2007), pp. 2371–2380. ISSN: 0090-6778. DOI: 10.1109/TCOMM.2007.910702.

[46] Che-Chen Chou and Jen-Ming Wu. "Low-complexity MIMO precoder design with channel decomposition". In: *IEEE Transactions on Vehicular Technology* 60.5 (2011), pp. 2368–2372. ISSN: 0018-9545. DOI: 10.1109/TVT.2011.2151889.

[47] Jaehak Chung et al. "A random beamforming technique in MIMO systems exploiting multiuser diversity". In: *IEEE Journal on Selected Areas in Communications* 21.5 (2003), pp. 848–855. ISSN: 0733-8716. DOI: 10.1109/JSAC.2003.810355.

[48] Cisco. "Cisco Visual Networking Index: Forecast and Methodology, 2014–2019". In: *White Paper [Online]. Available: http://www.cisco.com* (2015).

[49] B. Clerckx et al. "Explicit vs. Implicit Feedback for SU and MU-MIMO". In: (2010), pp. 1–5. ISSN: 1930-529X. DOI: 10.1109/GLOCOM.2010.5683816.

[50] P. Comon and G. H. Golub. "Matrix Computations". In: *The John Hopkins University Press London* (1983).

[51] P. Comon and G. H. Golub. "Tracking a few extreme singular values and vectors in signal processing". In: *Proceedings of the IEEE* 78.8 (1990), pp. 1327–1343. ISSN: 0018-9219. DOI: 10.1109/5.58320.

[52] M. Crocco and A. Trucco. "Design of Superdirective Planar Arrays With Sparse Aperiodic Layouts for Processing Broadband Signals via 3-D Beamforming". In: *IEEE/ACM Transactions on Audio, Speech, and Language Processing* 22.4 (2014), pp. 800–815. ISSN: 2329-9290. DOI: 10.1109/TASLP.2014.2304635.

[53] R. C. Daniels and R. W. Heath. "60 GHz Wireless Communications: Emerging Requirements and Design Recommendations". In: *IEEE Vehicular Technology Magazine* 2.3 (2007), pp. 41–50. ISSN: 1556-6072. DOI: 10.1109/MVT.2008.915320.

[54] Z. Ding, F. Adachi, and H. V. Poor. "The Application of MIMO to Non-Orthogonal Multiple Access". In: *IEEE Transactions on Wireless Communications* 15.1 (2016), pp. 537–552. ISSN: 1536-1276. DOI: 10.1109/TWC.2015.2475746.

[55] Z. Ding, M. Peng, and H. V. Poor. "Cooperative Non-Orthogonal Multiple Access in 5G Systems". In: *IEEE Communications Letters* 19.8 (2015), pp. 1462–1465. ISSN: 1089-7798. DOI: 10.1109/LCOMM.2015.2441064.

[56] Z. Ding, R. Schober, and H. V. Poor. "A General MIMO Framework for NOMA Downlink and Uplink Transmission Based on Signal Alignment". In: *IEEE Transactions on Wireless Communications* 15.6 (2016), pp. 4438–4454. ISSN: 1536-1276. DOI: 10.1109/TWC.2016.2542066.

[57] H. T. Do and S. Y. Chung. "Linear beamforming and superposition coding with common information for the gaussian MIMO broadcast channel". In: *IEEE Transactions on Communications* 57.8 (2009), pp. 2484–2494. ISSN: 0090-6778. DOI: 10.1109/TCOMM.2009.08.070419.

[58] N. T. Do et al. "A BNBF User Selection Scheme for NOMA-Based Cooperative Relaying Systems with SWIPT". In: *IEEE Communications Letters* PP.99 (2016), pp. 1–1. ISSN: 1089-7798. DOI: 10.1109/LCOMM.2016.2631606.

[59] Tuan Do-Hong and P. Russer. "A new design method for digital beamforming using spatial interpolation". In: *IEEE Antennas and Wireless Propagation Letters* 2.1 (2003), pp. 177–181. ISSN: 1536-1225. DOI: 10.1109/LAWP.2003.817612.

[60] M. Dohler et al. "IEEE 5G and Beyond: Technology Roadmap White Paper". In: (2017).

[61] M. Dong et al. "Simulation study on millimeter wave 3D beamforming systems in urban outdoor multi-cell scenarios using 3D ray tracing". In: (2015), pp. 2265–2270. DOI: 10.1109/PIMRC.2015.7343675.

[62] D. L. Donoho. "Compressed sensing". In: *IEEE Transactions on Information Theory* 52.4 (2006), pp. 1289–1306. ISSN: 0018-9448. DOI: 10.1109/TIT.2006.871582.

[63] ECMA International Standard. "ECMA-387 High Rate 60 GHz PHY, MAC and HDMI PALs". In: ().

[64] O. El Ayach et al. "Spatially Sparse Precoding in Millimeter Wave MIMO Systems". In: *IEEE Transactions on Wireless Communications* 13.3 (2014), pp. 1499–1513. ISSN: 1536-1276. DOI: 10.1109/TWC.2014.011714.130846.

[65] S. Farzaneh and A. Sebak. "Microwave Sampling Beamformer—Prototype Verification and Switch Design". In: *IEEE Transactions on Microwave Theory and Techniques* 57.1 (2009), pp. 36–44. ISSN: 0018-9480. DOI: 10.1109/TMTT.2008.2009080.

[66] FCC Document. "Revision of part 15 of the commission's rules". In: (2013).

[67] H. T. Friis. "A note on a simple transmission formula". In: *Proc. IRE* 34.5 (1946), pp. 254–256.

[68] X. Gao et al. "Near-Optimal Beam Selection for Beamspace MmWave Massive MIMO Systems". In: *IEEE Communications Letters* 20.5 (2016), pp. 1054–1057. ISSN: 1089-7798. DOI: 10.1109/LCOMM.2016.2544937.

[69] X. Gao et al. “Reliable Beamspace Channel Estimation for Millimeter-Wave Massive MIMO Systems with Lens Antenna Array”. In: *IEEE Transactions on Wireless Communications* 16.9 (2017), pp. 6010–6021. ISSN: 1536-1276. DOI: 10.1109/TWC.2017.2718502.

[70] Y. Gao et al. “Rotman Lens Based Hybrid Analog–Digital Beamforming in Massive MIMO Systems: Array Architectures, Beam Selection Algorithms and Experiments”. In: *IEEE Transactions on Vehicular Technology* 66.10 (2017), pp. 9134–9148. ISSN: 0018-9545. DOI: 10.1109/TVT.2017.2714693.

[71] A. Goldsmith et al. “Capacity limits of MIMO channels”. In: *IEEE Journal on Selected Areas in Communications* 21.5 (2003), pp. 684–702. ISSN: 0733-8716. DOI: 10.1109/JSAC.2003.810294.

[72] F. B. Gross. “Smart Antenna For Wireless Communication With MATLAB”. In: *McGraw-Hill New York* (2005).

[73] J. Guillory et al. “Radio over Fiber tunnel for 60 GHz wireless home network”. In: (2011), pp. 1–3.

[74] U. Habib et al. “Radio over fiber transport of mm-Wave 2X2 MIMO for spatial diversity and multiplexing”. In: (2016), pp. 39–42. DOI: 10.1109/MWP.2016.7791280.

[75] H. Haci, H. Zhu, and J. Wang. “Performance of non-orthogonal multiple access (NOMA) with a novel asynchronous interference cancellation technique”. In: *To appear in IEEE Transactions on Wireless Communications* (2017). ISSN: 1053-587X. DOI: 10.1109/TSP.2011.2140112.

[76] Shuangfeng Han et al. “Large scale antenna system with hybrid digital and analog beamforming structure”. In: (2014), pp. 842–847. ISSN: 2164-7038. DOI: 10.1109/ICCW.2014.6881305.

[77] Shuangfeng Han et al. “Large-Scale Antenna Systems with Hybrid Analog and Digital Beamforming for Millimeter Wave 5G”. In: *IEEE Communications Magazine* 53.1 (2015), pp. 186–194. ISSN: 0163-6804. DOI: 10.1109/MCOM.2015.7010533.

[78] Y. Han et al. “Design of double codebook based on 3D dual-polarized channel for multiuser MIMO system”. In: *EURASIP J. Adv. Signal Process.* 2014 (2014). DOI: https://doi.org/10.1186/1687-6180-2014-111.

[79] K. Haneda, C. Gustafson, and S. Wyne. “60 GHz Spatial Radio Transmission: Multiplexing or Beamforming?” In: *IEEE Transactions on Antennas and Propagation* 61.11 (2013), pp. 5735–5743. ISSN: 0018-926X. DOI: 10.1109/TAP.2013.2279091.

[80] M. F. Hanif et al. “A Minorization-Maximization Method for Optimizing Sum Rate in the Downlink of Non-Orthogonal Multiple Access Systems”. In: *IEEE Transactions on Signal Processing* 64.1 (2016), pp. 76–88. ISSN: 1053-587X. DOI: 10.1109/TSP.2015.2480042.

[81] C. J. Hansen. “WiGiG: Multi-gigabit wireless communications in the 60 GHz band”. In: *IEEE Wireless Communications* 18.6 (2011), pp. 6–7. ISSN: 1536-1284. DOI: 10.1109/MWC.2011.6108325.

[82] M. Hawes et al. “Bayesian Compressive Sensing Approaches for Direction of Arrival Estimation With Mutual Coupling Effects”. In: *IEEE Transactions on*

Antennas and Propagation 65.3 (2017), pp. 1357–1368. ISSN: 0018-926X. DOI: 10.1109/TAP.2017.2655013.

[83] F. F. He et al. "Low-Cost 60-GHz Smart Antenna Receiver Subsystem Based on Substrate Integrated Waveguide Technology". In: *IEEE Transactions on Microwave Theory and Techniques* 60.4 (2012), pp. 1156–1165. ISSN: 0018-9480. DOI: 10.1109/TMTT.2012.2184127.

[84] J. Hogan and A. Sayeed. "Beam selection for performance-complexity optimization in high-dimensional MIMO systems". In: (2016), pp. 337–342. DOI: 10.1109/CISS.2016.7460525.

[85] K. Hosoya et al. "Multiple Sector ID Capture (MIDC): A Novel Beamforming Technique for 60-GHz Band Multi-Gbps WLAN/PAN Systems". In: *IEEE Transactions on Antennas and Propagation* 63.1 (2015), pp. 81–96. ISSN: 0018-926X. DOI: 10.1109/TAP.2014.2365209.

[86] Z. Hu et al. "Work in progress: 3D beamforming methods with user-specific elevation beamfoming". In: (2014), pp. 383–386. DOI: 10.1109/CHINACOM.2014.7054323.

[87] G. Huang et al. "A Low Profile and Low Sidelobe Wideband Slot Antenna Array Feb by an Amplitude-Tapering Waveguide Feed-Network". In: *IEEE Transactions on Antennas and Propagation* 63.1 (2015), pp. 419–423. ISSN: 0018-926X. DOI: 10.1109/TAP.2014.2365238.

[88] K.C. Huang and Z. Wang. "Millimeterwave Communication Systems". In: *Hoboken, NJ, USA: Wiley/IEEE Press* (2011).

[89] X. Huang, Y. J. Guo, and J. D. Bunton. "A hybrid adaptive antenna array". In: *IEEE Transactions on Wireless Communications* 9.5 (2010), pp. 1770–1779. ISSN: 1536-1276. DOI: 10.1109/TWC.2010.05.091020.

[90] Sooyoung Hur et al. "Millimeter wave beamforming for wireless backhaul and access in small cell networks". In: *IEEE Transactions on Communications* 61.10 (2013), pp. 4391–4403. ISSN: 0090-6778. DOI: 10.1109/TCOMM.2013.090513.120848.

[91] C. I et al. "Toward green and soft: a 5G perspective". In: *IEEE Communications Magazine* 52.2 (2014), pp. 66–73. ISSN: 0163-6804. DOI: 10.1109/MCOM.2014.6736745.

[92] "IEEE 802.11-1999, IEEE Standard for Local and Metropoltian Area Networks – Wireless LAN Medium Access Control (MAC) and Physical Layer (PHY) Specifications, ISO/IEC 8802-11:1999 (E)". In: (1999). DOI: https://doi.org/10.1186/1687-6180-2014-111.

[93] S. Jiang et al. "802.11ad Key Performance Analysis and Its Application in Home Wireless Entertainment". In: (2014), pp. 1595–1598. DOI: 10.1109/CSE.2014.294.

[94] D. H. Johnson and D. E. Dudgeon. "Array Signal Processing: Concepts and Techniques". In: *Englewood Cliffs, NJ, USA: Prentice-Hall* (1993).

[95] A. Kammoun et al. "Preliminary results on 3D channel modeling: from theory to standardization". In: *IEEE Journal on Selected Areas in Communications* 32.6 (2014), pp. 1219–1229. ISSN: 0733-8716. DOI: 10.1109/JSAC.2014.2328152.

[96] F. Khan, Z. Pi, and S. Rajagopal. "Millimeter-wave mobile broadband with large scale spatial processing for 5G mobile communication". In: (2012), pp. 1517–1523. DOI: 10.1109/Allerton.2012.6483399.

[97] F. Khan, Z. Pi, and S. Rajagopal. "Millimeter-wave mobile broadband with large scale spatial processing for 5G mobile communication". In: (2012), pp. 1517–1523. DOI: 10.1109/Allerton.2012.6483399.

[98] M. R. Khawer, J. Tang, and F. Han. "A Proactive Small Cell Interference Mitigation Strategy for Improving Spectral Efficiency of LTE Networks in the Unlicensed Spectrum". In: *IEEE Transactions on Wireless Communications* 15.3 (2016), pp. 2303–2311. ISSN: 1536-1276. DOI: 10.1109/TWC.2015.2502263.

[99] C. Kim, T. Kim, and J. Seol. "Multi-beam transmission diversity with hybrid beamforming for MIMO-OFDM systems". In: (2013), pp. 61–65. ISSN: 2166-0077. DOI: 10.1109/GLOCOMW.2013.6824962.

[100] Jongmok Kim et al. "Design of User Clustering and Precoding for Downlink Non-Orthogonal Multiple Access (NOMA)". In: (2015), pp. 1170–1175. DOI: 10.1109/MILCOM.2015.7357604.

[101] K. Kim et al. "A fast minimum variance beamforming method using principal component analysis". In: *IEEE Transactions on Ultrasonics, Ferroelectrics, and Frequency Control* 61.6 (2014), pp. 930–945. ISSN: 0885-3010. DOI: 10.1109/TUFFC.2014.2989.

[102] Kyuhong Kim et al. "A fast minimum variance beamforming method using principal component analysis". In: *IEEE Transactions on Ultrasonics, Ferroelectrics, and Frequency Control* 61.6 (2014), pp. 930–945. ISSN: 0885-3010. DOI: 10.1109/TUFFC.2014.2989.

[103] H. Krim and M. Viberg. "Two decades of array signal processing research: the parametric approach". In: *IEEE Signal Processing Magazine* 13.4 (1996), pp. 67–94. ISSN: 1053-5888. DOI: 10.1109/79.526899.

[104] R. Kumaresan and A. Shaw. "High resolution bearing estimation without eigen decomposition". In: *ICASSP '85. IEEE International Conference on Acoustics, Speech, and Signal Processing* 10 (1985), pp. 576–579. DOI: 10.1109/ICASSP.1985.1168370.

[105] E. G. Larsson et al. "Massive MIMO for next generation wireless systems". In: *IEEE Communications Magazine* 52.2 (2014), pp. 186–195. ISSN: 0163-6804. DOI: 10.1109/MCOM.2014.6736761.

[106] J. Lee, G. Gil, and Y. H. Lee. "Exploiting spatial sparsity for estimating channels of hybrid MIMO systems in millimeter wave communications". In: (2014), pp. 3326–3331. ISSN: 1930-529X. DOI: 10.1109/GLOCOM.2014.7037320.

[107] Moon-Sik Lee, V. Katkovnik, and Yong-Hoon Kim. "Minimax robust M-beamforming for radar array with antenna switching". In: *IEEE Transactions on Antennas and Propagation* 53.8 (2005), pp. 2549–2557. ISSN: 0018-926X. DOI: 10.1109/TAP.2005.852302.

[108] Y. Leiba et al. "Report on Beam Steerable Directive Antennas". In: *EU H2020 Programme Project: RAPID ICT-643297* (2017). URL: https://kar.kent.ac.uk/71363/.

[109] G. Y. Li et al. "Energy-efficient wireless communications: tutorial, survey, and open issues". In: *IEEE Wireless Communications* 18.6 (2011), pp. 28–35. ISSN: 1536-1284. DOI: 10.1109/MWC.2011.6108331.

[110] Yong Li et al. "Simulation and analysis of 60GHz millimeter-wave propagation characteristics in indoor complex environment". In: (2016), pp. 278–280. DOI: 10.1109/COMPEM.2016.7588613.

[111] L. Liang, W. Xu, and X. Dong. "Low-Complexity Hybrid Precoding in Massive Multiuser MIMO Systems". In: *IEEE Wireless Communications Letters* 3.6 (2014), pp. 653–656. ISSN: 2162-2337. DOI: 10.1109/LWC.2014.2363831.

[112] L. Liu, R. Zhang, and K. C. Chua. "Wireless Information and Power Transfer: A Dynamic Power Splitting Approach". In: *IEEE Transactions on Communications* 61.9 (2013), pp. 3990–4001. ISSN: 0090-6778. DOI: 10.1109/TCOMM.2013.071813.130105.

[113] P. Liu, M. Di Renzo, and A. Springer. "Line-of-Sight Spatial Modulation for Indoor mmWave Communication at 60 GHz". In: *IEEE Transactions on Wireless Communications* 15.11 (2016), pp. 7373–7389. ISSN: 1536-1276. DOI: 10.1109/TWC.2016.2601616.

[114] W. Liu and S. Weiss. "Wideband Beamforming: Concepts and Techniques". In: *Hoboken, NJ, USA: Wiley* (2010).

[115] Y. Liu et al. "Cooperative Non-orthogonal Multiple Access With Simultaneous Wireless Information and Power Transfer". In: *IEEE Journal on Selected Areas in Communications* 34.4 (2016), pp. 938–953. ISSN: 0733-8716. DOI: 10.1109/JSAC.2016.2549378.

[116] H. Lou et al. "A comparison of implicit and explicit channel feedback methods for MU-MIMO WLAN systems". In: (2013), pp. 419–424. ISSN: 2166-9570. DOI: 10.1109/PIMRC.2013.6666172.

[117] D. J. Love and R. W. Heath. "Limited feedback unitary precoding for spatial multiplexing systems". In: *IEEE Transactions on Information Theory* 51.8 (2005), pp. 2967–2976. ISSN: 0018-9448. DOI: 10.1109/TIT.2005.850152.

[118] D.J. Love, R.W. Heath, and T. Strohmer. "Grassmannian beamforming for multiple-input multiple-output wireless systems". In: *IEEE Transactions on Information Theory* 49.10 (2003), pp. 2735–2747. ISSN: 0018-9448. DOI: 10.1109/TIT.2003.817466.

[119] L. Lu et al. "An Overview of Massive MIMO: Benefits and Challenges". In: *IEEE Journal of Selected Topics in Signal Processing* 8.5 (2014), pp. 742–758. ISSN: 1932-4553. DOI: 10.1109/JSTSP.2014.2317671.

[120] V. Madisetti and Eds. D. Williams. "The Digital Signal Processing Handbook". In: 57.8 (1997), pp. 1408–1418.

[121] A. Maltsev et al. "Performance analysis of spatial reuse mode in millimeter-wave WPAN systems with multiple links". In: (2008), pp. 1–4. ISSN: 2166-9570. DOI: 10.1109/PIMRC.2008.4699891.

[122] T. Manabe, Y. Miura, and T. Ihara. "Effects of antenna directivity and polarization on indoor multipath propagation characteristics at 60 GHz". In: *IEEE Journal on Selected Areas in Communications* 14.3 (1996), pp. 441–448. ISSN: 0733-8716. DOI: 10.1109/49.490229.

[123] T. Manabe, Y. Miura, and T. Ihara. “Effects of antenna directivity and polarization on indoor multipath propagation characteristics at 60 GHz”. In: *IEEE Journal on Selected Areas in Communications* 14.3 (1996), pp. 441–448. ISSN: 0733-8716. DOI: 10.1109/49.490229.

[124] Xiaohong Mao, Yee Hui Lee, and Boon Chong Ng. “Wideband channel modelling in UHF band for urban area”. In: (2008), pp. 240–244. ISSN: 2154-0217. DOI: 10.1109/ISWCS.2008.4726054.

[125] H. Mehrpouyan et al. “Hybrid millimeter-wave systems: a novel paradigm for hetnets”. In: *IEEE Communications Magazine* 53.1 (2015), pp. 216–221. ISSN: 0163-6804. DOI: 10.1109/MCOM.2015.7010537.

[126] J. Mietzner et al. “Multiple-antenna techniques for wireless communications - a comprehensive literature survey”. In: *IEEE Communications Surveys Tutorials* 11.2 (2009), pp. 87–105. ISSN: 1553-877X. DOI: 10.1109/SURV.2009.090207.

[127] J. Moghaddasi and K. Wu. “Millimeter-Wave Multifunction Multiport Interferometric Receiver for Future Wireless Systems”. In: *IEEE Transactions on Microwave Theory and Techniques* 66.3 (2018), pp. 1452–1466. ISSN: 0018-9480. DOI: 10.1109/TMTT.2017.2772927.

[128] B. Mondal et al. “3D channel model in 3GPP”. In: *IEEE Communications Magazine* 53.3 (2015), pp. 16–23. ISSN: 0163-6804. DOI: 10.1109/MCOM.2015.7060514.

[129] H. Q. Ngo, E. G. Larsson, and T. L. Marzetta. “Energy and Spectral Efficiency of Very Large Multiuser MIMO Systems”. In: *IEEE Transactions on Communications* 61.4 (2013), pp. 1436–1449. ISSN: 0090-6778. DOI: 10.1109/TCOMM.2013.020413.110848.

[130] T. Nishio et al. “A high-speed adaptive antenna array with simultaneous multibeam-forming capability”. In: *IEEE Transactions on Microwave Theory and Techniques* 51.12 (2003), pp. 2483–2494. ISSN: 0018-9480. DOI: 10.1109/TMTT.2003.819770.

[131] Y. Niu et al. “Boosting Spatial Reuse via Multiple-Path Multihop Scheduling for Directional mmWave WPANs”. In: *IEEE Transactions on Vehicular Technology* 65.8 (2016), pp. 6614–6627. ISSN: 0018-9545. DOI: 10.1109/TVT.2015.2479633.

[132] J. Nsenga, A. Bourdoux, and F. Horlin. “Mixed Analog/Digital Beamforming for 60 GHz MIMO Frequency Selective Channels”. In: (2010), pp. 1–6. ISSN: 1938-1883. DOI: 10.1109/ICC.2010.5502689.

[133] J. Nsenga et al. “Joint Transmit and Receive Analog Beamforming in 60 GHz MIMO Multipath Channels”. In: (2009), pp. 1–5. ISSN: 1938-1883. DOI: 10.1109/ICC.2009.5199125.

[134] H. Osman et al. “Achievable Rate Evaluation of In-Building Distributed Antenna Systems”. In: *IEEE Transactions on Wireless Communications* 12.7 (2013), pp. 3510–3521. ISSN: 1536-1276. DOI: 10.1109/TWC.2013.060513.121755.

[135] Seok-Hwan Park et al. “A new beamforming structure based on transmit-MRC for closed-loop MIMO systems”. In: *IEEE Transactions on Communications* 57.6 (2009), pp. 1847–1856. ISSN: 0090-6778. DOI: 10.1109/TCOMM.2009.06.070520.

[136] C. E. Patterson et al. “A 60-GHz Active Receiving Switched-Beam Antenna Array With Integrated Butler Matrix and GaAs Amplifiers”. In: *IEEE Transactions on Microwave Theory and Techniques* 60.11 (2012), pp. 3599–3607. ISSN: 0018-9480. DOI: 10.1109/TMTT.2012.2213834.

[137] Z. Pi and F. Khan. “System design and network architecture for a millimeter-wave mobile broadband (MMB) system”. In: (2011), pp. 1–6. DOI: 10.1109/SARNOF.2011.5876444.

[138] M. A. Piqueras et al. “Optically beamformed beam-switched adaptive antennas for fixed and mobile broad-band wireless access networks”. In: *IEEE Transactions on Microwave Theory and Techniques* 54.2 (2006), pp. 887–899. ISSN: 0018-9480. DOI: 10.1109/TMTT.2005.863049.

[139] J. Qiao et al. “MAC-Layer Concurrent Beamforming Protocol for Indoor Millimeter-Wave Networks”. In: *IEEE Transactions on Vehicular Technology* 64.1 (2015), pp. 327–338. ISSN: 0018-9545. DOI: 10.1109/TVT.2014.2320830.

[140] T. Quinlan and S. Walker. “A 16.8dBi quasi-discoidal radiation pattern antenna array for 60GHz non-line-of-sight applications”. In: (2014), pp. 210–213. DOI: 10.1109/LAPC.2014.6996360.

[141] V. Raghavan, J. J. Choi, and D. J. Love. “Design Guidelines for Limited Feedback in the Spatially Correlated Broadcast Channel”. In: *IEEE Transactions on Communications* 63.7 (2015), pp. 2524–2540. ISSN: 0090-6778. DOI: 10.1109/TCOMM.2015.2442978.

[142] D. Ramasamy, S. Venkateswaran, and U. Madhow. “Compressive tracking with 1000-element arrays: A framework for multi-Gbps mm wave cellular downlinks”. In: (2012), pp. 690–697. DOI: 10.1109/Allerton.2012.6483285.

[143] T. S. Rappaport et al. “Millimeter Wave Mobile Communications for 5G Cellular: It Will Work!” In: *IEEE Access* 1 (2013), pp. 335–349. ISSN: 2169-3536. DOI: 10.1109/ACCESS.2013.2260813.

[144] W. Roh et al. “Millimeter-Wave Beamforming as an Enabling Technology for 5G Cellular Communications: Theoretical Feasibility and Prototype Results”. In: *IEEE Communications Magazine* 52.2 (2014), pp. 106–113. ISSN: 0163-6804. DOI: 10.1109/MCOM.2014.6736750.

[145] R. Roy and T. Kailath. “ESPRIT-Estimation of signal parameters via rotation invariance techniques”. In: *IEEE Transactions on Acoustic and Speech Signal Processing* 37.7 (1989), pp. 984–995.

[146] C. Rusu et al. “Low complexity hybrid sparse precoding and combining in millimeter wave MIMO systems”. In: (2015), pp. 1340–1345. ISSN: 1550-3607. DOI: 10.1109/ICC.2015.7248509.

[147] E.L. Santos, M.D. Zoltowski, and M. Rangaswamy. “Indirect dominant mode rejection: A solution to low sample support beamforming”. In: *IEEE Transactions on Signal Processing* 55.7 (2007), pp. 3283–3293. ISSN: 1053-587X. DOI: 10.1109/TSP.2007.893926.

[148] A. Sayeed and N. Behdad. “Continuous aperture phased MIMO: Basic theory and applications”. In: (2010), pp. 1196–1203. DOI: 10.1109/ALLERTON.2010.5707050.

[149] A. M. Sayeed. "Deconstructing multiantenna fading channels". In: *IEEE Transactions on Signal Processing* 50.10 (2002), pp. 2563–2579. ISSN: 1053-587X. DOI: 10.1109/TSP.2002.803324.

[150] R. Schmidt. "Multiple emitter location and signal parameter estimation". In: *IEEE Transactions on Antennas and Propagation* 34.3 (1986), pp. 276–280. ISSN: 0018-926X. DOI: 10.1109/TAP.1986.1143830.

[151] M. Sharif and B. Hassibi. "On the capacity of MIMO broadcast channels with partial side information". In: *IEEE Transactions on Information Theory* 51.2 (2005), pp. 506–522. ISSN: 0018-9448. DOI: 10.1109/TIT.2004.840897.

[152] N. Sharma and L. H. Ozarow. "A study of opportunism for multiple-antenna systems". In: *IEEE Transactions on Information Theory* 51.5 (2005), pp. 1804–1814. ISSN: 0018-9448. DOI: 10.1109/TIT.2005.846410.

[153] J. Shen et al. "Repeater-enhanced millimeter-wave systems in multi-path environments". In: (2015), pp. 769–774. DOI: 10.1109/PIMRC.2015.7343401.

[154] H. Shokri-Ghadikolaei, L. Gkatzikis, and C. Fischione. "Beam-searching and transmission scheduling in millimeter wave communications". In: (2015), pp. 1292–1297. ISSN: 1550-3607. DOI: 10.1109/ICC.2015.7248501.

[155] S. Singh et al. "Millimeter Wave WPAN: Cross-Layer Modeling and Multi-Hop Architecture". In: (2007), pp. 2336–2340. ISSN: 0743-166X. DOI: 10.1109/INFCOM.2007.276.

[156] F. Sohrabi and W. Yu. "Hybrid digital and analog beamforming design for large-scale MIMO systems". In: (2015), pp. 2929–2933. ISSN: 1520-6149. DOI: 10.1109/ICASSP.2015.7178507.

[157] In Keun Son et al. "On frame-based scheduling for directional mmWave WPANs". In: (2012), pp. 2149–2157. ISSN: 0743-166X. DOI: 10.1109/INFCOM.2012.6195598.

[158] P. Stoica and A. Nehorai. "MUSIC, maximum likelihood, and Cramer-Rao bound". In: *IEEE Transactions on Acoustics, Speech, and Signal Processing* 37.5 (1989), pp. 720–741. ISSN: 0096-3518. DOI: 10.1109/29.17564.

[159] P. Stoica and A. Nehorai. "MUSIC, maximum likelihood, and Cramer-Rao bound: further results and comparisons". In: *IEEE Transactions on Acoustics, Speech, and Signal Processing* 38.12 (1990), pp. 2140–2150. ISSN: 0096-3518. DOI: 10.1109/29.61541.

[160] P. Sudarshan et al. "Channel Statistics-Based RF Pre-Processing with Antenna Selection". In: *IEEE Transactions on Wireless Communications* 5.12 (2006), pp. 3501–3511. ISSN: 1536-1276. DOI: 10.1109/TWC.2006.256973.

[161] S. Sun et al. "MIMO for Millimeter-Wave Wireless Communications: Beamforming, Spatial Multiplexing, or Both?" In: *IEEE Communications Magazine* 52.12 (2014), pp. 110–121. ISSN: 0163-6804. DOI: 10.1109/MCOM.2014.6979962.

[162] Shu Sun et al. "MIMO for Millimeter-Wave Wireless Communications: Beamforming, Spatial multiplexing, or Both". In: *IEEE Communications Magazine* 52.12 (2014), pp. 110–121. ISSN: 0163-6804. DOI: 10.1109/MCOM.2014.6979962.

[163] A. L. Swindlehurst et al. "Millimeter-wave massive MIMO: the next wireless revolution?" In: *IEEE Communications Magazine* 52.9 (2014), pp. 56–62. ISSN: 0163-6804. DOI: 10.1109/MCOM.2014.6894453.

[164] T. S. Rappaport and R. W. Heath Jr. and R. C. Daniels and J. N. Murdock. "Millimeter Wave Wireless Communications". In: *Englewood Cliffs, NJ, USA: Prentice-Hall* (2014).

[165] T. A. Thomas et al. "3D mmWave Channel Model Proposal". In: (2014), pp. 1–6. ISSN: 1090-3038. DOI: 10.1109/VTCFall.2014.6965800.

[166] E. Torkildson, U. Madhow, and M. Rodwell. "Indoor Millimeter Wave MIMO: Feasibility and Performance". In: *IEEE Transactions on Wireless Communications* 10.12 (2011), pp. 4150–4160. ISSN: 1536-1276. DOI: 10.1109/TWC.2011.092911.101843.

[167] H. L. Van Trees. "Part IV of Estimation and Modulation Theory: Optimum Array Processing". In: *Hoboken, NJ, USA: Wiley* (2004).

[168] J. A. Tropp and A. C. Gilbert. "Signal Recovery From Random Measurements Via Orthogonal Matching Pursuit". In: *IEEE Transactions on Information Theory* 53.12 (2007), pp. 4655–4666. ISSN: 0018-9448. DOI: 10.1109/TIT.2007.909108.

[169] N. Valliappan, A. Lozano, and R. W. Heath. "Antenna Subset Modulation for Secure Millimeter-Wave Wireless Communication". In: *IEEE Transactions on Communications* 61.8 (2013), pp. 3231–3245. ISSN: 0090-6778. DOI: 10.1109/TCOMM.2013.061013.120459.

[170] B. D. Van Veen and K. M. Buckley. "Beamforming: a versatile approach to spatial filtering". In: *IEEE ASSP Magazine* 5.2 (1988), pp. 4–24. ISSN: 0740-7467. DOI: 10.1109/53.665.

[171] V. Venkateswaran and A. van der Veen. "Analog Beamforming in MIMO Communications With Phase Shift Networks and Online Channel Estimation". In: *IEEE Transactions on Signal Processing* 58.8 (2010), pp. 4131–4143. ISSN: 1053-587X. DOI: 10.1109/TSP.2010.2048321.

[172] J. L. Vicario et al. "Beam Selection Strategies for Orthogonal Random Beamforming in Sparse Networks". In: *IEEE Transactions on Wireless Communications* 7.9 (2008), pp. 3385–3396. ISSN: 1536-1276. DOI: 10.1109/TWC.2008.060794.

[173] P. Viswanath, D. N. C. Tse, and R. Laroia. "Opportunistic beamforming using dumb antennas". In: *IEEE Transactions on Information Theory* 48.6 (2002), pp. 1277–1294. ISSN: 0018-9448. DOI: 10.1109/TIT.2002.1003822.

[174] J. Wang, H. Zhu, and N. J. Gomes. "Distributed Antenna Systems for Mobile Communications in High Speed Trains". In: *IEEE Journal on Selected Areas in Communications* 30.4 (2012), pp. 675–683. ISSN: 0733-8716. DOI: 10.1109/JSAC.2012.120502.

[175] J. Wang et al. "Low-Complexity Beam Allocation for Switched-Beam Based Multiuser Massive MIMO Systems". In: *IEEE Transactions on Wireless Communications* 15.12 (2016), pp. 8236–8248. ISSN: 1536-1276. DOI: 10.1109/TWC.2016.2613517.

[176] Junyi Wang et al. "Beam codebook based beamforming protocol for multi-Gbps millimeter-wave WPAN systems". In: *IEEE Journal on Selected Areas*

in Communications 27.8 (2009), pp. 1390–1399. ISSN: 0733-8716. DOI: 10.1109/JSAC.2009.091009.

[177] L. Wang et al. "Secure communication in cellular networks: The benefits of millimeter wave mobile broadband". In: (2014), pp. 115–119. ISSN: 1948-3244. DOI: 10.1109/SPAWC.2014.6941328.

[178] H. Wei et al. "Mutual Coupling Calibration for Multiuser Massive MIMO Systems". In: *IEEE Transactions on Wireless Communications* 15.1 (2016), pp. 606–619. ISSN: 1536-1276. DOI: 10.1109/TWC.2015.2476467.

[179] WGA-D1.0. "Wireless gigabit alliance draft specification". In: (2010).

[180] WirelessHD. "Specification Version 1.1 Overview". In: (2010).

[181] S. Wu et al. "Robust Hybrid Beamforming with Phased Antenna Arrays for Downlink SDMA in Indoor 60 GHz Channels". In: *IEEE Transactions on Wireless Communications* 12.9 (2013), pp. 4542–4557. ISSN: 1536-1276. DOI: 10.1109/TWC.2013.072313.121749.

[182] S. Wyne et al. "Beamforming Effects on Measured mm-Wave Channel Characteristics". In: *IEEE Transactions on Wireless Communications* 10.11 (2011), pp. 3553–3559. ISSN: 1536-1276. DOI: 10.1109/TWC.2011.083111.100195.

[183] M. Xia, Y. Wu, and S. Aissa. "Non-Orthogonal Opportunistic Beamforming: Performance Analysis and Implementation". In: *IEEE Transactions on Wireless Communications* 11.4 (2012), pp. 1424–1433. ISSN: 1536-1276. DOI: 10.1109/TWC.2012.020812.110311.

[184] P. Xia et al. "Multi-Stage Iterative Antenna Training for Millimeter Wave Communications". In: (2008), pp. 1–6. ISSN: 1930-529X. DOI: 10.1109/GLOCOM.2008.ECP.908.

[185] Z. Xiao, L. Bai, and J. Choi. "Iterative Joint Beamforming Training with Constant-Amplitude Phased Arrays in Millimeter-Wave Communications". In: *IEEE Communications Letters* 18.5 (2014), pp. 829–832. ISSN: 1089-7798. DOI: 10.1109/LCOMM.2014.040214.140351.

[186] Y. Xin et al. "Area Spectral Efficiency and Area Energy Efficiency of Massive MIMO Cellular Systems". In: *IEEE Transactions on Vehicular Technology* 65.5 (2016), pp. 3243–3254. ISSN: 0018-9545. DOI: 10.1109/TVT.2015.2436896.

[187] Hao Xu, V. Kukshya, and T.S. Rappaport. "Spatial and Temporal Characteristics of 60-GHz Indoor Channels". In: *IEEE Journal on Selected Areas in Communications* 20.3 (2002), pp. 620–630. ISSN: 0733-8716. DOI: 10.1109/49.995521.

[188] G. Yan and D. P. Liu. "An anti-blocking scheme with spatial reuse for mmWave wireless networks". In: (2012), pp. 1–6. DOI: 10.1109/WCSP.2012.6542834.

[189] H. Yang et al. "Impact Analysis of Directional Antennas and Multiantenna Beamformers on Radio Transmission". In: *IEEE Transactions on Vehicular Technology* 57.3 (2008), pp. 1695–1707. ISSN: 0018-9545. DOI: 10.1109/TVT.2007.907308.

[190] L. Yang, Y. Zeng, and R. Zhang. "Channel Estimation for Millimeter-Wave MIMO Communications With Lens Antenna Arrays". In: *IEEE Transactions*

on Vehicular Technology 67.4 (2018), pp. 3239–3251. ISSN: 0018-9545. DOI: 10.1109/TVT.2017.2779828.

[191] S. K. Yong and C. Chong. "An overview of multigigabit wireless through millimeter wave technology: Potentials and technical challenges". In: *EURASIP Journal Wireless Communication Networks* 2007 (2006, article ID 78907), pp. 202–208.

[192] Su-Khiong Yong, Pengfei Xia, and Alberto Valdes-Garcia. "60GHz Technology for Gbps WLAN and WPAN: From Theory to Practice". In: (2011). DOI: 10.1002/9780470972946.ch1. URL: https://ieeexplore.ieee.org/document/8045322.

[193] Y. Zeng, L. Yang, and R. Zhang. "Multi-User Millimeter Wave MIMO With Full-Dimensional Lens Antenna Array". In: *IEEE Transactions on Wireless Communications* 17.4 (2018), pp. 2800–2814. ISSN: 1536-1276. DOI: 10.1109/TWC.2018.2803180.

[194] Y. Zeng and R. Zhang. "Millimeter Wave MIMO With Lens Antenna Array: A New Path Division Multiplexing Paradigm". In: *IEEE Transactions on Communications* 64.4 (2016), pp. 1557–1571. ISSN: 0090-6778. DOI: 10.1109/TCOMM.2016.2533490.

[195] Y. Zeng, R. Zhang, and Z. N. Chen. "Electromagnetic Lens-Focusing Antenna Enabled Massive MIMO: Performance Improvement and Cost Reduction". In: *IEEE Journal on Selected Areas in Communications* 32.6 (2014), pp. 1194–1206. ISSN: 0733-8716. DOI: 10.1109/JSAC.2014.2328151.

[196] H. Zhang et al. "Interference management for heterogeneous networks with spectral efficiency improvement". In: *IEEE Wireless Communications* 22.2 (2015), pp. 101–107. ISSN: 1536-1284. DOI: 10.1109/MWC.2015.7096292.

[197] R. Zhang and C. K. Ho. "MIMO Broadcasting for Simultaneous Wireless Information and Power Transfer". In: *IEEE Transactions on Wireless Communications* 12.5 (2013), pp. 1989–2001. ISSN: 1536-1276. DOI: 10.1109/TWC.2013.031813.120224.

[198] X. Zhang et al. "Improving network throughput in 60GHz WLANs via multi-AP diversity". In: (2012), pp. 4803–4807. ISSN: 1938-1883. DOI: 10.1109/ICC.2012.6364506.

[199] Xinying Zhang, A. F. Molisch, and Sun-Yuan Kung. "Variable-phase-shift-based RF-baseband codesign for MIMO antenna selection". In: *IEEE Transactions on Signal Processing* 53.11 (2005), pp. 4091–4103. ISSN: 1053-587X. DOI: 10.1109/TSP.2005.857024.

[200] Q. Zhao and J. Li. "Rain attenuation in millimeter wave ranges". In: *Proc. Int. Symp. Antennas Propag. EM Theory* (2006), pp. 1–4.

[201] X. Zheng et al. "MIMO Transmit Beamforming Under Uniform Elemental Power Constraint". In: *IEEE Transactions on Signal Processing* 55.11 (2007), pp. 5395–5406. ISSN: 1053-587X. DOI: 10.1109/TSP.2007.896058.

[202] L. Zhou and Y. Ohashi. "Efficient codebook-based MIMO beamforming for millimeter-wave WLANs". In: (2012), pp. 1885–1889. ISSN: 2166-9589. DOI: 10.1109/PIMRC.2012.6362659.

[203] G. Zhu et al. “Hybrid Beamforming via the Kronecker Decomposition for the Millimeter-Wave Massive MIMO Systems”. In: *IEEE Journal on Selected Areas in Communications* 35.9 (2017), pp. 2097–2114. ISSN: 0733-8716. DOI: 10.1109/JSAC.2017.2720099.

[204] H. Zhu. “Performance Comparison Between Distributed Antenna and Microcellular Systems”. In: *IEEE Journal on Selected Areas in Communications* 29.6 (2011), pp. 1151–1163. ISSN: 0733-8716. DOI: 10.1109/JSAC.2011.110604.

[205] M. Zhu et al. “Radio-Over-Fiber Access Architecture for Integrated Broadband Wireless Services”. In: *Journal of Lightwave Technology* 31.23 (2013), pp. 3614–3620. ISSN: 0733-8724. DOI: 10.1109/JLT.2013.2286564.